A. R. A. P.

AERONAUTICAL RESEARCH ASSOCIATES of PRINCETON, INC.

(14) Rept. no. ARAP-63

~~ARAP REPORT NO. 63~~

(6) EXPERIMENTS ON FREE AND IMPINGING UNDEREXPANDED JETS FROM A CONVERGENT NOZZLE,

(10) by
Richard S. Snedeker
and
Coleman duP. Donaldson ,

Sponsored by
Advanced Research Projects Agency
Ballistics Missile Defense Systems Branch
(16) ARPA Order ~~No.~~ 149-60

This research was supported by the Advanced Research Projects Agency, Ballistic Missile Defense Systems Branch, and was monitored by ~~the U. S. Naval Research Laboratory~~ (Code 6240) under (15) Contract ~~No.~~ Nonr-3903(00)(X), (00)(X).

(5) Aeronautical Research Associates of Princeton, Inc., N. J.
~~50 Washington Road, Princeton, New Jersey~~

(11) Sept~~ember~~ 1964,

edc

ABSTRACT

Experiments were performed in which the velocity profiles and decay and spreading properties of free underexpanded jets of cold air were measured. Stagnation point heat transfer parameters for impingement of these jets on various surface shapes were evaluated and correlations made with the free jet data. Pressure distribution and photographic studies of the free and impinging jets revealed that an unusual separated flow phenomenon can exist under certain impingement conditions. Problems associated with changes in jet stability and the effects of interference due to geometric arrangement of the apparatus were considered in a qualitative way.

CONTENTS

1. INTRODUCTION

The problem of estimating the stagnation point heat transfer from a jet of hot gas to a cold surface upon which it impinges can be treated by applying the usual techniques of stagnation point heat transfer computation. These solutions are generally expressed with the stagnation point velocity gradient $(du_e/dr)_{r=0}$ as a parameter (see, e.g. [1]). For the case of the impinging jet, this parameter can be readily determined from the pressure distribution measured on the impingement surface. In order to provide suitable data for such determinations, a broad experimental study was made of a number of different jet impingement cases. This study included the impingement of an unheated, turbulent, axially symmetric jet of air on several different surface shapes. The jet, which issued from a convergent nozzle, was run at several pressure ratios, both subsonic and sonic (underexpanded), and the impingement distance was varied through a wide range. The surface shapes used were a convex hemisphere, a flat plate, a concave hemisphere, and a shallow cylindrical cup.

In addition to the stagnation point radial velocity gradient itself, the correlation of this gradient with measured free jet properties was evaluated. One correlation was based on properties of the free jet at the nozzle exit, and another was based on local properties of the free jet at the same location as the impingement surface. These parameters are discussed in 3.2.3.

Although the primary characteristics of turbulent free jets (axial decay, radial spread, etc.) are well known, several interrelated secondary factors which influence their detailed structure should be considered if one is to correlate data resulting from tests made with different nozzles and supporting structures. In the present context, in which it is assumed that solid boundaries may exist within a few

nozzle diameters of the jet source, the most important of these factors are thought to be (a) a dynamic instability effect and (b) a blockage or interference effect. The dynamic instability referred to is characterized by a primarily lateral oscillation or "flapping" of the entire jet flow field, and is to be distinguished from the shear induced instabilities of the turbulent mixing flow field which are, in general, of higher frequency and lower amplitude. The blockage effect is distinguished by changes in core length and spreading rate due to the presence of obstructions in the entrained flow field. Since the external configuration of the nozzle itself can thus be a factor, it is important to consider this effect in determining jet flow field momentum balances. A jet with a coaxial free stream velocity superimposed about it is, in a sense, equivalent to a free jet with a prescribed entrainment flow. Studies which reveal the changes in core length and spreading for different ratios of jet to free stream velocity are thus indicative of some of the effects to be expected due to blockage. In addition to the two secondary effects just described, there is an interdependence of the nature of the instability upon structural interference through, for example, the reflection and/or excitation of acoustic disturbances. The aforementioned effects and their qualitative influence on the measurements are discussed more fully in 2.2.4.

In recognition of the importance of the above factors, a thorough experimental survey was made of the same free jets that were used in the impingement studies using the identical test setup. In this way, it was hoped that more meaningful correlations of impingement heat transfer parameters could be obtained.

Also of interest, in the over-all program, was the evaluation of effects due to the shock structure present in the core of underexpanded jets. Decay and spreading parameters

were determined for a number of combinations of jet pressure ratio (subsonic and underexpanded) and axial location. The results of this free jet study as well as a general discussion of free jet structure are presented in Section 2. The impingement studies and the correlations based on the free jet data are treated in Section 3.

2. FREE JET STUDIES

2.1. Structure of the turbulent axially symmetric free jet.

Although an extensive literature on the structure of turbulent free jets exists (see, e.g. [2]), relatively little quantitative information is available on decay and spreading behavior for underexpanded cases [3,4,5,17,23]. Analytical and semi-empirical methods for determining these characteristics have usually been restricted to either subsonic or properly expanded supersonic jets. In the present study, however, it is of interest to determine not only the local details of the flow within the jet core, but the effects of underexpansion on decay and spreading rates in the downstream portions of the jet. Only recently has interest in the characteristics of rocket exhaust plumes at high altitudes and in space spurred efforts to understand such structural details. Some specific problems which have been studied involve pressure, thermal, and shock interference effects on adjacent structure, as well as vehicle stability effects, and the blocking of communication signals due to ionization radiation in the plume. The emphasis, however, has been on the determination of initial spreading boundaries of the plume and the strength and location of the initial shock structure [6-17,21,22,24,25,26] rather than decay processes. Other recent studies have been concerned with jet applications in the fluid amplifier field [18] and the interrelation between underexpanded jet stability and associated sound generation phenomena [19].

The general structural features of turbulent free jet flows are well known. If we consider the flow issuing from a simple, circular, convergent nozzle*, three major variations

*Because of the specific interest in underexpanded jets, the convergent nozzle was considered to be well suited to a study of basic effects since there is no dependence of the degree of underexpansion on area ratio or nozzle divergence angle. The following discussion is thus limited to convergent nozzle flows, and the description of certain aspects such as shock formation is not to be considered general.

of the flow pattern are possible, depending upon the pressure ratio through the nozzle. (Although a properly expanded Mach 1 jet can exist in principle, it is not treated in the present discussion.) The idealized structural features of each of these variations as well as the nomenclature and symbols used to describe these jets throughout the remainder of this report are shown in Figure 1. The pressure ratio values given are for air. A typical schlieren picture of each jet type is shown in Figure 2.

2.1.1. Subsonic jet. A region of turbulent mixing between jet and ambient fluid begins to form a short distance away from the nozzle lip. Radial diffusion or spreading of this region continues both inward and outward as the distance downstream increases until finally the inward diffusion reaches the jet axis. At this point, the "potential" core ends, but the outward diffusion and entrainment of ambient air continue. After a so-called "transition" region, at a point somewhat farther downstream, the decay of axial velocity on the center line and the radial spread of the velocity profile behave in a manner consistant with the self-similarity of velocity profiles from that point on. The jet is now said to be fully developed. For air, the jet will be subsonic for isentropic pressure ratios $1 > p_\infty/p^0_{sc} > .528$. Throughout this range it can be assumed that $p_1/p_\infty = 1$.

It should be noted that an ideally expanded* supersonic jet, which contains no shock waves, has essentially the same structure as the subsonic jet. Effects due to compressibility, however, become much more important in determining the core length and decay.

---

*"Ideally expanded" refers to a properly expanded jet issuing from a nozzle with zero exit divergence angle, i.e. with parallel flow at the exit.

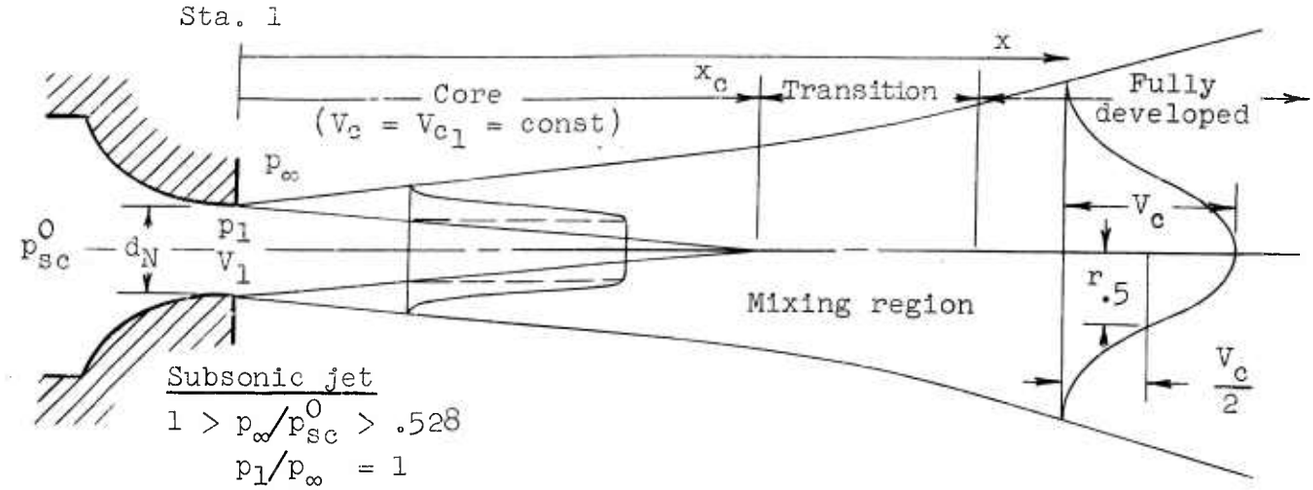

Subsonic jet

$1 > p_\infty/p^o_{sc} > .528$

$p_1/p_\infty = 1$

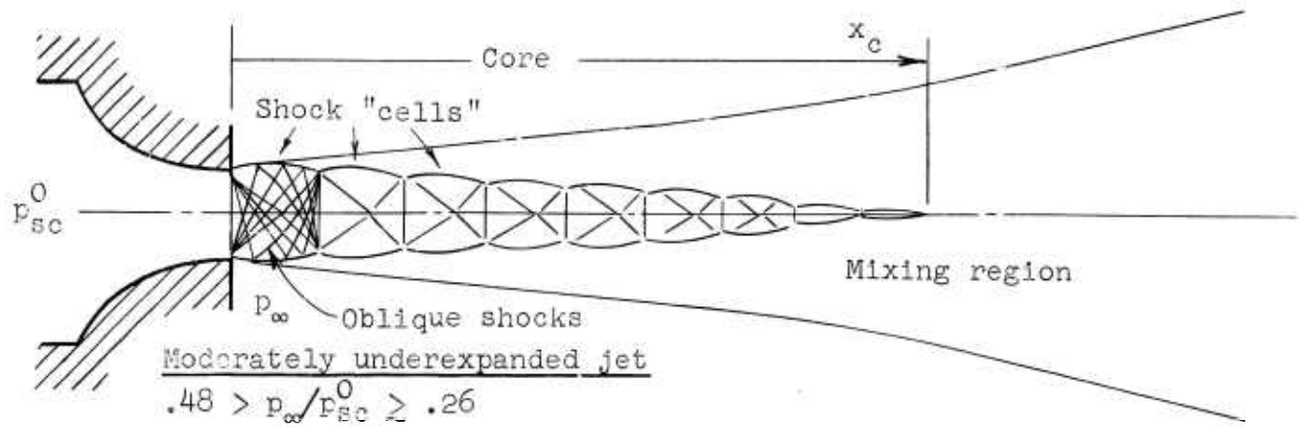

Moderately underexpanded jet

$.48 > p_\infty/p^o_{sc} \geq .26$

$1.1 < p_1/p_\infty \lesssim 2$

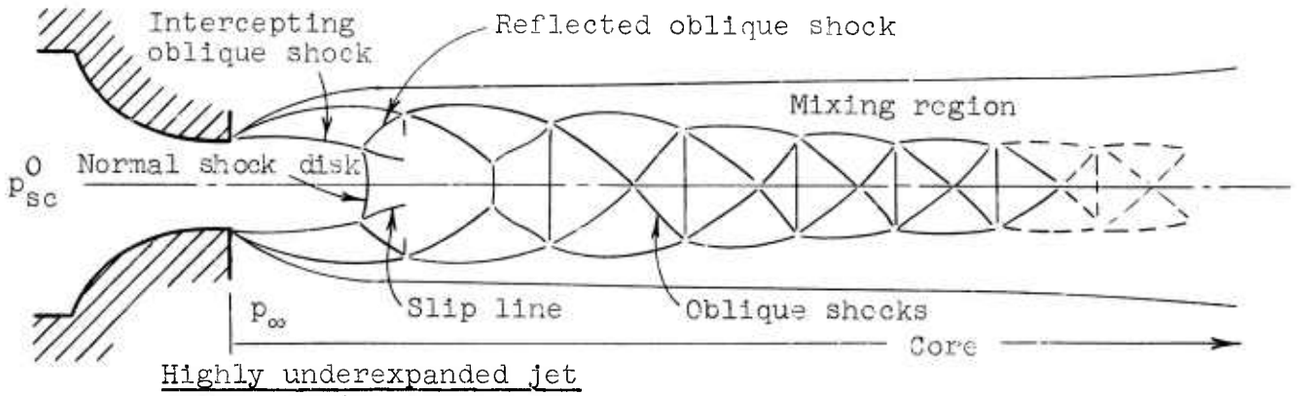

Highly underexpanded jet

$.26 \gtrsim p_\infty/p^o_{sc} > 0$

$2 \lesssim p_1/p_\infty < \infty$

Figure 1. Three major variations of jet flow from a sonic nozzle.

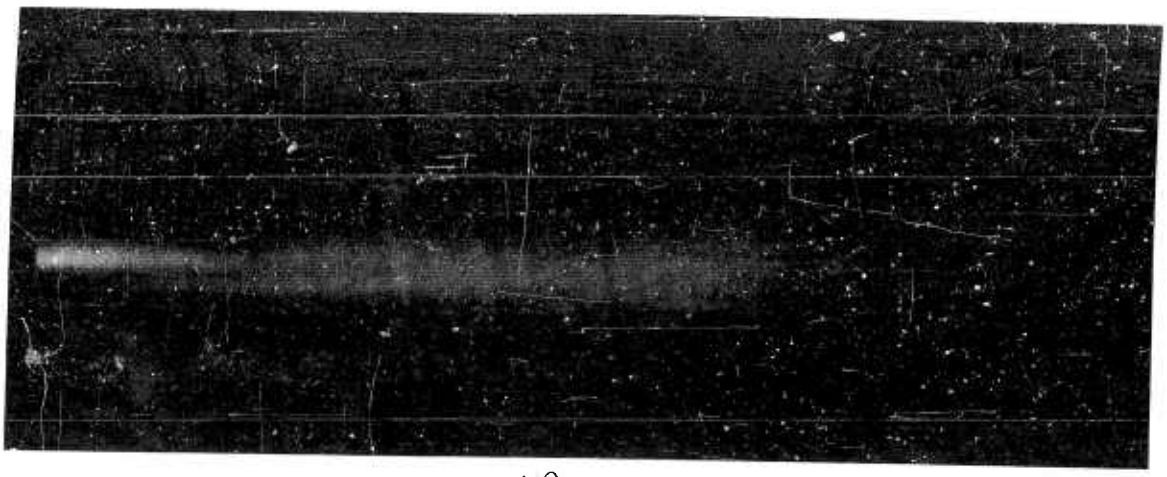

Subsonic jet: $p_\infty / p^0_{sc} = .552$

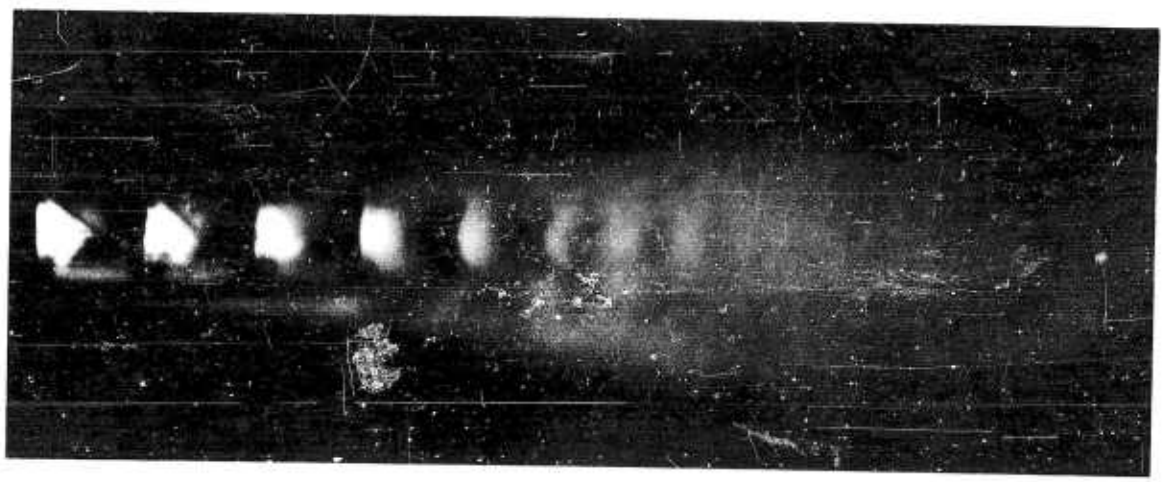

Moderately underexpanded jet: $p_1 / p_\infty = 1.42$

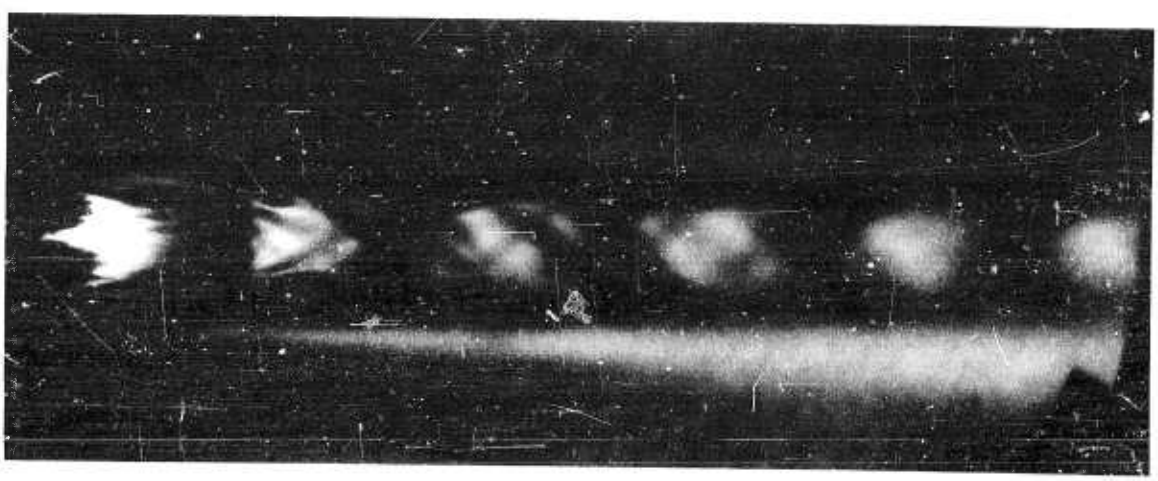

Highly underexpanded jet: $p_1 / p_\infty = 3.57$

Figure 2. Schlieren photographs of typical jet types shown in Figure 1.

2.1.2. Moderately underexpanded jet. When the sonic, or critical, pressure ratio is reached, a very weak normal shock forms at the exit. This shock diminishes in size rapidly with increasing pressure ratio, however, and at $p_1/p_\infty \approx 1.1$ the familiar pattern of "shock diamonds" or "cells" composed of intersecting oblique shocks is established in the core. Except for a lengthening and broadening of the first few cells as jet pressure ratio is increased, this structure persists until $p_1/p_\infty \approx 2$.* The term "moderately underexpanded" is used herein to denote jets within this pressure ratio interval ($1.1 \lesssim p_1/p_\infty \lesssim 2$). Because of the additional expansion required in the unconfined jet flow beyond the nozzle, the boundaries of what was once the potential core, in the subsonic case, are now determined by the requirement of pressure equilibrium between the outermost portion of the flow within the shock structure and the surrounding ambient air. The initial underexpanded condition and the accompanying shock pattern result in a flow which soon becomes overexpanded at a point in the central portion of each cell. In this region, the local Mach number exceeds that which would obtain in a properly expanded jet with the same pressure ratio p_1/p_∞. The inward diffusion of the mixing region, however, does continue, although to a relatively lesser degree at first, and ultimately results in the complete dissipation of the shock dominated core. (In the absence of viscous and shock effects, the flow would continue a sequence of expansion to overexpansion and recompression to underexpansion.) Because of the gradients of pressure, density, and Mach number that exist in the core, the impingement of this portion of such a jet

*Although the value of $p_1/p_\infty \approx 2$, at which the normal shock disk reappears for a sonic exit, has been predicted analytically and verified experimentally by several authors (see, e.g. [11]), any dependence on interference and stability effects does not appear to have been investigated specifically.

might be expected to result in surface pressure distributions that are quite sensitive to impingement distance. Downstream of the core, of course, after the jet has become subsonic, the impingement behavior should be similar to that of a totally subsonic jet.

Within the moderately underexpanded range, effects due to instabilities in the over-all jet flow field are usually found to have an increased influence in determining its decay and spreading characteristics, both actual and measured. This problem is discussed in detail in 2.2.4.

2.1.3. Highly underexpanded jet. At a pressure ratio p_1/p_∞ of approximately 2, the form of the shock structure in the initial cell begins to change. Along the centerline, where the expansion is a maximum, the pressure becomes so low (or the Mach number so high) relative to ambient pressure that the recompression possible in the remainder of the cell through the existing oblique shocks is insufficient to raise the pressure (or lower the Mach number) to the required initial level at the end of the cell. In order to provide the required compression, a normal shock disk forms on the centerline. As the pressure ratio p_1/p_∞ is further increased, this normal shock increases both in strength and diameter. At the same time, the original oblique shock structure is maintained in the periferal region, although altered somewhat in strength and shape due to the additional expansion required and the presence of the normal shock. For very high pressure ratios, the normal shock dominates the structure of the first cell. For example, with $p_1/p_\infty \approx 20$, it comprises about 40 per cent of the total cross-sectional area within the jet boundaries [11]. It has also been found [11] that the pressure ratio at which the normal shock disk reappears is not invariant with exit Mach number and nozzle angle. The value $p_1/p_\infty \approx 2$ applies only to a sonic nozzle.

Immediately downstream of the normal shock, the flow is subsonic. Since the surrounding flow in the oblique shock region remains supersonic, a slip line exists at the boundary between the two concentric regions. For a fairly high degree of underexpansion, say $p_1/p_\infty \simeq 4$, the central subsonic region is quickly accelerated so that approximately sonic conditions prevail near the beginning of the second cell. In this case, the second cell may resemble the first and even require its own normal shock. For very high pressure ratios, the structure just downstream of the first cell is not well defined (for a recent investigation, see [17]). However, it is probable that the jet will be dominated for some distance downstream by the very strong normal shock in the first cell. Ultimately, it decays through a structure with only oblique shocks. The mixing region surrounds the core as usual, but its radial diffusion rate is small at first with the result that the effective core of the highly underexpanded jet can be extremely long. It should be noted that while a strict definition of core length for any underexpanded jet may be given as the point at which the shock structure disappears, effects due to the instabilities present make this point difficult to define for a real jet. The downstream behavior in such cases, therefore, is best given in terms of the point at which the core's influence ceases. As in the case of other jet strengths, this may be taken as the point beyond which velocity profiles are self similar.

2.2. Experimental program.

Since each of the three major jet variations described above was expected to exhibit an impingement behavior somewhat different from the others, a typical case representative of each regime was chosen for detailed study. Values of radial spread and axial decay for each of these jets were

used later to correlate the results of impingement measurements made using jets with these same strengths. The jets used to provide these correlation data are listed below. The pressure ratio for each is given in two ways, viz. p_∞/p^0_{sc} and p_1/p_∞, where p_∞ is the ambient pressure into which the jet exhausts, p^0_{sc} is the stagnation pressure in the settling chamber, and p_1 is the static pressure (assumed to be constant) in the jet exit plane.

Subsonic jet:

$$p_\infty/p^0_{sc} = .834$$

$$p_1/p_\infty = 1$$

$$M_1 = .52$$

Moderately underexpanded jet:

$$p_\infty/p^0_{sc} = .372$$

$$p_1/p_\infty = 1.42$$

$$M_1 = 1$$

Highly underexpanded jet:

$$p_\infty/p^0_{sc} = .148$$

$$p_1/p_\infty = 3.57$$

$$M_1 = 1$$

Velocity profiles of each of the above listed jets were measured at several axial locations. These locations were chosen to represent each of the regions of basically different structure within a typical free jet of high subsonic Mach number. They are listed in terms of nozzle diameters

d_N downstream from the exit as follows:

x/d_N	Region of typical subsonic jet
1.96	Core
7.32	End of core (transition region)
23.50	Fully developed
39.10	Fully developed

In addition to the cases listed above, a number of others were studied in less detail. The entire program is tabulated in Appendix 1.

2.2.1. Apparatus and instrumentation. A convergent nozzle with an exit diameter d_N = .511 inches and exhausting to atmospheric pressure was used. This nozzle was mounted on a 4.75-inch i.d. settling chamber which was supplied with air from a storage tank through an automatic regulator valve. The maximum storage pressure was 220 psig and the maximum settling chamber stagnation pressure was 125 psig. The settling chamber and nozzle are shown in Figure 3, which also shows the flat plate model used in a portion of the impingement studies described in Section 3.

Local velocities were computed from measured Pitot and static pressure profiles. The Pitot and static pressure probes used were mounted on a common base which could traverse the jet in a vertical plane at any axial location up to about 60 nozzle diameters downstream from the exit. Both probe tips were made of .032-inch o.d. stainless steel tubing; the Pitot tip was cut off square, and the static tip was a slender ogive with two .0135-inch holes on opposite sides 5/16 inch from the tip. A sketch of this probe and its mounting is shown in Figure 4. Pressures were measured on liquid manometers or with Bourdon-type test gauges according to the pressure level encountered. Readings for each run were

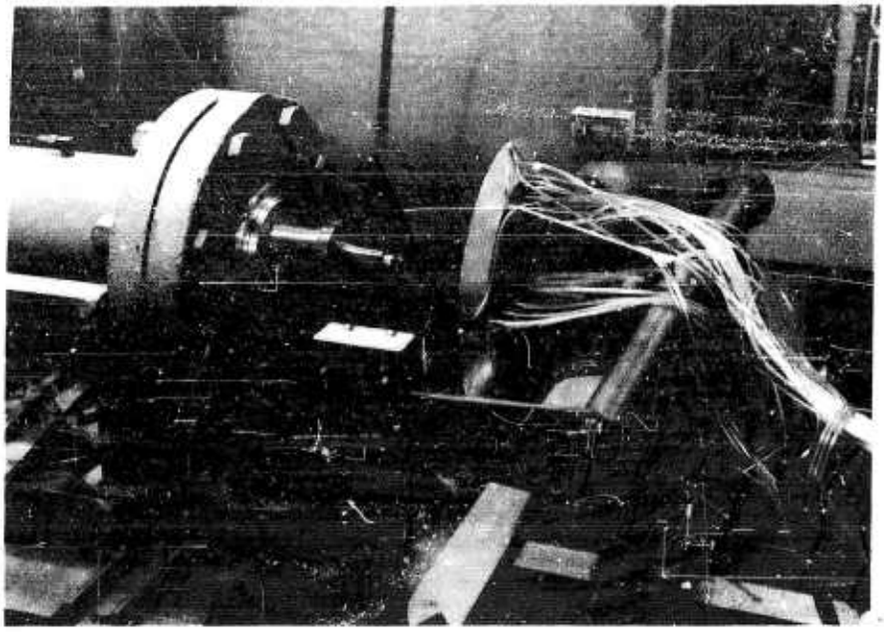

Figure 3. Nozzle and impingement model setup.

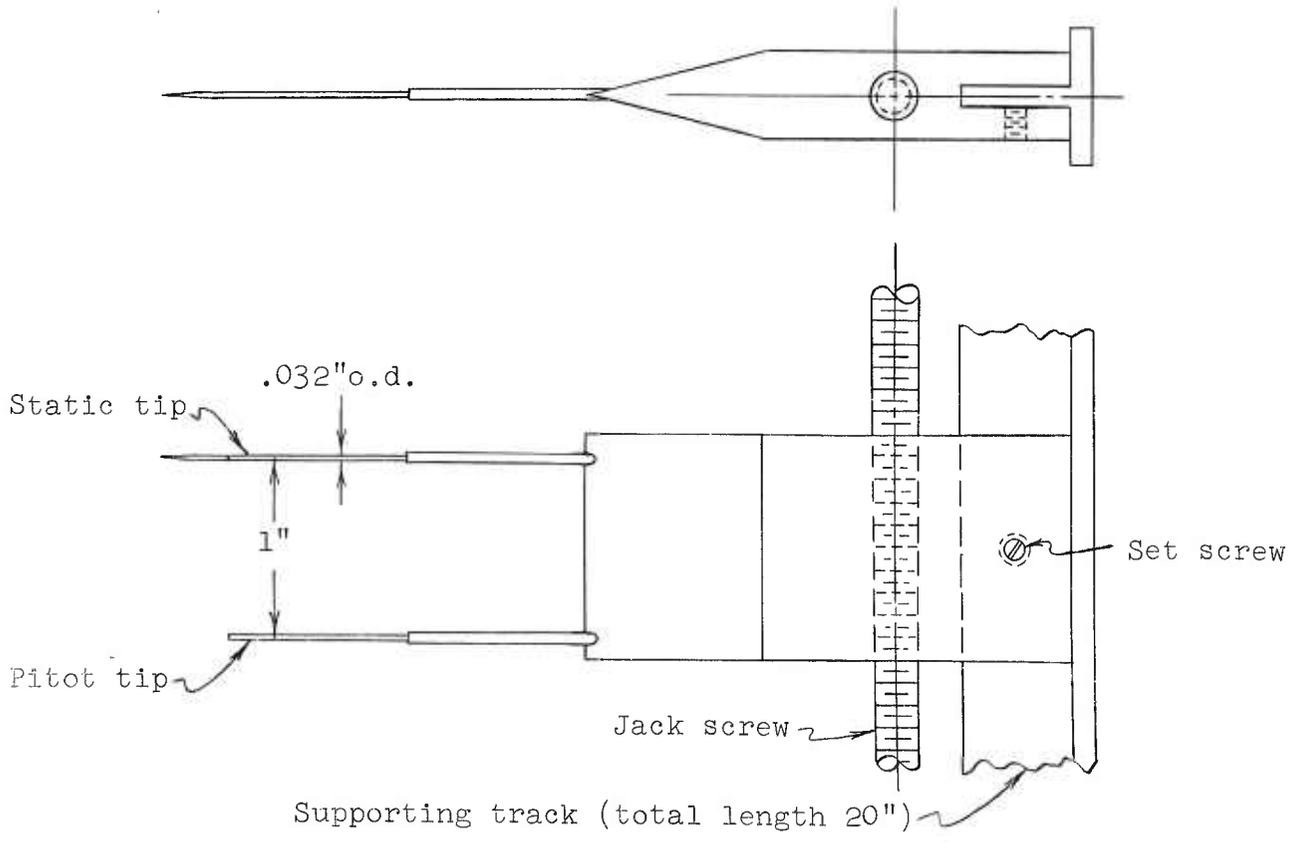

Figure 4. Combination probe used in free jet surveys.

recorded photographically. The stagnation temperature was measured with a bare copper-constantan thermocouple in the settling chamber.

Photographic studies of the jet were made using several techniques. Schlieren pictures and shadowgraphs were taken with both continuous and instantaneous light sources. A coaxial type spark source with a duration of less than 1 μsec was used. The basic optical system was of the usual single pass, off-axis, parallel-light type employing two spherical mirrors of 6-inch diameter and 60-inch focal length. In addition, a limited number of pictures were taken using a more sensitive double pass coincident system with a single mirror. While the resolution of these latter pictures is inherently less than that achieved with the single pass system, the extra sensitivity provides a useful qualitative picture of certain structural features (see Subsection 2.2.3.).

2.2.2. Results of velocity profile and photographic studies. Results of the free jet measurements for each of the specified cases chosen for detailed study are presented in the following paragraphs. Basic data for these and the remaining cases tabulated in Appendix 1 are to be found in Appendix 2.

For each typical jet, the measured total and static pressure profiles are presented with a spark schlieren photograph to the same scale showing that jet for the first 10 nozzle diameters downstream (Figures 5, 7, and 10). Both total and static pressures are plotted in the form of a pressure coefficient expressing the local value as a percentage of settling chamber gauge pressure. The local total pressure is p_j^0 and the local static pressure is p_j. Velocity profiles, and spreading and decay characteristics calculated from the pressure measurements are given in Figures 6, 8, and 11. In Figure 12, the spreading character-

istics of all three jets are replotted together in order to emphasize certain basic differences.

Local velocities were computed on the basis of the measured local pressure ratio and the measured stagnation temperature with the aid of compressible flow tables. The pressure ratio at each point was evaluated from curves faired through the data for each pressure.* Because of the uncertainty in locating the true mean axis of symmetry before running the jet, the probes were traversed through a range well to either side of the assumed axis. The true jet axis was then taken to be the axis of symmetry of the measured profile. The data were then replotted with reference to this true axis and the curves drawn. In some cases, the radial traverse extended outward only far enough to give a proper determination of the spreading parameter $r_{.5}$, the radius at which the velocity is one-half the maximum value. In Figures 5, 7, and 10, a number of data points have been omitted to avoid crowding. The velocities shown in the profiles of Figures 6, 8, and 11 are nondimensionalized on the maximum velocity, even if it does not occur on the centerline. The radial coordinate is nondimensionalized on $r_{.5}$. In the plot of decay and spreading behavior, the velocity on the centerline V_c is given as a percentage of its value V_{c_1} at the nozzle exit. The centerline value of the total pressure coefficient is also plotted. Specific structural features revealed by the pictures and data for each of the three jets will now be discussed.

Subsonic jet ($M_1 = .52$). The pressure and velocity profiles of Figures 5 and 6 clearly reveal the expected structural features. The core with its profile of uniform velocity near the centerline ($x/d_N = 1.96$ and 3.92) and the fully developed region with self-similar profiles ($x/d_N = 11.7, 23.5, 39.1$, and 58.7) have

*For the subsonic case, the static pressure was measured only for the three stations farthest downstream. At other points, it was assumed that $p_j \approx p_\infty$.

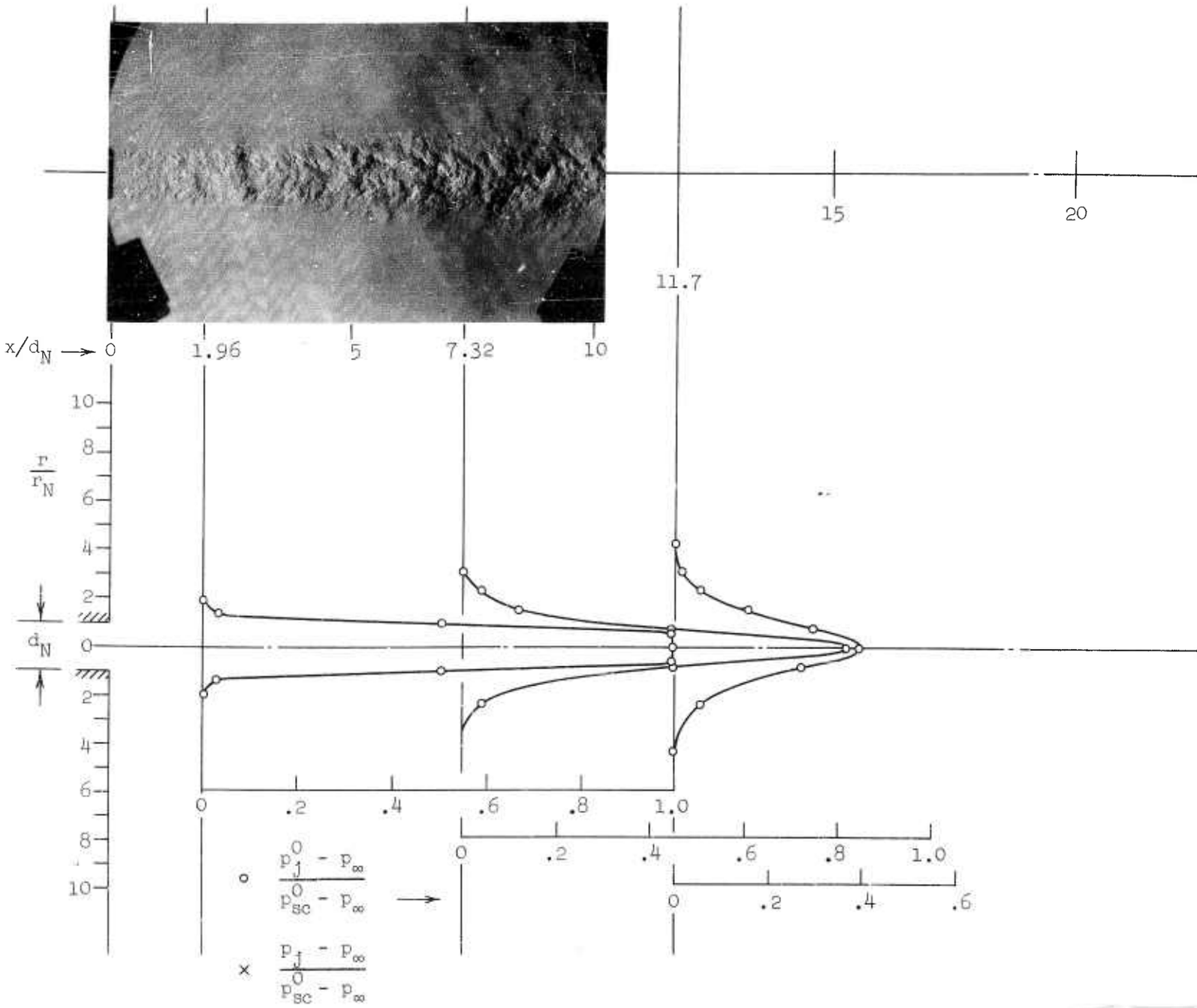
15
20
11.7
x/d_N → 0
1.96
5
7.32
10
r/r_N
10
8
6
4
2
d_N
0
2
4
6
8
10
0
.2
.4
.6
.8
1.0
o (p_j^0 - p_∞)/(p_sc^0 - p_∞) →
× (p_j - p_∞)/(p_sc^0 - p_∞)

1

Figure 5. Measured jet total and static pressure distributions.

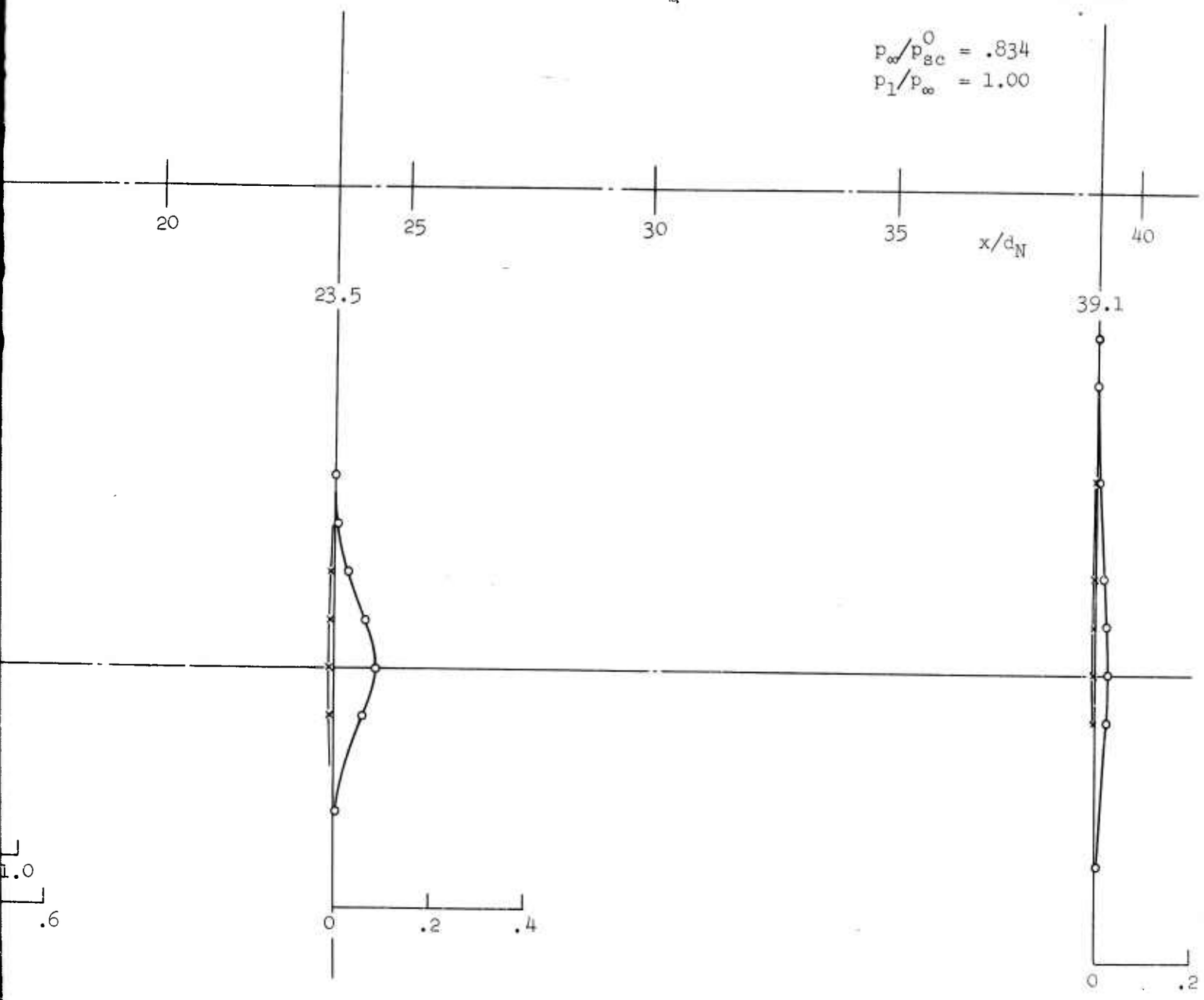

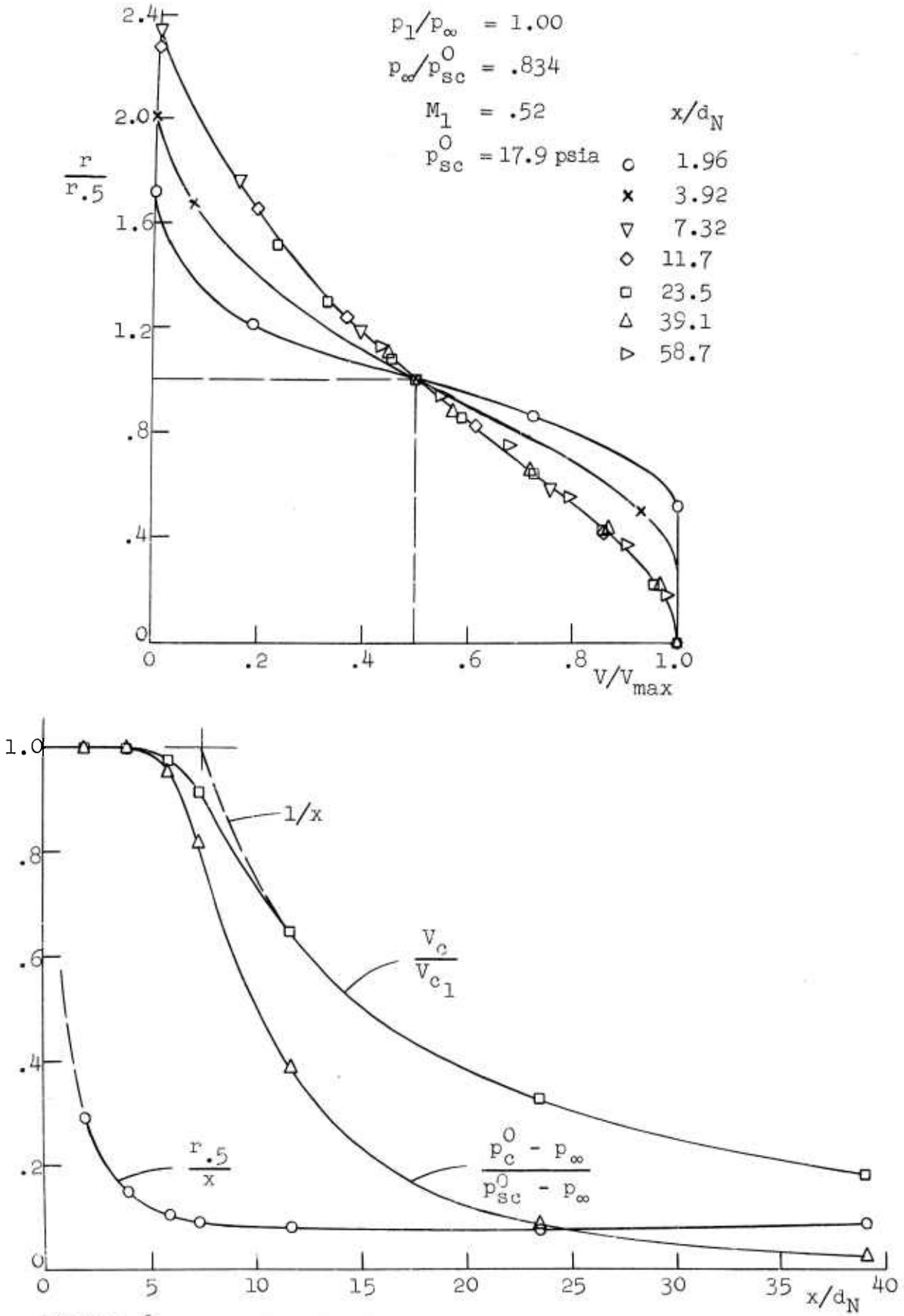

Figure 6. Normalized jet velocity profiles and axial decay and spreading characteristics.

the usual appearance.* Although the decay curve (V_c/V_{c_1}) shows the $x/d_N = 7.32$ station to be in what is probably the transition region, the velocity profile does not exhibit any noticeable core effect. Downstream of $x/d_N \approx 11$, the decay is seen to follow a characteristic incompressible 1/x-dependence quite closely. If this curve is extended back upstream to a value of unity, thus neglecting the transition region, an apparent core length x_c/d_N of about 7.5 is found. While this is in approximate numerical agreement with the results of other studies for similar subsonic Mach numbers, the meaning of such absolute comparisons is limited, even for subsonic jets, by the secondary effects already mentioned. The experiments of Warren [20], for example, with $M_1 = .69$, give a core length $x_c/d_N = 7.2$ with a value of $x/d_N \approx 10$ for the start of the fully developed region. Since this shorter core length with a higher Mach number is in contradiction with the usually observed core length-Mach number dependence, it is possible that differences in the secondary factors affecting the two experiments may be important enough to account for this apparent anomaly. This is not to imply, however, that experimental errors could not account for a difference of this magnitude.

The spreading behavior is best observed on a plot of $r_{.5}/r_N$ as a function of x/d_N (Figure 12). It is seen that the initial spreading rate decreases slightly for the first four or five nozzle diameters downstream. The rate then increases until, at $x/d_N \approx 11$, it becomes fairly constant. A "transition" region defined in the interval in which the spreading rate is changing most rapidly is seen to

---

*Strictly speaking, "fully developed" self-similar velocity profiles imply a fixed relationship between spreading and decay rates. However, because it is difficult to detect and confirm small deviations from self-similarity in the present data, "fully developed" is used only in a relative sense in these discussions.

match very closely a region similarly defined on the basis of the decay curve, i.e. $5 < x/d_N < 11$. (Note that a different transition region is shown schematically in Figure 1. In that case it was defined as beginning at the end of the core as a convenience in designating the idealized core length.) In the "fully developed" region ($x/d_N > 11$), the data indicate continued slight deviations from a truly linear spread. While it is felt that these deviations exceed experimental error, it is not possible to conclude how much the spreading rate actually varies because of the unknown magnitude of jet stability and turbulence effects. It is shown that spreading rates based on measured static pressure, are slightly higher than those based on a constant ambient static pressure. If a constant spreading rate is determined by a straight line fitted among the three points farthest downstream (x/d_N = 23.5, 39.1, and 58.7), a spreading angle of 5.5° is found. Using the ambient static pressure data, the angle is 5.2°. In either case, these values exceed Warren's result of 4.1° by an amount that is probably more than should be expected on the basis of the Mach number difference alone. Warren's data however are based on surveys downstream only to $x/d_N = 25$. Using the present data for a similar axial interval, with the static pressure assumed equal to ambient as in Warren's case, an angle of 4.2° results. Only if one can assume that differences due to secondary effects as well as Mach number are small for the interval of axial distance and Mach number being considered, can it be concluded that the agreement is quite good.

The schlieren picture shows the characteristic subsonic turbulent jet mixing region, including the initial stages of the mixing process just outside the nozzle exit. The core, however, is not readily discernable because of the three-dimensional visual blocking effect of the mixing disturbances (cf. the continuous light schlieren picture shown in

Figure 2 for the same case, but made with the double pass system, in which the core is more easily recognized).

Moderately underexpanded jet ($p_1/p_\infty = 1.42$). Effects due to underexpansion are at once apparent, especially in the axial decay curve (V_c/V_{c_1}) of Figure 8. The centerline velocity is observed to be supersonic in the core region at the three points chosen for the measurements. However, because of the local velocity variations to be expected within the length of each shock cell, these three points alone are insufficient to show the detailed core structure, and the curve through them is thus drawn dashed. Although additional measurements of velocity were not made in this region, the highly detailed survey of Pitot pressure shown in Figure 39 is indicative of the kind of axial variations to be expected.

The velocity profiles show clearly the local effects of expansion in the core. At $x/d_N = 1.96$, for example, the central portion of the profile is seen to be supersonic. In addition, there is a marked radial gradient of velocity with the peak occurring some distance from the centerline. Supersonic central portions are also observed for $x/d_N = 3.92$ and 7.32, although the position of the peak velocity is different in each case. For $x/d_N = 11.7$, the profile is subsonic throughout, but still shows a slight flattening near the centerline. Apparently fully developed subsonic profiles are observed for $x/d_N = 23.5$, 39.1, and 58.7.

The behavior of the measured spreading parameter $r_{.5}/r_N$, is different from that observed for the subsonic jet (see Figure 12). Beginning at an axial distance of about 20 nozzle diameters downstream, and continuing to at least 40 diameters, the spreading rate in each axial portion is substantially higher. Farther downstream, the rate decreases. As a means of comparing apparent changes in spreading rate in different regions of the jet, several spreading angles have been computed. In the interval

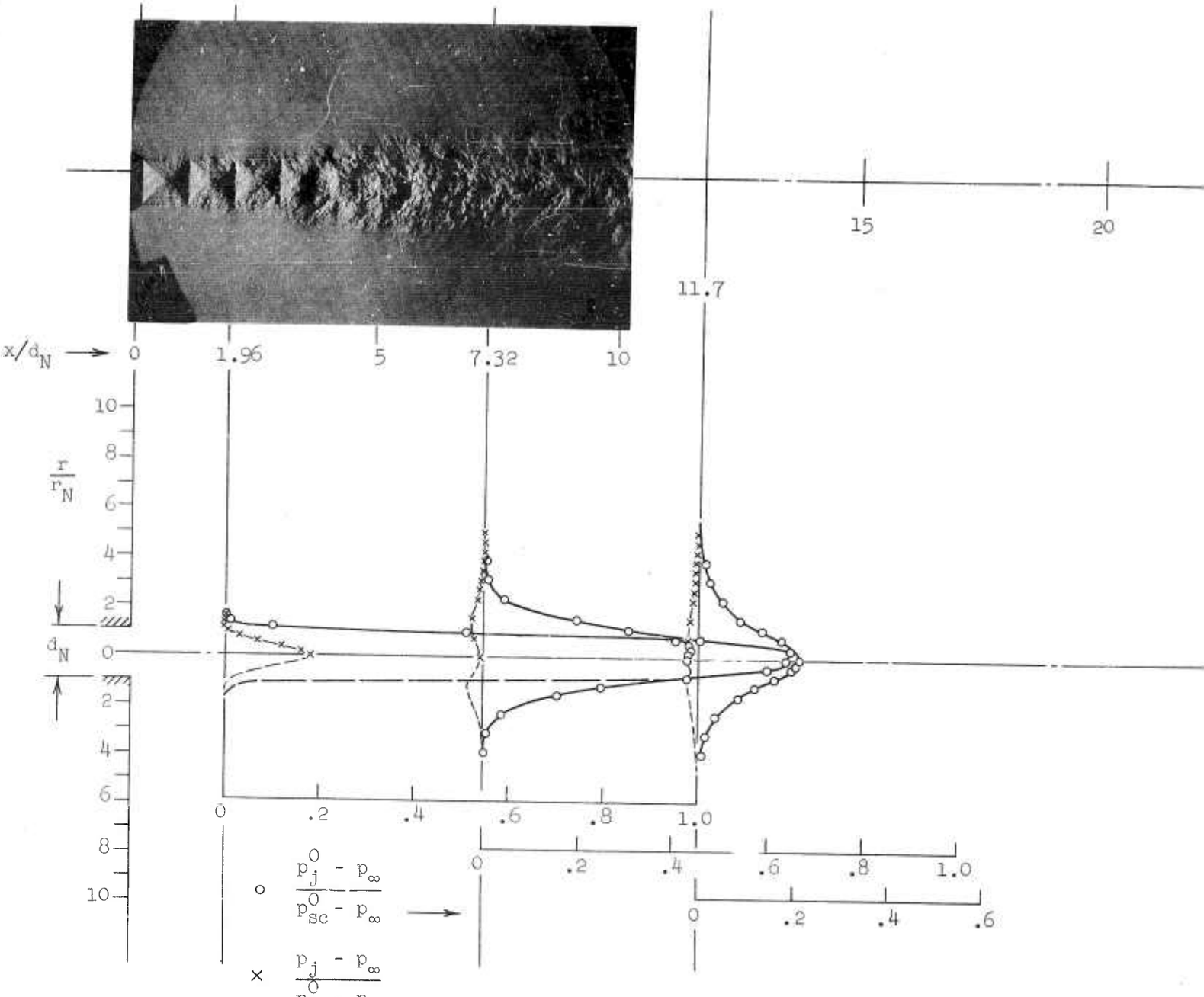
15
20
11.7
x/d_N
0
1.96
5
7.32
10
r/r_N
10
8
6
4
2
d_N
0
2
4
6
8
10
0
.2
.4
.6
.8
1.0
o (p_j^0 - p_∞)/(p_sc^0 - p_∞)
× (p_j - p_∞)/(p_sc^0 - p_∞)

1

Figure 7. Measured jet total and static pressure distributions.

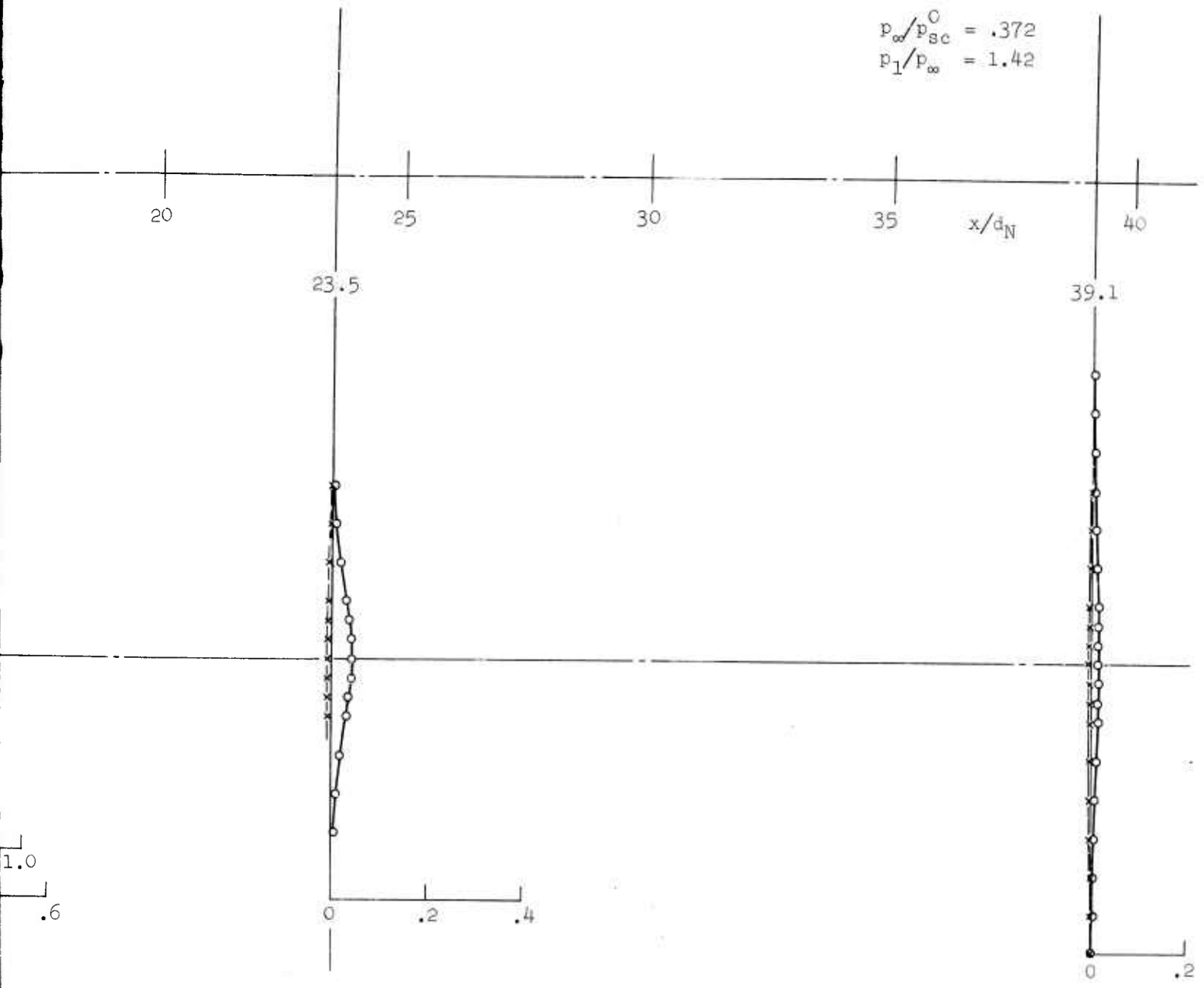

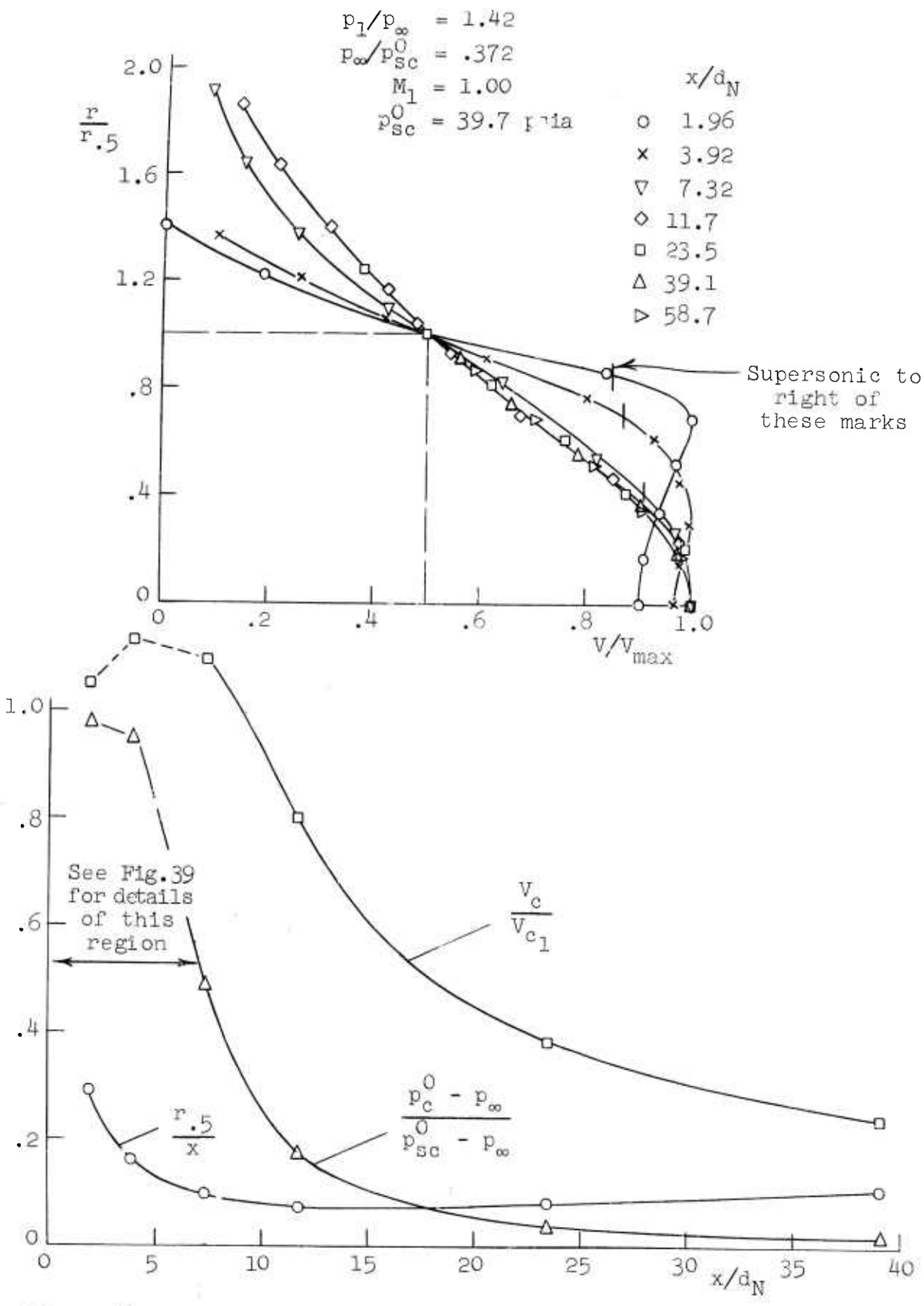

Figure 8. Normalized jet velocity profiles and axial decay and spreading characteristics.

$4 \leq x/d_N \leq 20$ the angle is only 3.0° but for $20 < x/d_N \leq 40$ it is 7.4°. Using the two points farthest downstream ($x/d_N = 39.1$ and 58.7), an angle of 4.8° results for the data based on measured static pressure, with an angle of 4.5° for the data based on ambient static pressure. It is believed that the increased spreading observed nearest the nozzle exit ($x/d_N < 4$) is due to the widening of the jet as it expands on leaving the nozzle. Throughout the remaining region of high spreading rate (out to, say, $x/d_N = 40$) there is reason to believe that the observed rates are at least partly the result of jet instability. Photographic evidence in support of this belief is discussed in 2.2.3. The possible consequences of instability effects insofar as the measurements are concerned can only be suggested qualitatively (see 2.2.4) on the basis of the present data. Far downstream, the return to a lower spreading rate more typical of an incompressible flow appears to be consistent with expected trends.

Of particular interest in the pressure distributions, shown in Figure 7, is the behavior of the static pressure in the core region (also see Figures AII-9 and 10). At $x/d_N = 1.96$, a strong radial gradient is observed, with a maximum pressure on the centerline which is considerably higher than ambient, and a minimum pressure near the edges of the jet which is lower than ambient. At points farther downstream, the central peak remains, but the over-all pressure level in the core drops below ambient pressure. Finally, at a point beyond the end of the core, the central peak disappears and the over-all level gradually increases toward the ambient value. While this behavior is qualitatively, both axially and radially, the same as that found to exist in subsonic and properly expanded supersonic jets (see, for example, [20]), a comparison with the present case can be misleading without further clarification. An axial survey of centerline static pressure was made, therefore, to

help in understanding this situation. Figure 9 presents the results of this survey for a subsonic jet (p_∞/p^0_{sc} = .552) as well as the underexpanded jet ($p_1/p_\infty = 1.42$) in question. The core shock structure for the latter case is sketched to scale so that the pressures may be referred to their approximate locations in the jet. The dashed curve interpolated among the data is, of course, only a qualitative suggestion of the actual behavior. As such it is based not only on the measured points, but also on the assumption that minimum and maximum pressures occur near the center and end points, respectively, of each cell. In any case, the extreme gradients within the core are clearly evident, and it is seen that the values found during profile measurements (solid symbols) cannot be interpreted as indicating a smooth variation in the axial direction. Also of interest is the fact that the measured pressure at the center of the jet exit plane ($(p_1 - p_\infty)/(p^0_{sc} - p_\infty) = .291$ at $x/d_N = 0$) is higher than that indicated by the nominal pressure ratio $p_1/p_\infty = 1.42$ (or $(p_1 - p_\infty)/(p^0_{sc} - p_\infty) = .247$). In addition, the axial variation near the end of the core and farther downstream closely resembles the typical subsonic behavior. It is therefore suggested that the extreme pressure gradients due to shocks are modified by a superimposed radial and axial distribution which is similar to that existing in a subsonic or properly expanded supersonic turbulent jet. Velocity profiles determined from the pressure ratios at an axial station in the shock structure would thus reflect a combination of two effects (resulting, e.g. in a peak velocity off the centerline), and would, of course, be expected to vary in shape from point to point along the axis. The profiles shown in Figure 8 for the core stations, therefore, are not necessarily representative of a smooth transition of profile shape from one axial location to another.

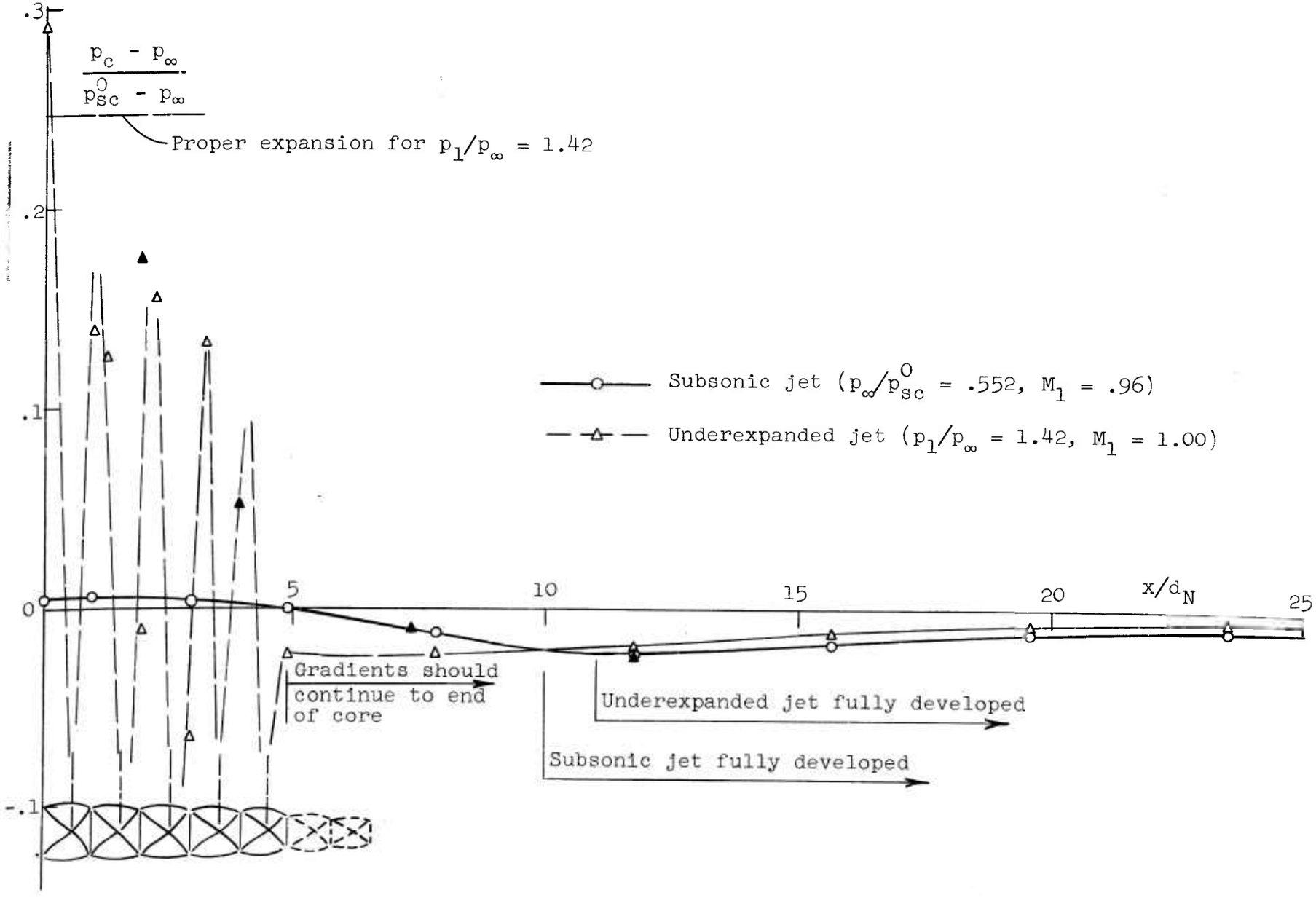

Figure 9. Measured static pressure variation along centerline of free jet.

The spark photograph of this jet, shown in Figure 7, reveals some distortion of the stable core structure as early as the second cell. Farther downstream, the core becomes highly unstable, and the shock cells appear to break up and diffuse into the surrounding mixing region. In the continuous light picture of Figure 2, which portrays the time-average appearance, the downstream cells are more easily recognized. Weak sound waves emanating from the mixing region can be detected in the spark picture.

Highly underexpanded jet ($p_1/p_\infty = 3.57$). It is clear from the velocity profile and decay data (Figure 10 and 11), that the distinguishing structural feature of this jet in the upstream region is the normal shock disk in the first cell. The picture shows that this shock occurs at $x/d_N = 1.58$. Just downstream of this point, at $x/d_N = 1.96$, the velocity profile exhibits the expected subsonic central region. Within this region, the minimum velocity appears to occur just inside the slip boundary, while the peak subsonic velocity lies on the axis. In the surrounding region of supersonic flow, a peak Mach number of 1.9 is reached, which, coincidentally, happens to correspond to the Mach number for proper isentropic expansion to $p_1/p^0_{sc} = .148$. It is felt, however, that at a point somewhat upstream of this, an even higher Mach number associated with an over-expanded condition should exist. The photographs of Figure 10 and Figure 2 both reveal an apparent normal shock in the second cell at $x/d_N = 3.3$. Slightly downstream of this point, at $x/d_N = 3.92$, the velocity profile again shows a subsonic central region, although the radial extent is much less than it is for the $x/d_N = 1.96$ case. At $x/d_N = 7.32$, the entire central region is supersonic, but the maximum velocity still does not occur on the centerline. In this respect, the profile is similar to some of those found in the core of the moderately underexpanded jet. A substantial

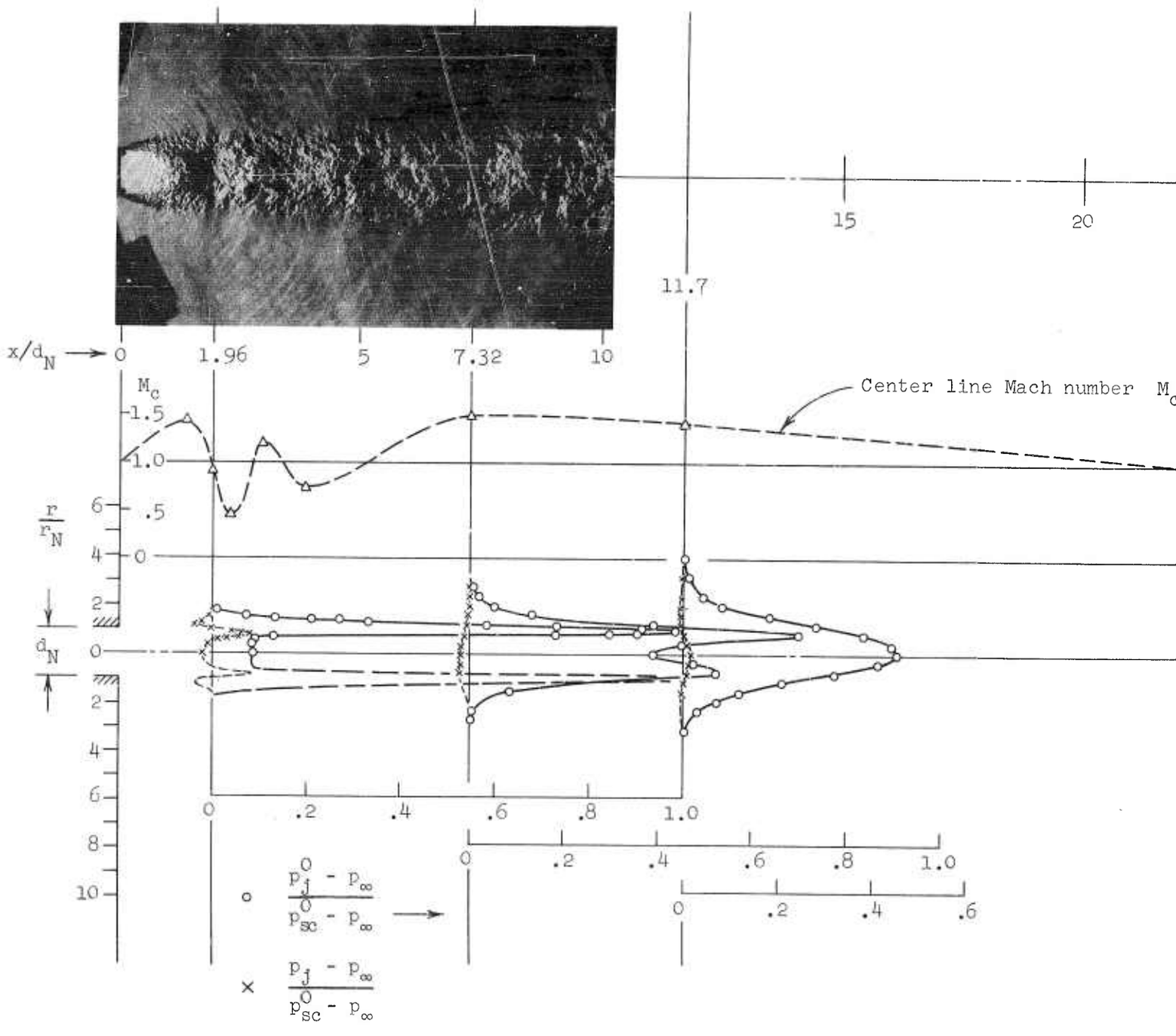
15
20
11.7
x/d_N
0
1.96
5
7.32
10
M_c
1.5
1.0
.5
Center line Mach number M_c
$\frac{r}{r_N}$
6
4
2
0
d_N
2
4
6
8
10
0
.2
.4
.6
.8
1.0
$\circ \quad \frac{p_j^0 - p_\infty}{p_{sc}^0 - p_\infty}$
$\times \quad \frac{p_j - p_\infty}{p_{sc}^0 - p_\infty}$

1

Figure 10. Measured jet total and static pressure distributions.

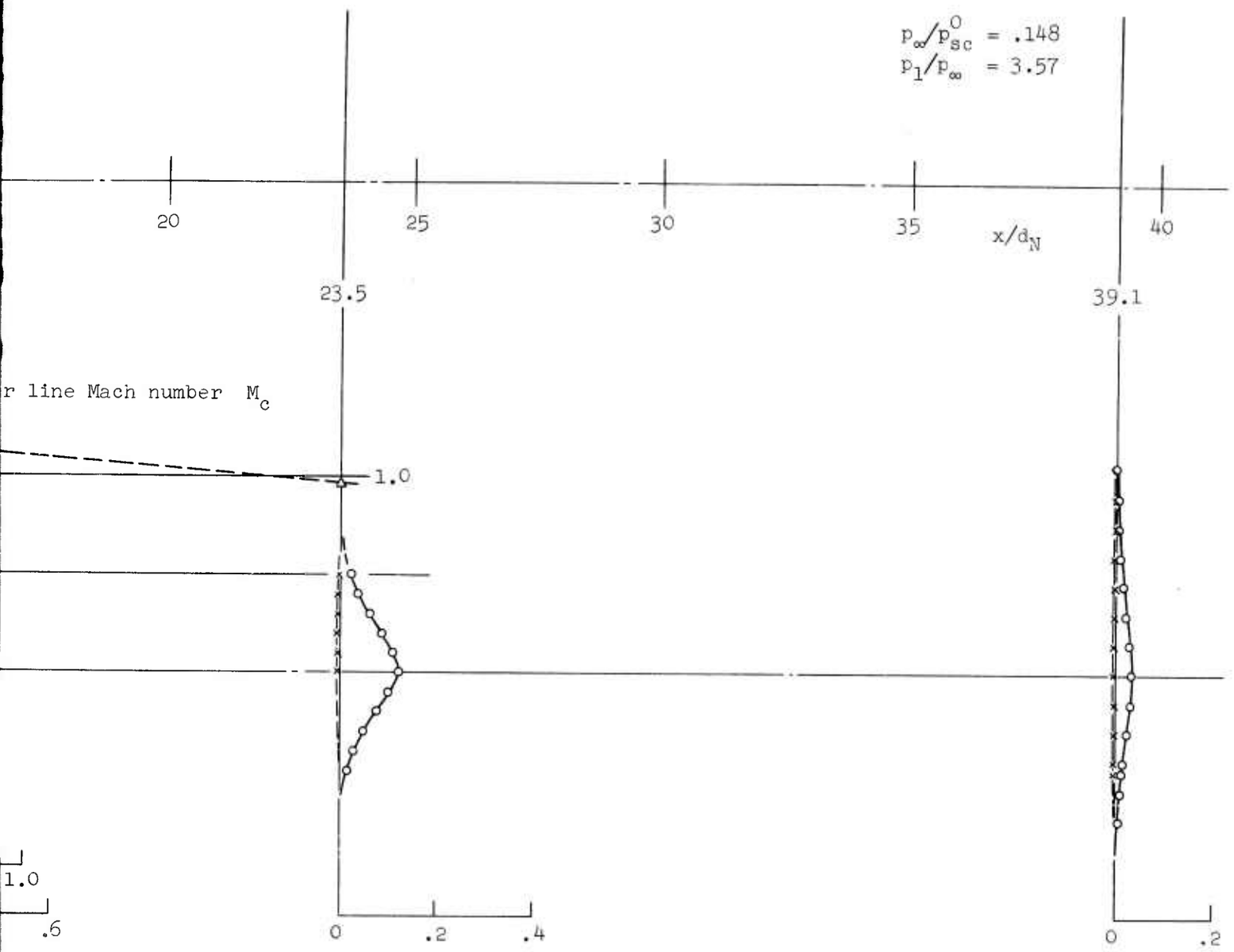

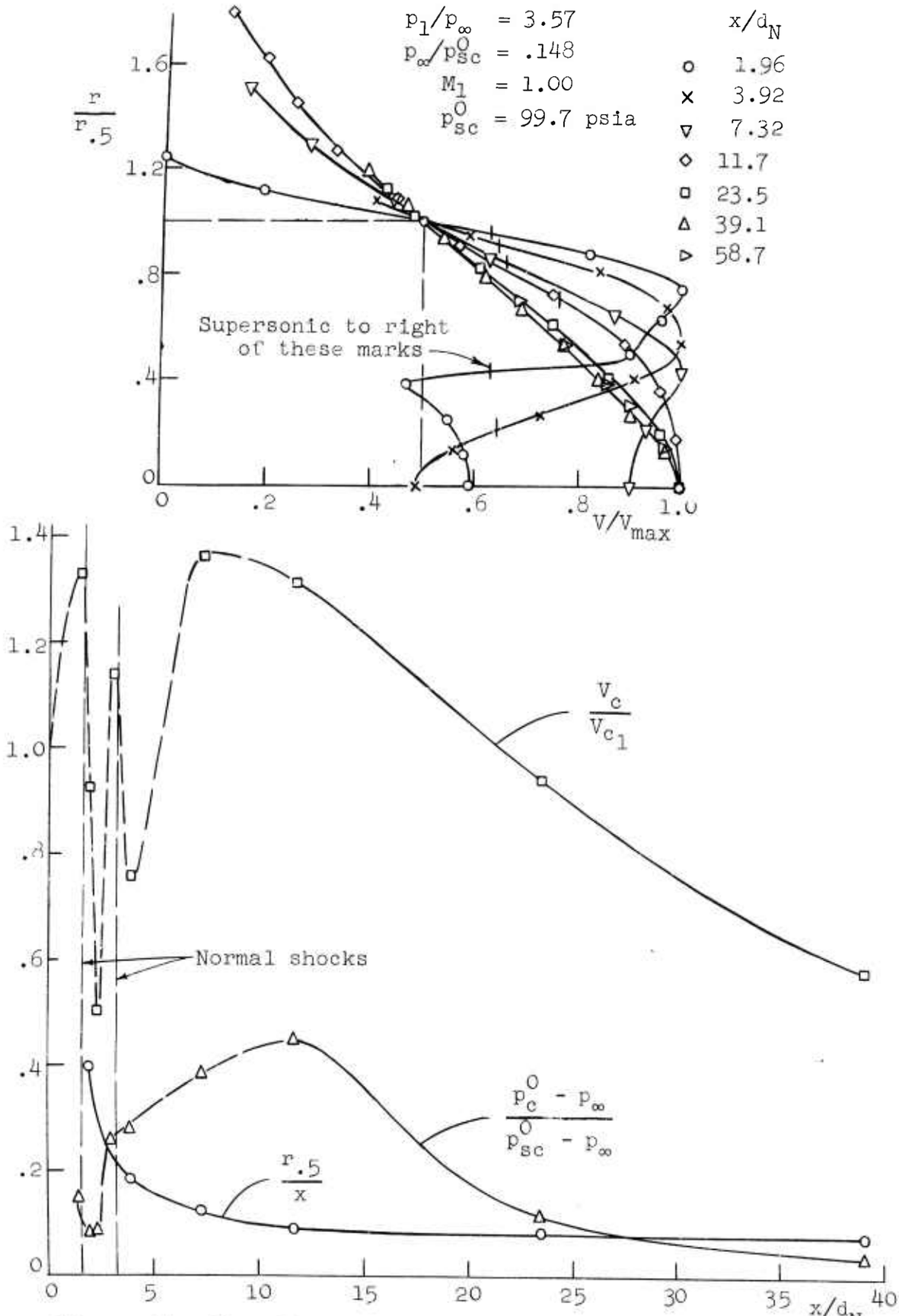

Figure 11. Normalized jet velocity profiles and axial decay and spreading characteristics.

supersonic core remains at $x/d_N = 11.7$, although, at least at this specific point, the peak velocity lies on the axis. While the oblique shock structure in the region between the last normal shock and the end of the core may not consist of well-defined cells such as those found in the moderately underexpanded case, it is likely that whatever shocks are present will produce local periodic changes in the velocity profile as long as they are of sufficient strength. Thus, no smooth variation from profile to profile should be inferred from the data presented for this region. Farther downstream, it is observed that the centerline velocity is just subsonic at $x/d_N = 23.5$. Reference to the spreading parameter $(r_{.5}/r_N)$ behavior and the velocity profiles for the $x/d_N = 23.5$, 39.1, and 58.7 stations reveals that a fully developed jet flow may not occur short of at least 30 or 40 nozzle diameters downstream.

The results of a highly detailed Pitot pressure survey on the centerline of this jet are given in Figure 39. This survey is indicative of the local effects due to the normal shocks present and the subsequent oblique shock structure in the core. Of particular interest is the substantial recovery of Pitot pressure relatively far downstream.

In order to verify the presence of a normal shock disk in the second cell, some additional Pitot-static pressure measurements were made on the centerline at selected points in the region of interest. The Mach number distribution resulting from these measurements is shown in Figure 10. The subsonic region just downstream of each normal shock is apparent. It is interesting to note the sharp increase in Mach number from .45 to at least 1.2 just upstream of the second shock.

The velocity spread data for this jet (Figure 12) reveal a somewhat erratic behavior. In the region immediately downstream of the nozzle exit, the bulge observed is

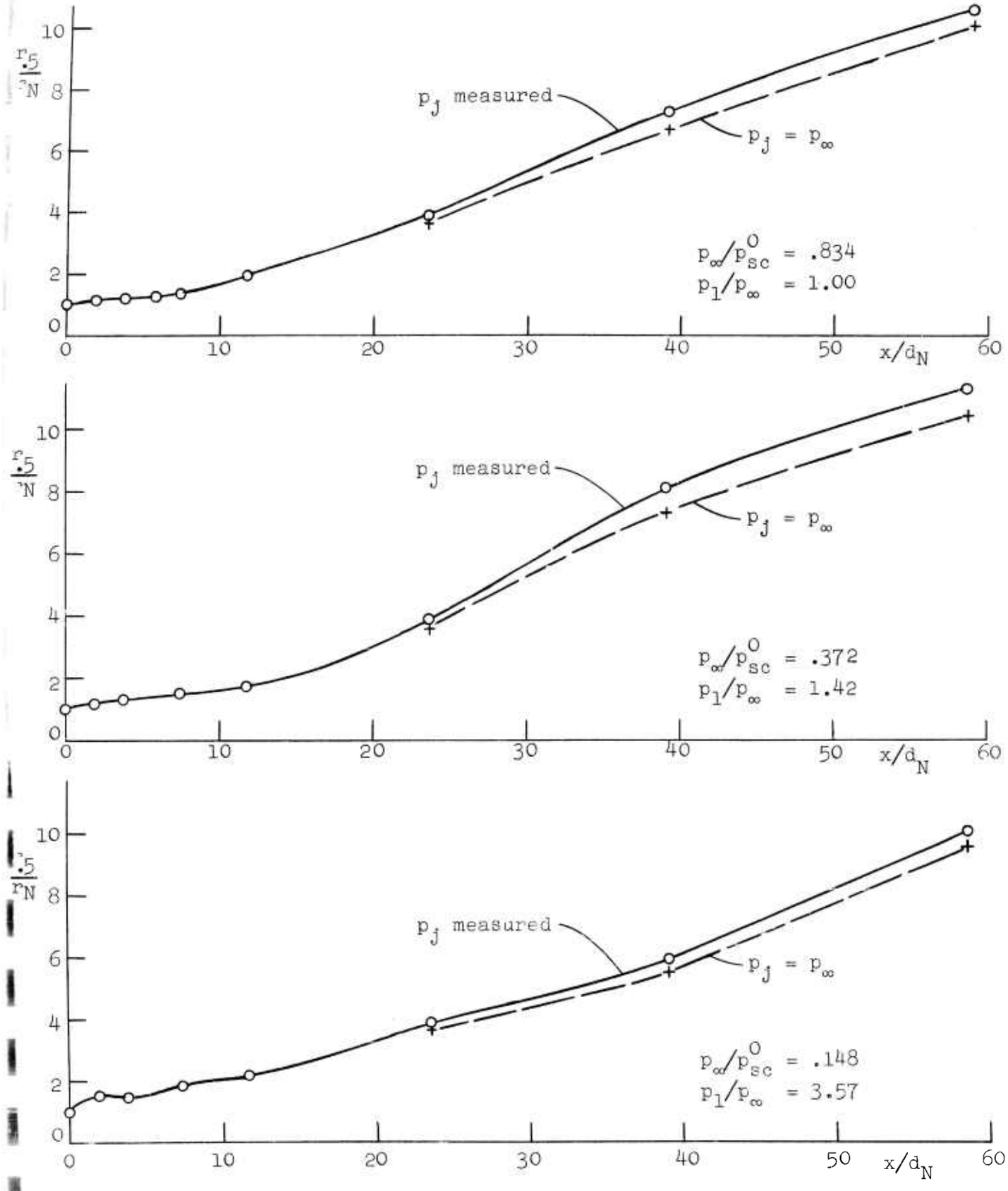

Figure 12. Measured radial spread of subsonic and underexpanded free jets.

consistent with the boundary shape assumed by the expanding flow in the first few shock cells. Except for slight deviations, the spreading rate is then essentially constant for a considerable distance downstream ($x/d_N \approx 40$). In the interval $4 \leq x/d_N \leq 12$, the spreading angle is 2.5°, and for $12 < x/d_N \leq 40$, an angle of 3.9° is found using the data for measured static pressure. The very low spreading angle for $4 \leq x/d_N \leq 12$ is in agreement with the slight apparent spread observed in the schlieren picture for this case in Figure 2. Downstream of $x/d_N \approx 40$, the measured spread increases. Although an increase in this region seems to be consistent with the appearance of essentially fully developed velocity profiles at $x/d_N = 39.1$ and 58.7, the angle of 6.0°, based on the two data points, is somewhat higher than might be expected for such a region of subsonic decay.

The continuous light schlieren picture of this jet in Figure 2 reveals a structure downstream of the second cell that seems to differ somewhat from the relatively well-defined oblique shock cells observed at lower pressure ratios. Although oblique shocks appear to be present, the structure is more like that of a properly expanded supersonic jet with Mach waves in its core.

2.2.3. Special schlieren study of underexpanded jet. A series of continuous light schlieren pictures was taken using the high sensitivity double-pass coincident optical system. In this series, the jet pressure ratio p_1/p_∞ was varied in small increments through a range from 1.00 to more than 4. In Figure 13, a selection of these pictures is shown in order of increasing pressure ratio. (A subsonic case is shown for reference.) It is observed that an intensified image of the mixing region is obtained. Because of the relatively long exposure time (1/50 sec.), this image is representative of the time average appearance. It is at once

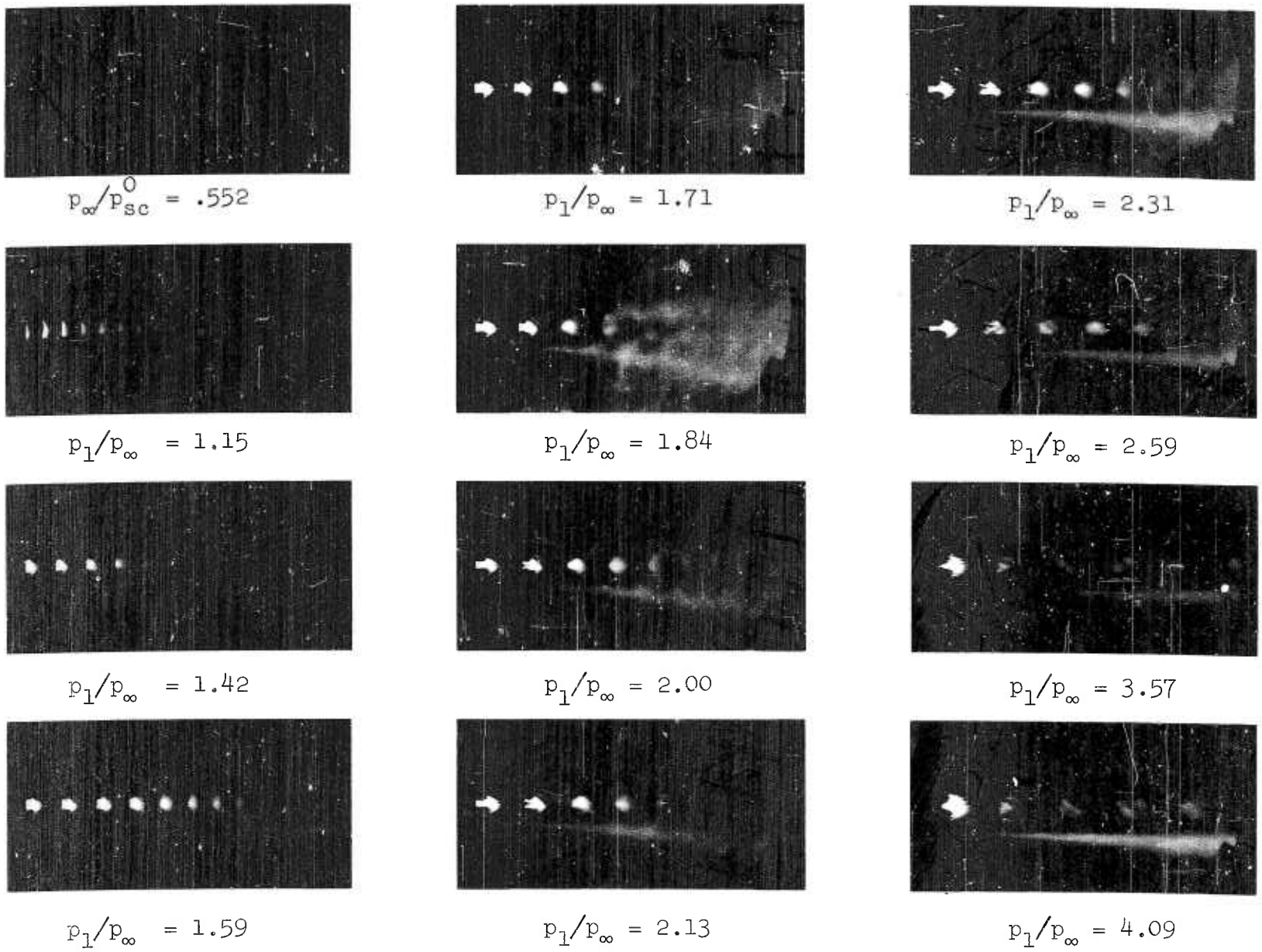

Figure 13. Free jet from convergent nozzle photographed with double-pass schlieren system.

apparent that there is considerable variation of the observed spread of the jet as the pressure ratio is changed. This variation is interpreted as being due to changes in the stability characteristics of the entire jet flow field. Although the instantaneous details of the structural degradation of the jet due to instabilities are readily observed in spark pictures, the intensity or amplitude of the motion is difficult to interpret from single pictures because of its three-dimensional nature. The pictures of Figure 13, therefore, are useful in making qualitative comparisons of overall stability effects for jets of different strengths. It has been demonstrated [19] that the stability of a given jet can depend not only upon the pressure ratio, but also upon geometric or interference effects as well as the cross-coupling of acoustic disturbances generated within the jet. Because of this dependence, it is probable that the changes in stability observed in Figure 13 are unique for this particular test apparatus. As an example of this uniqueness, it has been found that the proximity of the mirror (about 4") to the jet in this optical setup produces a shift in what is believed to be a region of high instability in the $p_1/p_\infty = 1.42$ jet. A curve of spreading parameter measured with the mirror in place is given in Figure AII-14 in order to illustrate this effect. The corresponding change in the decay curve (Figure AII-16), however, is relatively small. This is consistent with the assumptions about stability effects on profile measurements discussed in 2.2.4.

As the pressure ratio is increased, two distinct ranges are noted in which the instability appears to be very intense. An increase of pressure ratio from 1.15 to 1.42 and then further to 1.59, spans the first such range, with the $p_1/p_\infty = 1.59$ case appearing to be relatively stable. A second range of even greater instability seems to center about the case for $p_1/p_\infty = 1.84$. At a pressure ratio of 2.00, the normal shock disk is first observed. Within the

region covered by the pictures, the degree of instability appears to lessen with further increases in pressure ratio above 2. It should be noted that although the jet chosen ($p_1/p_\infty = 1.42$) for detailed study in the moderately underexpanded case appears to fall within one of the ranges of high instability, the behavior shown in the picture is not in itself conclusive because of the aforementioned mirror proximity effect.

The time-average appearance of the core shock structure is also of interest. As might be expected, the more unstable jets show fewer well-defined cells. The contrast is particularly great between the cases for $p_1/p_\infty = 1.59$ and 1.84. Once the normal shock occurs in the first cell, there is a gradual change in the appearance of cells farther downstream. At first, these cells seem to follow the characteristics-type of pattern used as a model for the moderately underexpanded jet. However, between the pressure ratios 2.59 and 3.57, the regular cellular division seems to give way to a more continuous pattern of intersecting oblique shocks.

2.2.4. Factors affecting profile measurements. The velocity profiles upon which the jet spreading and decay results are based were, of course, determined from measurements made with Pitot and static pressure probes. Inherent in such measurements are certain limitations introduced by the properties of the flow itself. In the case of turbulent jets, the most important limiting factors are thought to be the turbulence in the mixing region and the over-all jet instability. (It is felt that alignment errors due to neglect of the radial component of the mean velocity and probe "angle-of-attack" errors due to the shear flow mean profile are of minor importance.) Although no quantitative evaluation of these factors is possible on the basis of the existing data, some general conclusions about the relative validity of the measurements should be possible.

The pressure sensed by a static pressure orifice is affected by transverse velocity components arising from turbulence as well as any other phenomenon having a cross-wise component. The magnitude and sign of the resulting error, however, depend on a complex relationship among probe size, turbulence scale, and the magnitude and space correlation of local velocity fluctuations. In general, therefore, the validity of the static pressure measurements can be assumed to be the greatest in regions of the jet where turbulence and instability are the least relative to the magnitude of the mean motion, namely, in the upstream regions.

In many cases, jet velocity profiles are determined from the measurement of Pitot pressures alone, with the static pressure considered to be constant and equal to ambient pressure. In the present experiments, in which static pressures were measured in most cases, it is possible to compare profile parameters determined in both ways. In Figure 12, values of the spreading parameter based on ambient static pressure are shown for several cases. It is seen that a somewhat larger spreading rate results when measured static pressures are used. It is not possible, however, to determine the degree to which these measured pressures actually contribute to the determination of a true profile because the measurements are most in doubt where they can have the greatest influence, i.e. in the outer portion of the downstream region where they approach the magnitude of the total pressure level.

While total or Pitot pressure measurements are also affected by turbulent velocity components, it is felt that over-all jet instability effects may be of greater importance in some of the present cases. In such cases, the response of the Pitot tube at each point in the profile can be considered to be that resulting from a fluctuating velocity at that point. If it is assumed that this response

represents the time-average value of the fluctuation, a typical jet mixing profile measured in this way will differ from its instantaneous shape. Assuming a lateral disturbance motion whose mean amplitude is distributed axisymmetrically, the measured profile would appear to be somewhat flattened at the center and spread out at the edges. Spreading and decay rates based on such time-average profiles would, of course, be larger than those based on instantaneous profiles.

Because of the foregoing factors, it is clear that the measurement, for example, of a high spreading rate for a given jet may only be indicative of the fact that the jet is highly unstable. The instability would then have to be either eliminated or evaluated by other means before the true viscous spreading rate could be determined.

2.3. Discussion of results and comparison with theory.

The main objective of the foregoing study of free jet properties has been the determination of spreading and decay characteristics to be used to correlate the results of impingement experiments using the same jet apparatus. By using such data in this way, the influence on the correlation of secondary effects such as jet stability might be expected to be minimized. Also of interest in this study has been the general behavior and structure of free jets themselves, especially cases in which the jet is underexpanded.

The results of the three typical cases presented in detail in 2.2.2 confirm a number of expected similarities as well as important differences among the basic flow types. In the core region of each jet, the differences are most in evidence. The core of the subsonic jet is, of course, determined by the inward diffusion of the turbulent mixing region, whereas the moderately underexpanded jet has an

additional determining influence in the system of oblique shocks present. For the highly underexpanded case, the normal shock disk is a dominant factor in the local structure of the core. Because of the very presence of shocks in the underexpanded cases, however, it is difficult to specify a consistent criterion for core length that can be applied with equal pertinence to all the jets. It is felt, therefore, that the most meaningful basis of comparison is the downstream behavior in terms of the point at which a fully developed turbulent mixing profile is observed. The present data are sufficiently detailed to be used in this way.

Using the measured velocity profiles by themselves, it is found that the subsonic jet can be considered fully developed somewhere between $x/d_N = 7.32$ and 11.7. The constant relationship between centerline velocity decay and jet width or spread, which is thus implicit and which must hold if axial momentum is to be conserved, is fairly well confirmed in separate plots of these two parameters. The moderately underexpanded jet ($p_1/p_\infty = 1.42$), however, exhibits a profile at $x/d_N = 11.7$ that still does not match those far downstream. It has been pointed out that this particular jet appears to be quite unstable and that measured velocity profiles may represent a distortion of the actual instantaneous profile. Because of this, the definition of a fully developed region is difficult. It is seen, for example, that the velocity profiles are very close to being similar for $x/d_N = 23.5$, 39.1, and 58.7, while at the same time there is a marked decrease in the spreading rate in the same range. This situation could result if jet instabilities were stronger in the upstream region and thus resulted in broader measured profiles there. In fact, if it is assumed that the measurements far downstream at $x/d_N = 58.7$ are relatively unaffected by instability, it is found that the over-all spreading rate required

to reach the measured width at that point is very nearly the same as that required for the subsonic jet at the same point. The highly underexpanded jet is apparently dominated by a very long supersonic core, as shown by the low initial spreading rate and the centerline Mach number survey. It is doubtful, in fact, that a fully developed region occurs at all within the range of the measurements. Velocity profiles for $x/d_N = 39.1$ and 58.7 are essentially similar, but the spreading rate between these points is higher (6.0°) than that usually associated with a fully developed subsonic mixing region.

A comparison has been made between the results of this study and the semi-empirical integral analysis of Warren [20] based on Prandtl's constant exchange coefficient concept. This theory differs from the usual mixing length hypothesis in that it defines the effective eddy viscosity or exchange coefficient ϵ directly in terms of the mean flow properties. For a typical fully developed jet mixing region, it is assumed that

$$\epsilon = Kr_{.5}\left(\frac{V_c}{2}\right)$$

where K is a proportionality constant to be determined experimentally. Warren found that K could be correlated with M_1 within his experimental range. This correlation, which was based on Warren's data for both subsonic and ideally expanded supersonic jets, is given by

$$K = .0430 - .0069\ M_1$$

The principal objective of the present comparison is to see how well the decay behavior of an underexpanded jet may be correlated with that for a jet that is properly expanded at the same pressure ratio. Although it is probable that the

relationship of K and M_1 is unique for a given test condition, the determination of such a relationship is not within the scope of the present experiments.* Therefore the comparison with Warren's method is carried out on the basis of his correlation of K and M_1.

In order to compare the measured decay of a given underexpanded jet and that computed for a properly expanded jet of the same pressure ratio p_∞/p^o_{sc}, it is first assumed that the jet exit locations coincide. The nondimensional axial coordinate x/d_N of the computed jet is then based on a diameter given by the area ratio for proper isentropic expansion to the given pressure ratio with the throat area equal to that of the actual nozzle. Similarly, the ratio of the exit velocity of the equivalent properly expanded jet to that measured at the sonic exit of the underexpanded jet is used to scale the entire computed decay curve. The results of this type of comparison for several cases are given in Figure 14. It is seen that the degree of correlation is very good for the subsonic jet, but somewhat varied for the other cases. In Figure 15, the ratio of measured to computed decay parameter $(V_{c_{exp}}/V_{c_{th}})$ is plotted as a function of jet pressure ratio in the underexpanded regime for several axial locations.** Within a range of pressure ratios centered about that for the formation of the normal shock, the agreement is no better than 60-70 per cent. For pressure ratios $p_1/p_\infty > 3$, however, the agreement is much better. It is also

---

*In fact, it is possible that a better correlation can be found if K is assumed to be a function of some local Mach number which is characteristic of the flow at each axial station. Three such Mach numbers which have been suggested are those on the centerline, on the dividing streamline, and on the streamline at $r_{.5}$.

**The pressure ratio for appearance of the normal shock shown in Figure 15 was determined from a plot of shock diameter as a function of pressure ratio by extrapolating the shock diameter to zero.

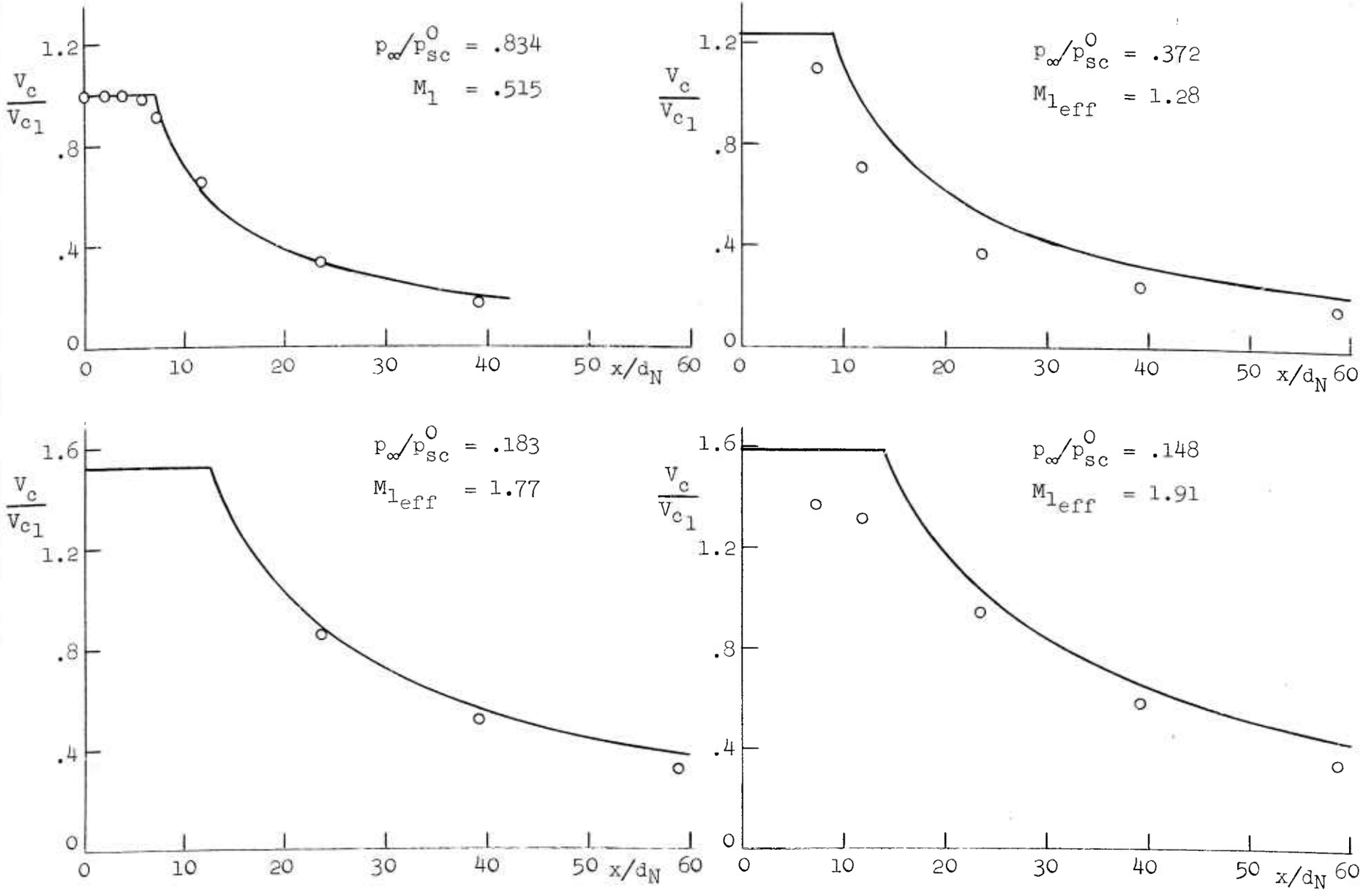

Figure 14. Comparison of measured velocity decay with that given by application of Warren's method for an equivalent properly expanded jet of the same pressure ratio and a Mach number $M_{1_{eff}}$.

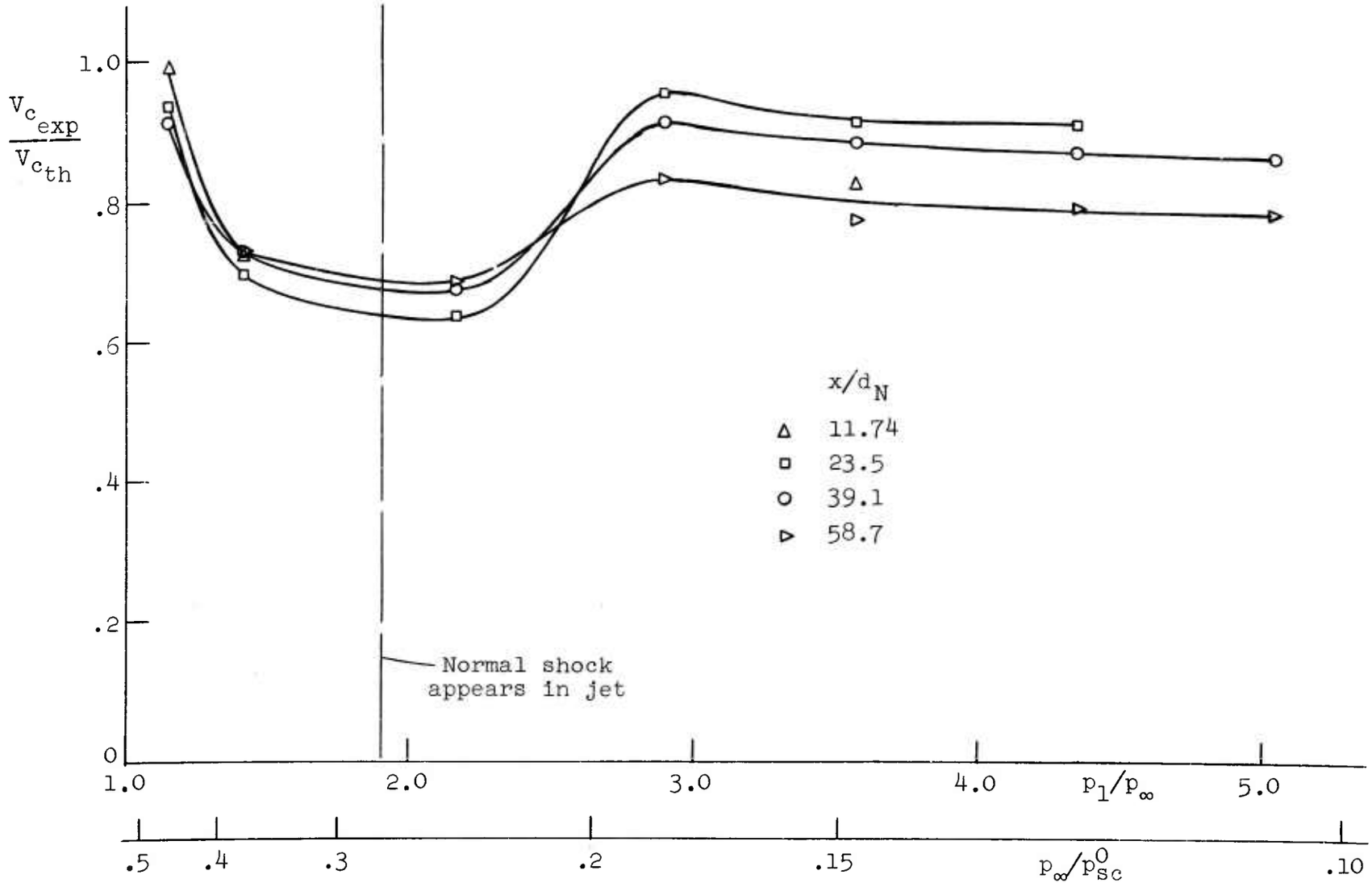

Figure 15. Ratio of measured centerline velocity to that found for equivalent jet vs. jet pressure ratio.

observed that while the per cent agreement falls off with axial distance, the difference in agreement due to the pressure ratio effect is also less far downstream. Since the theory does not account for secondary effects, these results lead to conclusions that are quite consistent with those based on photographic evidence and measured spreading rates alone, namely, that jet instability effects may be large in the moderately underexpanded range, and that such effects are diminished at points far downstream. It is also evident that, except in the moderately underexpanded range, the semi-empirical method used for a properly expanded jet results in a reasonably good approximation to the underexpanded jet within the range of pressure ratios investigated. While the core shock structure can, under certain conditions, have a definite influence on the stability of the jet, it is apparent that its over-all effect on decay rates is minor.

It should be pointed out that the known applications of Warren's method to properly expanded jets have usually been restricted to axial distances of less than $x/d_N = 25$. For this reason, it is not possible to verify that the method is any better for properly expanded jets far downstream than it is for the present underexpanded ones. The single point for $M_1 = .515$ at $x/d_N = 39.1$ shown in Figure 14 is, of course, by itself inconclusive.

3. IMPINGEMENT STUDIES

3.1. Basic flow characteristics.

Recent interest in ground effects machines, V/STOL aircraft, and the vertical launching and landing of rockets has led to a number of studies of various aspects of the jet impingement problem. In addition, there has been increased study of certain industrial processes involving heating by impinging hot jets and flames. In the ground effects and V/STOL field, the need to understand impingement processes has arisen not only with regard to increasing the vehicle's lifting effectiveness while in ground proximity [27-34], but also in connection with downwash erosion effects on the ground below [35]. Study of the ground erosion effect has also been extended to the problem of landing rockets on hypothetical lunar and planetary surfaces [36-40]. Problems associated with the impingement and deflection of rocket exhausts and the resulting loading of adjacent surfaces have been treated both theoretically and experimentally [41-45]. The basic problem of determining heat transfer between surfaces and impinging jet flows has also been investigated in a variety of ways [46-59]. Other investigators have emphasized the basic aspects of flow processes involved in impingement [60-68] as well as certain special problems such as noise generation [69].

The flow field produced when an axially symmetric air jet impinges on a solid surface held normal to it consists of three general regimes. First, there is the jet itself, upstream of the point where any local influences due to the strong interaction of the impingement are felt. Throughout this regime, of course, secondary effects (such as those described in Section 2) produced by the impingement surface will undoubtedly play a part in determining the exact jet characteristics. The second regime of interest is the

impingement regime, wherein the flow properties are primarily determined by the direct interaction of the jet and the solid surface. It is here that the large gradients of pressure, density, and velocity associated with the rapidly changing flow direction occur. Once the flow has been completely turned in a direction parallel to the impingement surface and is no longer influenced locally by impingement processes, it enters the third basic regime, that of the wall jet. Here the primarily radial flow develops into a fully developed wall jet characterized by an inner layer of boundary layer-like flow and an outer layer of free shear turbulent mixing. It is probable, of course, that the character of at least the first two of these regimes will be highly sensitive to local changes in the structure of the impinging jet, especially for cases in which an underexpanded jet impinges at close range. Each of the basic regimes and the symbols used to designate certain quantities are shown in Figure 16.

In order to estimate the heat transfer at the stagnation point of an impinging flow such as that just described, the local radial velocity gradient $(du_e/dr)_{r=0}$ which appears as a parameter in the usual stagnation point heat transfer equation must be evaluated. This can be done experimentally by relating the parameter to the static pressure distribution on the surface in the immediate vicinity of the stagnation point. Assuming the flow outside the boundary layer to be locally incompressible, the local pressure in the laminar boundary layer may be written

$$p = p_P^0 - \frac{1}{2}\rho_e u_e^2 \tag{1}$$

or

$$\frac{dp}{dr} = -\rho_e u_e \frac{du_e}{dr} - \frac{1}{2}u_e^2 \frac{d\rho_e}{dr} \tag{2}$$

where p_P^0 is the total pressure at the stagnation point (i.e. where $u_e = 0$), u_e is the velocity at the edge of

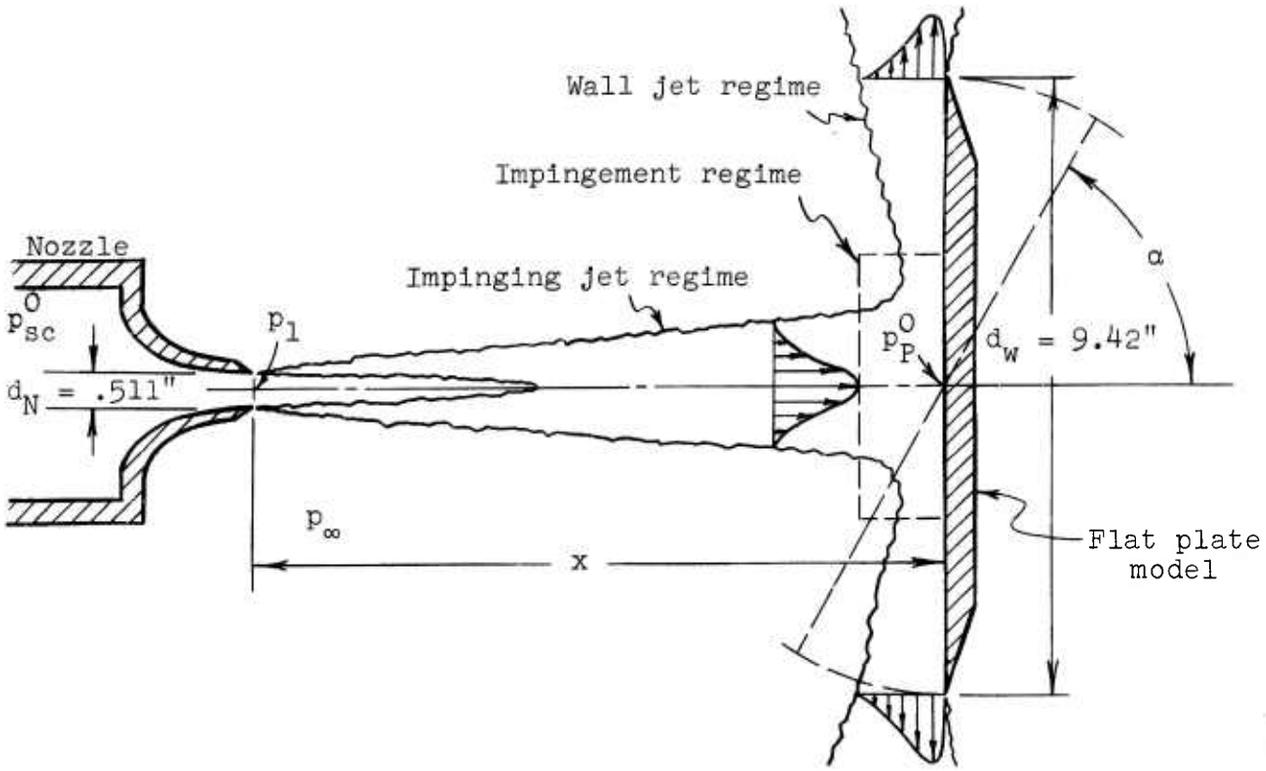

Figure 16. Schematic view of impingement flow with flat plate model in place.

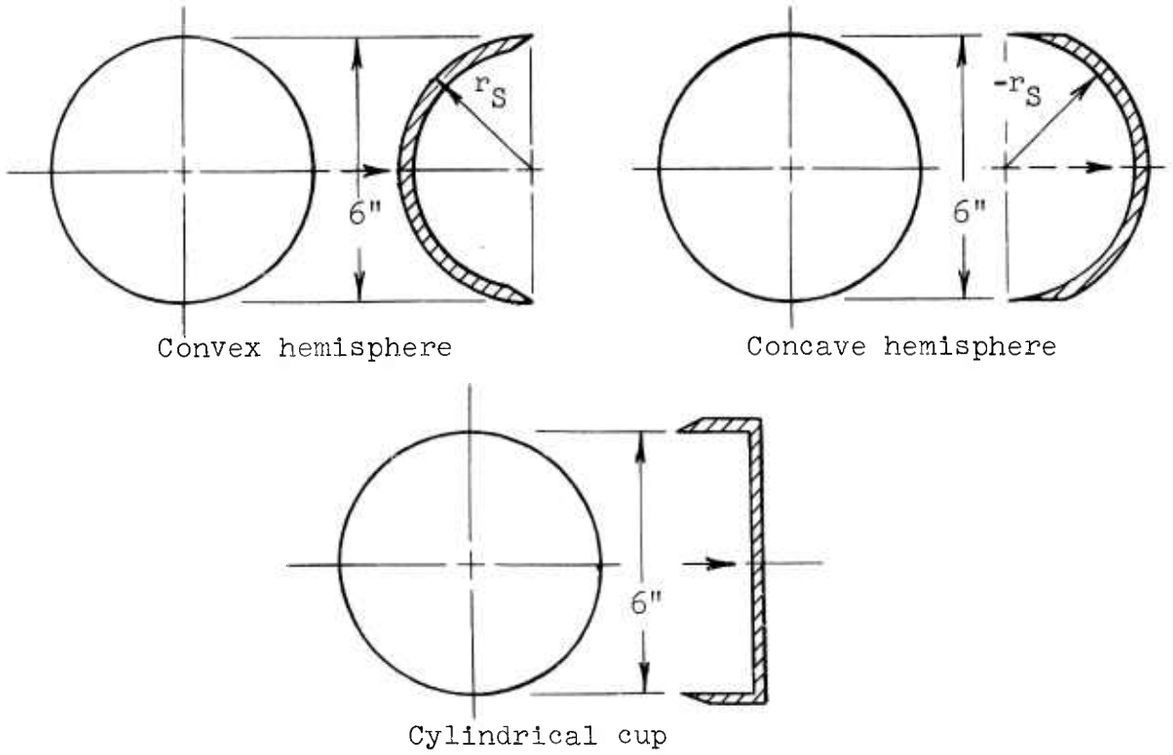

Figure 17. Basic impingement model shapes.

the boundary layer, and ρ_e is the local density. Neglecting the second term on the right, since $d\rho_e/dr = 0$,

$$\frac{d^2p}{dr^2} = -\rho_e u_e \frac{d^2u_e}{dr^2} - \rho_e r \left(\frac{du_e}{dr}\right)^2 \tag{3}$$

At $r = 0$, $u_e = 0$, so that

$$\left(\frac{d^2p}{dr^2}\right)_{r=0} = -\rho_e \left(\frac{du_e}{dr}\right)^2_{r=0} \tag{4}$$

Thus the parameter in question is proportional to the square root of the curvature of the pressure distribution at the stagnation point. For the purpose of evaluating $(du_e/dr)_{r=0}$ directly from measured pressure data, however, an alternate form of this relation is derived directly from Equation 1 making use of the equation of state $p_p^0 = \rho_e RT^0$. Thus, expanding u_e in a power series about the stagnation point $r = 0$,

$$\begin{aligned} \frac{p}{p_p^0} &= 1 - \frac{1}{2}\frac{\rho_e}{p_p^0} u_e^2 \\ &= 1 - \frac{1}{2}\frac{\rho_e}{p_p^0}\left(\frac{du_e}{dr}\right)^2_{r=0} r^2 \\ &= 1 - \frac{1}{2}\frac{r_w^2}{RT^0}\left(\frac{du_e}{dr}\right)^2_{r=0}\left(\frac{r}{r_w}\right)^2 \end{aligned} \tag{5}$$

where r_w is the wetted radius of the impingement surface, T^0 is the stagnation temperature of the flow, and R is the specific gas constant. Solving for $(du_e/dr)_{r=0}$

we have

$$\left(\frac{du_e}{dr}\right)_{r=0} = \sqrt{\frac{2R}{r_w^2}}\sqrt{\frac{T^0}{(r/r_w)^2}\left(1 - \frac{p}{p_P^0}\right)} \qquad (6)$$

The evaluations of this parameter for a number of impingement conditions are given in 3.2.3. The experimental program is described in detail in the next subsection.

3.2. Experimental program.

The bulk of the experimental program was devoted to a study of the normal impingement ($\alpha = 90^\circ$) of the three basic jet types described in Section 2. Each of these jets was impinged upon four different model shapes and the stagnation region pressure distributions determined. Stagnation point radial velocity gradients were then computed. In addition, two methods of nondimensionalizing the measured gradients in terms of known jet properties were evaluated. One such method was based on conditions at the jet nozzle exit, and the other on local conditions at the impingement station in the free jet. These nondimensional forms are discussed in 3.2.3.

The three jets used for the impingement studies were as listed in the discussion of the free jet program in 2.2, except for the subsonic jet which had a negligibly different pressure ratio, i.e. $p_\infty/p_{sc}^0 = .800$ rather than .834. The moderately underexpanded jet had $p_\infty/p_{sc}^0 = .372$, and the highly underexpanded jet had $p_\infty/p_{sc}^0 = .148$. The impingement distances chosen were also the same as those for the free jet experiments, i.e. $x/d_N = 1.96$, 7.32, 23.5, and 39.1. In addition, several other locations were used in order to fill in data in regions of special interest. The entire

program of normal impingement cases, which included measurements of over-all surface pressure distributions and certain additional studies with the flat plate model, as well as the detailed stagnation region measurements is tabulated in Appendix III. An additional program devoted primarily to the study of impingement on the flat plate at oblique angles ($\alpha < 90^{\circ}$) is to be reported separately.

3.2.1. Apparatus and instrumentation. Except for the impingement models themselves, the test setup was exactly the same as that used for the free jet studies (2.2.1). In Figure 3, the nozzle is shown with the flat plate model mounted in position. The mounting was designed so that fine centering adjustment could be made either horizontally or vertically. The impingement angle was adjusted by means of a jack screw which rotated each model about a horizontal line passing through its stagnation point. Axial changes in impingement distance were made by shifting the entire model supporting structure to the desired location along two steel angle rails at the bottom. The mounting as a whole was made to be rigid enough to minimize deflection under jet dynamic loading, while at the same time having the main members as far removed as feasible from the impingement region so as to minimize the possibility of interference with the flow.

All of the impingement models were made with the same wetted diameter, i.e. the distance along the impingement surface from edge to edge through the center. This distance, based on a hemisphere model diameter of 6 inches was 9.42 inches. The individual model characteristics were as follows (see Figure 17):

Flat plate: Aluminum disk, 1/2 inch thick and 9.42 inches in diameter. 27 pressure taps along vertical diameter and 15 along horizontal diameter.

Convex and concave hemispheres: Fiber glass-epoxy resin molded shells, about 3/8 inch thick and 6 inches in diameter. Concave model made first on male mold; concave model then used as mold for convex model. 27 pressure taps along vertical diameter and 5 along horizontal diameter.

Cylindrical cup: Brass flat plate 1/2 inch thick and 6 inches in diameter with brass cylindrical rim 1/8 inch thick and 1.71 inches high. 28 pressure taps along vertical diameter including rim and 11 along horizontal diameter.

All the pressure tap holes were drilled with a number 75 drill except for four closely spaced (1/16 inch spacing) holes including the stagnation point hole which were number 80 (.0135 inch). The latter holes were along the vertical diameter.

Pressure readings for each run were made on multiple manometers or test gauges and were recorded photographically. The stagnation temperature was measured as before.

3.2.2. Results of pressure distribution measurements and photographic studies.

Pressure distributions. For each of the basic combinations of jet strength and impingement distance, both detailed stagnation region and over-all pressure distributions were measured for each model. Of particular importance in obtaining these results was the initial alignment of the models relative to the jet flow. A model was first aligned parallel to the jet exit plane by means of direct measurement between its outer edges and a straightedge held across the nozzle exit. Vertical and horizontal centering were then accomplished with the jet running by nulling the pressure differential between pressure taps equidistant from the

center tap. Although the initial parallel alignment cannot take into account the fact that the jet may not issue from the nozzle exactly coaxial with it or that interference or buoyant effects may change the jet's direction slightly, it was found that stagnation region distributions were quite insensitive to small changes in impingement angle. Thus it was felt that these factors could be neglected as long as the model was centered.

In order to obtain high resolution distributions in the vicinity of the stagnation point, a technique was used of translating the model slightly between each of several jet runs. In this case, the model was exactly centered only horizontally. The vertical centering adjustment was then used to shift the model slightly up or down in its own surface plane so as to bring the central pressure taps to a different point in the flow. Because of the usually consistent data obtained, it was assumed that the maximum over-all translation of about 1/8 inch had little or no effect on the absolute position of the jet. A typical pressure distribution resulting from the use of this technique is shown in Figure 18.

The results of these detailed stagnation point measurements are shown for all the basic combinations in Figures 19 through 30. On these plots the pressure is given as a ratio of local to stagnation point absolute value, while the radial distance is given in nozzle radii from the stagnation point. In order to show clearly the slight differences between the distributions for different shapes on each plot, the data points have been omitted. For reference, the Pitot pressure profile of the free jet at each axial location is also plotted.

Except for the case $p_1/p_\infty = 3.57$; $x/d_N = 1.96$, it is observed that the pressure distributions follow the general local character of the free jet (cf. Figures 5, 7, and 10), although there is a tendency for the impingement distribution

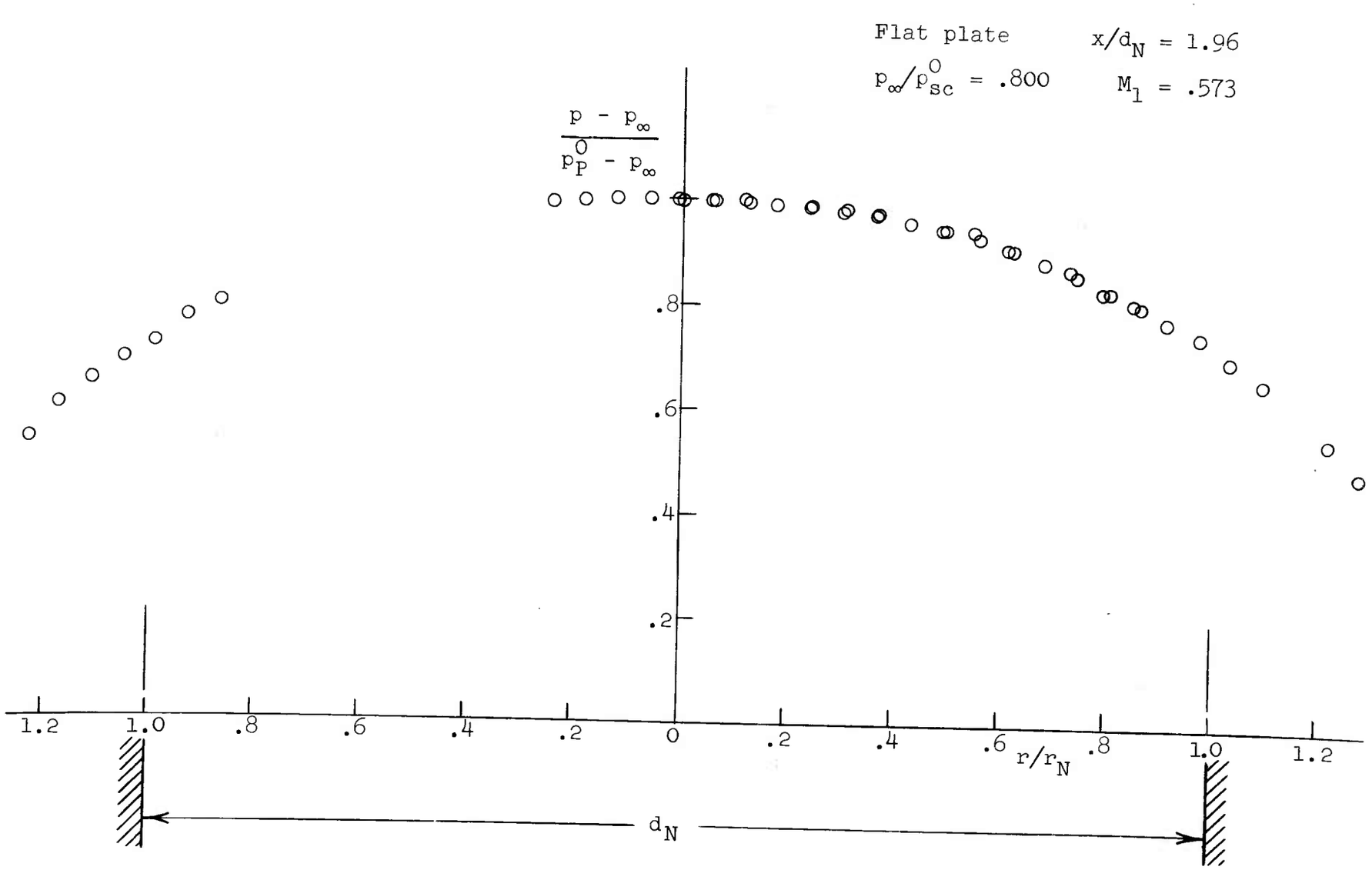

Figure 18. Typical stagnation region pressure distribution.

$x/d_N = 1.96$ $\alpha = 90^\circ$

$p_\infty/p^o_{sc} = .800$ $p_1/p_\infty = 1.00$

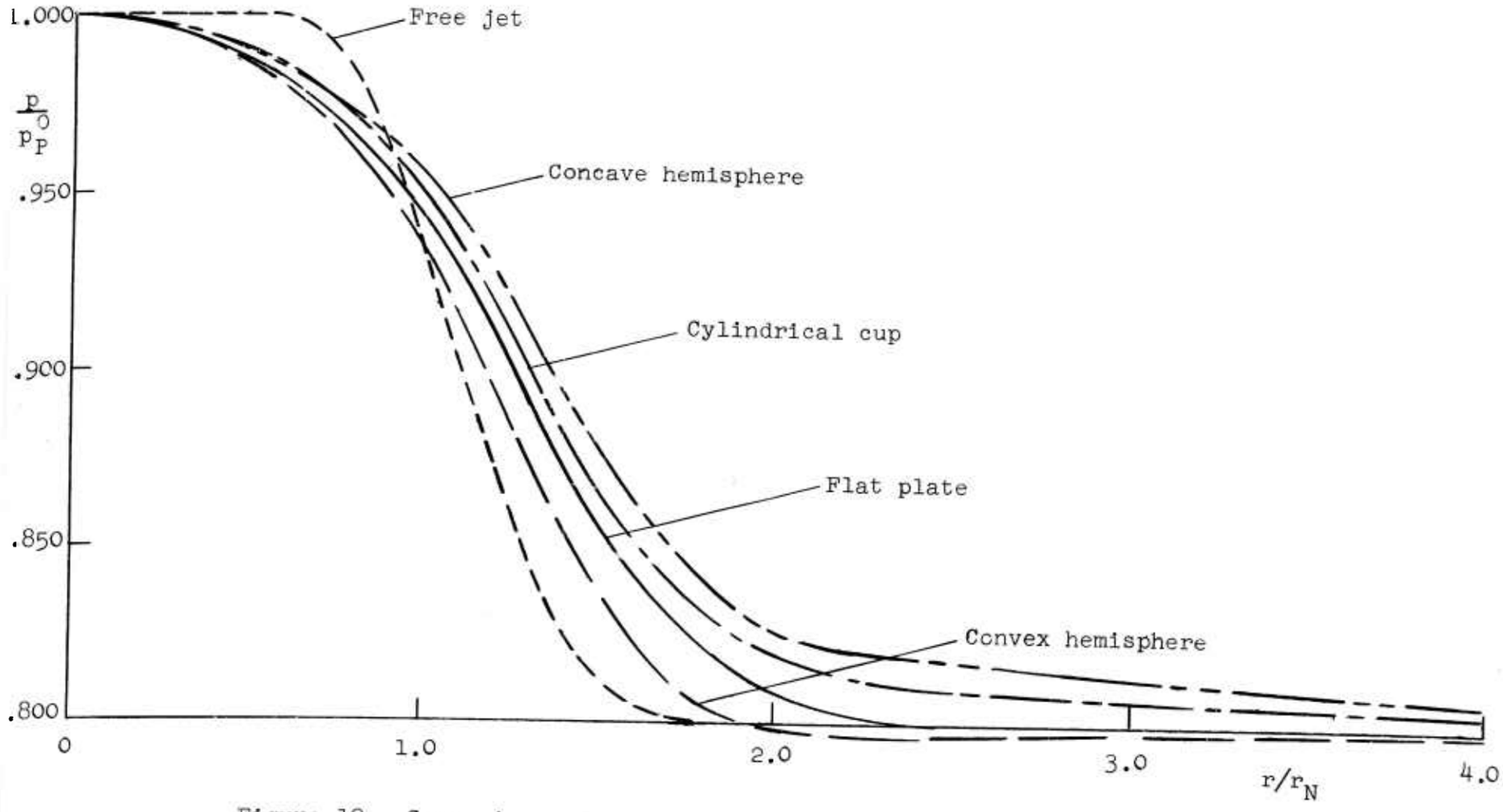

Figure 19. Comparison of measured stagnation region pressure distributions for several surface shapes.

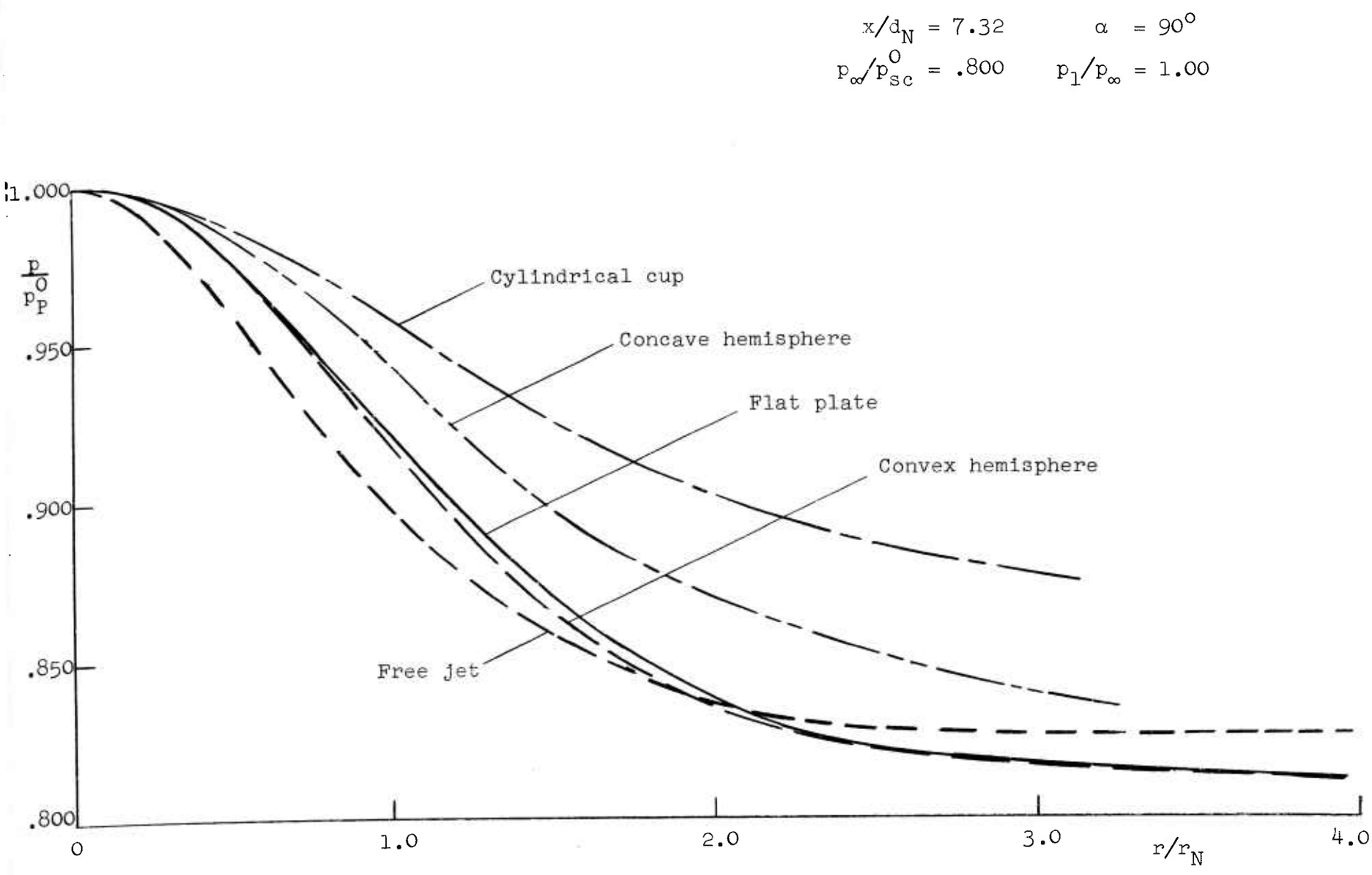

Figure 20. Comparison of measured stagnation region pressure distributions for several surface shapes.

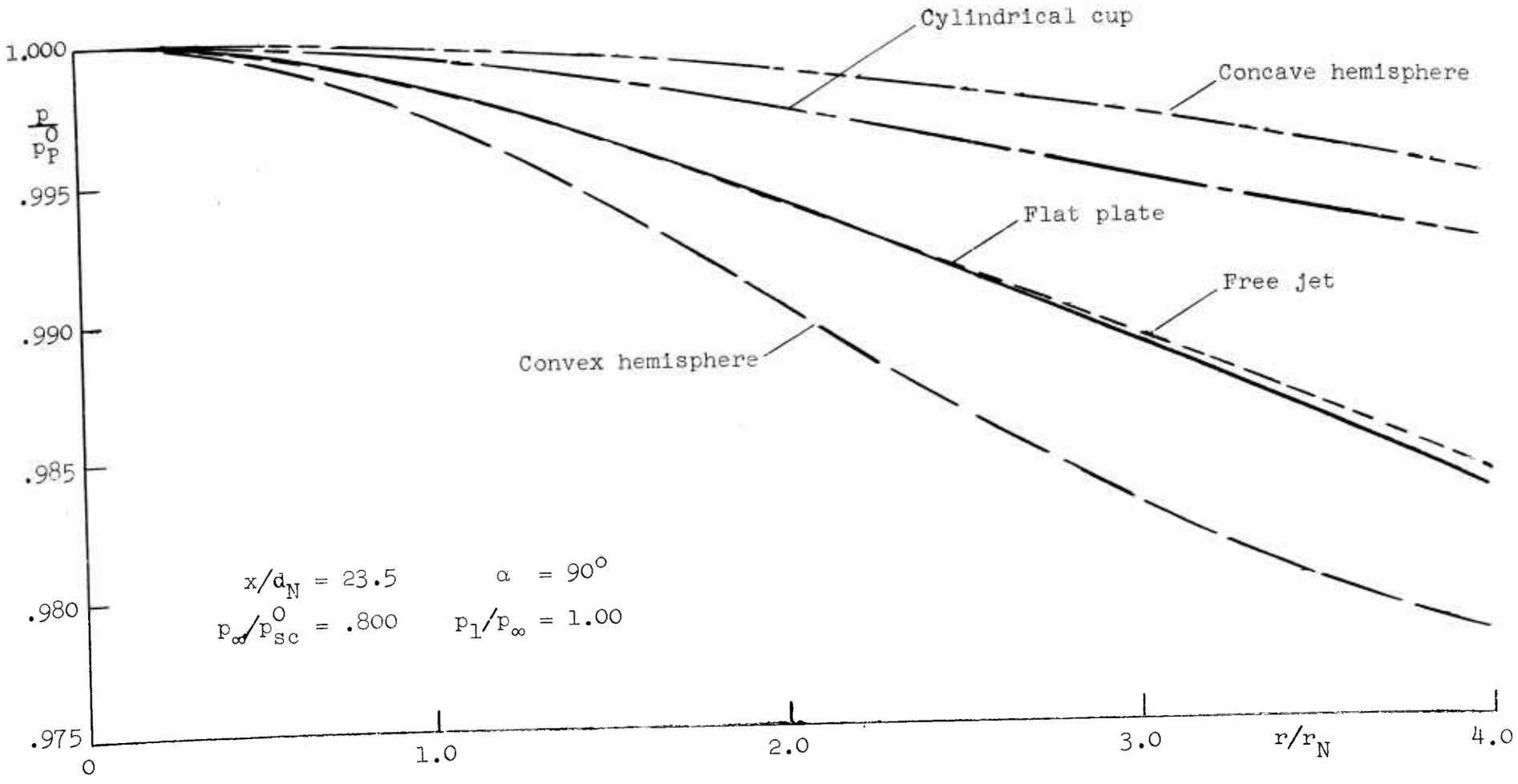

Figure 21. Comparison of measured stagnation region pressure distributions for several surface shapes.

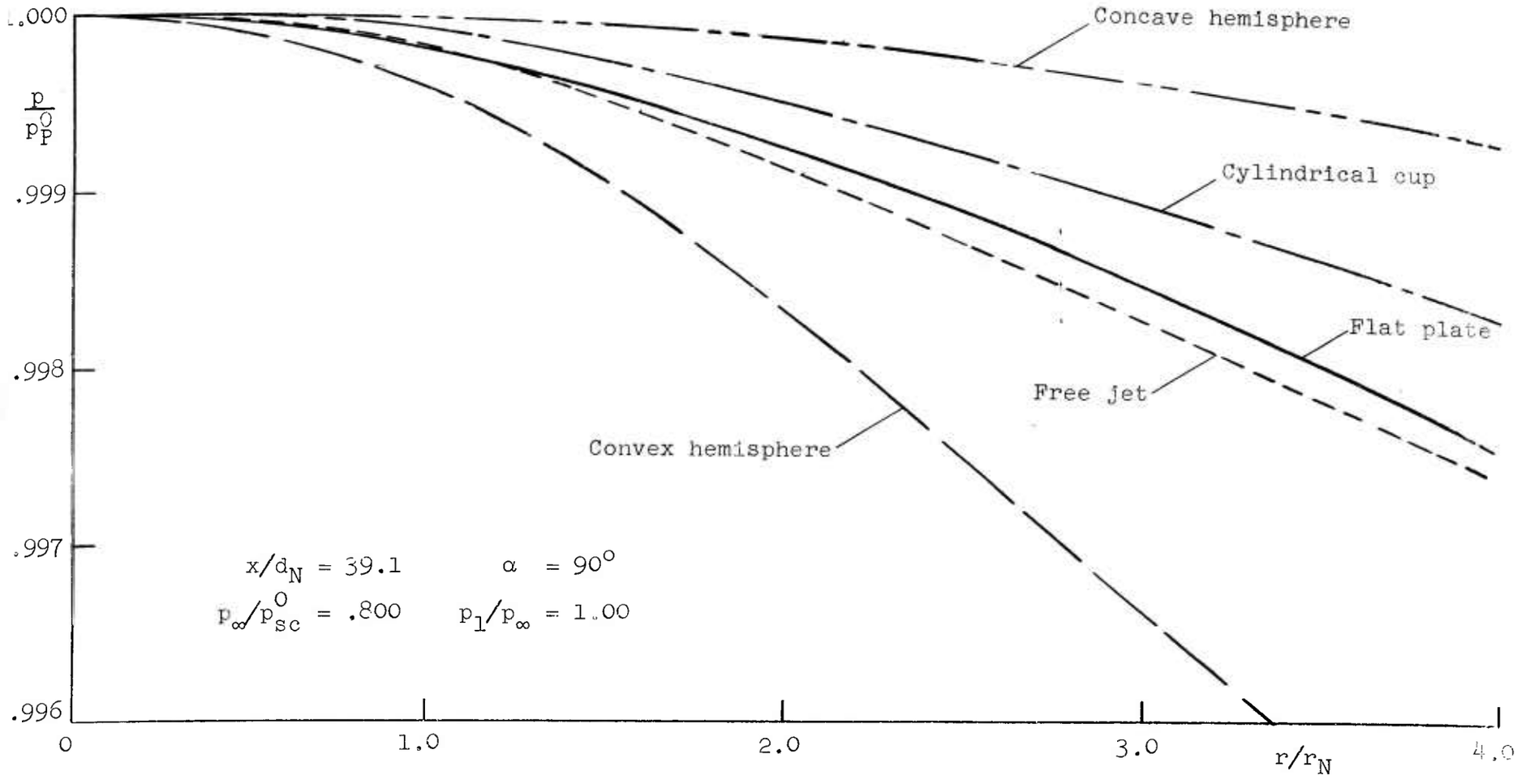

Figure 22. Comparison of measured stagnation region pressure distributions for several surface shapes.

$x/d_N = 1.96$ $\alpha = 90^o$

$p_\infty/p^o_{sc} = .372$ $p_1/p_\infty = 1.42$

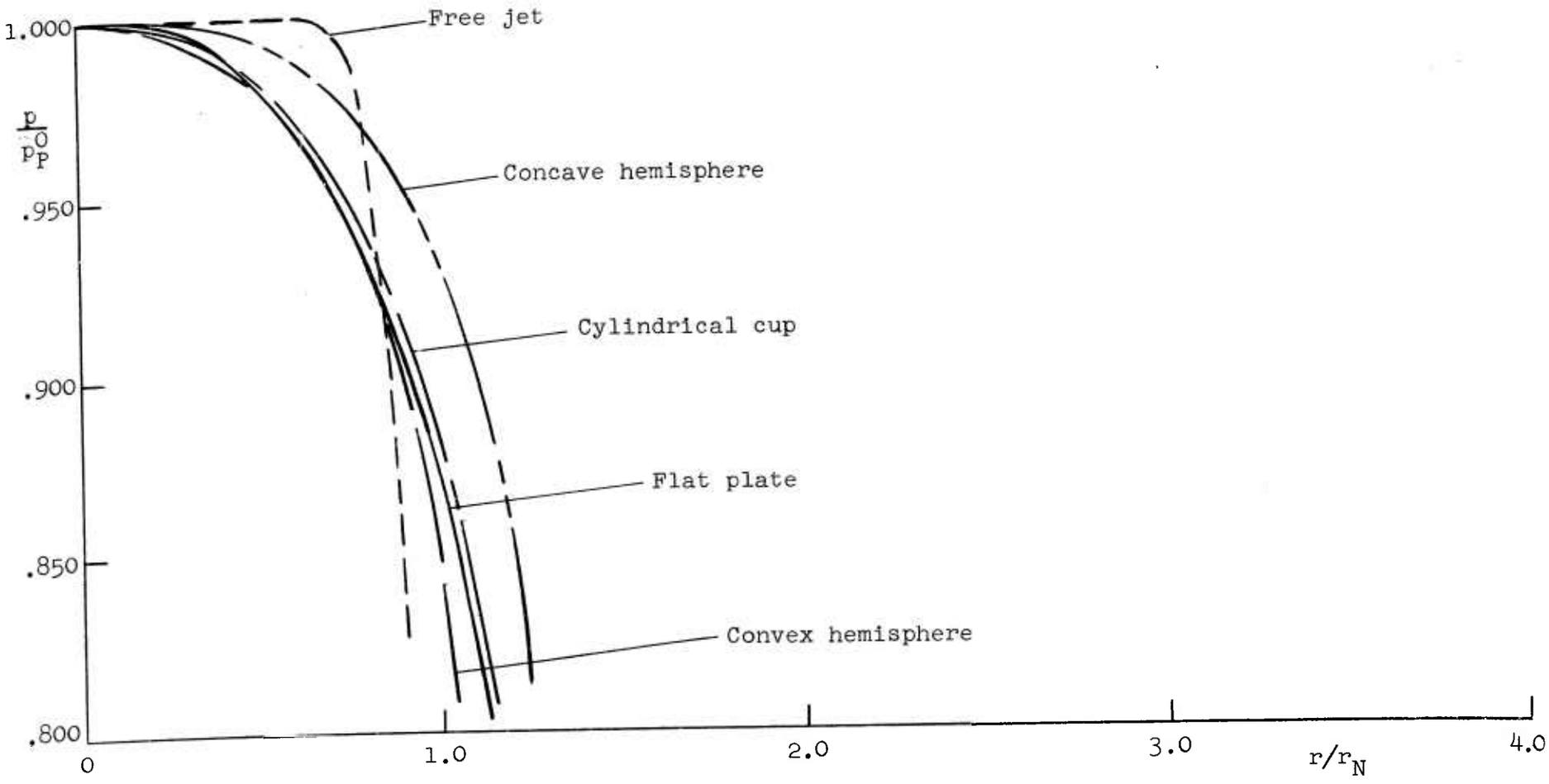

Figure 23. Comparison of measured stagnation region pressure distributions for several surface shapes.

$x/d_N = 7.32$ $\alpha = 90^\circ$

$p_\infty/p^o_{sc} = .372$ $p_1/p_\infty = 1.42$

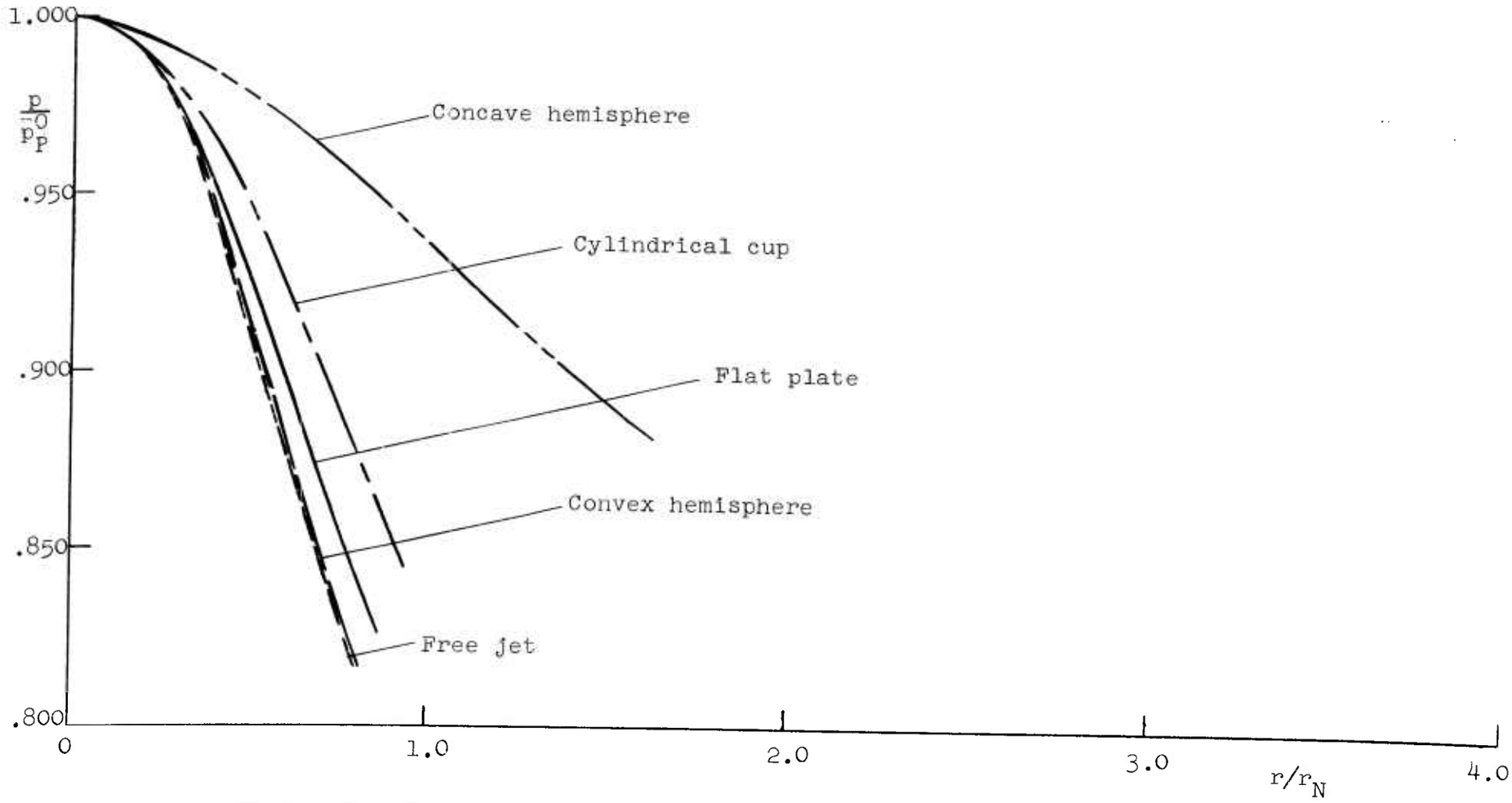

Figure 24. Comparison of measured stagnation region pressure distributions for several surface shapes.

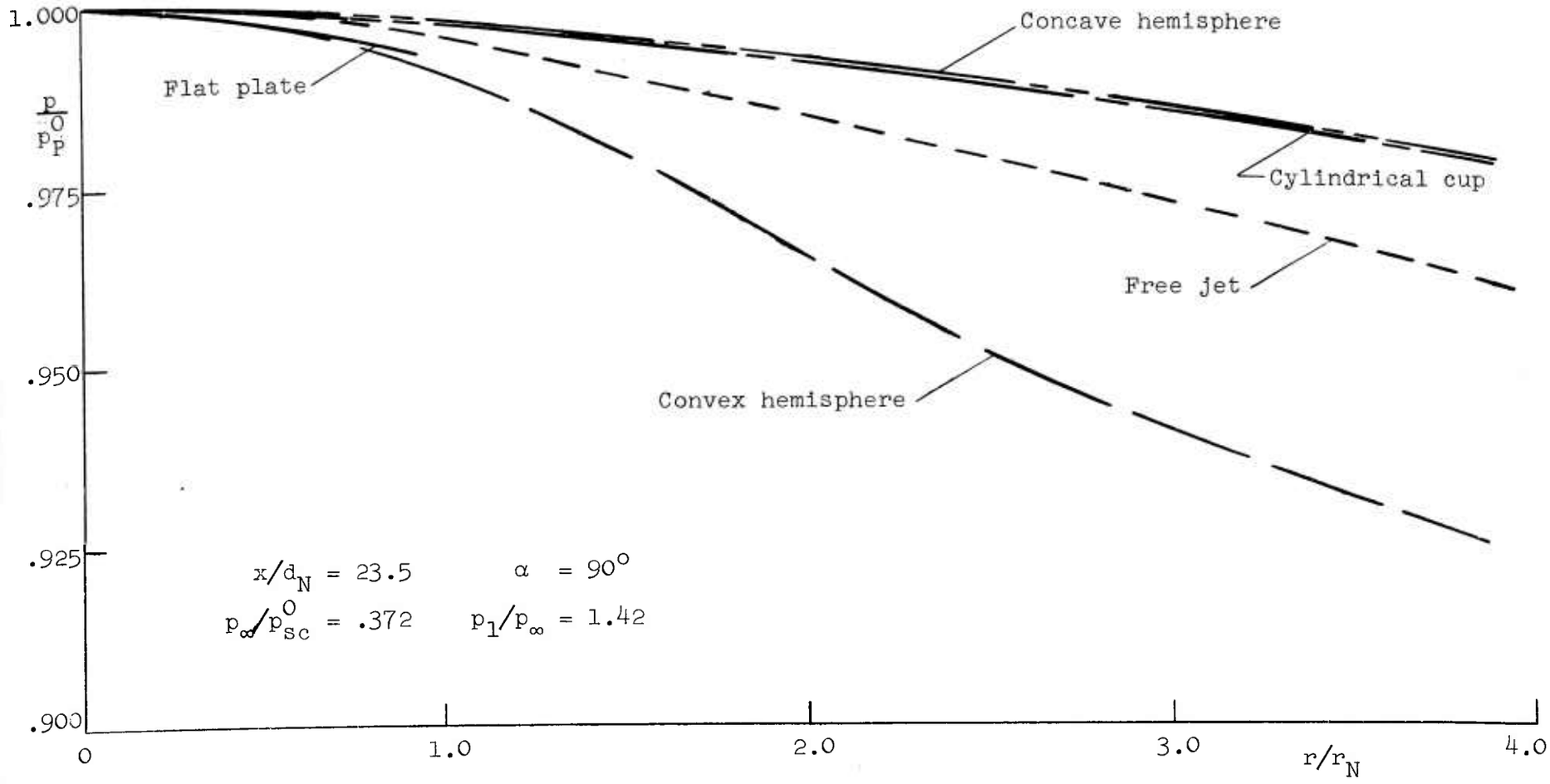

Figure 25. Comparison of measured stagnation region pressure distributions for several surface shapes.

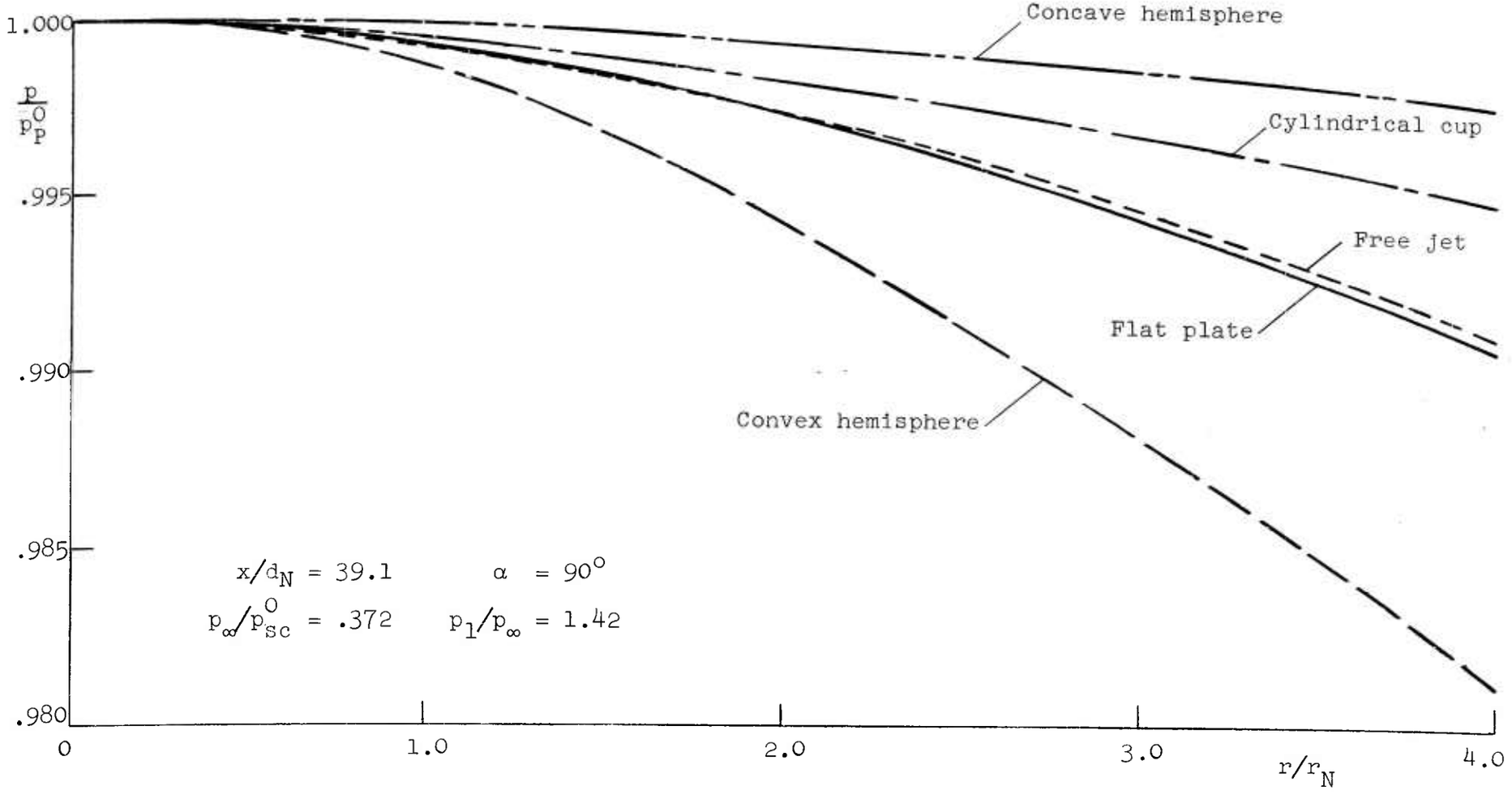

Figure 26. Comparison of measured stagnation region pressure distributions for several surface shapes.

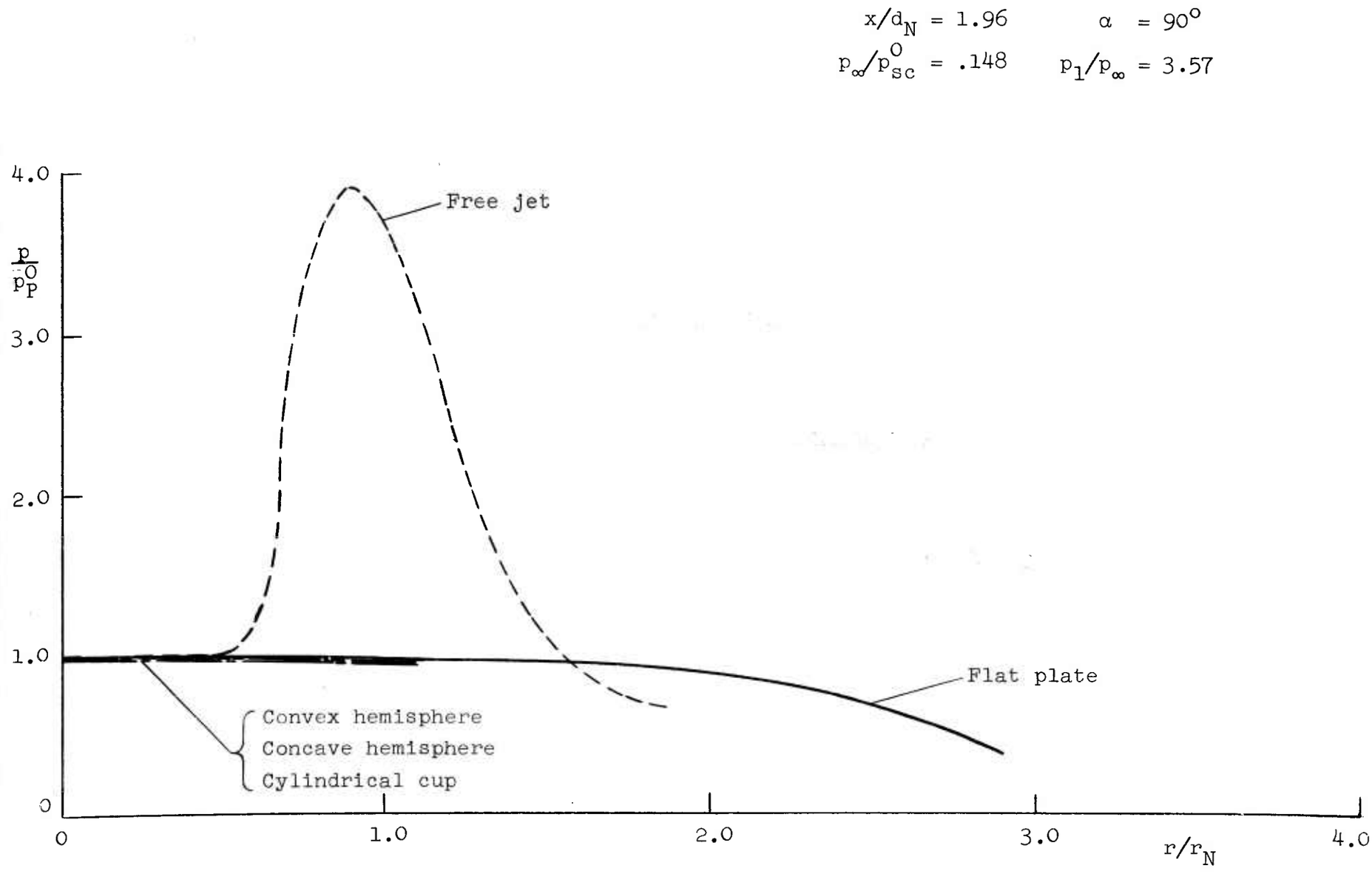

Figure 27. Comparison of measured stagnation region pressure distributions for several surface shapes.

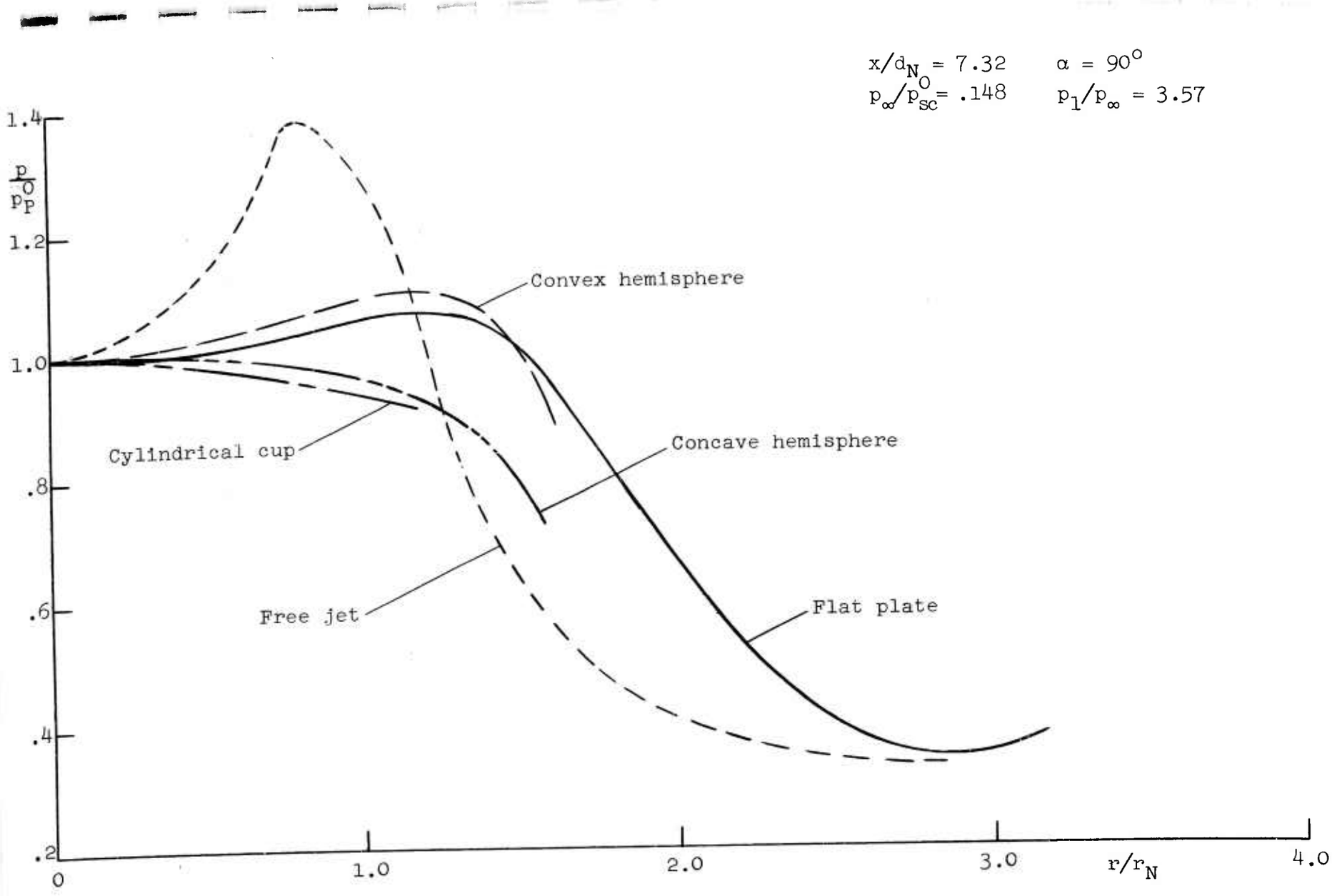

Figure 28. Comparison of measured stagnation region pressure distributions for several surface shapes.

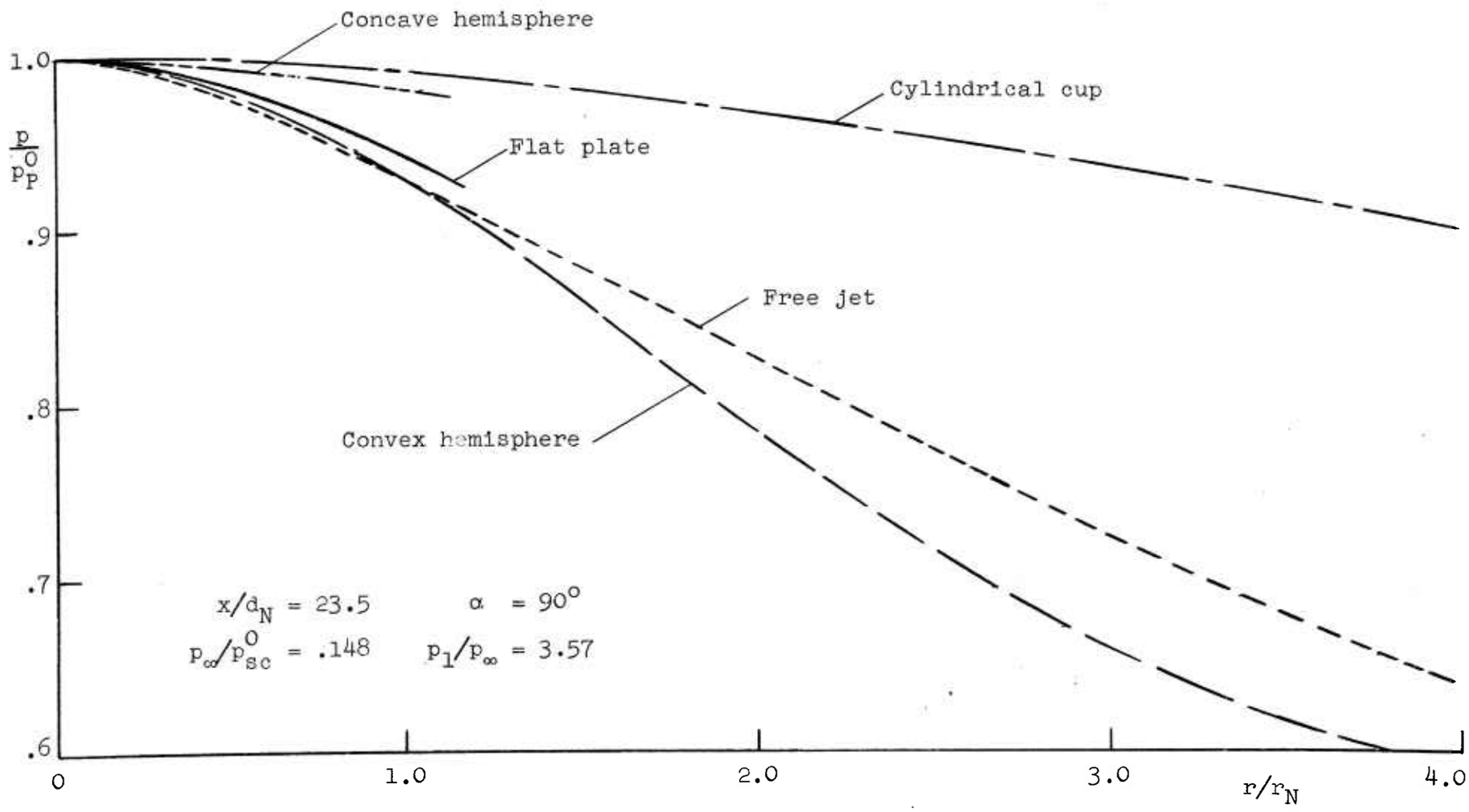

Figure 29. Comparison of measured stagnation region pressure distributions for several surface shapes.

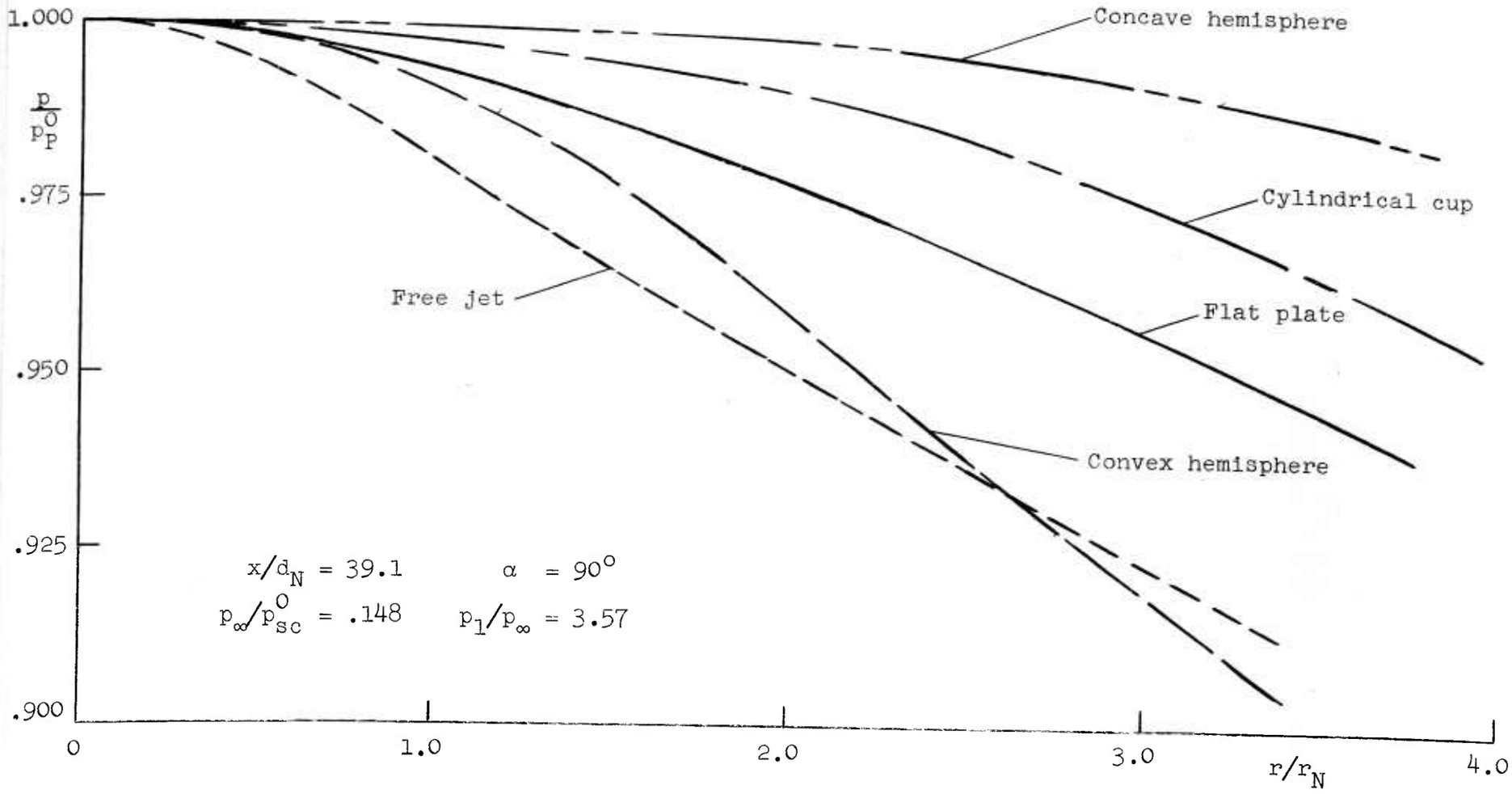

Figure 30. Comparison of measured stagnation region pressure distributions for several surface shapes.

to be relatively spread out. The excepted case exhibits a flattened distribution with no distinct peaks. Other cases involving the highly underexpanded jet show apparent stagnation points to either side of the center with a relatively flat distribution or a third peak at the center. This behavior has been investigated further and is discussed in 3.2.4. A consistent trend is that due to surface shape. The convex hemisphere distributions always drop off more rapidly than those of the flat plate, while those for the concave shapes drop off less rapidly. The relative behavior of the cylindrical cup and concave hemisphere shapes appears to depend on the impingement distance.

Over-all pressure distributions, measured from edge to edge across the vertical wetted diameter of each model, are shown in Figures 31 through 38 for each jet strength and model shape. These data are plotted with the local pressure as a percentage of its value p_p^o at the stagnation point. Thus it is possible to note the relative change in shape of the distributions for different impingement distances. Plots of these same data given in terms of the jet settling chamber stagnation pressure are included in Appendix IV.

In general, the effect of distance as shown in Figures 31 through 38, is as might be expected, with the pressure distribution following the basic spreading trends of the free jet. Certain details, however, are apparent which are not observed in the free jet data. In particular, there is often a distinct reversal of the radial pressure gradient in a short interval between 2 and 3 nozzle radii from the stagnation point when $x/d_N = 1.96$ and 7.32.* This reversal depends to some extent on the surface shape, being strongest

*This reversal is to be distinguished from that found near the center for the $p_1/p_\infty = 3.57$ jet which <u>does</u> occur in the free jet and which is apparently associated with the jet normal shock disk.

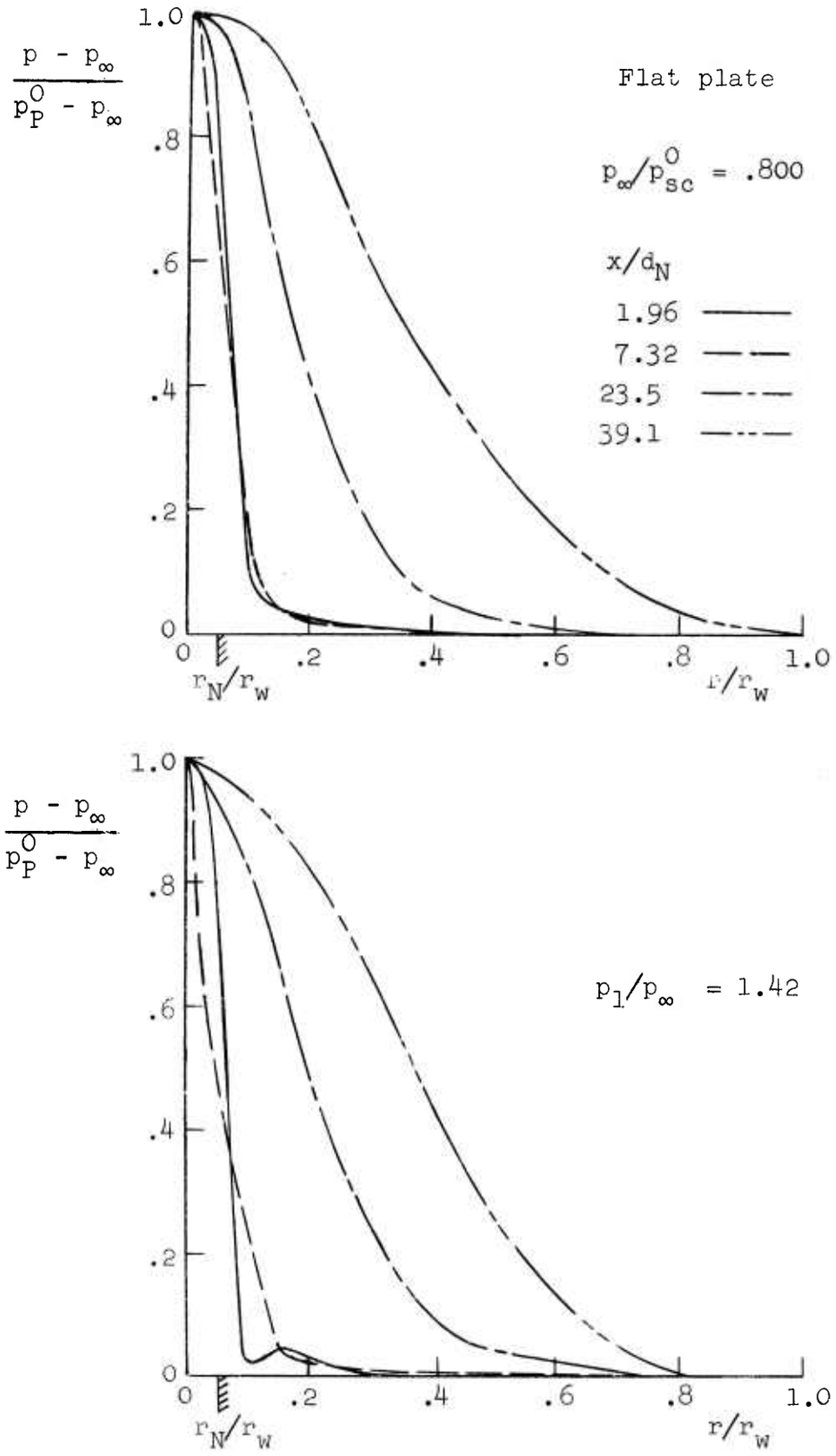

Figure 31. Measured over-all pressure distributions.

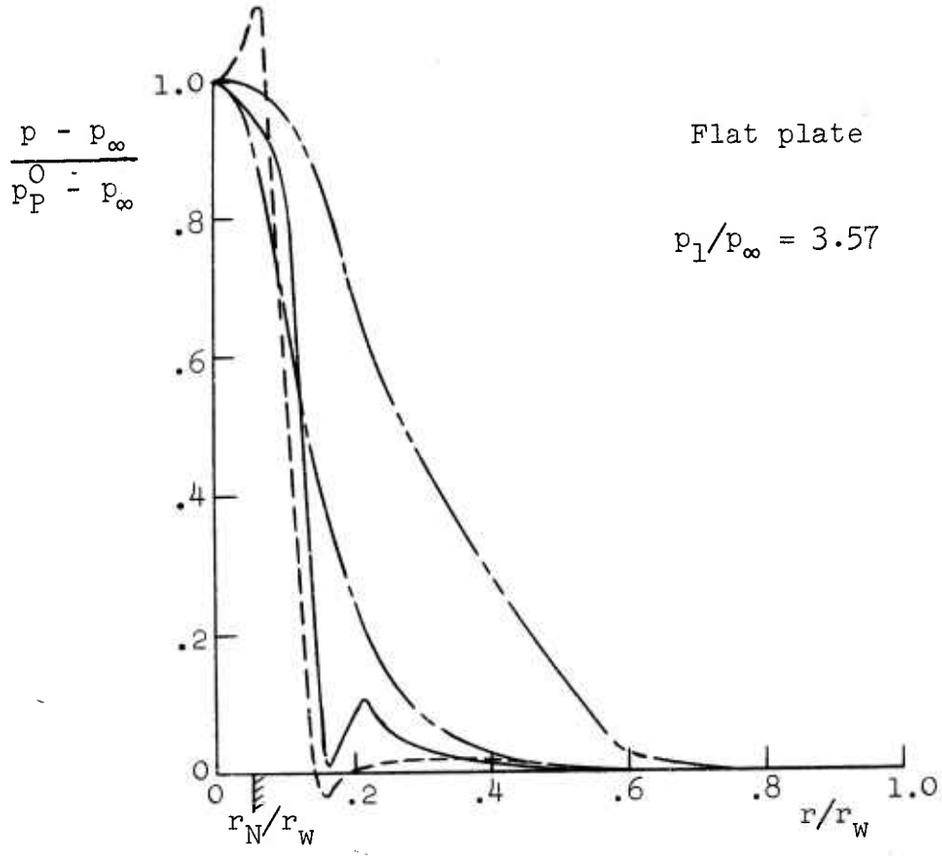

Figure 32. Measured over-all pressure distributions.

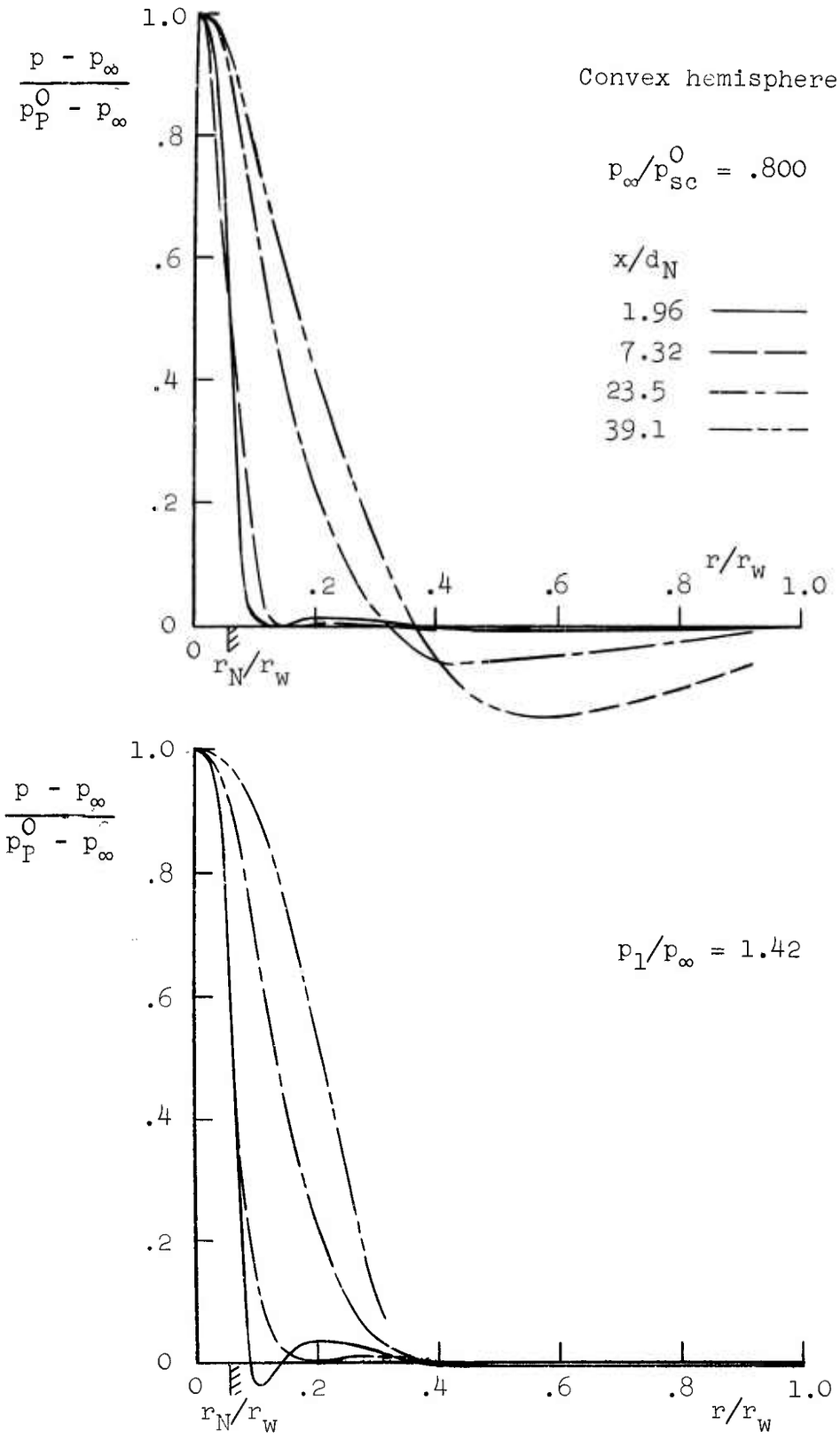

Figure 33. Measured over-all pressure distributions.

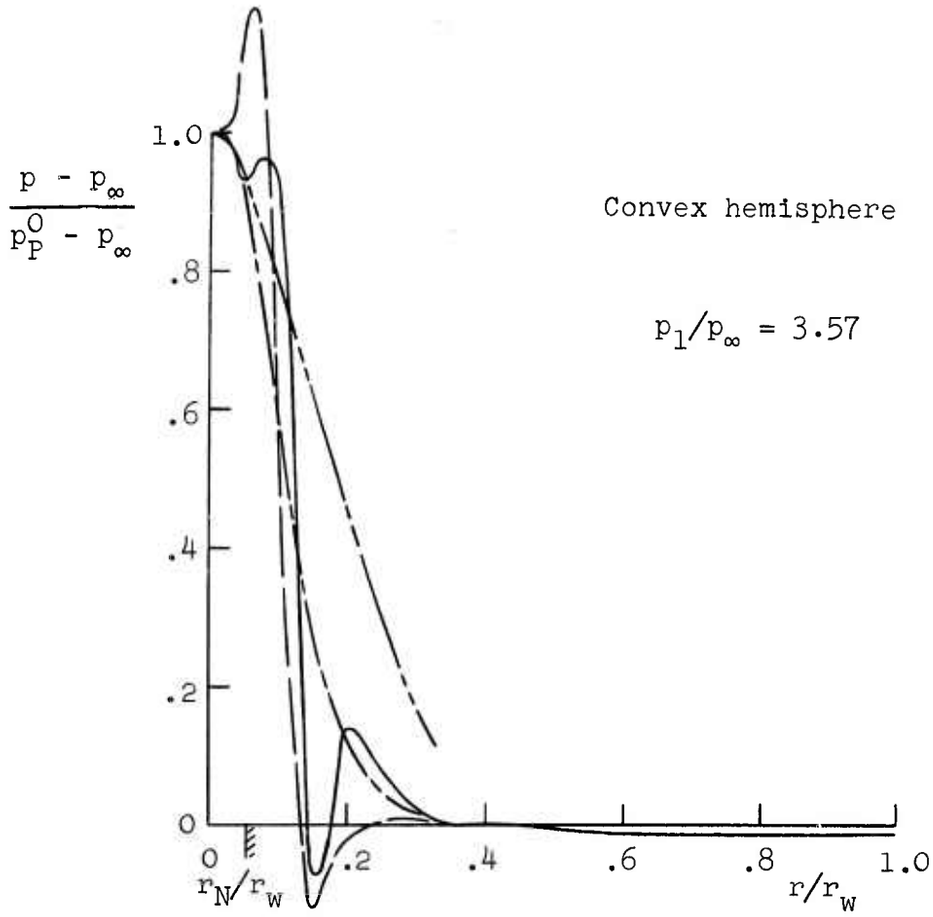

Figure 34. Measured over-all pressure distributions.

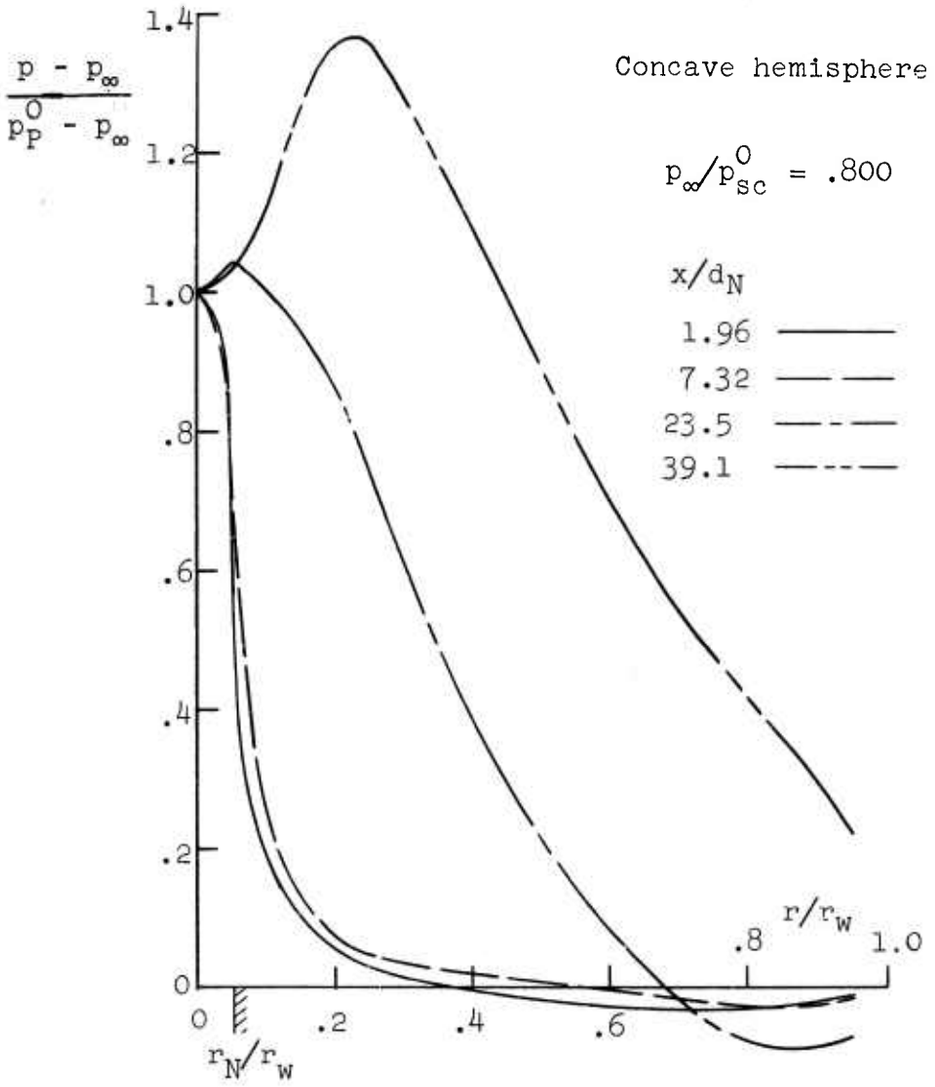

Figure 35. Measured over-all pressure distributions.

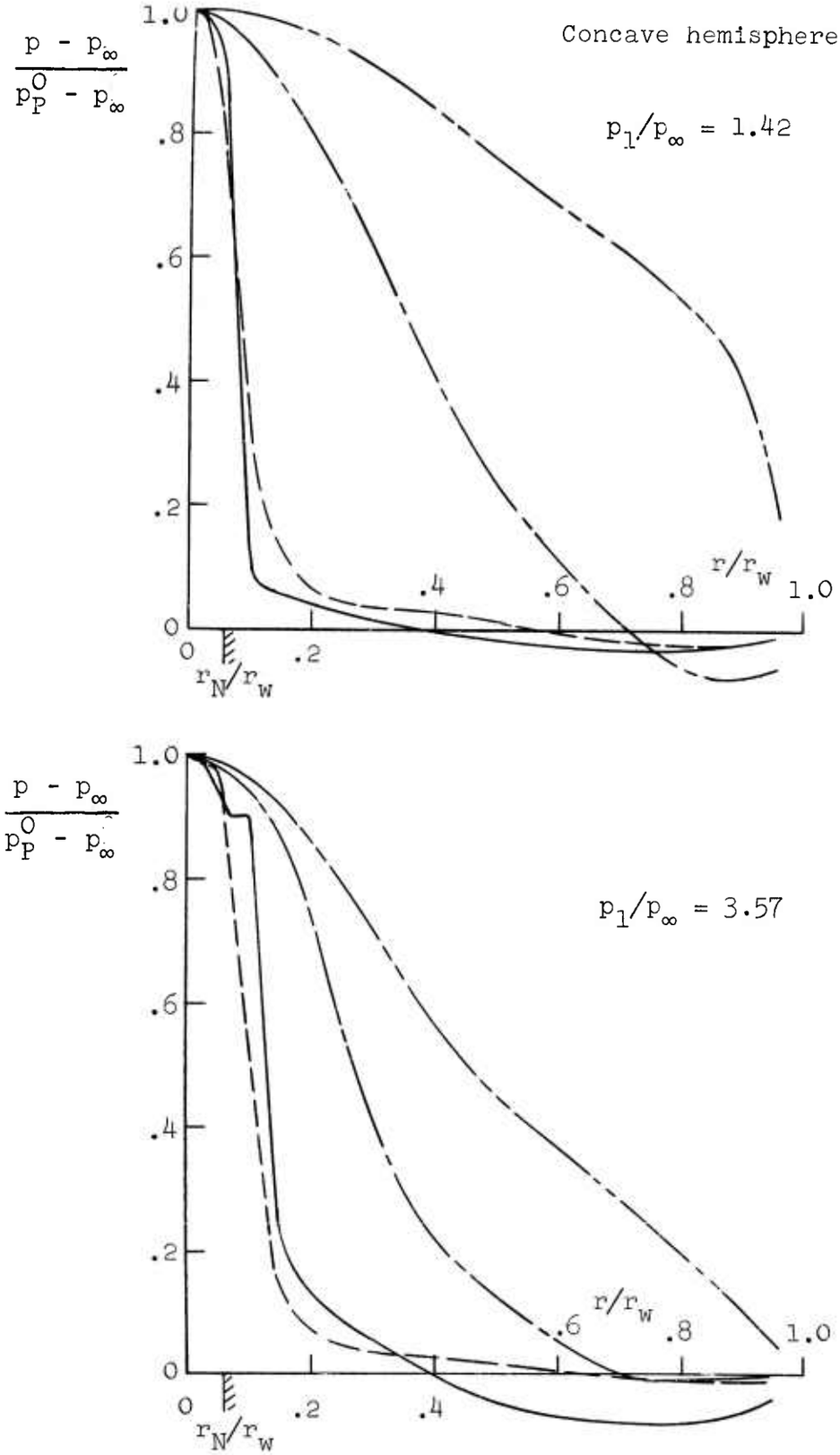

Figure 36. Measured over-all pressure distributions.

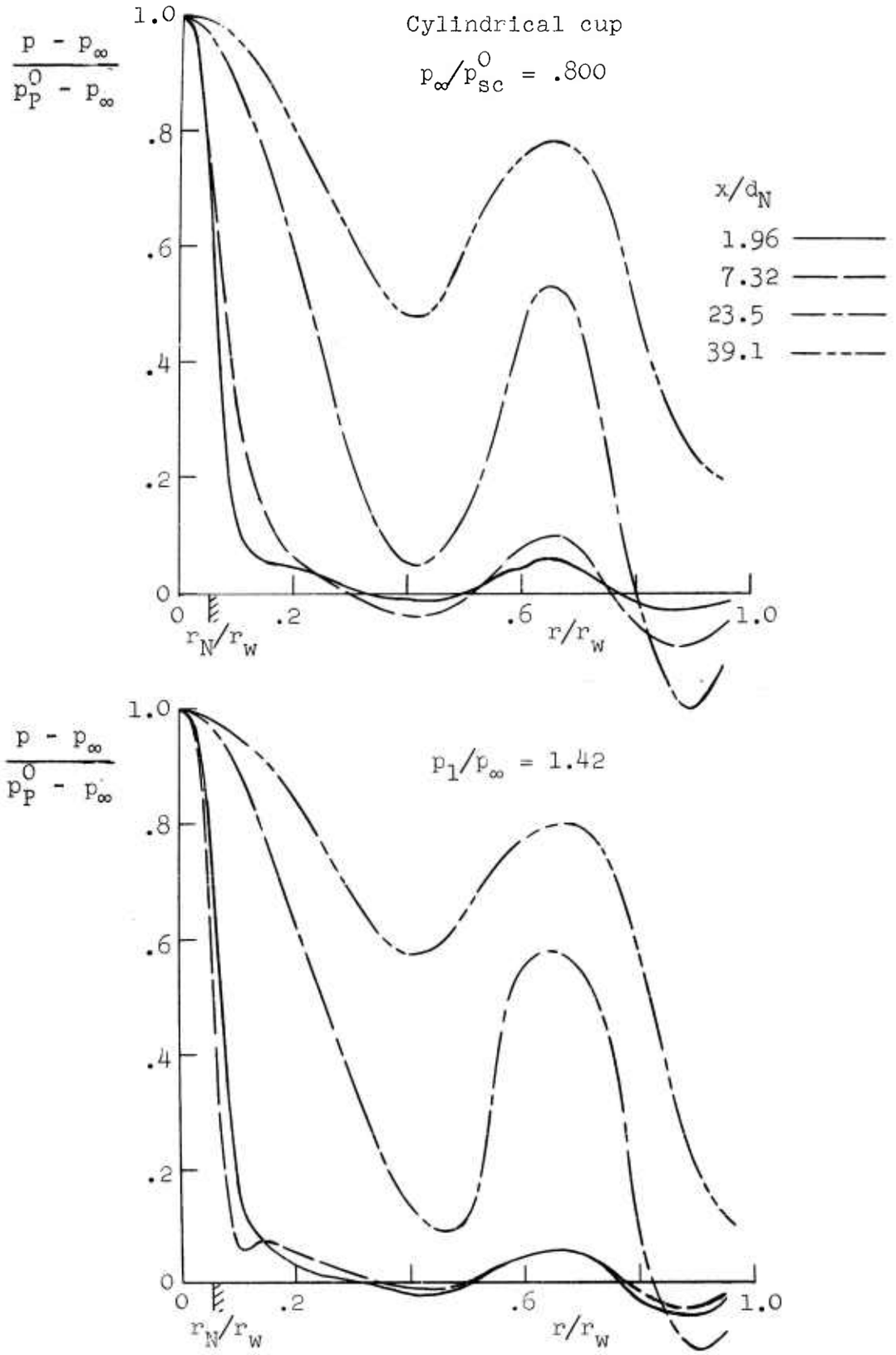

Figure 37. Measured over-all pressure distributions.

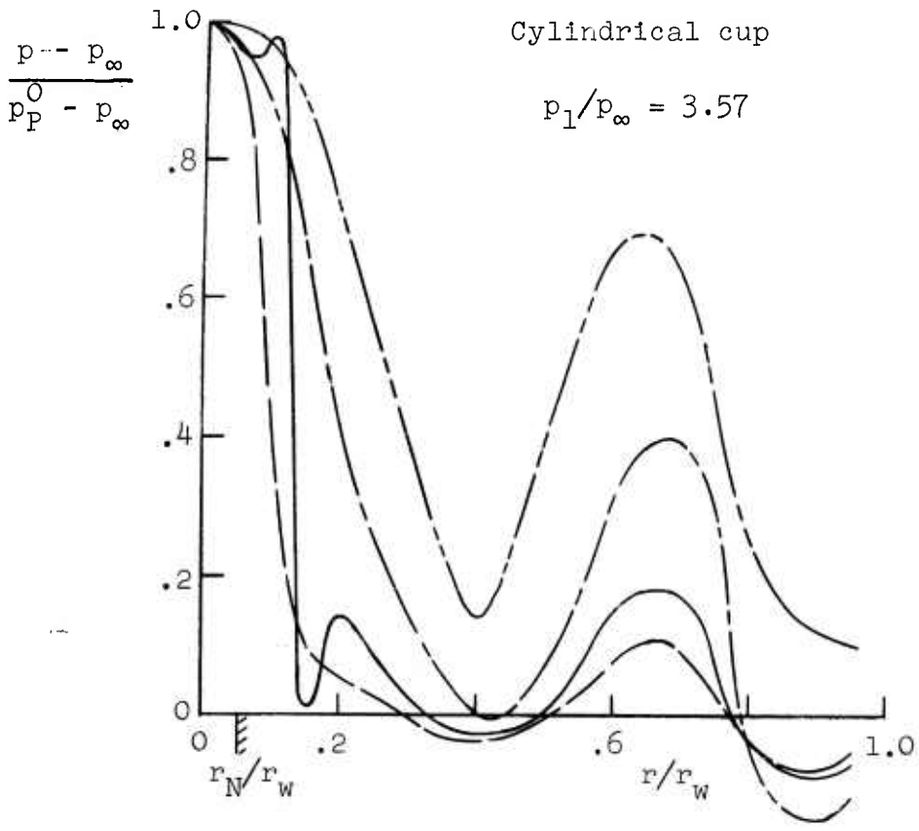

Figure 38. Measured over-all pressure distributions.

for the convex hemisphere. Since it occurs for this shape even for subsonic impingement, it appears not to be associated specifically with jet underexpansion phenomena. Whether or not the reversed gradient is sufficient to cause local separation is impossible to determine from these data alone. Another region of reversed gradient occurs near the outer edges for all the surfaces but the flat plate, although, again, separation cannot be confirmed.

The behavior of the concave shapes (hemisphere and cup) for impingement far downstream is of particular interest. In these cases, it is seen that a large portion of the surface is subjected to a pressure nearly as high as that at the stagnation point. In effect, the entire flow inside these shapes approaches a stagnation condition when the jet has spread to a size comparable to that of the model. In the cylindrical cup, the stagnation regions in the sharp corner are quite clear. The over-all stagnating effect is approached the closest for this model, especially in the case of impingement by the moderately underexpanded jet ($p_1/p_\infty = 1.42$). It is seen that the corner stagnation pressures are as high as 80 per cent of those at the central stagnation points.

The results of a highly detailed axial survey of the pressure at the center of the flat plate model are given in Figure 39. Also plotted is a similar survey of the Pitot pressure at the center of each free jet. Pitot pressure is plotted because the total pressure loss due to the stand-off normal shock cannot be determined for the impingement case. The data points for the free jet have been omitted for clarity, a measurement having been made at intervals of 0.2 nozzle diameters through most of the range $0 \leq x/d_N < 10$. The values of x_c/d_N shown represent core lengths for an equivalent properly expanded jet of the same pressure ratio computed using Warren's method (see 2.3). For the subsonic case, as might be expected, the curves are very close. In fact, as plotted on the present scale, they cannot be

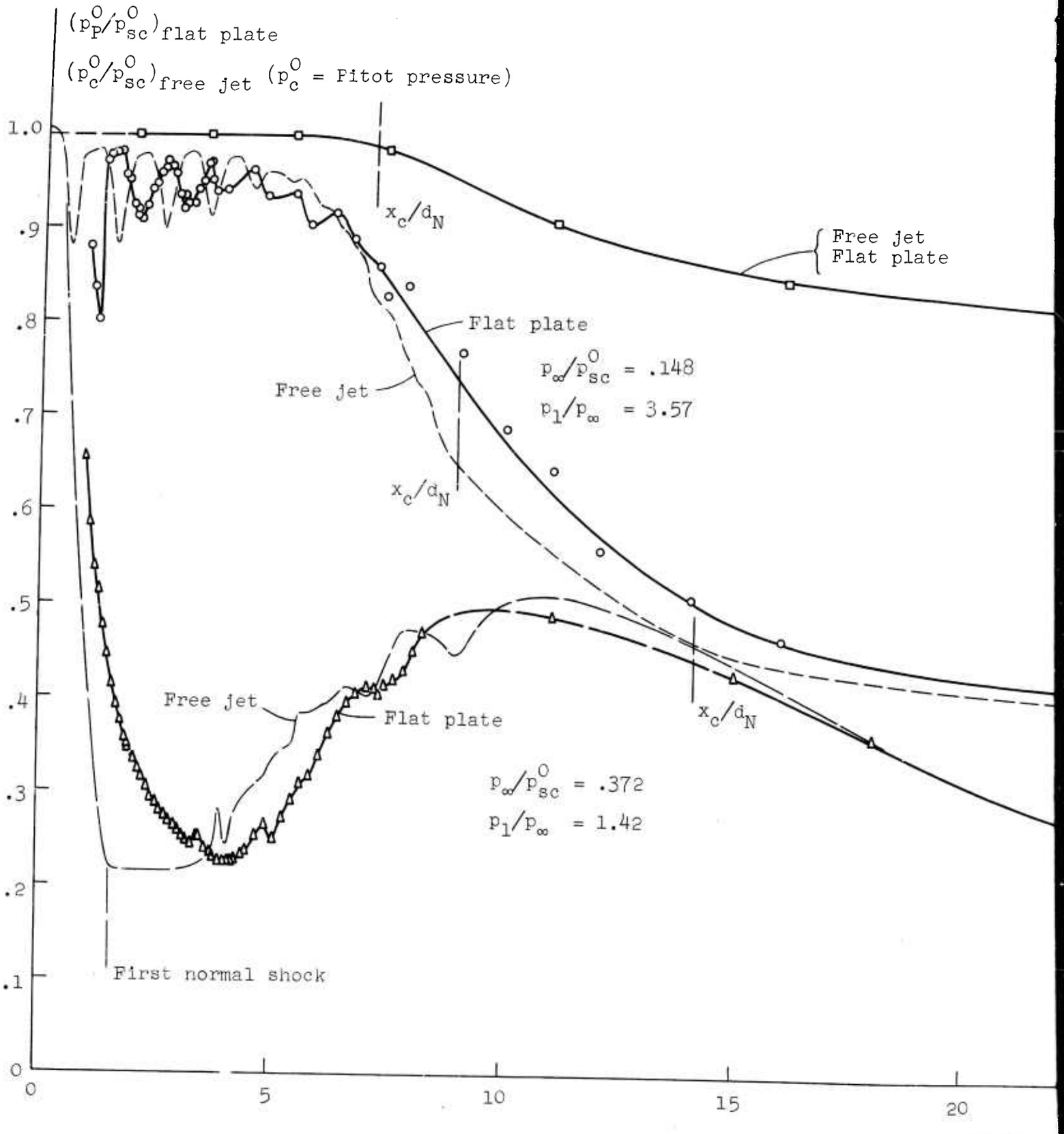
$(p_p^o/p_{sc}^o)_{flat\ plate}$
$(p_c^o/p_{sc}^o)_{free\ jet}$ (p_c^o = Pitot pressure)
1.0
.9
.8
.7
.6
.5
.4
.3
.2
.1
0
0
5
10
15
20
x_c/d_N
Free jet
Flat plate
Free jet
Flat plate
p_∞/p_{sc}^o = .148
p_1/p_∞ = 3.57
x_c/d_N
Free jet
Flat plate
x_c/d_N
p_∞/p_{sc}^o = .372
p_1/p_∞ = 1.42
First normal shock

1

Figure 39. Comparison of pressures at center of flat plate model with Pitot pressures on free jet center line.

$\alpha = 90^{o}$

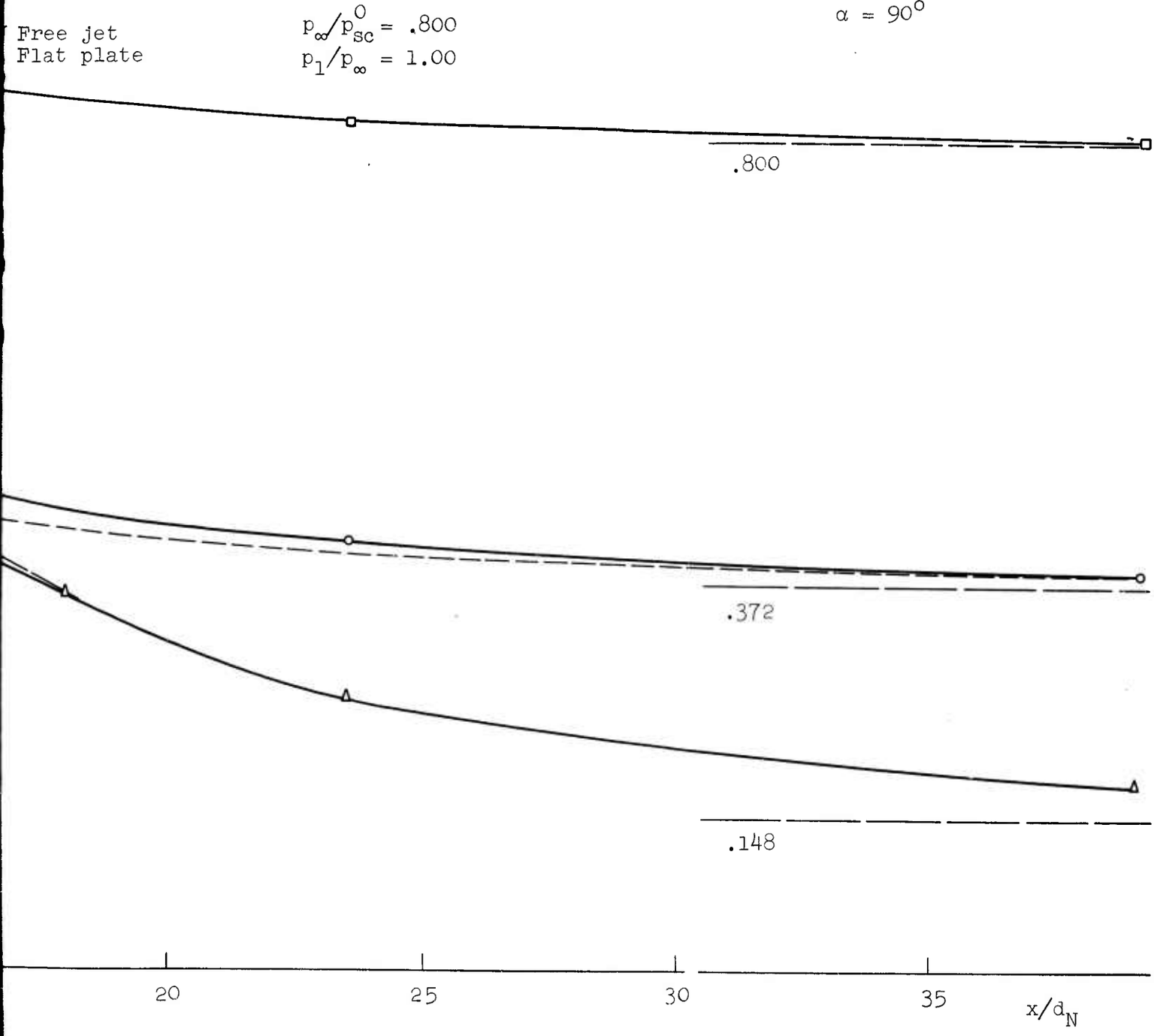

separated. Both of the underexpanded cases reveal the degree to which small local changes due to shock structure are duplicated in the two kinds of measurement. The most important difference observed between the free jet and impingement data, is an axial shift such that the plate is seen to experience a pressure which actually occurs in the free jet at a point upstream of the plate location. This shifting effect is thought to be at least partly the result of the different stand-off distances of the impingement normal shocks. Since for a given Mach number the stand-off distance of a normal shock increases with the effective bluntness of the body, it is clear that the probe stand-off distance must be considerably less than that for the plate. Other factors contributing to the shift may involve possible changes in the stability of the jet itself due to the secondary interference effect of the plate on the jet flow field. In this regard, it is interesting to note that in the case for $p_1/p_\infty = 1.42$ the shift continues in the same direction to points well downstream of the supersonic portion of the jet. Some evidence has been given that seems to show this free jet to be highly unstable at a considerable distance downstream. Characteristics associated with this instability are increased decay and spreading rates. If it were assumed that the presence of the flat plate and its supporting structure had a net stabilizing influence on the jet in this axial range, the higher impingement pressures observed in the downstream region could be at least partially accounted for. There is, however, no other evidence to support such an assumption. For the highly underexpanded jet $p_1/p_\infty = 3.57$, the shift is seen to disappear near the end of the supersonic portion $x/d_N \approx 20$. In the range $10 < x/d_N < 18$, however, the apparent reversal of the shift may only be the result of limited data taken in a region where values are still quite sensitive to axial location because of the oblique shock structure. Both curves in this region are

based on only three data points. An interesting feature of this jet is the large recovery of Pitot pressure in the core downstream of the normal shock disks.

Photographic studies. Photographs were made of the impingement flow on the flat plate model by means of schlieren and shadow techniques. A selection of the schlieren photographs, taken with a spark light source, is reproduced here in Figures 40 and 41 for the moderately and highly underexpanded jets, respectively. For these pictures, the knife edge is vertical so that density gradients in the axial direction predominate. Figure 42 shows a series of continuous light schlieren pictures taken under similar conditions for the highly underexpanded jet. In the impingement region, it is apparent that the character of the local structure as revealed by the density gradients varies considerably with impingement distance. No distinct normal shock is observed in this region, although this may be because it is masked by disturbances in the surrounding flow which are of comparable strength. As the impingement distance is decreased, there is a definite distortion of the jet structure upstream. For the $p_1/p_\infty = 3.57$ case the axial location of the jet normal shock disk is seen to start moving upstream for an impingement distance between $x/d_N = 6.24$ and 5.32. The continuous light pictures show the distortion as a sort of "telescoping" effect in the core. Possible changes in the stability characteristics of these jets due to impingement cannot be deduced from these pictures.

The radiation of strong sound waves from the impingement region is quite clear for both jet strengths. At small impingement distances, there is considerable interaction between these waves and the jet itself.

Another series of schlieren pictures was taken in hopes of revealing a visible correlation with the measured changes in sign of the radial pressure gradient for some of the

Free jet

Figure 40.

Spark schlieren photos of air jet from sonic nozzle impinging on flat plate.

$p_1/p_\infty = 1.42$

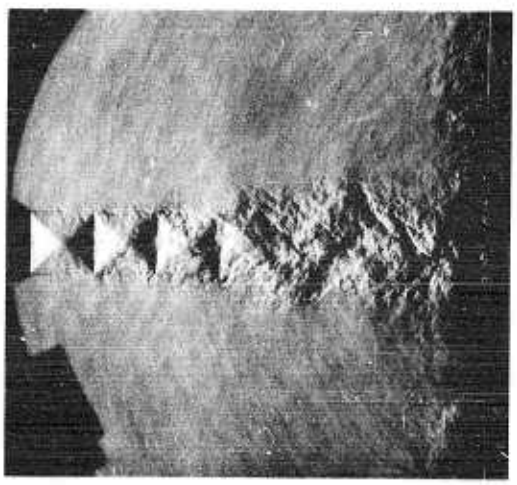

$x/d_N = 7.32$

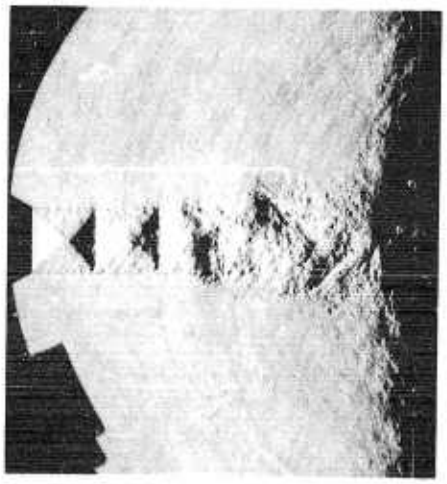

$x/d_N = 6.24$

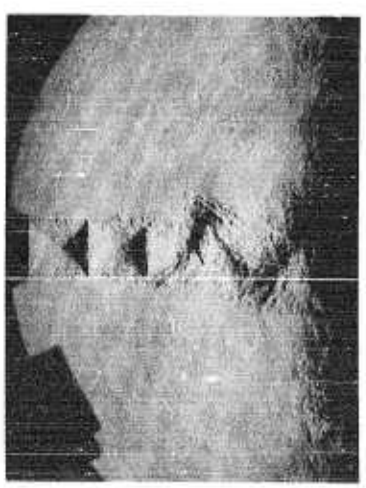

$x/d_N = 5.32$

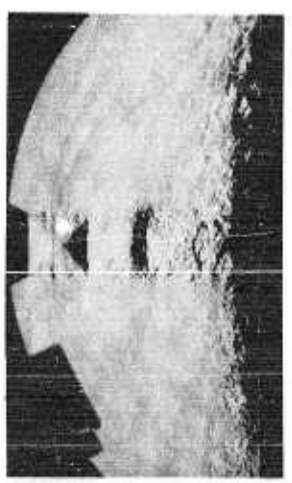

$x/d_N = 3.91$

$x/d_N = 2.60$

$x/d_N = 1.96$

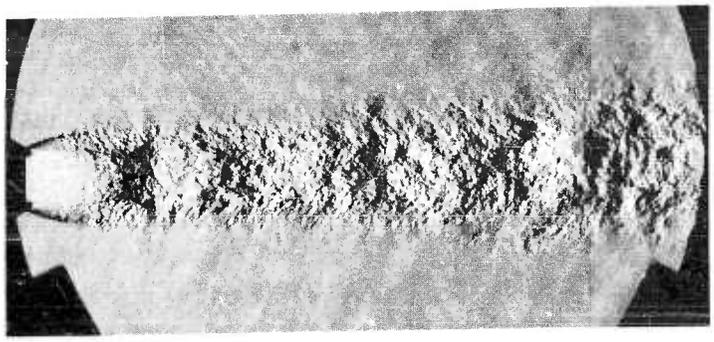

Free jet

Figure 41.

Spark schlieren photos of air jet from sonic nozzle impinging on flat plate.

$p_1/p_\infty = 3.57$

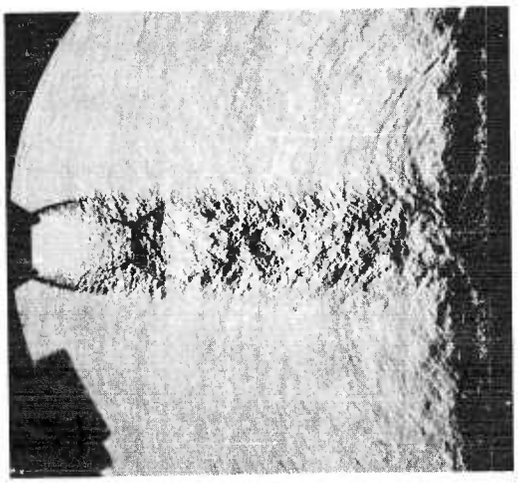

$x/d_N = 7.32$

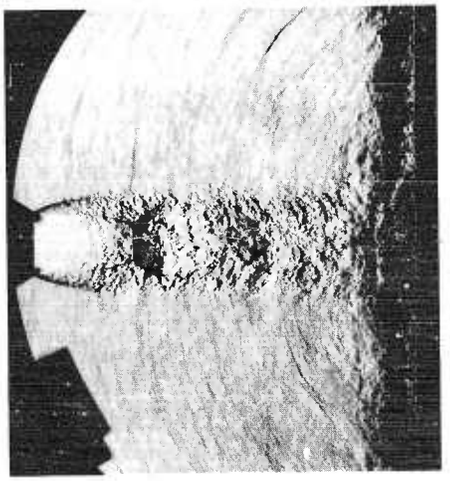

$x/d_N = 6.24$

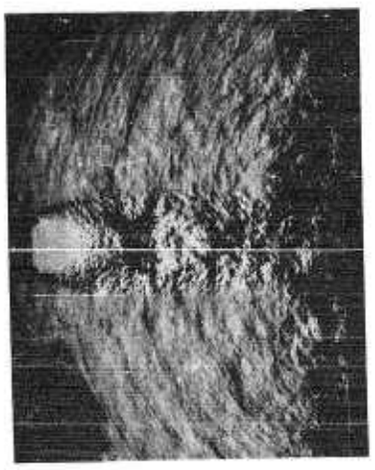

$x/d_N = 5.32$

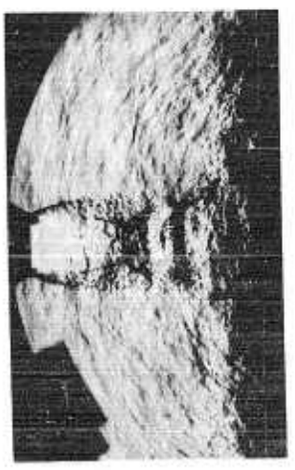

$x/d_N = 3.91$

$x/d_N = 2.60$

$x/d_N = 1.96$

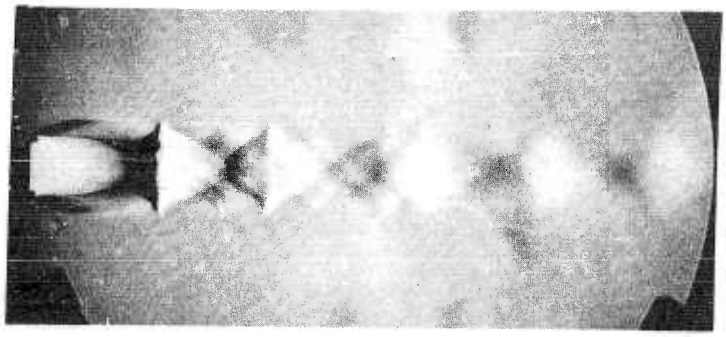

Free jet

Figure 42.

Continuous light schlieren photos of air jet from sonic nozzle impinging on flat plate.

$p_1/p_\infty = 3.57$

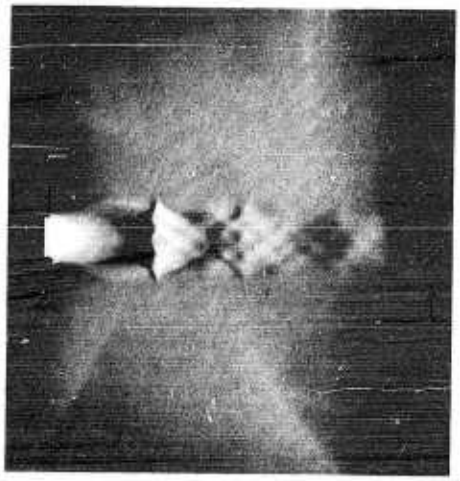

$x/d_N = 7.32$

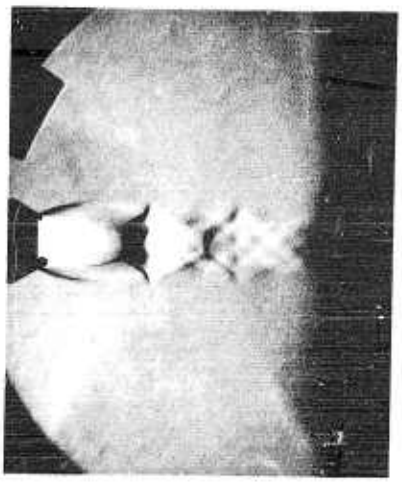

$x/d_N = 6.24$

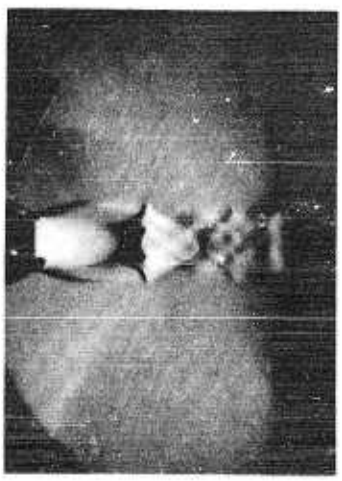

$x/d_N = 5.32$

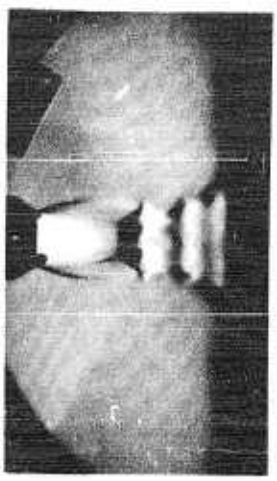

$x/d_N = 3.91$

$x/d_N = 2.60$

$x/d_N = 1.96$

cases cited earlier. In order to distinguish gradients in the radial direction, the knife edge was held horizontal. With the flat plate at an axial distance $x/d_N = 1.96$, the jet pressure ratio was varied in small increments in the range $1.00 < p_1/p_\infty < 5$. This series of pictures is shown in Figure 43. It is seen that definite gradients of density appear in a concentric pattern about the stagnation region. These gradients are visible in every picture although they are relatively weak for the pressure ratios used in the bulk of this study. Nevertheless, they do occur at radial positions corresponding to those of the measured changes in pressure gradient. These pictures also show the stand-off shock in the impingement region very clearly for the lower pressure ratios. The decrease in stand-off distance with increasing pressure ratio is evident. Also of interest is the change observed when the pressure ratio is increased from 1.88 to 1.95. It is in this range that the normal shock disk appears in the free jet. In the impingement case shown, the shock apparently forms at about the same pressure ratio even though its position is shifted due to the short impingement distance.

3.2.3. Evaluation of heat transfer parameter $(du_e/dr)_{r=0}$. The stagnation point radial velocity gradient $(du_e/dr)_{r=0}$ was evaluated from the detailed stagnation region pressure distributions given in 3.2.2. The calculations were made by fitting the data to Equation 6 at the stagnation point. In order to assure the best possible fit exactly at $r = 0$, the pressure data were first plotted as a function of $(r/r_w)^2$. The slope of the resulting curve was determined graphically at $r = 0$, and the value of $(du_e/dr)_{r=0}$ was then computed. In most cases the data fell close to a straight line for a reasonable distance from $r = 0$, so that the slope evaluation was not difficult. The values computed in this manner are shown plotted as a function of impingement distance for

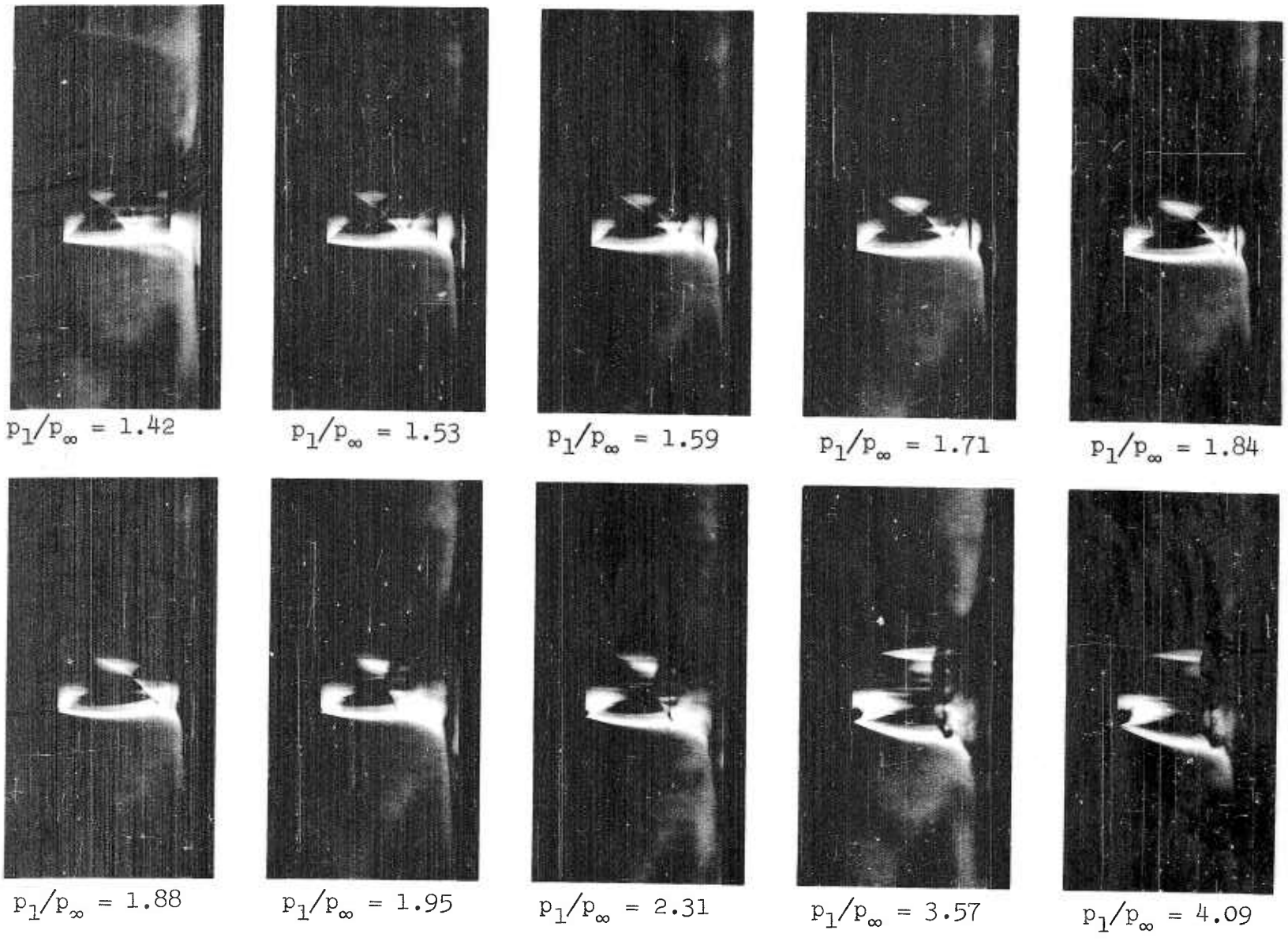

Figure 43. Schlieren pictures of impingement on flat plate at $x/d_N = 1.96$. Knife edge horizontal.

each jet strength and model shape in Figures 44, 45, 46, and 47. Referring to the flat plate results, which are more detailed, there is a tendency for $(du_e/dr)_{r=0}$ to increase at first until a maximum is reached at a point near the end of the free jet core. Farther downstream, a characteristic decay is observed. This behavior appears to be a logical consequence of the axial changes in jet total pressure and velocity profiles, since the radial gradients of these quantities are smaller near the centerline in both the core and fully developed regions. In the core of the moderately underexpanded jet, it is seen that the values fluctuate sharply in a manner similar to that observed for the Pitot pressure (Figure 39). In the case of the highly underexpanded jet, the negative value is a result of the reversed radial pressure gradient found to exist for some distance downstream of the normal shock disk. The existence of such a gradient strongly suggests that there is a separated region of reversed flow in the immediate vicinity of the usual stagnation point. A flow visualization study that seems to confirm this condition is discussed in 3.2.4.

Figures 45, 46, and 47 show that while the general axial variation of $(du_e/dr)_{r=0}$ is not highly dependent on surface shape, the magnitude is. This dependence is made clear in Figures 48, 49, and 50, which show the values for all four shapes plotted together for each jet pressure ratio. A curve is drawn only for the more detailed flat plate data. It is seen that the values for the convex hemisphere are always higher and those for the concave shapes always lower than those for the flat plate. This is, of course, the same as the effect noted in the discussion of the pressure distributions themselves.

Two methods of presenting measured values of $(du_e/dr)_{r=0}$ in terms of measured jet behavior are given. The first method, which should be useful when little or no information is available about the decay and spread of the impinging jet,

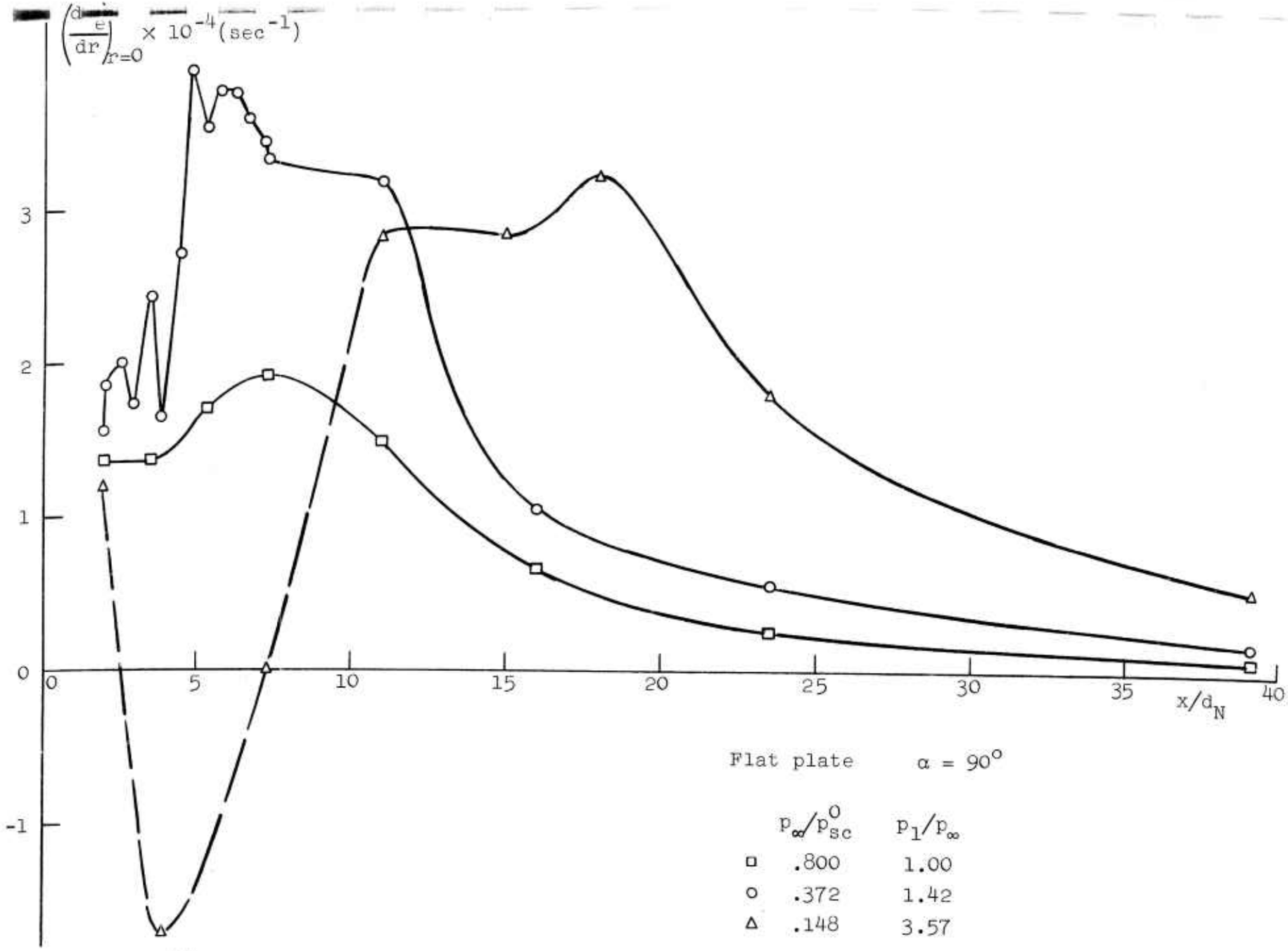

Figure 44. Variation of stagnation point radial velocity gradient with impingement distance for several jet pressure ratios.

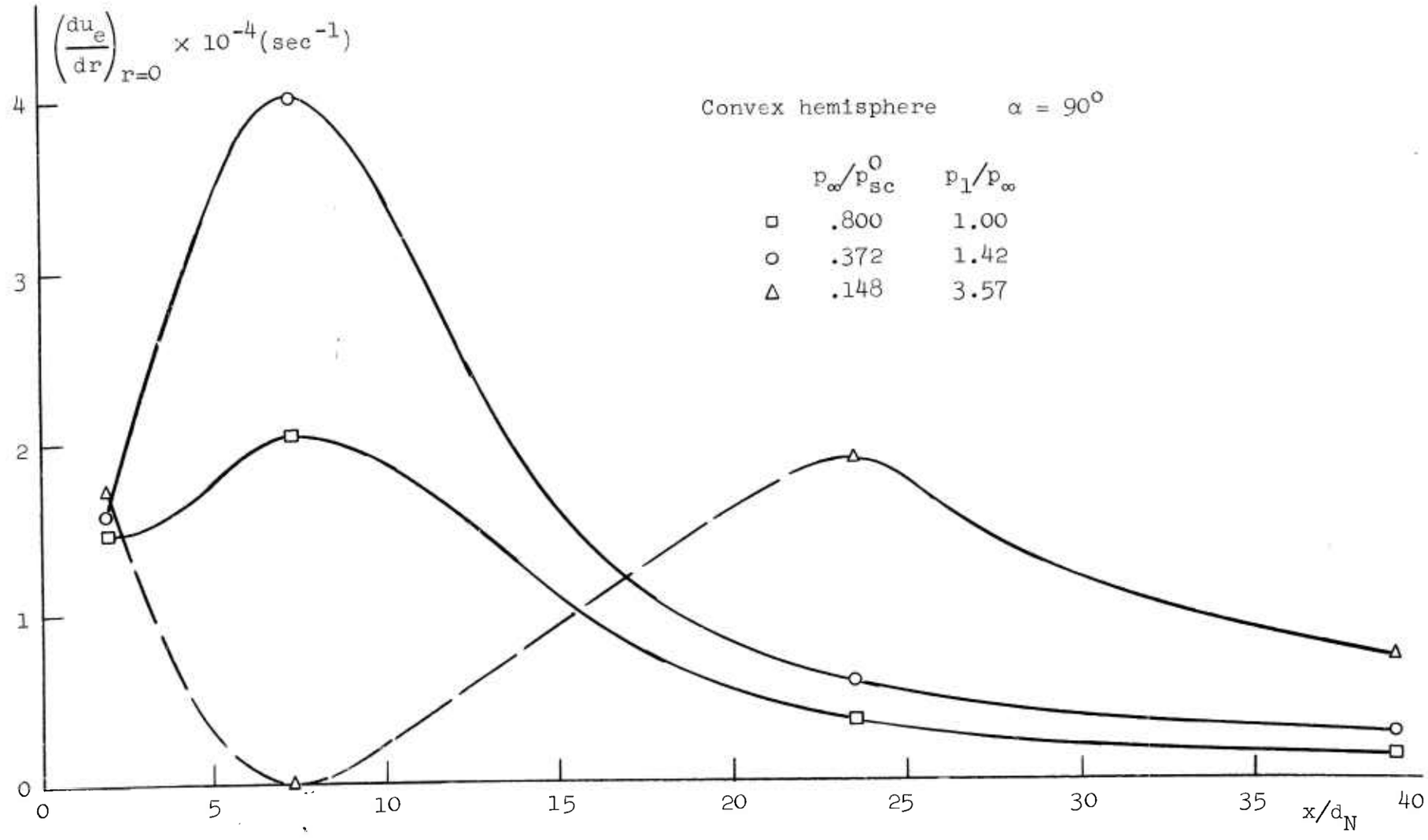

Figure 45. Variation of stagnation point radial velocity gradient with impingement distance for several jet pressure ratios.

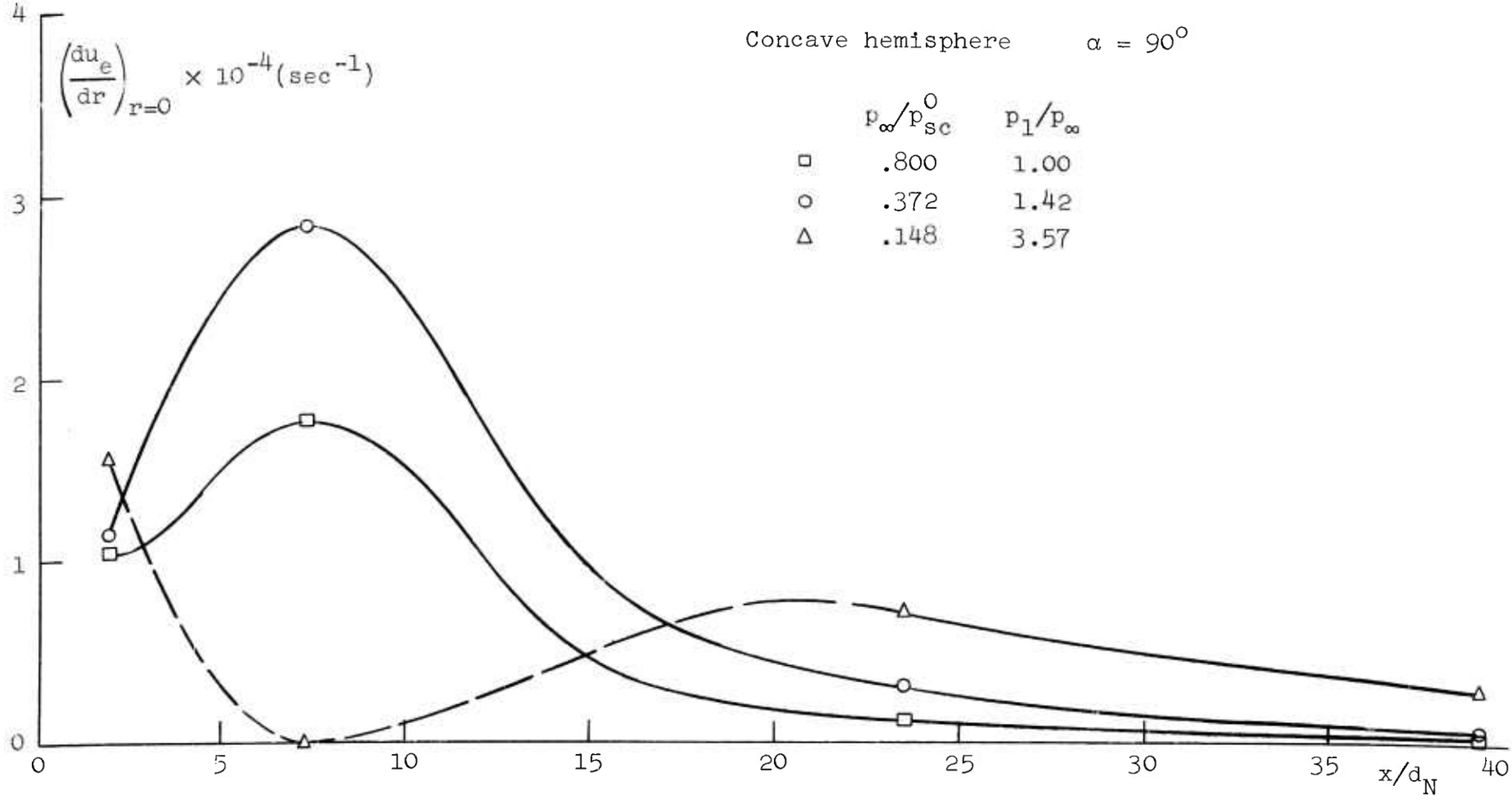

Figure 46. Variation of stagnation point radial velocity gradient with impingement distance for several jet pressure ratios.

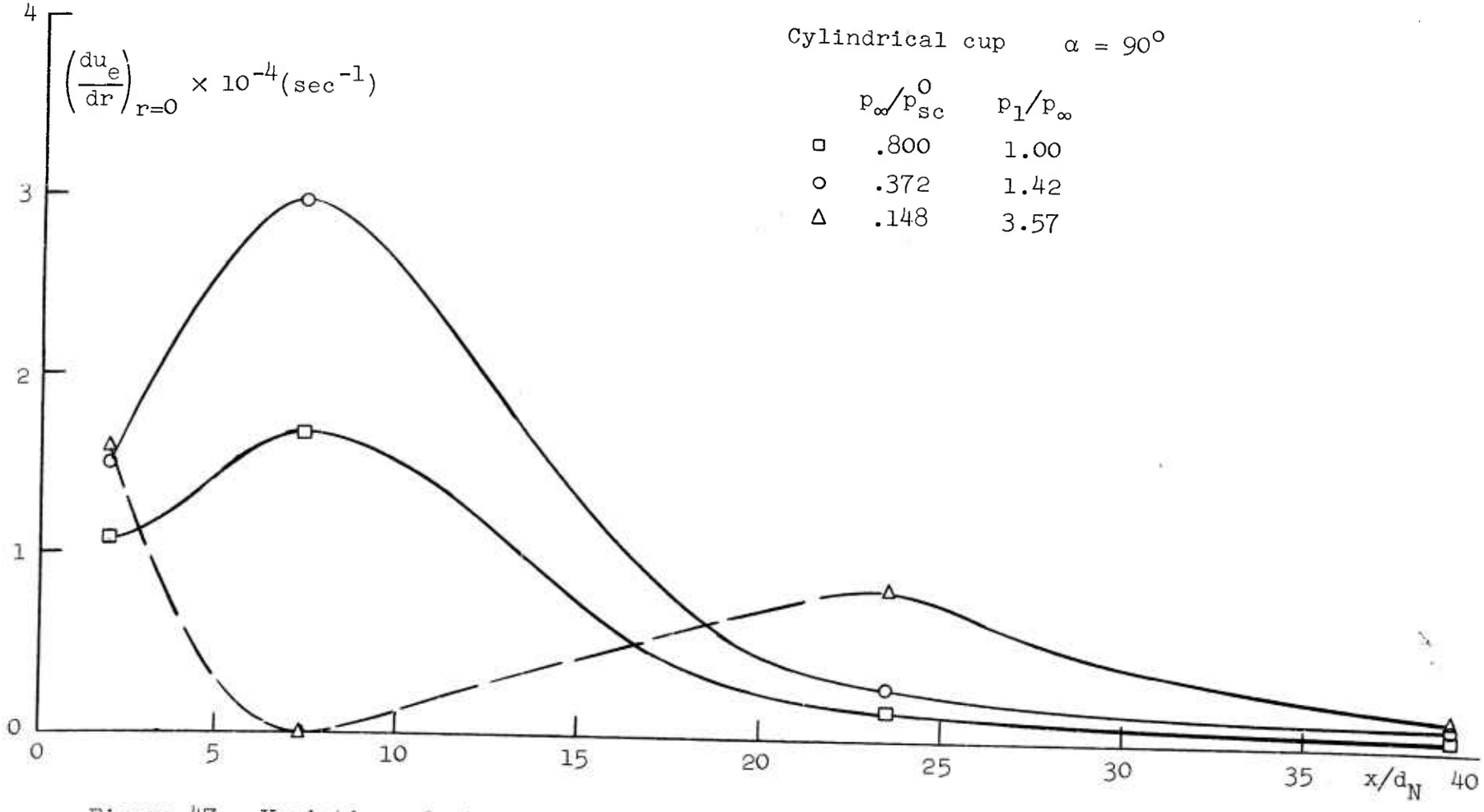

Figure 47. Variation of stagnation point radial velocity gradient with impingement distance for several jet pressure ratios.

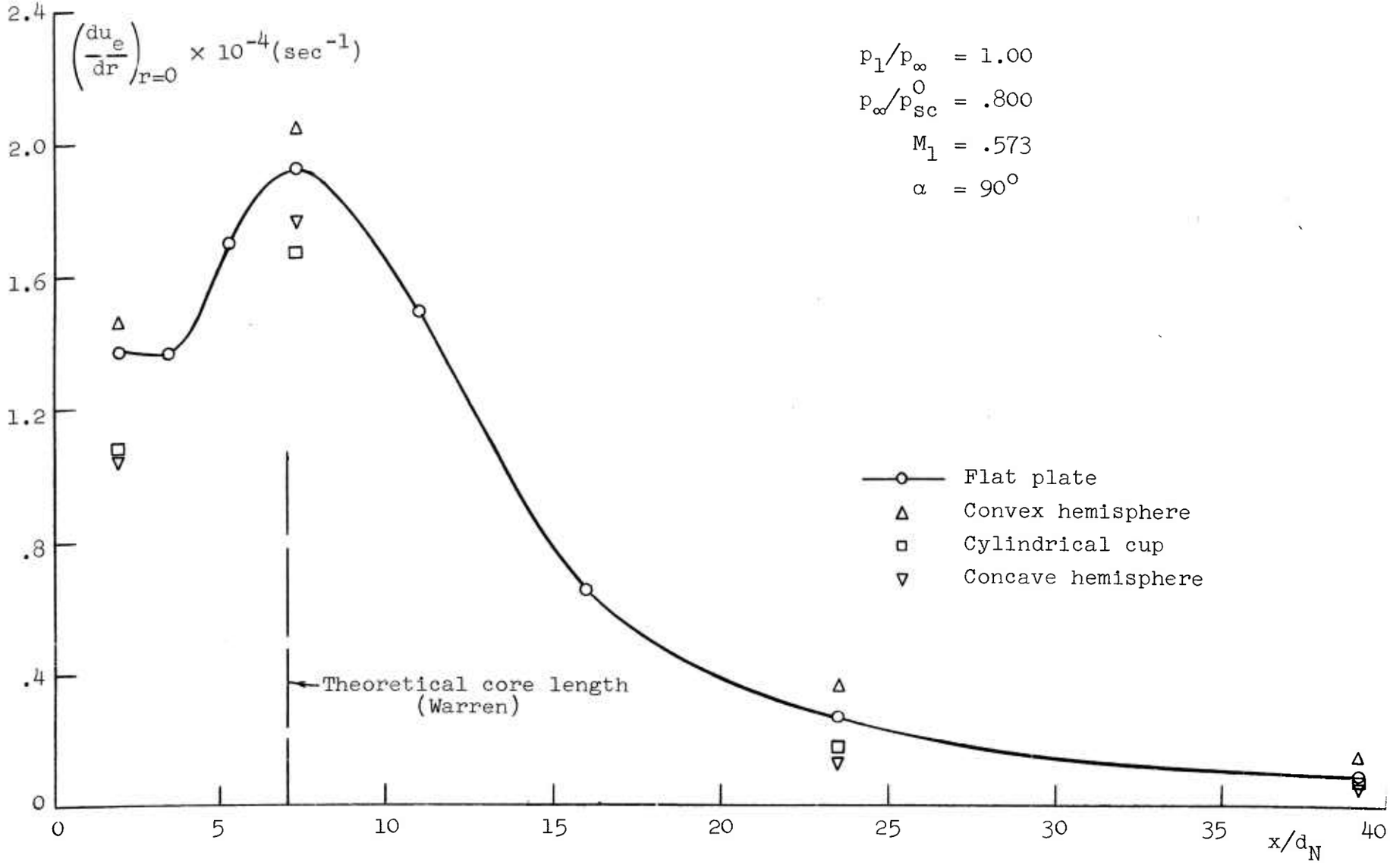

Figure 48. Comparison of stagnation point radial velocity gradient for a jet impinging on several surface shapes.

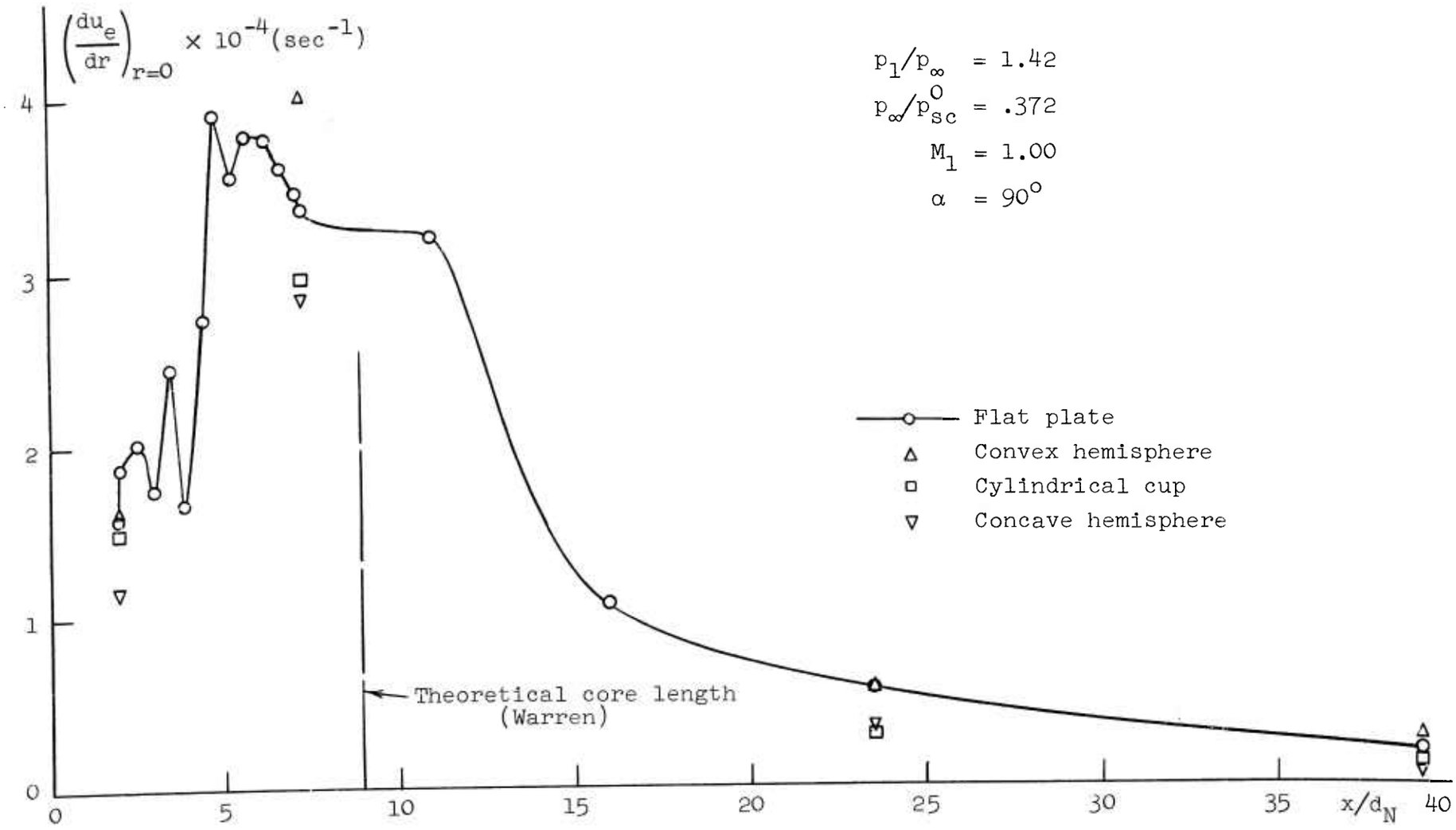

Figure 49. Comparison of stagnation point radial velocity gradient for a jet impinging on several surface shapes.

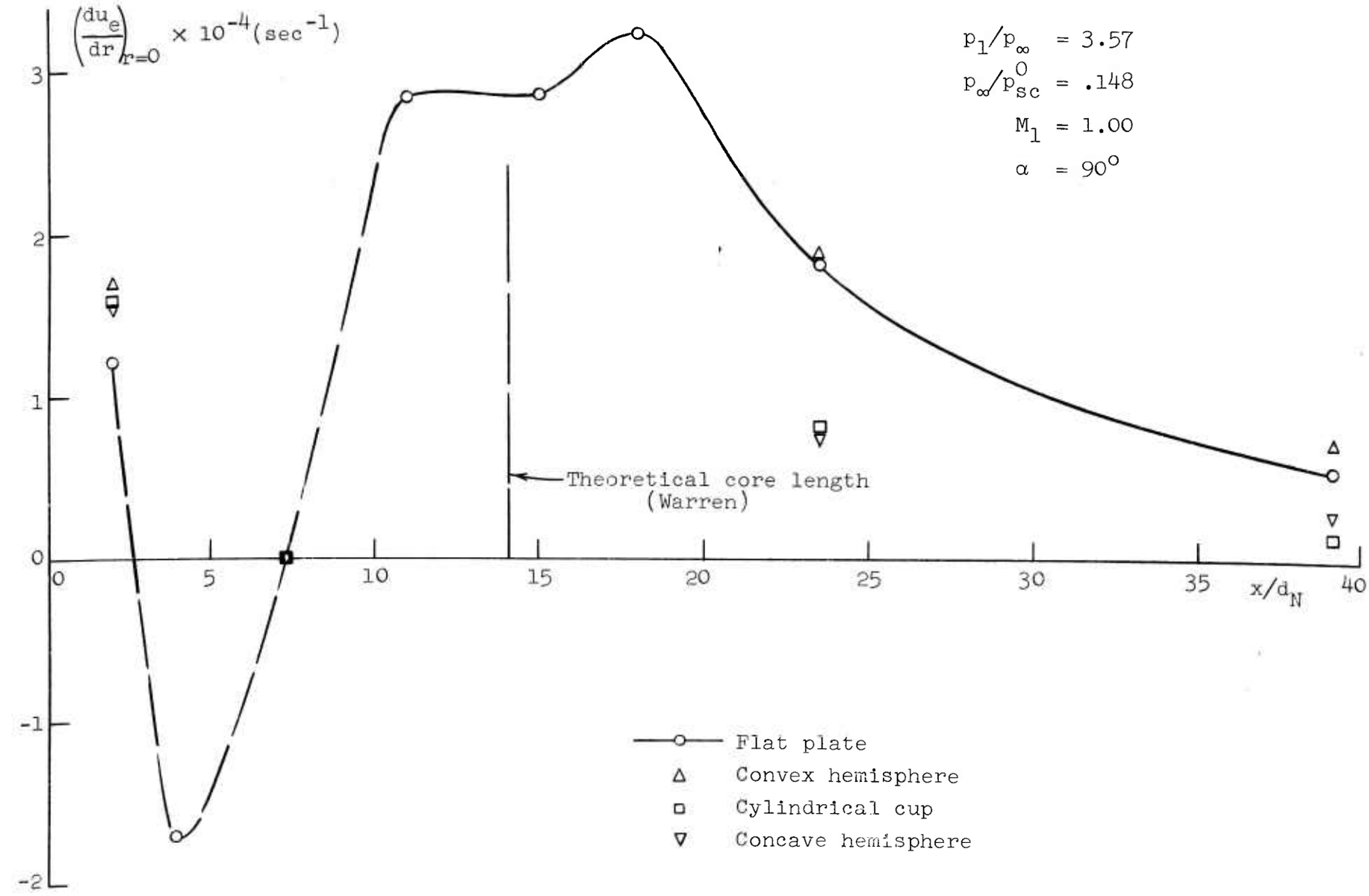

Figure 50. Comparison of stagnation point radial velocity gradient for a jet impinging on several surface shapes.

makes the stagnation point velocity gradient nondimensional through the use of d_N and V_1, i.e.

$$\frac{d_N}{V_1}\left(\frac{du_e}{dr}\right)_{r=0}$$

The second method, which is more fundamental but which requires a knowledge of the decay and spread of the free jet, makes the stagnation point velocity gradient nondimensional through the use of measured local free jet conditions in the plane of impingement, i.e.

$$\frac{r_{.5}}{V_c}\left(\frac{du_e}{dr}\right)_{r=0}$$

The results of the first of these methods are shown in Figures 51-54, and those of the second method are shown in Figures 55-58.

Referring again to the flat plate data, the behavior of the nondimensional velocity gradient based on nozzle exit values is similar for the two weakest jets (cf. Figure 44). This similarity is indicative of the roughly equivalent core lengths and rates of decay as well as rather mild over-all effects due to shock patterns. For the highly underexpanded case, however, the behavior is quite different, with the effects of the much longer core region and strong shock structure clearly shown. Similar results are obtained for the other shapes, but the magnitudes are different, as expected.

The nondimensional gradient based on local free jet properties appears to achieve a rough correlation of the measured results, although the core effects of the strongest jet are still in evidence. In general, the two weakest jets

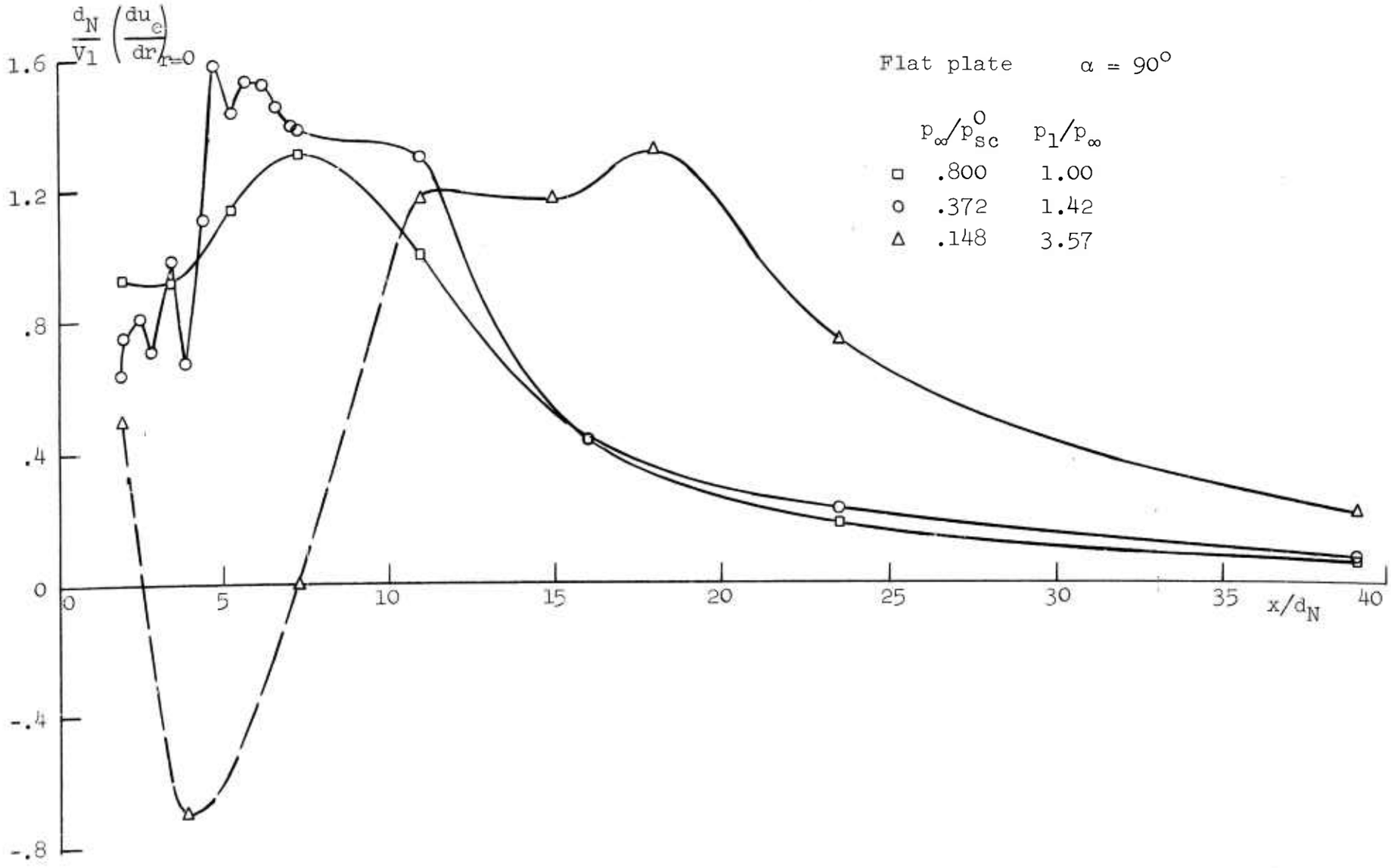

Figure 51. Variation of stagnation point nondimensional radial velocity gradient with impingement distance for several pressure ratios.

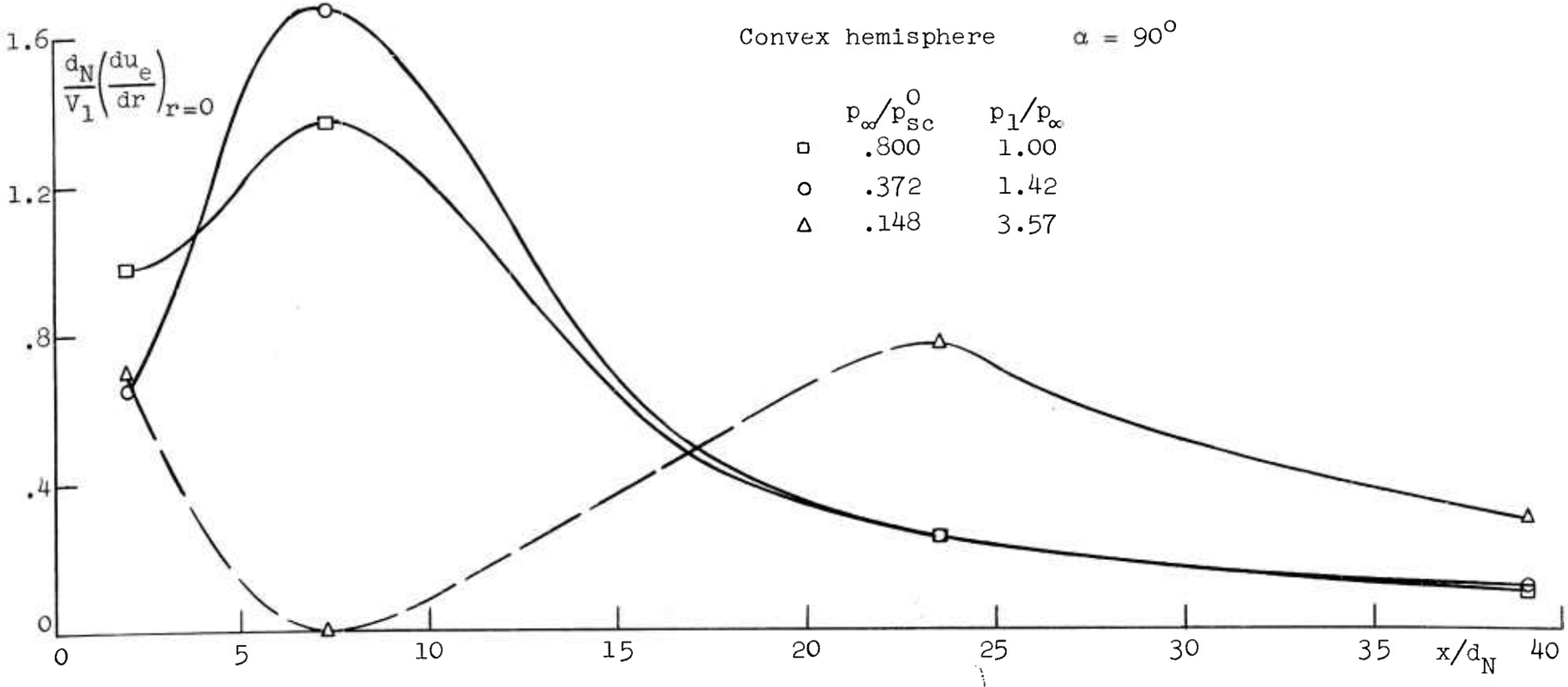

Figure 52. Variation of stagnation point nondimensional radial velocity gradient with impingement distance for several jet pressure ratios.

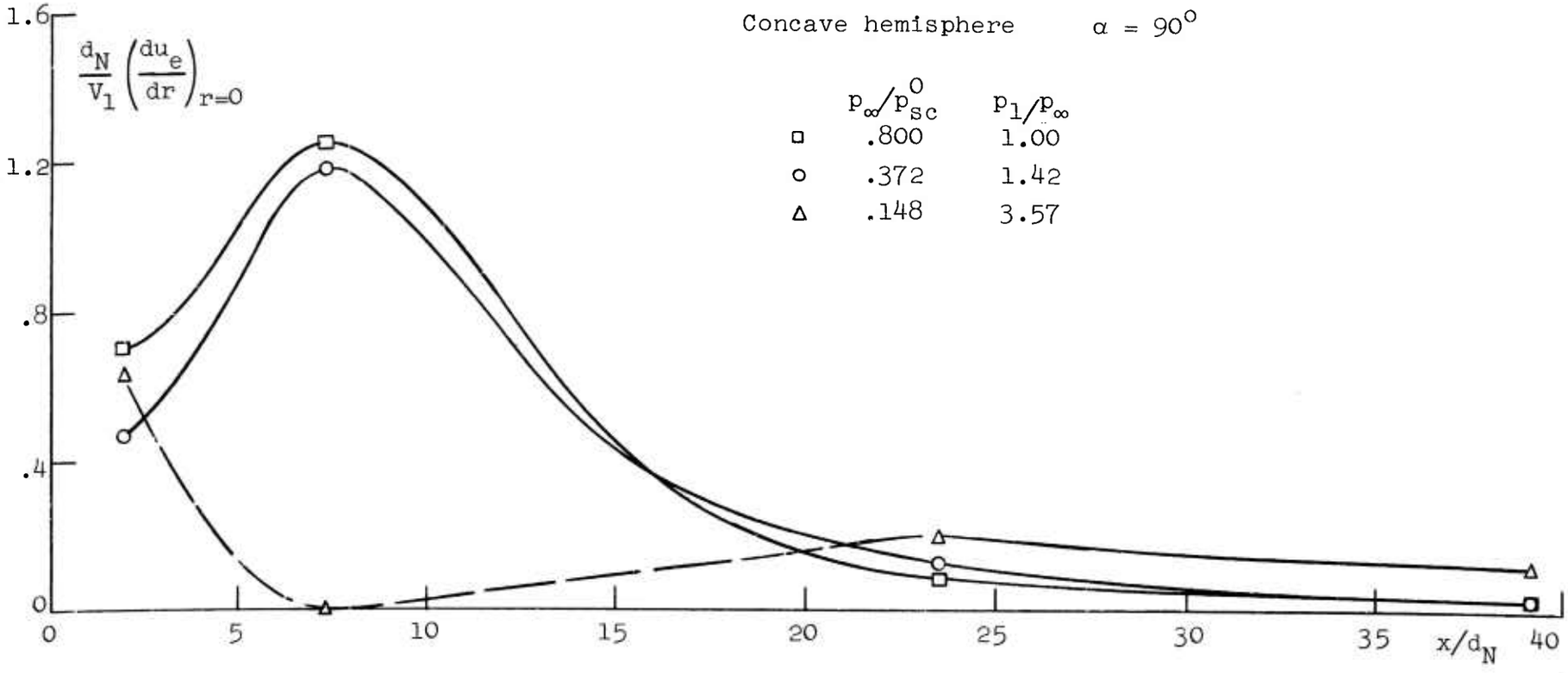

Figure 53. Variation of stagnation point nondimensional radial velocity gradient with impingement distance for several jet pressure ratios.

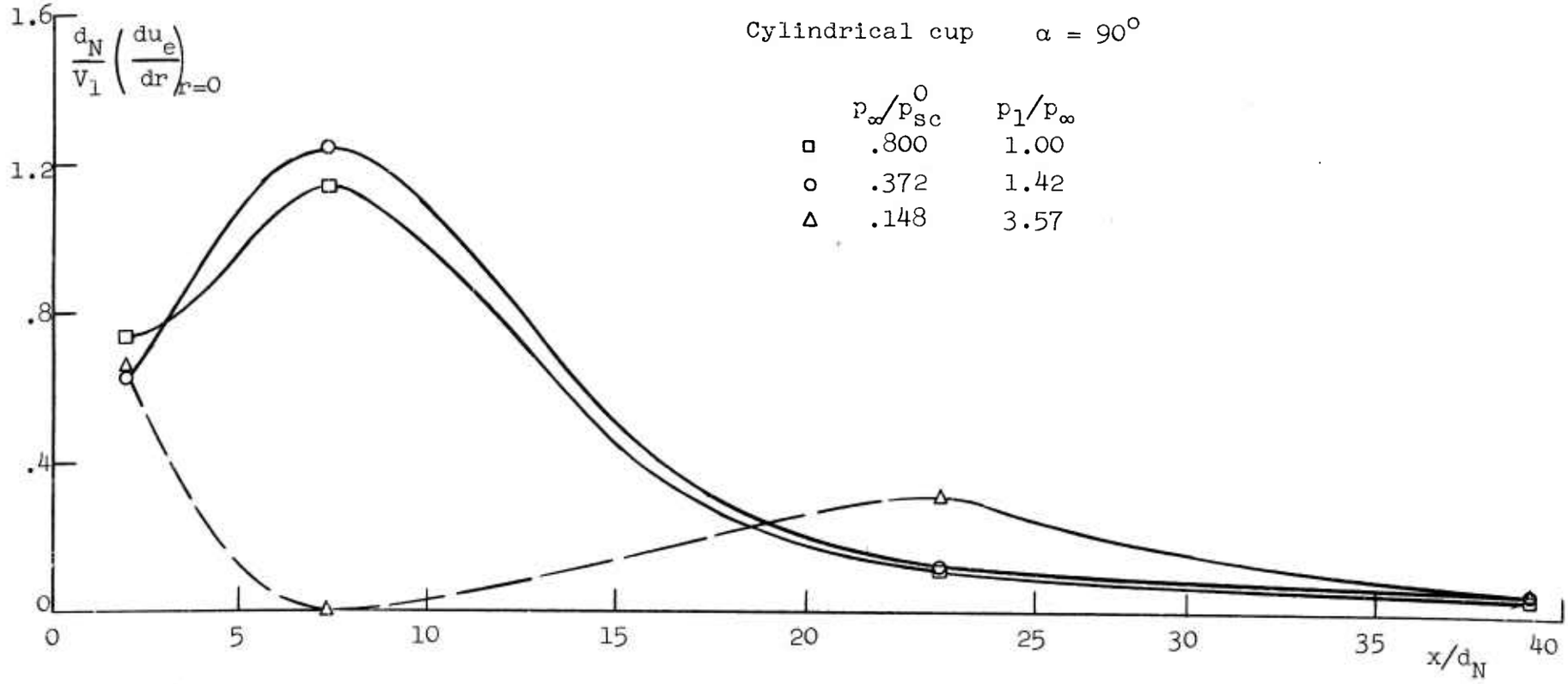

Figure 54. Variation of stagnation point nondimensional radial velocity gradient with impingement distance for several jet pressure ratios.

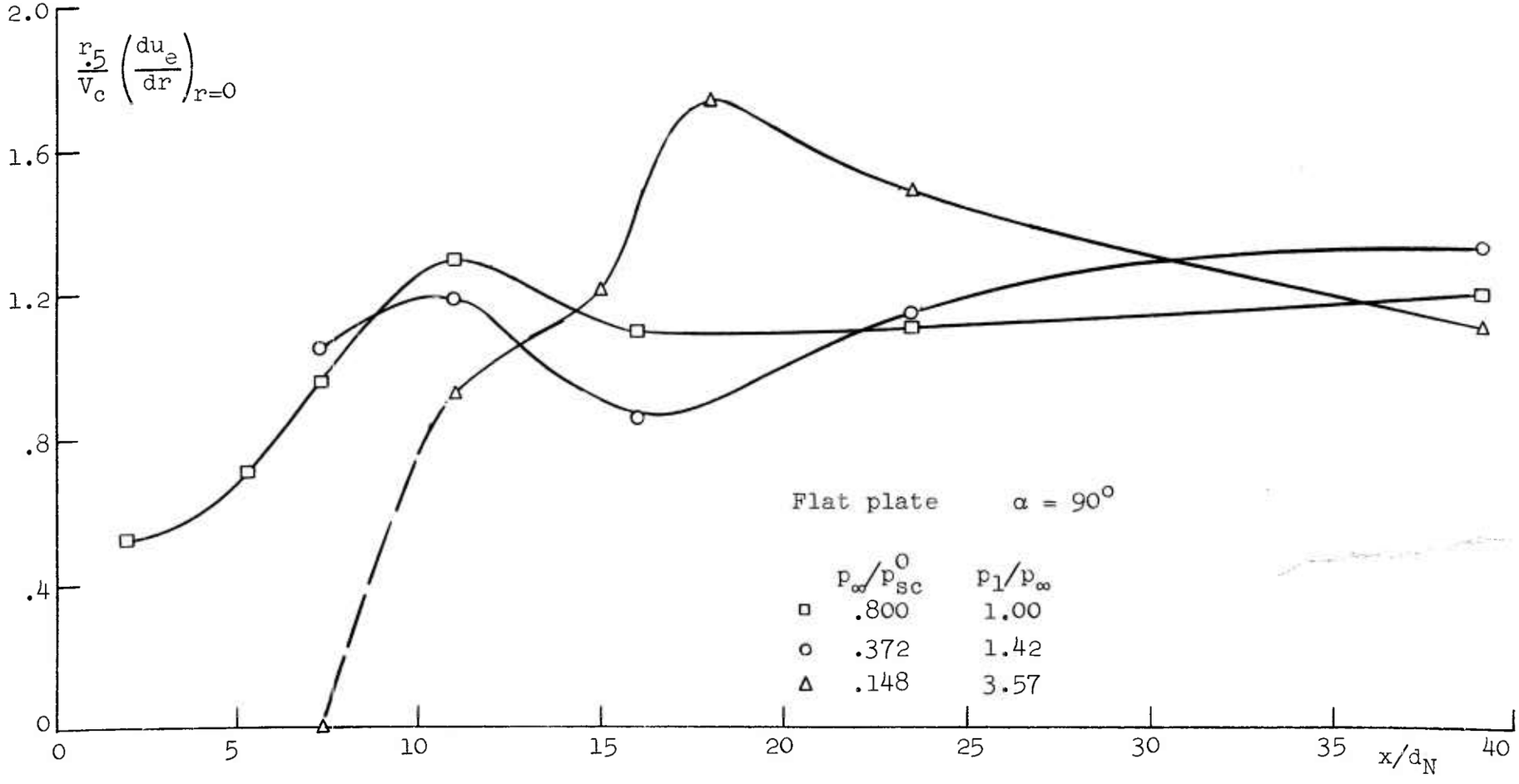

Figure 55. Variation of stagnation point nondimensional radial velocity gradient with impingement distance for several jet pressure ratios.

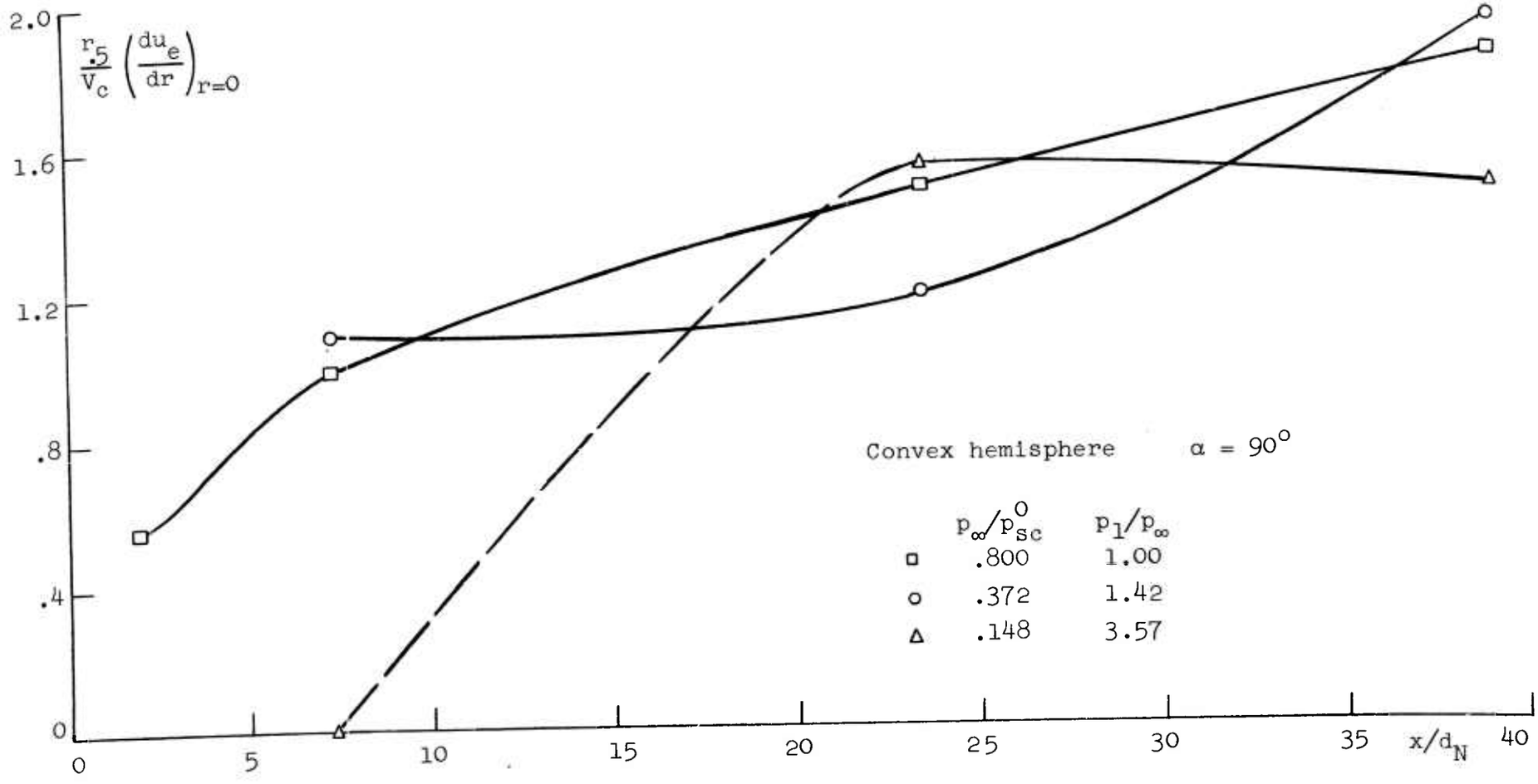

Figure 56. Variation of stagnation point nondimensional radial velocity gradient with impingement distance for several jet pressure ratios.

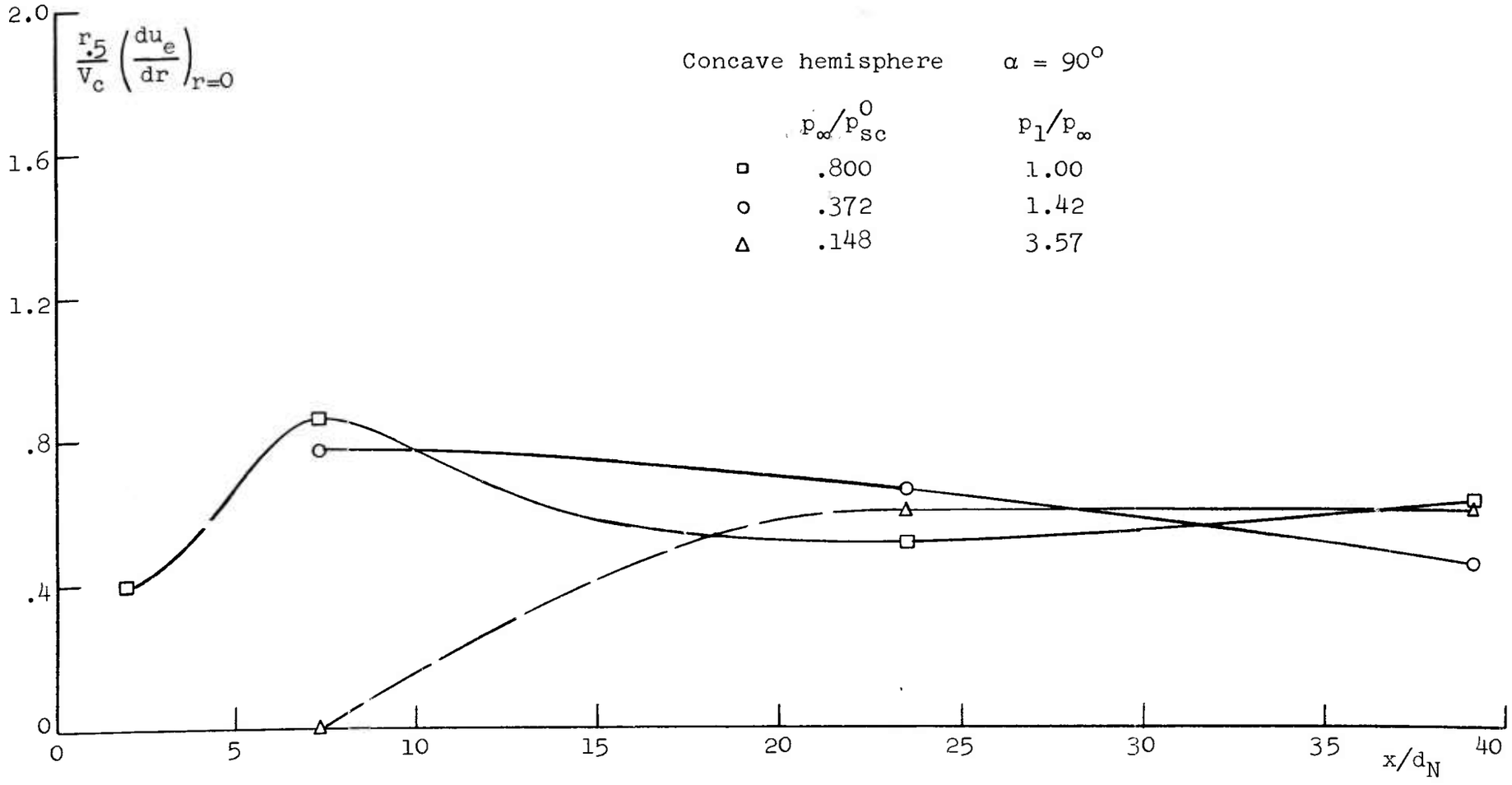

Figure 57. Variation of stagnation point nondimensional radial velocity gradient with impingement distance for several jet pressure ratios.

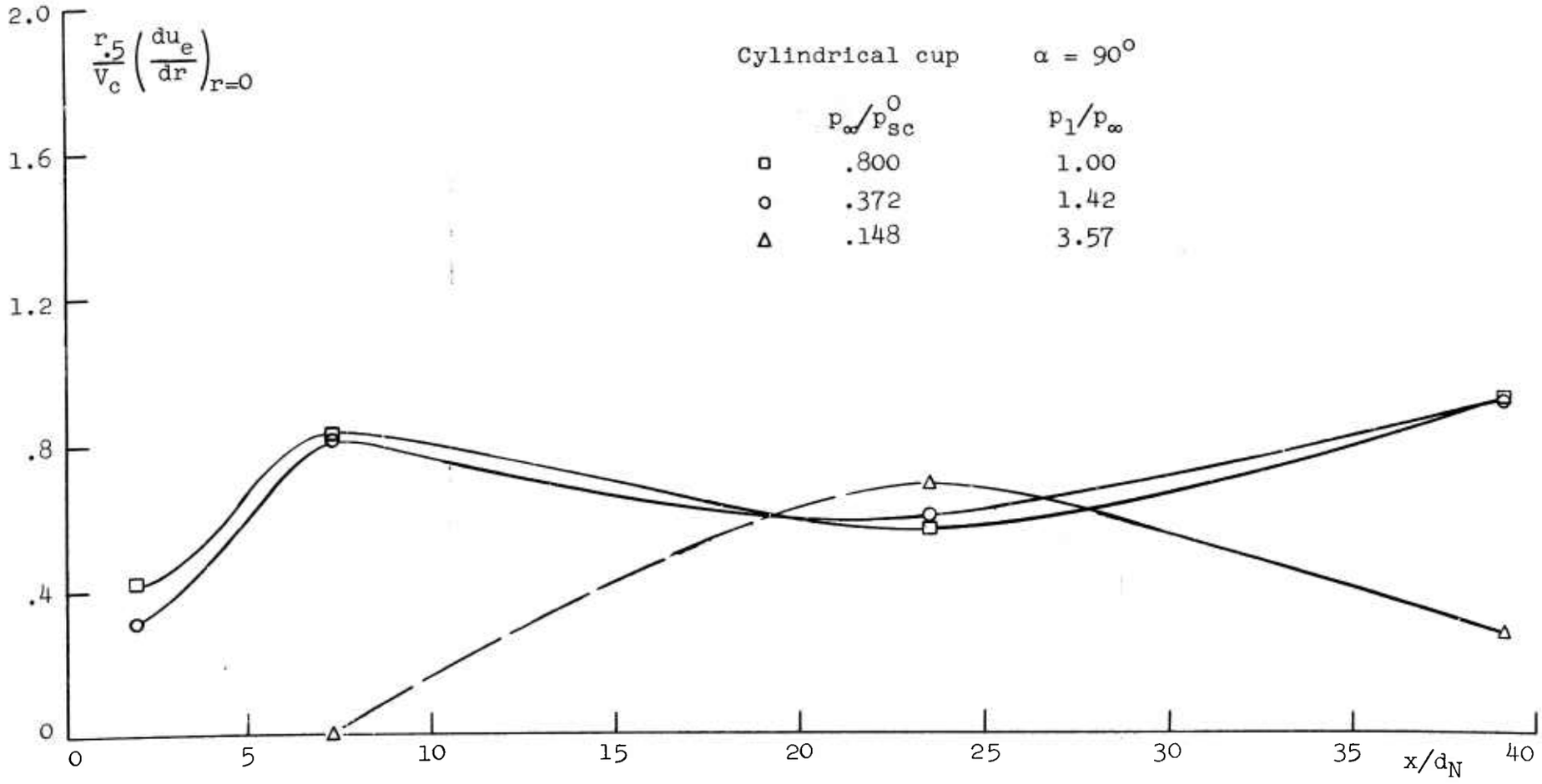

Figure 58. Variation of stagnation point nondimensional radial velocity gradient with impingement distance for several jet pressure ratios.

are well correlated about a value $(r_{.5}/V_c)(du_e/dr)_{r=0} \approx 1.1$ for a considerable distance. Far downstream, the strongest jet also approaches this value. Aside from factors limiting experimental accuracy, certain deviations may very likely stem from changes in the stability characteristics of the jet due to the presence of the plate. This is particularly true of the $p_1/p_\infty = 1.42$ jet. Of the other shapes, the best correlation is shown for the concave hemisphere. In general, however, the shape effect on magnitude is the same as that already noted, i.e., higher values for the convex shape and lower values for the concave shapes.

3.2.4. Visualization studies of stagnation region flow. The pressure distributions measured for impingement distances downstream of the normal shock disk in the highly underexpanded jet, show peaks of maximum pressure to either side of the usual centerline stagnation point. A typical example of such a distribution along with the Pitot and static pressure profiles in the free jet at the same axial distance is shown in Figure 59. The pressures are all shown as a fraction of the free jet centerline Pitot pressure so that relative changes in pressure level due to impingement may be observed. The shape of the free jet profile at this point is, of course, a result of the total pressure drop through the normal shock disks upstream. Even though there has been a substantial recovery on the centerline (see Figure 39), the outer region of the core retains its higher level from the beginning because of its structure of relatively weak oblique shocks. The corresponding impingement distribution shows the outer peak to be displaced outward, while the central region is relatively flat. At the same time, the magnitude of the outer peak is seen to be even less than that at the centerline of the free jet. This condition suggests the existence of a separated region caused by the reversed pressure gradient to the inside of the outer peak. The flow pattern based on

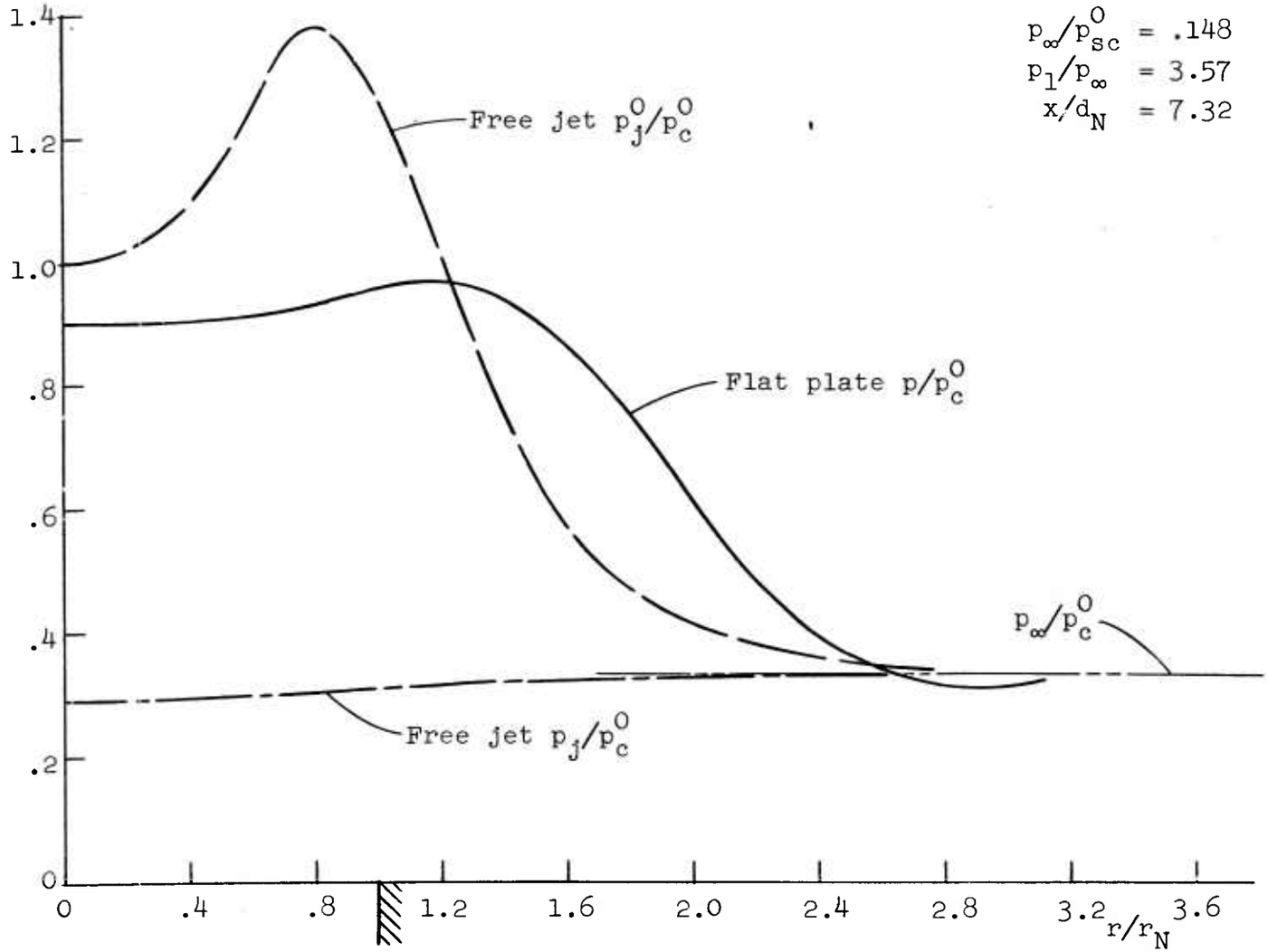

Figure 59. Comparison of measured pressure distributions on flat plate and in free jet.

this idea is shown in Figure 60. The usual central stagnation point is transformed into a ring surrounding the separated region. A pattern similar to this is known to exist under certain ground effects machines [27]. A consequence of such a flow in terms of heat transfer, of course, would be the existence of a cool central spot surrounded by a ring at stagnation point heating levels.

Although confirmation of the phenomenon by means of direct measurement of velocity or pressure gradients off the surface was felt to be impossible, a method was devised for observing surface streamlines. This method consisted of impinging the jet for a short time on a layer of highly viscous water pump grease applied to the surface of the flat plate. In order to achieve maximum visual contrast in the resulting pattern, the grease was mixed with lampblack, and the plate was given a smooth finish of white lacquer. Since it was found that the initial distribution or thickness of the grease did not affect the resulting pattern, the application method did not present a problem. With the grease applied in a small blob, the plate was covered with a baffle board in order to shield the grease from transient phenomena during the starting of the jet. When the jet reached the desired running condition, the baffle was withdrawn for a short time interval of about 3 to 5 seconds. After replacing the baffle, the jet was shut down.* Increasing the time of exposure to the jet was found only to remove more grease from the impingement region and not to change the pattern. Thus, it was determined not only that the phenomenon was basically a steady one, but that it was also quite repeatable. A photograph of this pattern for the highly underexpanded jet

*Because of the substantial jet pressure force, the baffle was made with two raised edges that rested on the plate surface away from the center. Exposure of the grease was accomplished by quickly sliding the baffle out of the way laterally.

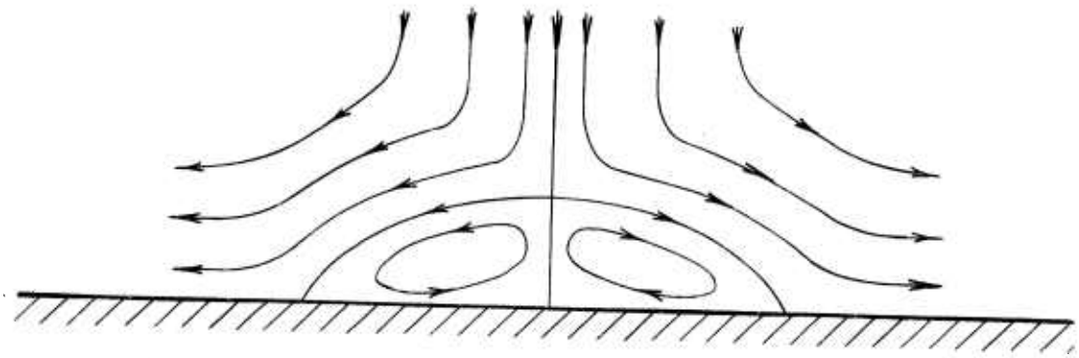

Figure 60. Flow pattern of separated region (distance normal to surface exaggerated).

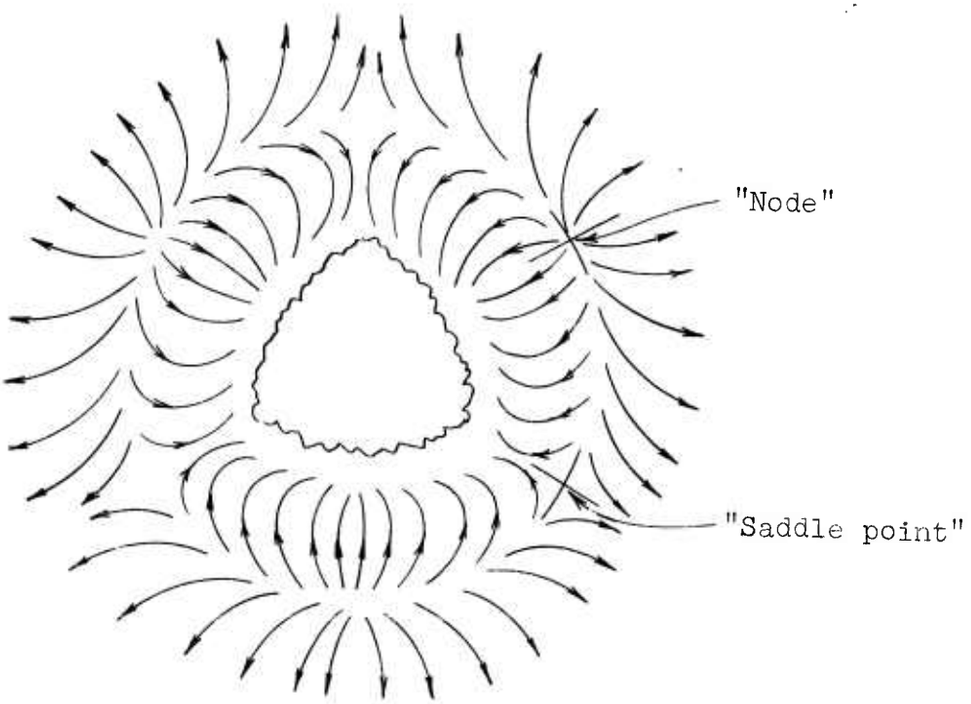

Figure 61. Typical surface streamline pattern based on grease streak pictures.

($p_1/p_\infty = 3.57$) at $x/d_N = 5.32$ is shown in Figure 62. The behavior of surface streamlines suggested by the observed patterns is shown schematically in Figure 61. It is seen that a dividing ring exists which apparently separates regions of inward and outward flow. To the inside, there is a central region of thick grease, while to the outside an alternating concentric pattern of more and less grease is observed. Of particular interest is the manner in which the streaks curve near the dividing ring resulting in segmentation of the central pattern. Along the dividing ring, each segment can be identified by two types of points having the topological character of nodes  and saddle points  . The number of segments in the pattern apparently decreases with increasing impingement distance. For this jet, the minimum number of three segments is observed for all distances beyond about $x/d_N = 4.5$ (see Figure 63). Another factor which was found to affect not only the number of segments at a given distance but also the orientation of the pattern, was the jet nozzle. Rotation of the nozzle about its axis between runs resulted in an identical rotation of the observed grease pattern. It was found that tiny nicks in the nozzle lip could be correlated with at least some of the pattern segments. Removal of the larger nicks resulted, for a fixed impingement distance, in fewer segments. The patterns shown in the present case, however, are those resulting from tests after the nicks had been removed from the nozzle. Under 10-power magnification, no nicks were observed that could be correlated with the resulting three equal pattern segments.

A comparison of schlieren photograph, grease pattern, and surface pressure distribution for a typical case is shown in Figure 64. It can be seen that local pressure peaks are definitely related to the observed patterns, with less grease remaining where the pressure is higher. These local pressure maxima also correspond to the dark regions of

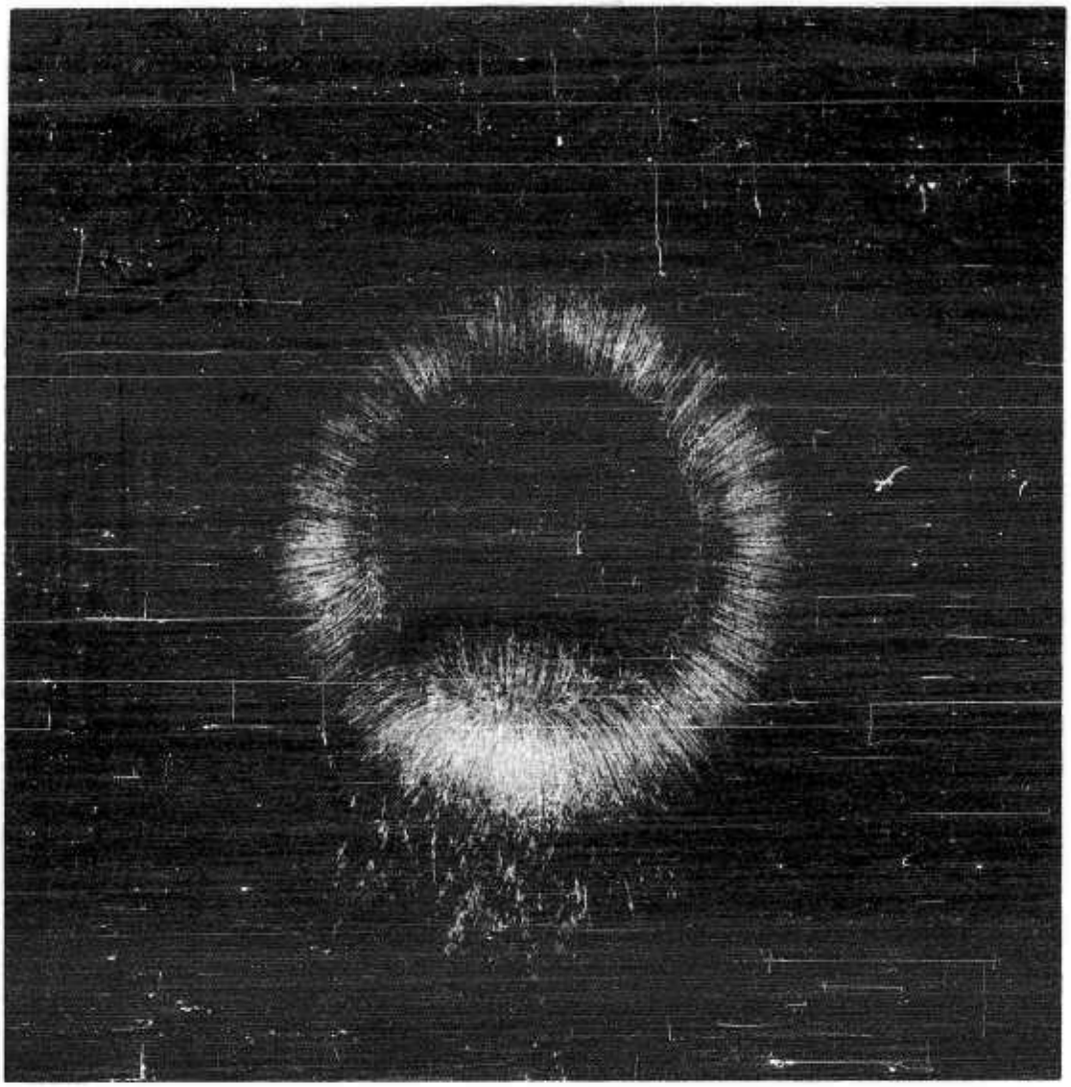

Figure 62. Typical grease streak photograph of flow pattern due to impingement on flat plate. $p_1/p_\infty = 3.57$; $x/d_N = 5.32$.

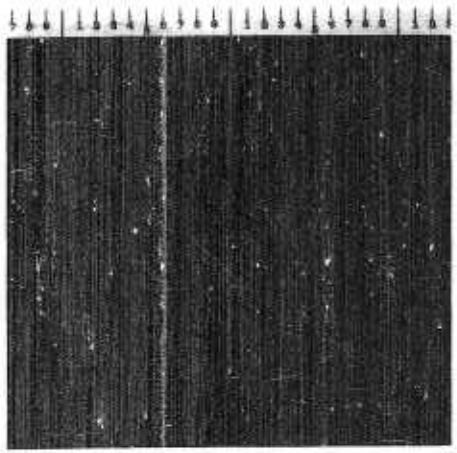

$x/d_N = 1.96$

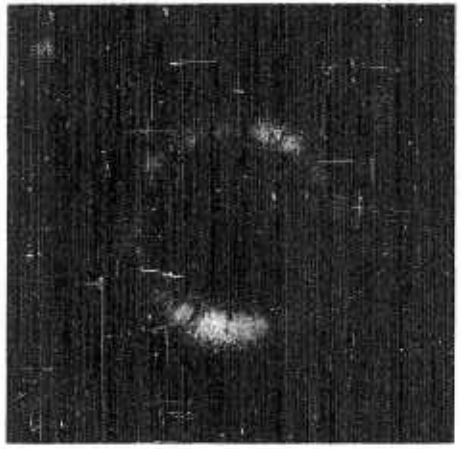

$x/d_N = 2.60$

$x/d_N = 3.91$

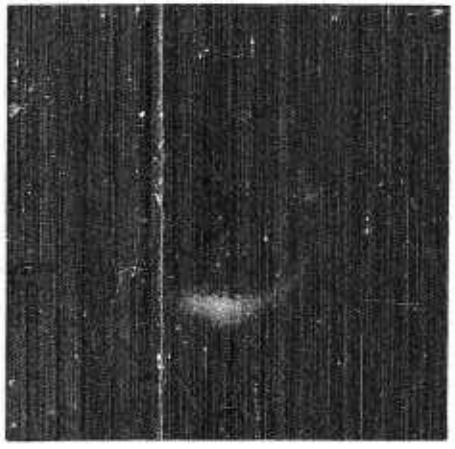

$x/d_N = 5.32$

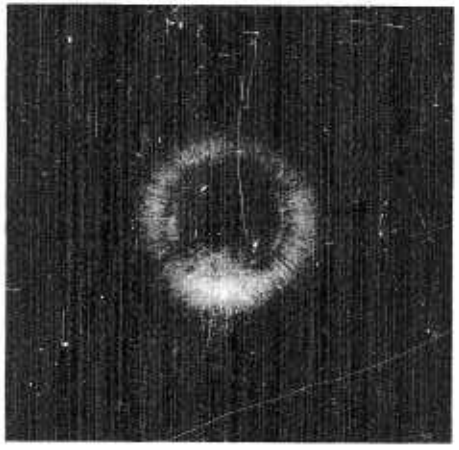

$x/d_N = 6.24$

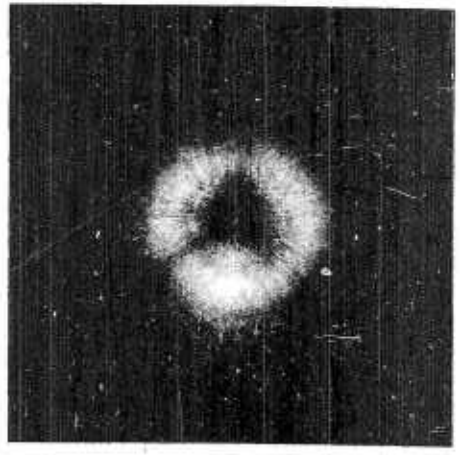

$x/d_N = 7.32$

Figure 63. Grease streak patterns for impinging jet; $p_1/p_\infty = 3.57$. The scale divisions are tenths of an inch.

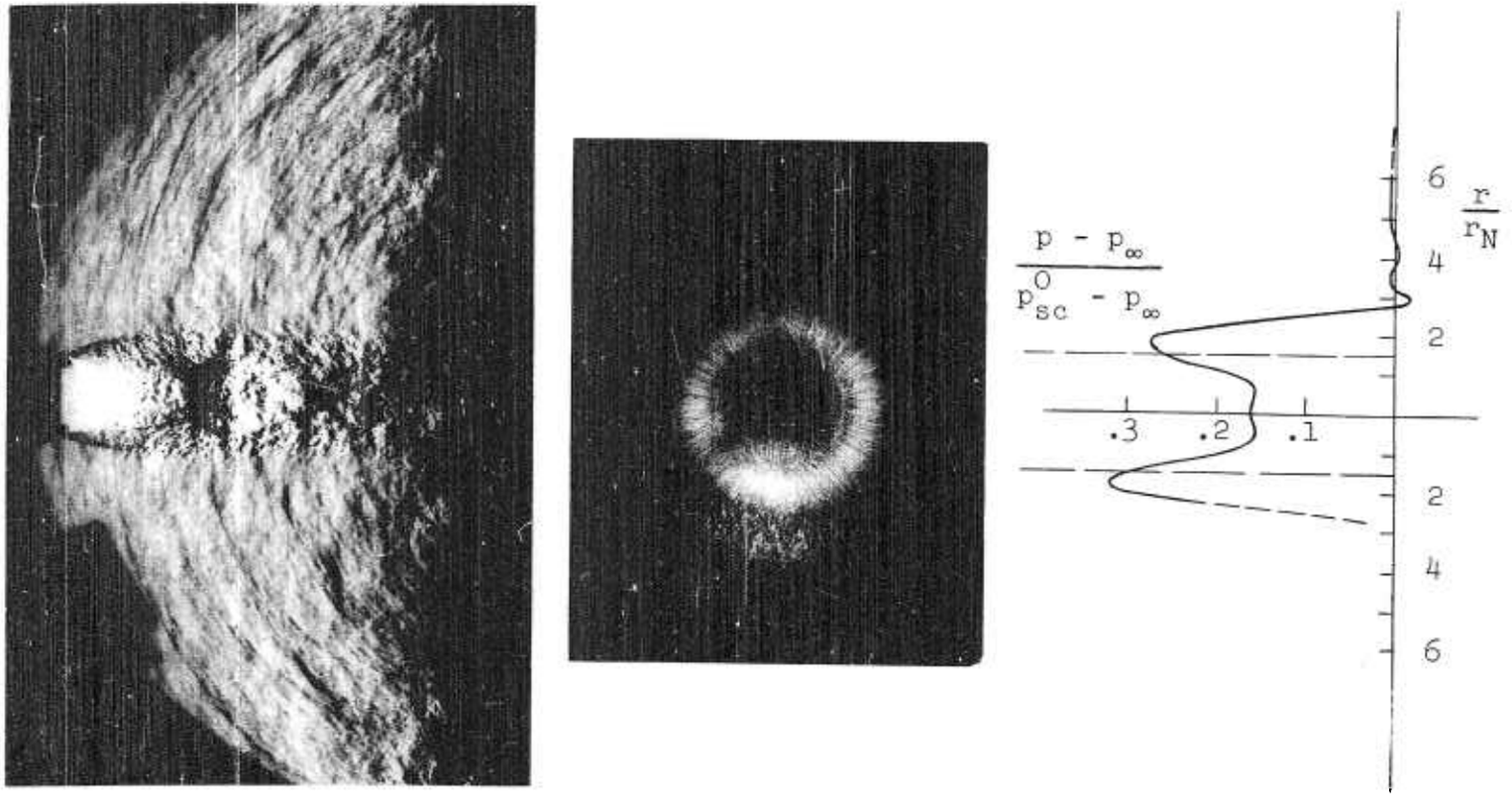

Figure 64. Typical jet impingement characteristics for a case in which a normal shock exists in the jet core. $p_1/p_\infty = 3.57$; $x/d_N = 5.32$.

increasing density near the surface as shown in the schlieren picture. In addition, the position of the streamline dividing ring, which can be thought of as a line of zero radial shear, is found not to correspond to the local pressure maximum.

3.2.5. Momentum balances and interference effects. In order to help clarify certain aspects of jet impingement flows, especially those which may involve interference in the entrained flow field, it is useful to consider qualitatively the balance of jet momentum fluxes with the pressure forces on the impingement surface. In Figure 65, four basic conditions are illustrated. Case 1 shows a free jet flow issuing from a nozzle of the type used in the present experiments, while Case 2 shows this jet impinging on a circular flat plate. Cases 3 and 4 represent corresponding flows but with a flat baffle plate inserted at the exit plane (AB). For convenience, a cylindrical control volume is defined by the impingement plate (surface CD), the baffle plate (surface AB), and the cylindrical surface S. The pressure is assumed to be unchanged across the free boundaries except within the confines of the nozzle. It is clear that the total axial momentum flux leaving the volume across surface CD in Case 1 is made up not only of that entering across AB through the nozzle (including the effect of any pressure difference across the nozzle exit plane) but also the sum of all the axial components of entrainment flow entering across the entire plane AB as well as the surface S. Moreover, a complete force balance for this system would also have to include the proper components of viscous forces at all the boundaries. For Case 2, neglecting viscous forces, the balance is primarily between the axial momentum flux of the jet (across AB and S) and the pressure force on the plate. It should be noted, however, that part of the axial flux across S is contained in the wall jet, which because of its

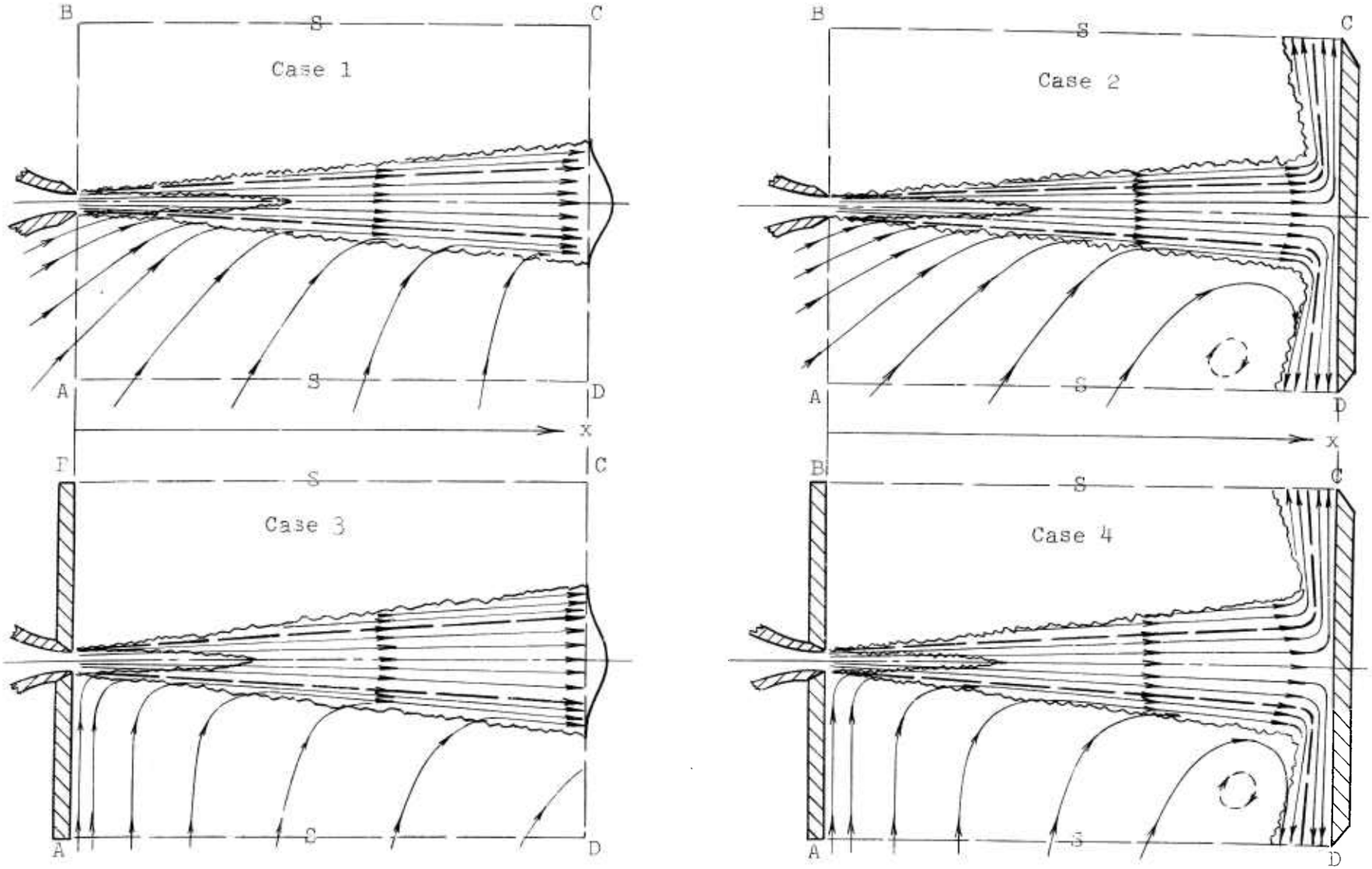

Figure 65. Impingement flow field patterns.

spread makes a contribution in the negative axial direction. The possible consequences of blockage due to a baffle plate are clear in Cases 3 and 4. It is seen that a large portion of the axial momentum flux is lost because of the solid boundary at AB. The entrainment flow is thus primarily radial. Because this flow must turn as it approaches the jet, however, a pressure gradient will be established on the surface AB which can result in an additional axial pressure force contribution. Basically, Case 4 represents a combination of Cases 2 and 3. Using the measurements of free jet velocity profiles and over-all flat plate pressure distributions, a comparison between jet axial momentum flux and plate pressure force has been made for the $p_1/p_\infty = 1.42$ jet. Each of these quantities is plotted as a function of axial distance in Figure 66. In addition, the free jet mass flux, the radial boundary of the nozzle mass flux $r_{\dot{M}_N}/r_N$ (i.e., the dividing streamline between nozzle and entrained flow), and the over-all jet spreading parameter $r_{.5}/r_N$ are given in Figure 67. The behavior of the jet momentum flux and plate force can be explained in terms of that portion of the over-all axial flux actually measured at each station. Near the nozzle, of course, the plate force represents practically all of the axial flux due to the nozzle as well as entrainment. It is seen that the jet alone accounts for only about one-half of this total force. The initial decrease of each parameter with axial distance is believed to be primarily due to pressure gradients which are known to exist across the boundary AB near the nozzle, but which were not evaluated. Farther downstream, the portion of the total control volume cross-section included in the free jet measurements increases because of jet spreading so that a larger portion of the total axial flux is accounted for. At the same time, since the jet diameter has grown to be nearly that of the plate, some of the jet flow is deflected around the plate without contributing to the force. This drop-off

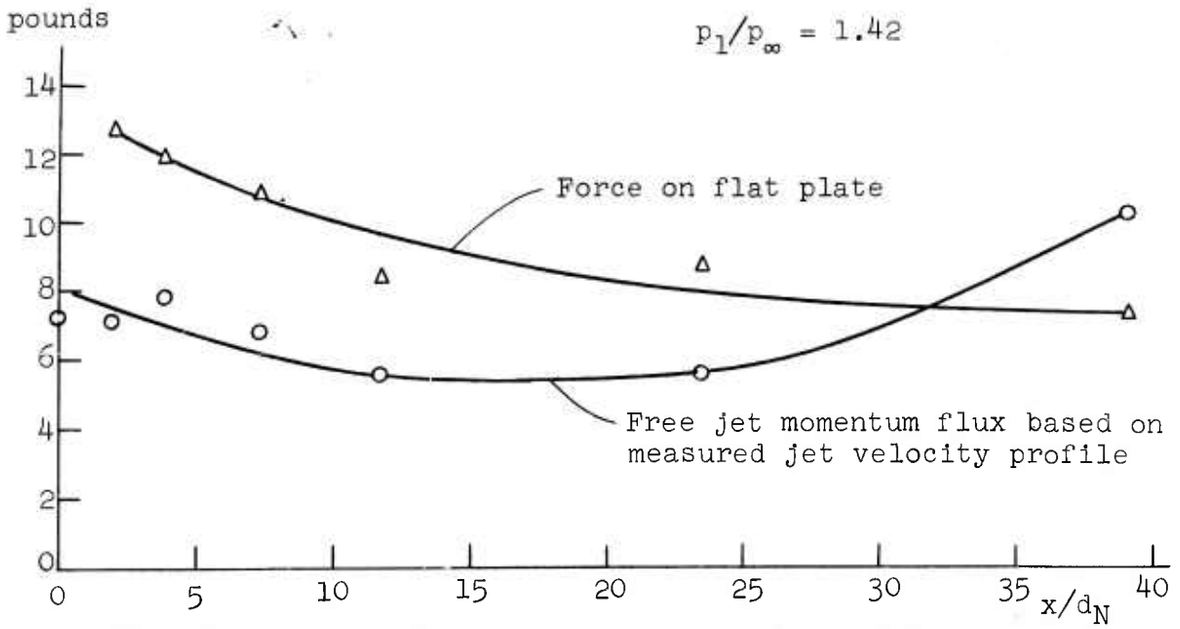

Figure 66. Comparison of free jet momentum flux and force on flat plate.

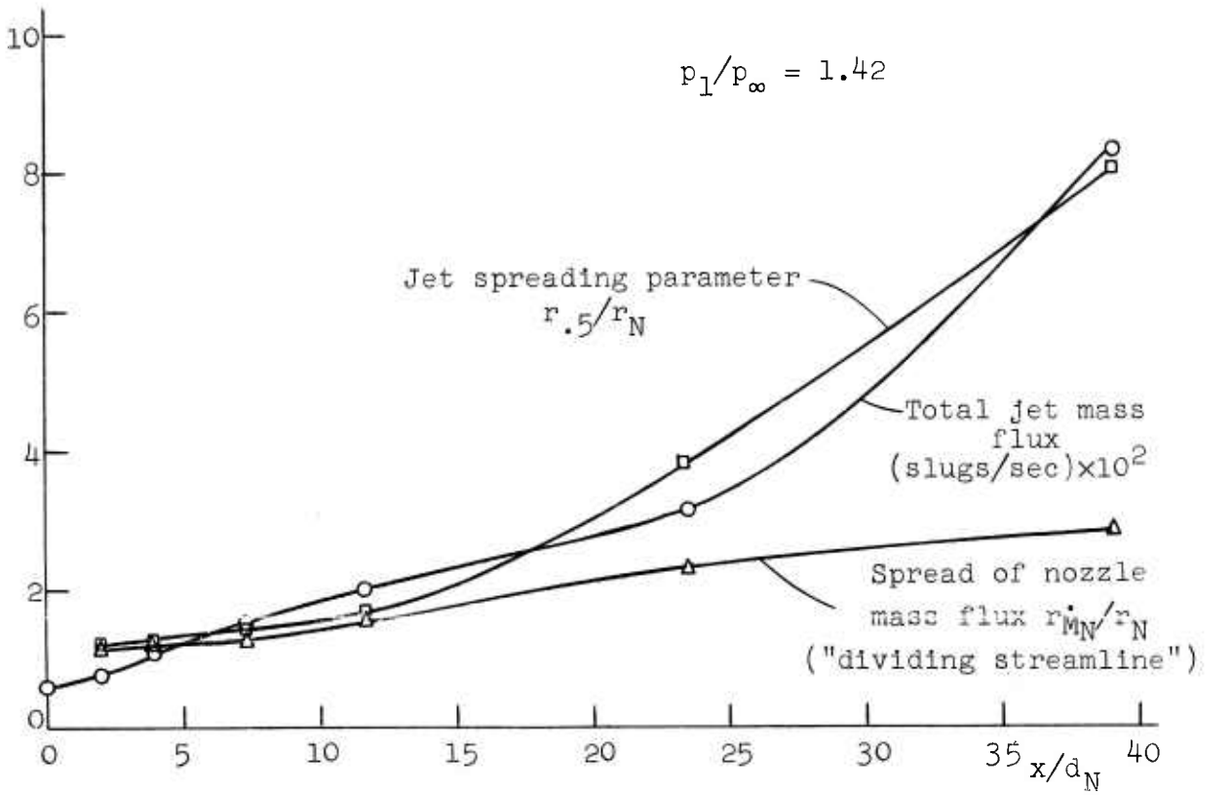

Figure 67. Measured total mass flux in free jet and spread of nozzle and total mass flux.

is slight within the range of these measurements.

The measured jet mass flux, as shown in Figure 67, is seen to increase more rapidly in the downstream portion. The possible existence of instabilities in this region has already been discussed. Because of probable measurement uncertainties in such a region, therefore, it is not clear how much of the increased flux is actually due to increased entrainment. Nevertheless, the total mass flux at $x/d_N \approx 40$ is seen to be approximately 14 times that of the jet alone. In order to illustrate the interference effect of a baffle plate at surface AB, several impingement conditions were rerun both with and without such a baffle plate. A comparison of impingement pressure distributions resulting from this test is shown in Figure 68. The change in distribution in this particular case is characterized by a decreased pressure near the center and an increase in the outer portions. While some of the few cases tested exhibited similar changes, others did not. On the whole, the relationship between jet and impingement behavior and interference effects is extremely complex and the present simple tests are intended to provide only some idea of the changes that can result from changes in geometry.

3.3. Discussion.

The experimental determination of stagnation point heat transfer parameters for normal jet impingement has been described in detail. It has been found that by making use of local free jet characteristics a reasonable correlation of the stagnation point velocity gradient $(du_e/dr)_{r=0}$ is achieved for a number of cases of jet strength and impingement distance. For impingement on a flat plate it was found that $(r_{.5}/V_c)(du_e/dr)_{r=0}$ fell within 20 per cent of a value of 1.1 at axial distances between 10 and 40 nozzle diameters downstream for a subsonic ($p_\infty/p^0_{sc} = .800$) jet and

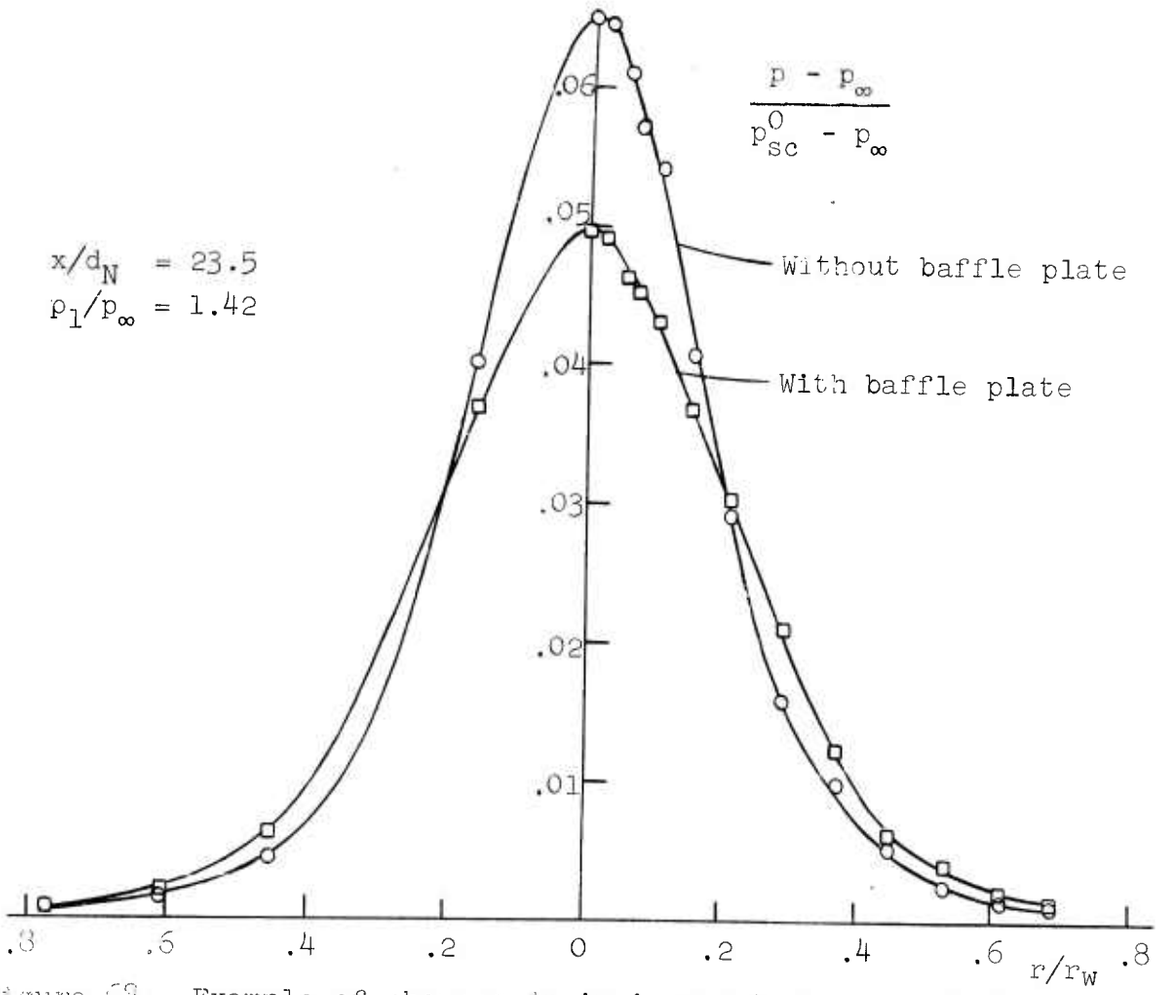

Figure 68. Example of changes in impingement pressure distribution due to baffle plate.

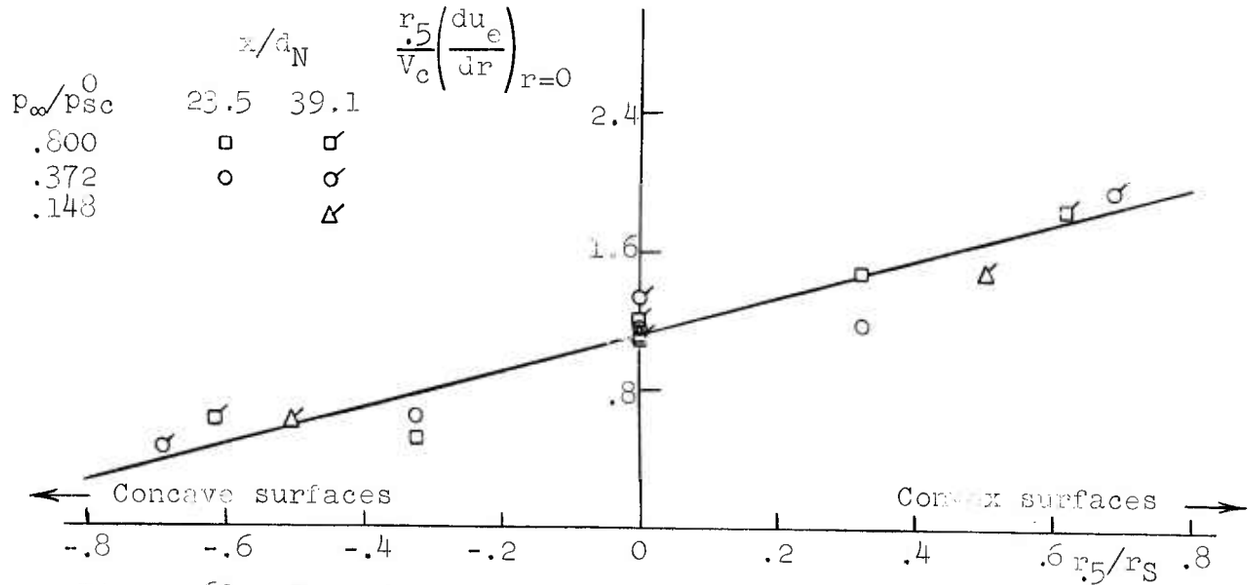

Figure 69. Dependence of correlated heat transfer parameter on surface shape.

a moderately underexpanded jet $(p_1/p_\infty = 1.42)$. For a highly underexpanded jet $(p_1/p_\infty = 3.57)$ a value of 1.1 was approached within 20 per cent downstream of 30 nozzle diameters. For a convex hemisphere, generally higher correlation values were found. These values showed an upward trend with increased axial distance. Such a trend might be expected since far downstream the axial drop-off of the gradient $(du_e/dr)_{r=0}$ itself is less rapid than it is for the flat plate. While the concave shapes exhibit lower values than for the flat plate, data do not clearly indicate the downward trend which might be expected on similar grounds. The correlation values can be related to the geometric conditions in terms of the free jet half-velocity radius $r_{.5}$ and the model surface radius of curvature r_s. With r_s defined negatively for the concave hemisphere, the values for the fully developed region of each jet are shown in Figure 69. In the range $-0.6 < r_{.5}/r_s < 0.6$, the surface curvature effect can be approximated by the linear relation

$$\frac{r_{.5}}{V_c}\left(\frac{du_e}{dr}\right)_{r=0} \approx 1.13 + 1.08\,\frac{r_{.5}}{r_s}$$

In addition to these basic measurements of $(du_e/dr)_{r=0}$, several other measurements and photographic studies have been made which help to illustrate certain features of impingement flows, particularly of highly underexpanded jets. It has been found that under conditions of impingement out to about 8 nozzle diameters for a jet with $p_1/p_\infty = 3.57$, a separated region may exist in the vicinity of the stagnation point with the result that maximum heat transfer may occur in a ring surrounding the central region. Some unusual features of this flow have been investigated by comparing impingement pressure distributions, surface streamline patterns, and schlieren photographs. Of special interest has been the manner in which the separated flow region becomes segmented along the ring dividing the inward from the outward flow on

the surface. It has also been found that the maximum impingement pressure occurs outside of this ring.

The problem of interference due to obstructions in the flow field surrounding the jet proper has been discussed briefly in a qualitative way. In particular, it has been stressed that the presence of such obstructions can result in substantial changes in the impingement pressure distribution. An example of this effect has been given in which interference was introduced by placing a baffle plate in the plane of the nozzle exit.

4. CONCLUSIONS

This study was performed in order to obtain a general knowledge of the behavior of free jets when they impinge normally on a flat surface. In particular, the general character of the stagnation point heat transfer parameter $(du_e/dr)_{r=0}$ and its dependence on shock structure and other features of the free jet were studied in detail.

The purpose of this investigation was to provide a general guide to the study of such matters at high enthalpy where the effects of density variations are of importance. It was felt that by knowing the general features of free jet impingement for low temperature constant density flows, a great deal of labor and expensive high temperature testing could be eliminated and a limited but essentially definitive test program for the high enthalpy problem evolved.

The results of the low temperature studies presented herein are thought to be sufficient to permit the order of magnitude of the stagnation point heat transfer parameter $(du_e/dr)_{r=0}$ to be estimated for the case of high enthalpy jets in a number of important practical applications.

The results of these low temperature studies of $(du_e/dr)_{r=0}$ were presented in two nondimensional forms. In the first form $(du_e/dr)_{r=0}$ was made dimensionless using the jet exit diameter and jet exit velocity, i.e.

$$\frac{d_N}{V_1}\left(\frac{du_e}{dr}\right)_{r=0}$$

This form is useful for quick estimates of $(du_e/dr)_{r=0}$ when information is not available concerning the decay of the free jet under consideration. The other method of presenting the data in nondimensional form attempts to correlate the stagnation point heat transfer parameter with local conditions in the free jet at the plane of impingement, i.e.

$$\frac{r_{.5}}{V_c}\left(\frac{du_e}{dr}\right)_{r=0}$$

The data show that such a correlation is useful in the region of fully developed free jet flow. In particular, for the case of normal impingement on a flat plate

$$\frac{r_{.5}}{V_c}\left(\frac{du_e}{dr}\right)_{r=0} \approx 1.13$$

The effect of curvature of the impingement surface on the stagnation point heat transfer parameter was also investigated. Typically, for fully developed jets when the ratio of the half width of the free jet $r_{.5}$ at the plane of impingement to the radius of curvature r_s of the impingement surface falls in the range $-0.6 < r_{.5}/r_s < 0.6$ (the plus sign refers to a convex surface and the minus sign to a concave surface), the effect of surface curvature on $(r_{.5}/V_c)(du_e/dr)_{r=0}$ is given approximately by the expression

$$\frac{r_{.5}}{V_c}\left(\frac{du_e}{dr}\right)_{r=0} \approx 1.13 + 1.08\,\frac{r_{.5}}{r_s}$$

In order to use this second method of nondimensionalizing the stagnation point heat transfer parameter, it is necessary to compute the properties of a given jet downstream of its point of issuance. This problem was also investigated. Comparisons were made between measured and computed values of $r_{.5}$ and V_c at various positions along the jet. Computed values were found by applying Warren's momentum integral method to all the cases studied including those for which the jet was underexpanded. It was found that the predicted decay rates based on this method agreed with the measured values quite well in the subsonic range. For moderately underexpanded jets, however, the agreement was no better than about 60 per cent. This is believed to be due primarily to the effects of

a large scale instability or "flapping" observed for these jets. The agreement was much better in the highly under-expanded range, although a steady drop-off in agreement with increasing jet strength and axial location was noted. Since the analytical method was based on a turbulent exchange coefficient that was assumed to be a function only of initial jet Mach number, it is felt that such a drop-off might be expected as the jet decays to subsonic velocities. These data would seem to indicate, therefore, that in the absence of jet "flapping", the core shock structure does not have a first-order effect in determining the decay rate of free jets. It appears that the disagreement is due primarily to the limitation imposed by assuming a constant exchange coefficient independent of position along the jet. Only in cases where shocks contribute to jet instability does it appear that they may influence over-all decay processes.

5. CITED REFERENCES

1. Reshotko, E., and Cohen, C.B. Heat transfer at the forward stagnation point of blunt bodies. NACA TN 3513, 1955.

2. Krzywoblocki, M.Z. Jets-Review of literature. Jet Prop., Vol. 26, No. 9, ppg. 760-779, Sept. 1956.

3. Anderson, A.R., and Johns, F.R. Characteristics of free supersonic jets exhausting into quiescent air. Jet Prop., pp. 13-15 and 25, Jan. 1955.

4. Seddon, J., and Haverty, L. Some tests on the spread of velocity in a cold jet discharging with excess pressure from a sonic exit into still air. A.R.C. Tech. Rept. C.P. No. 246, 1956.

5. Bazhenova, T.V., Leont'eva, Z.S., and Pushkin, V.S. Experimental investigation of the density distribution in a three-dimensional supersonic jet. Gas Dynamics and Physics of Combustion, Acad. of Sciences of the U.S.S.R., Moscow, 1959, English translation by the Israel Program for Scientific Translations, 1962.

6. Moe, M.M., and Froesch, B.A. Jet flows with shocks. ARS Journ. 30, 5, pp. 487-489, May 1960.

7. Eastman, D.W., and Radtke, L.P. Location of the normal shock wave in the exhaust plume of a jet. AIAA Journ. 1, 4, pp. 918-919, (1963).

8. Charwat, A.F. Boundary of underexpanded axisymmetric jets issuing into still air. AIAA Journ. 2, 1, pp. 161, 162, (1964).

9. Adamson, T.C., Jr. The structure of the rocket exhaust plume without reaction at various altitudes. Inst. of Sci. and Tech., Univ. of Mich. Rept. of BAMIRAC No. 4613-45-T, June 1963.

10. Woodley, J.G. Measurement of the flow field of an underexpanded jet in a hypersonic external stream. ($M = 6.8$). Roy. Aircraft Estab. Tech. Note No: AERO. 2733, Dec. 1960.

11. Love, E.S., Grigsby, C.E., Lee, L.P., and Woodling, M.J. Experimental and theoretical studies of axisymmetric free jets. NASA Tech. Rept. R-6, 1959.

12. Adamson, T.C., Jr., and Nicholls, J.A. On the structure of jets from highly underexpanded nozzles into still air. Journ. of the Aero. Sciences 26, 1, 16-24, (1959).

13. Lewis, C.H., and Carlson, D.J. Normal shock location in underexpanded gas and gas particle jets. AIAA Journ. 2, 776, 777, (1964).

14. Wang, C.J., and Peterson, J.B. Spreading of supersonic jets from axially symmetric nozzles. Jet Prop. 28, pp. 321-328, (195).

15. Lord, W.T. On rocket jet flow fields at high altitudes. Tech. Memo. No. Aero. 625, R.A.E., Farnborough, 1959.

16. Lord, W.T. On axisymmetrical gas jets, with application to rocket jet flow fields at high altitudes. Rept. No. Aero 2626, R.A.E., Farnborough, 1959.

17. D'Attore, L., and Harshbarger, F. Experimental and theoretical studies of underexpanded jets near the Mach disc. Gen. Dyn./Astro., GDA-DBE 64-008.

18. Olson, R.E., and Miller, D.P. Aerodynamic studies of free and attached jets. Res. Labs., United Aircraft Corp., A-1771-24, prepared for Harry Diamond Labs., ARMY Materiel Command, Oct. 1963.

19. Hammitt, A.G. The oscillation and noise of an overpressure sonic jet. Journ Aerosp. Sci. 28, 9, pp. 673-680, (1961).

20. Warren, W.R. An analytical and experimental study of compressible free jets. Princeton University Dept. of Aeronautical Engineering Report No. 381, 1957.

21. Latvala, E.K., and Anderson, T.P. Experimental determination of jet spreading from supersonic nozzles at high altitudes. AEDC-TN-58-98, Jan. 1959.

22. Latvala, E.K. Spreading of rocket exhaust jets at high altitudes. AEDC-TR-59-11, June 1959.

23. Owen, P.L., and Thornhill, C.K. The flow in an axially-symmetric supersonic jet from a nearly-sonic orifice into a vacuum. Brit. ARC Tech. Rept., R and M 2616, 1952.

24. Vick, A.R., and Andrews, E.H. An experimental investigation of high underexpanded free jets impinging upon a parallel flat surface. NASA TN D-2326, 1964.

25. Vick, A.R., Andrews, E.H., Jr., Dennard, J.S., and Craidon, C.B. Comparisons of experimental free jet boundaries with theoretical results obtained with the method of characteristics. NASA TN D-2327, 1964.

26. Vick, A.R., Cubbage, J.M., and Andrews, E.H., Jr. Rocket exhaust plume problems and some recent related research. Presented at Specialists Meet. on "The Fluid Dynamic Aspects of Space Flight" under the sponsorship of the Fluid Dynamics Panel of AGARD, Marseille, France, 1964.

27. Wernicke, K.G. (Bell Helicopter Co.) Performance testing of a five-foot air cushion model. Symp. on ground effect machines, p. 363, Princeton Univ., Oct. 1959.

28. Sutton, J.F. (Lockheed Aircraft Corp.) Propulsion systems experiments. Symp. on ground effect machines, p. 341, Princeton Univ., Oct. 1959.

29. Shen, Y.C. Theoretical analysis of jet-ground plane interaction. IAS Paper No. 62-144, IAS National Summer Meeting, June 1962.

30. Vidal, R.J. Aerodynamic processes in the downwash impingement problem. IAS Paper No. 62-36, IAS 30th Ann. Meeting, Jan. 1962.

31. Curtis, E.S., and Pfisterer, V.R. (Hydronautics, Inc.) Experimental investigation of the viscous effects on balanced jets in ground proximity (Final Report). TRECOM-TR-63-61; AD-426131; Tech. Rept. 41-3, (1963).

32. Vesigot, J.P., and Gire, E. Terrain de decollage ou atterrissage pour avion V/STOL. Symp. on VSTOL Aircraft, Part 2, AGARDograph 46, June 1960.

33. O'Malley, J.A., Jr. Flow phenomena experienced with VTOL aircraft in ground proximity. Symp. on VSTOL Aircraft, Part 2, AGARDograph 46, June 1960.

34. Grotz, C.A. Simulated VTOL exhaust impingement on ground surface. Symp. on VSTOL Aircraft, Part 2, AGARDograph 46, June 1960.

35. Kuhn, R.E. An investigation to determine conditions under which downwash from VTOL aircraft will start surface erosion from various types of terrain. NASA TN D-56, (1959).

36. Sibulkin, M., and Gallaher, W.H. Some aspects of the interaction of a jet with a dust covered surface in a vacuum environment. Gen. Dyn./Astronautics, Space Science Lab. Rept. No. ERR-AN-244, (1963).

37. Spady, A.A., Jr. An exploratory investigation of jet-blast effects on a dust-covered surface at low ambient pressure. NASA TN D-1017, (1962).

38. Stitt, L.E. Interaction of highly underexpanded jets with simulated lunar surfaces. NASA TN D-1095, (1961).

39. Sibulkin, M. Jet impingement on a dust-covered surface. Phys. of Fluids 7, 5, pp. 696-699, (1964).

40. Roberts, L. The action of a hypersonic jet on a dust layer. IAS Paper No. 63-50, IAS 31st Ann. Meeting, Jan. 1963.

41. Stitt, L.E., and Latto, W.T., Jr. Interaction of highly underexpanded exhaust jets with adjacent surfaces. IAS Paper 62-161, (1962).

42. Yoshihara, H. Rocket exhaust impingement on a ground surface. Gen. Dyn./Astronautics Rept. ERR-AN-177, 1962.

43. Eastman, D.W., and Radtke, L.P. Flow field of an exhaust plume impinging on a simulated lunar surface. AIAA Journ. 1, 6, pp. 1430-1431, (1963).

44. Anderson, A.R., Johns, F.R., and Hawkes, W.M. Nondimensional characteristics of free and deflected supersonic jets exhausting into quiescent air. U.S. Naval Air Development Center, NADC-ED-5401, (1954).

45. Henderson, L.F. The impingement of a supersonic jet on a flat plate. Australian Defense Scientific Service, Dept. of Supply, Mech. Engrg. Note 238.

46. Tachibana, F., and Naito, M. Heat transfer between a flat plate and a fluid jet. Preprint Japanese Soc. of Mech. Engrs. Meet., Dec. 1954, (in Japanese).

47. Perry, K.P. Heat transfer by convection from a hot gas jet to a plane surface. Proc. Institution of Mech. Engrs., London, 168, 30, pp. 775-780, (1954).

48. Nevins, R.G. The cooling power of an impinging jet. Ph.D. Thesis, Univ. of Illinois, 1953.

49. Nevins, R.G., and Ball, H.D. Heat transfer between a flat plate and a pulsating impinging jet. Kansas State Univ., Reprint No. 32.

50. Wolfshtein, M., and Stotter, A. Heat transfer between an impinging jet and a flat surface. Israel Journ. of Tech. 2, 131-134, (1964).

51. Baxter, A.N. The influence of jet properties on the design of uncooled deflecting surfaces. ARS Paper No. 625-58, ARS Semi-Ann. Meeting, June 1958.

52. Metzger, D.E. Spot cooling and heating of surfaces with high velocity impinging air jets, Part 1--Slot jets on plane surfaces. Stanford Univ. Rept. No. 52, (1962).

53. Gardon, R., and Cobonpue, J. Heat transfer between a flat plate and jets of air impinging on it. Intern'l. Developments in Heat Transfer, Part II, pp. 454-460, (1961).

54. Vickers, J.M.F. Heat transfer coefficients between fluid jets and normal surfaces. Industrial and Engrg. Chemistry 51, 8, pp. 967-972, (1959).

55. Freidman, S.J., and Mueller, A.C. Heat transfer to flat surfaces. Proc. General Discussion on Heat Trans., Institution of Mech. Engrs., London, pp. 138-142, (1951).

56. Sogin, H.H. Sublimation from disks to air streams flowing normal to their surfaces. Proc. ASME Ann. Meeting, New York, Paper No. 56-A-115, pp. 61-69, (1956).

57. Jakob, M., and Kezios, S.P. Heat transfer in the flow of air against plane surfaces. Proc. of the 6th Intern'l. Cong. for Appl. Mech., Sorbonne, Paris, France, (1946).

58. John, R.R., and Bade, W.L. Journ. Amer. Roc. Soc. 29, 7, pp. 523-525, (1959).

59. Smirnov, V.A., Verevochkin, G.E., and Brdlick, P.M. Heat transfer between a jet and a held plate normal to flow. Int. Journ. Heat Mass Transfer 2, pp. 1-7, (1961).

60. Leclerc, A. Deviation d'un jet liquide par une plaque normale a son axe (Deflection of a liquid jet by a plate perpendicular to its axis). La Houille Blanche, pp. 816-821, (1950).

61. Levey, H.C. The back effect of a wall on a jet. Journ. of Appl. Math. and Phys. (ZAMP), Vol. XI, Fasc. 2, pp. 152-157, (1960).

62. Bradshaw, P., and Love, E.M. The normal impingement of a circular air jet on a flat surface. ARC 21, 268, FM 2856, PL 20, R & M 3205, (1958).

63. Brady, W.G., and Ludwig, G. Theoretical and experimental studies of impinging uniform jets. IAS Paper 63-29, Jan. 1963.

64. Mathieu, J. Contribution a l'etude aerothermique d'un jet plan evoluant en presence d'une paroi. France, Ministere de l'Air, PST 374, Jan. 1961. SDIT, 2 Av. Porte-d'Issy, Paris 15.

65. Mathieu, J., and Tailland, A. Study of a plane jet directed tangentially to a wall. C.R. Acad. Sci. Paris 252, 24, pp. 3736-3738, June 1961.

66. Kadosch, M. The mechanism of jet deflection. Publ. Scient. Tech. Min. Air, France, No. 124, (1959).

67. Poreh, M., and Cermak, J.E. Flow characteristics of a circular submerged jet impinging normally on a smooth surface. Proc. of the 6th Midwestern Conf. on Flu. Mech., Univ. of Texas, Austin, Texas, pp. 198-212, (1959).

68. Finajero, A.A. David Taylor Model Basin Aero. Lab. Aero. Rept. 954 (TED TMB AD 3242).

69. Marsh, A.H. Noise measurements around a subsonic air jet impinging on a plane, rigid surface. Journ. of the Acoustical Soc. of Amer. 33, 8, pp. 1065-1066, (1961).

APPENDIX I

Summary of free jet cases for which velocity profiles were determined.

p_∞/p^0_{sc} \ x/d_N	0	1.96	3.92	5.87	7.32	11.74	23.5	39.1	58.7
.969	✓	✓	✓	✓	✓	✓	✓	✓	
.834	✓	✓	✓	✓	✓	✓	✓	✓	✓
.552		✓			✓	✓	✓	✓	✓
.458 (p_1/p_∞ = 1.14)					✓	✓	✓	✓	
.372 (p_1/p_∞ = 1.42)		✓	✓		✓	✓	✓	✓	✓
.148 (p_1/p_∞ = 3.57)		✓	✓		✓	✓	✓	✓	✓

In addition to the above listed cases, axial decay measurements alone were made at several of the same locations for the following jet pressure ratios:

p_∞/p^0_{sc} =	p_1/p_∞ =
.244;	2.16
.183	2.88
.121	4.36
.104	5.08

APPENDIX II

Pressure measurement data and computed velocity profiles for all of the free jet cases listed in Appendix I are included in the following pages.

Summary plots of the radial spread and axial decay characteristics of these jets are also included.

Note: For ease in making comparisons, all measured pressure data have been converted to the same units--inches of alcohol (s.g. = .820) gauge.

Subsonic Jet

$p_1/p_\infty = 1.00$

$p_\infty/p^0_{sc} = .969$

$T^0_{sc}/T_\infty = 1.00$

x/d_N
0
1.96
3.92
5.87
7.32
11.74

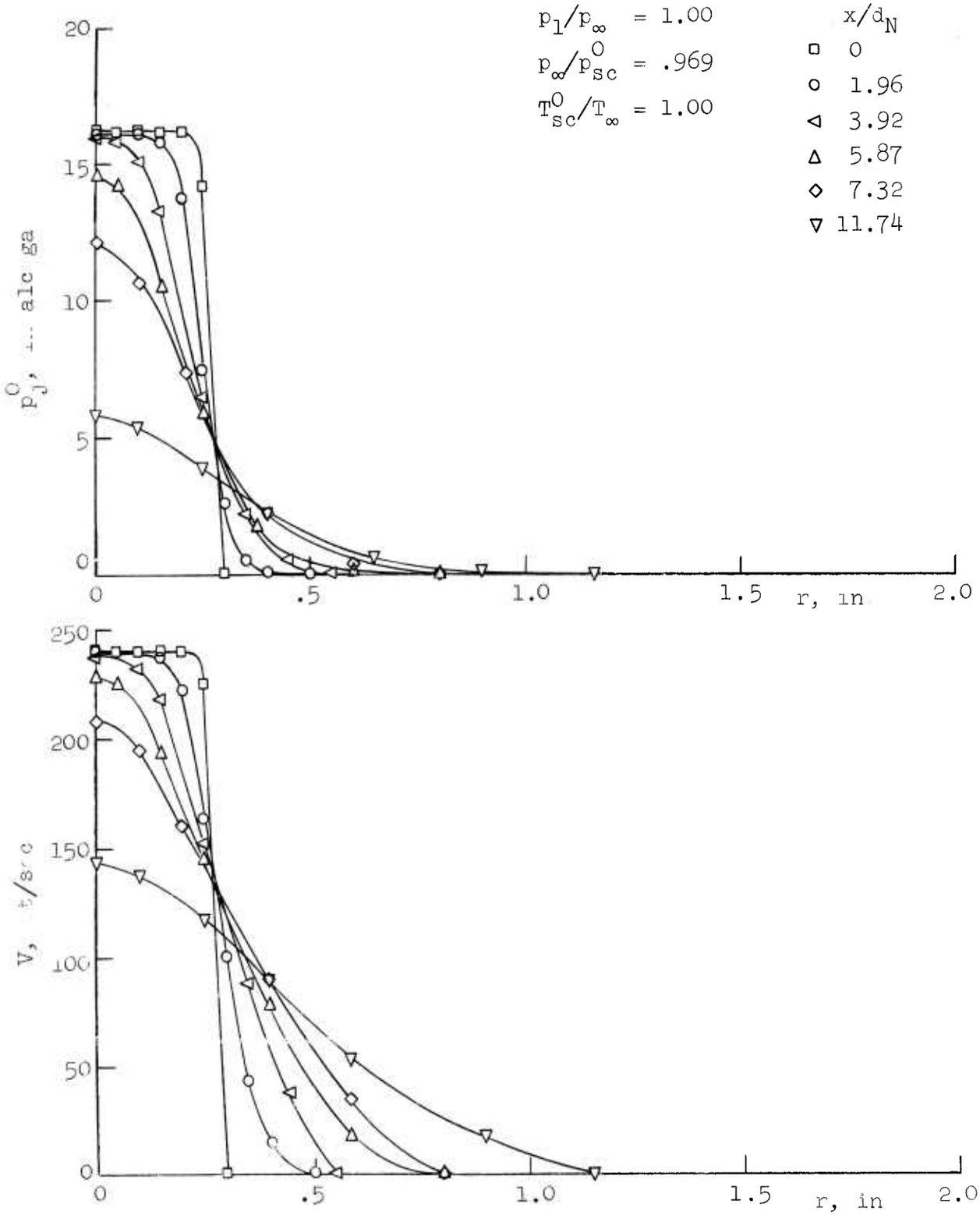

Figure AII-1

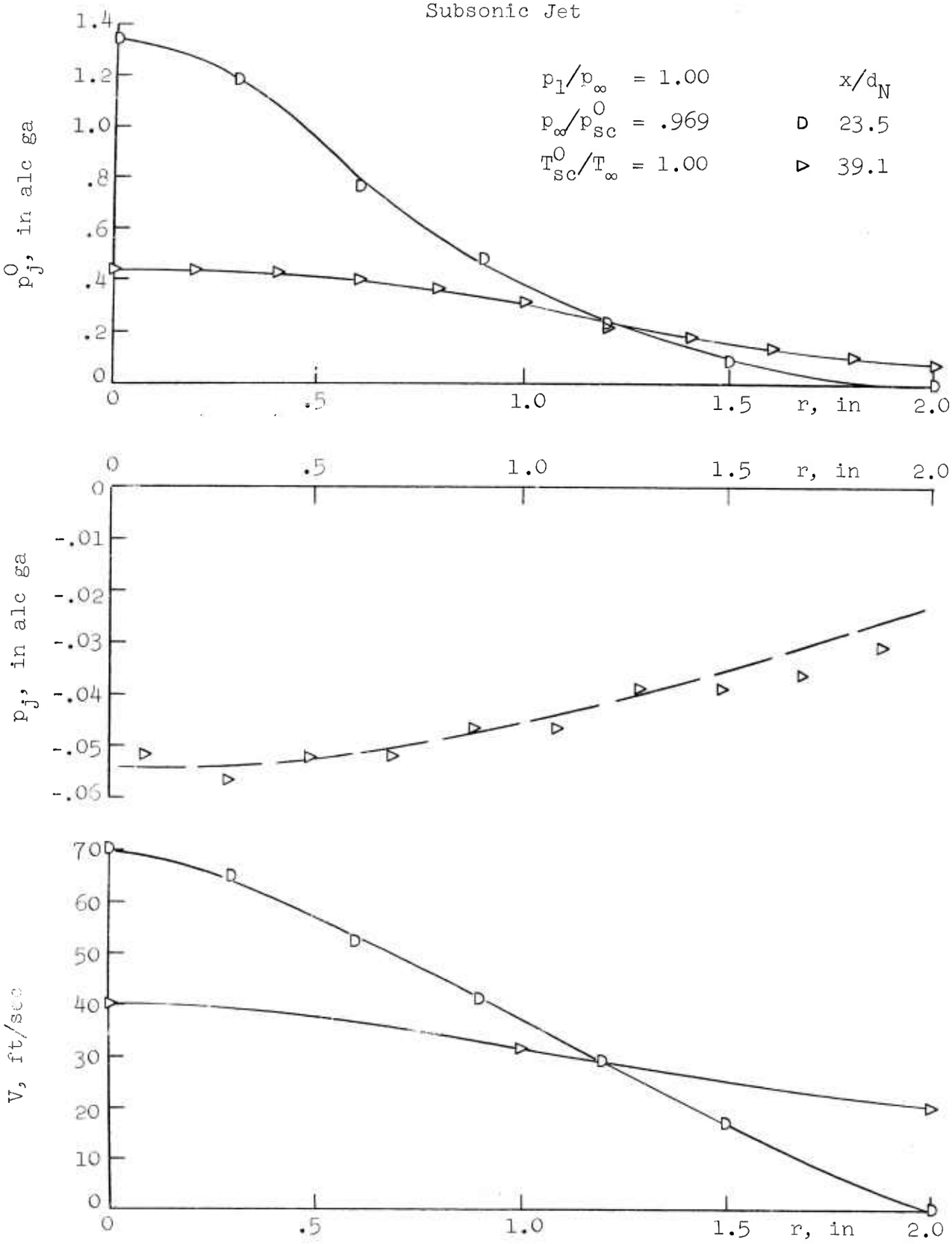
Subsonic Jet
p_1/p_∞ = 1.00
p_∞/p^O_{sc} = .969
T^O_{sc}/T_∞ = 1.00
x/d_N
D 23.5
▷ 39.1
p^O_j, in alc ga
1.4
1.2
1.0
.8
.6
.4
.2
0
0
.5
1.0
1.5
r, in
2.0
p_j, in alc ga
-.01
-.02
-.03
-.04
-.05
-.06
V, ft/sec
70
60
50
40
30
20
10

Figure AII-2

Subsonic Jet

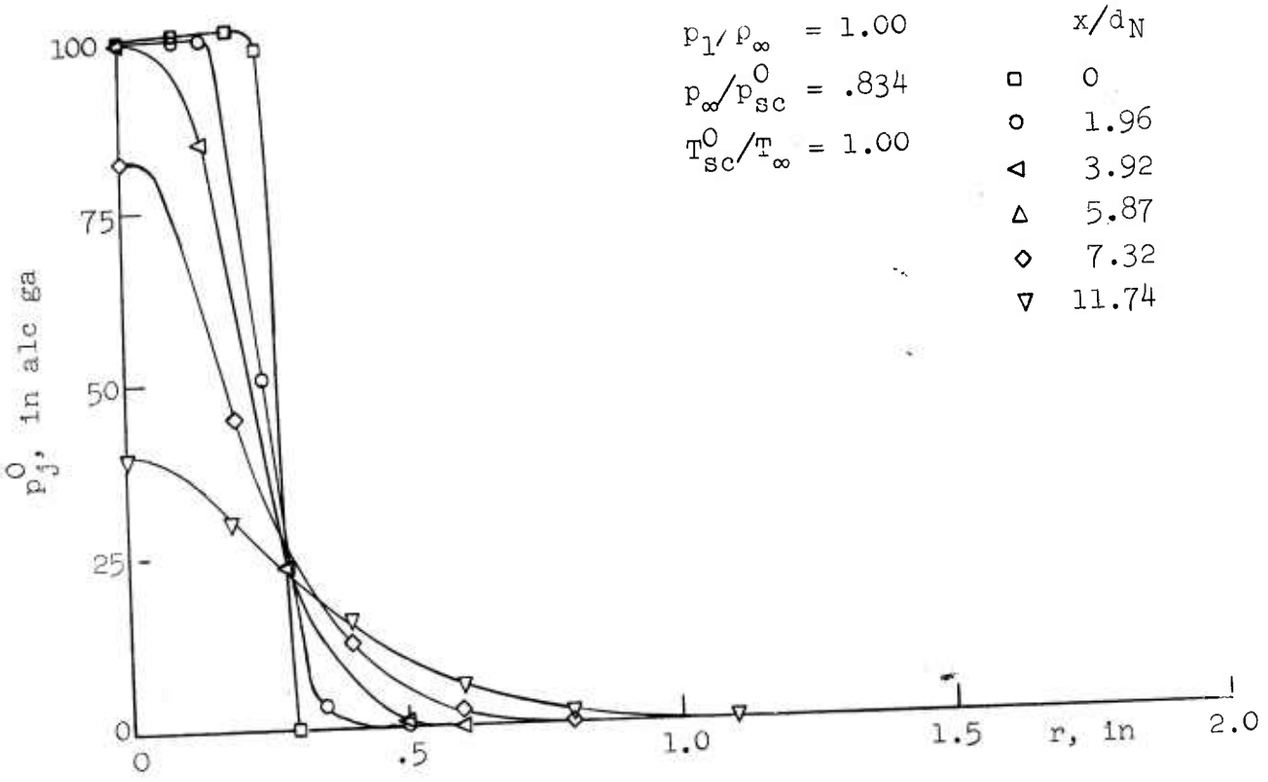

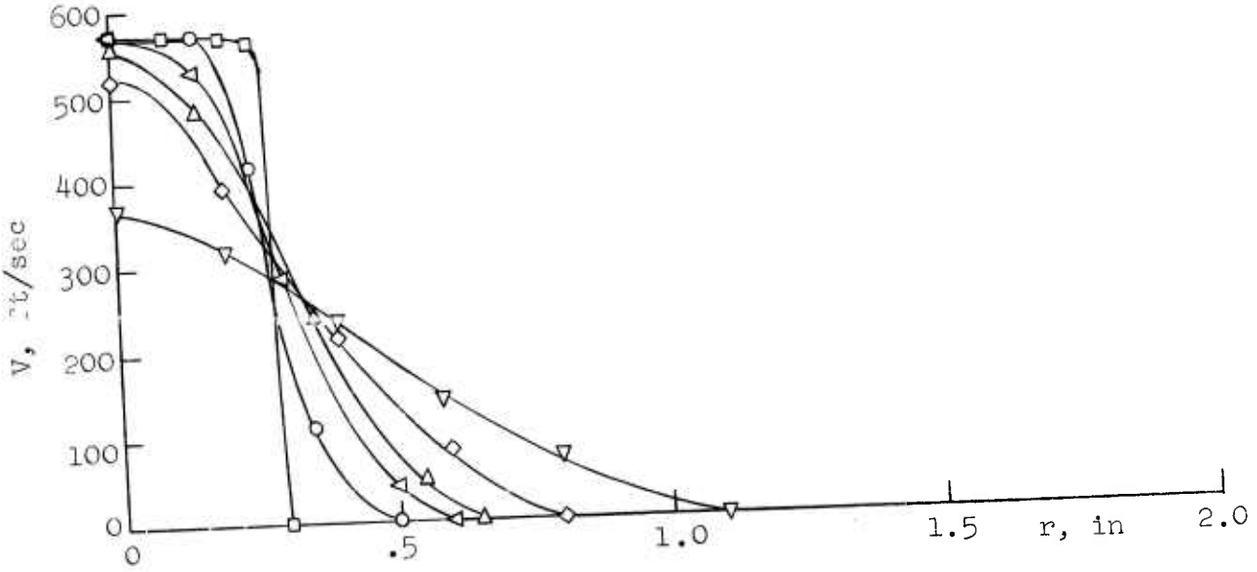

Figure AII-3

Subsonic Jet

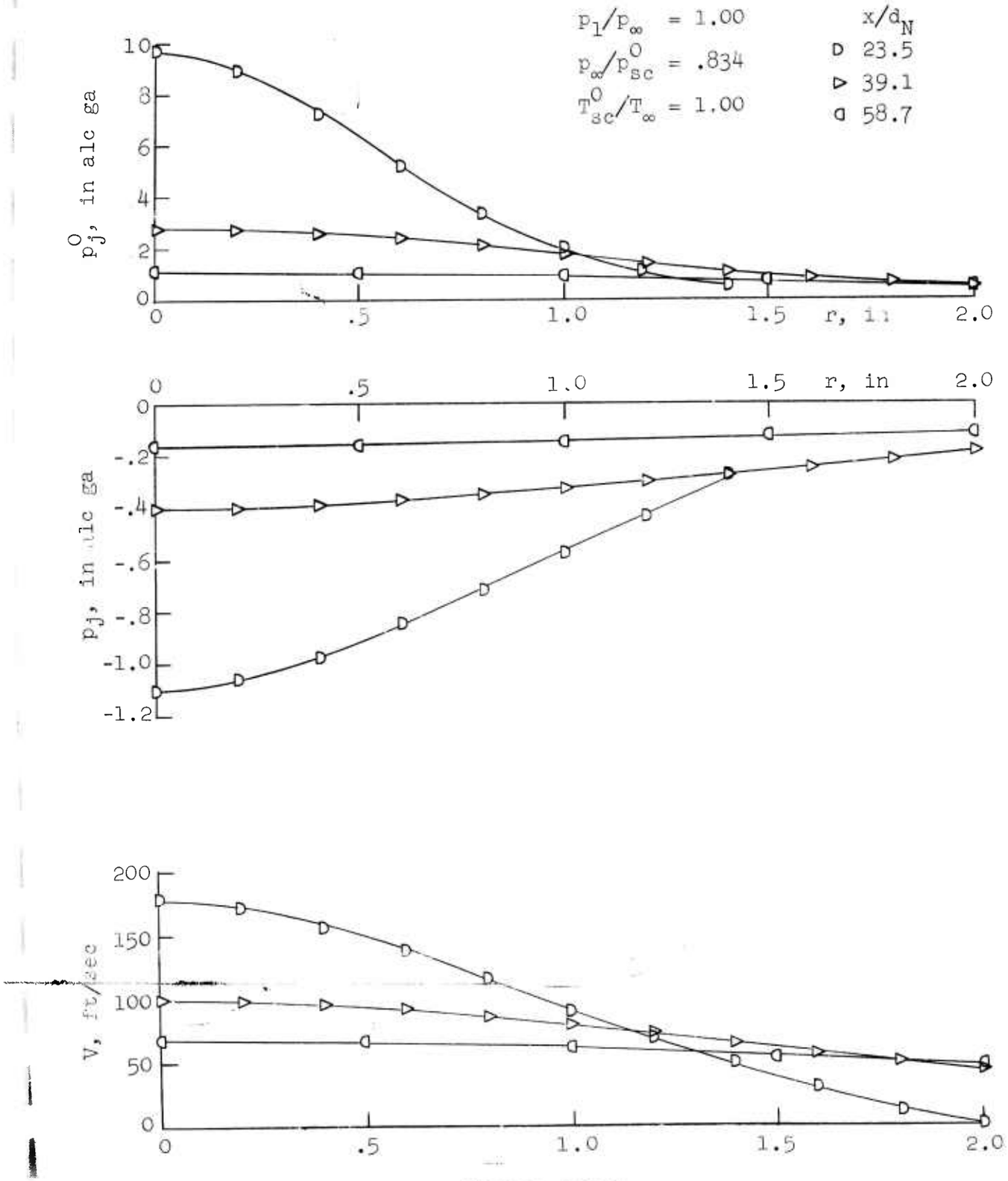

Figure AII-4

Subsonic Jet

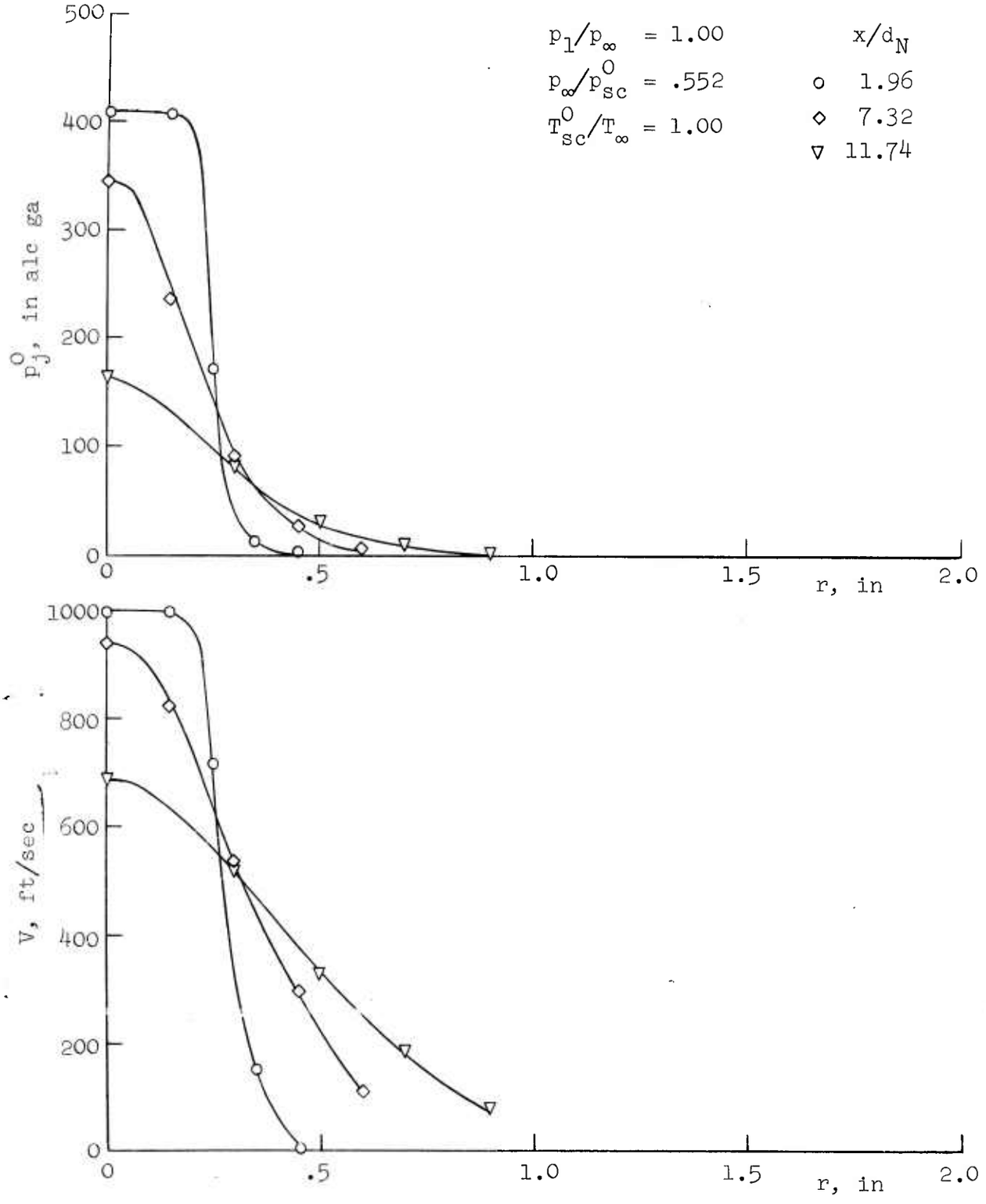

Figure AII-5

Subsonic Jet

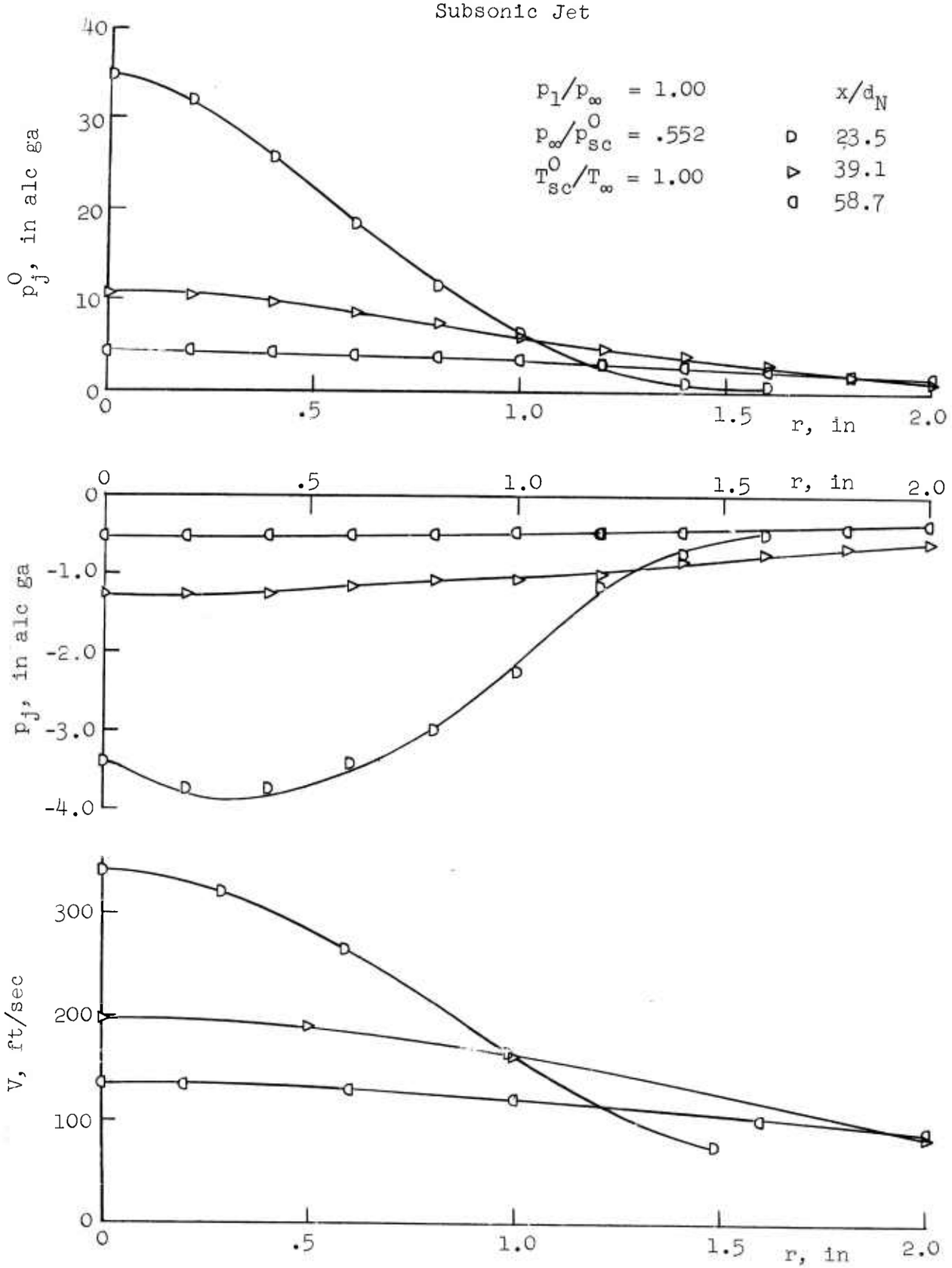

Figure AII-6

Moderately Underexpanded Jet

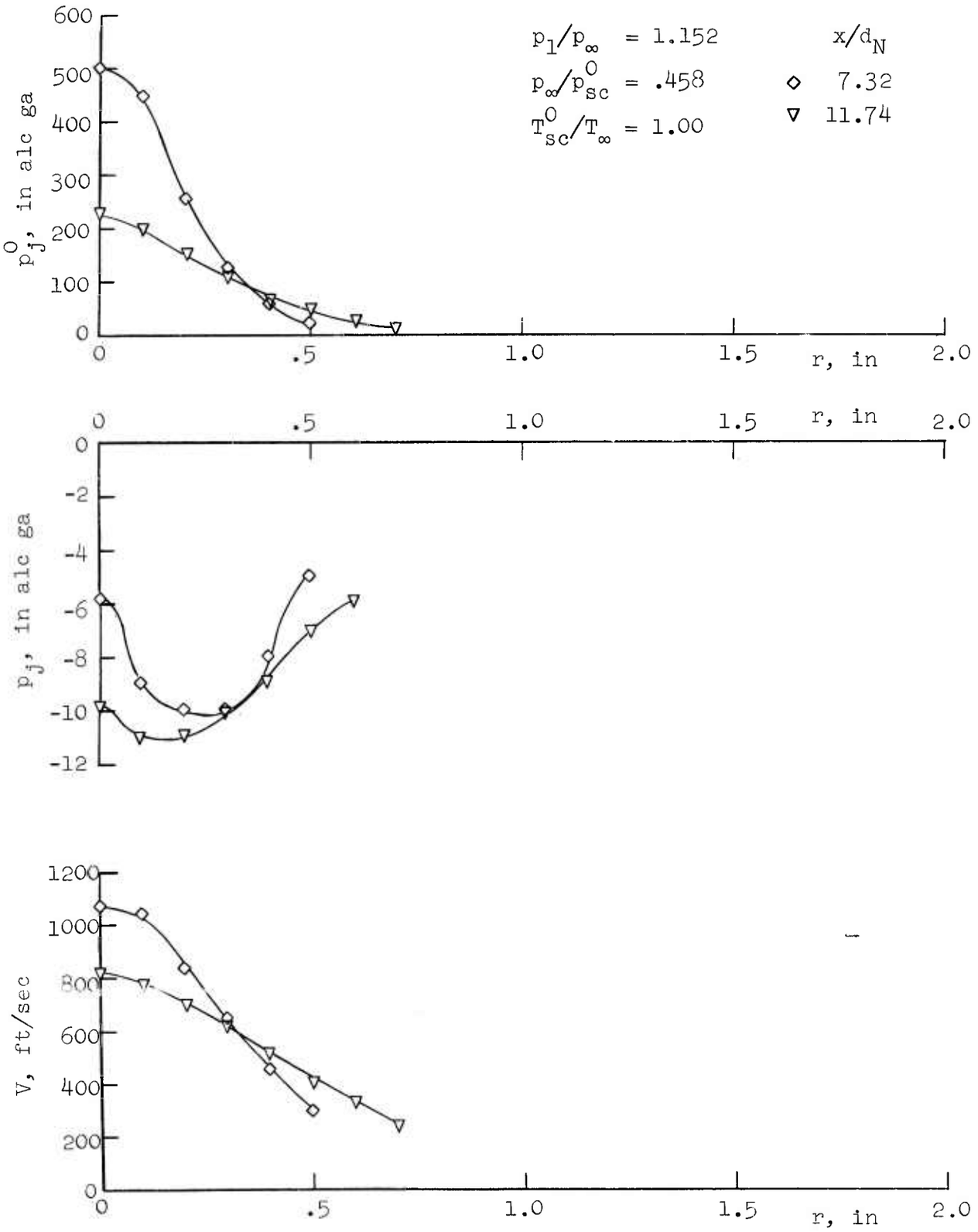

Figure AII-7

Moderately Underexpanded Jet

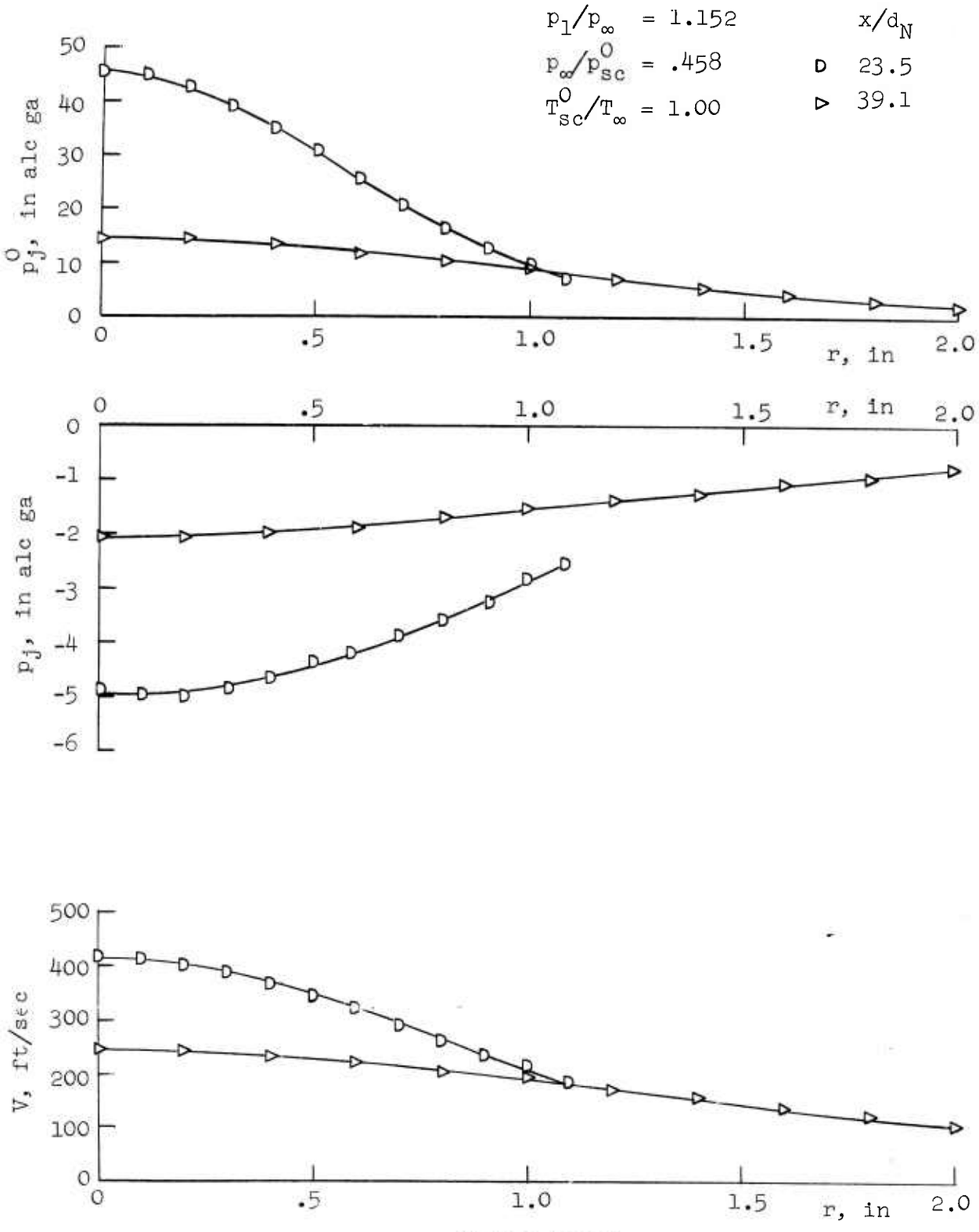

Figure AII-8

Moderately Underexpanded Jet

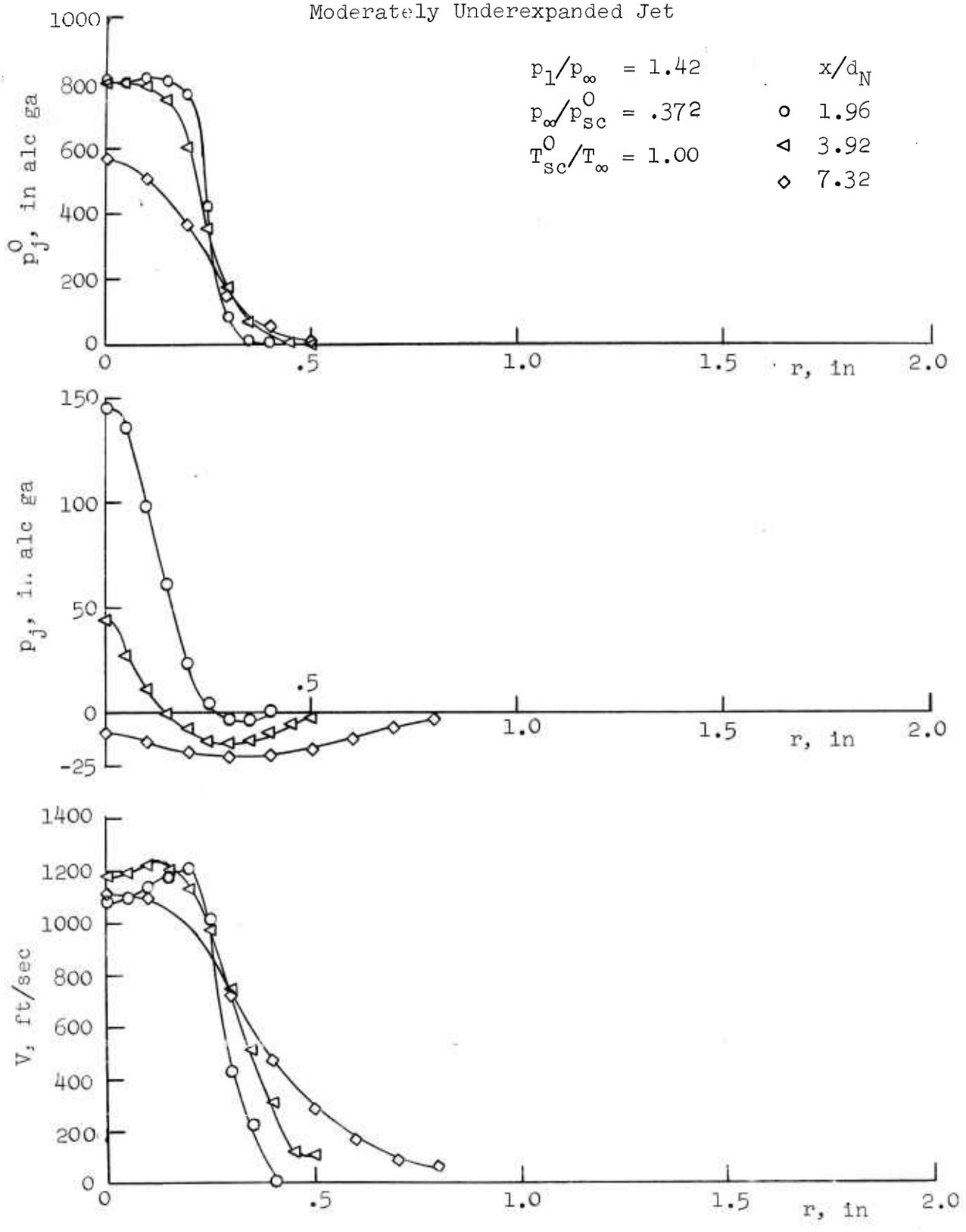

Figure AII-9

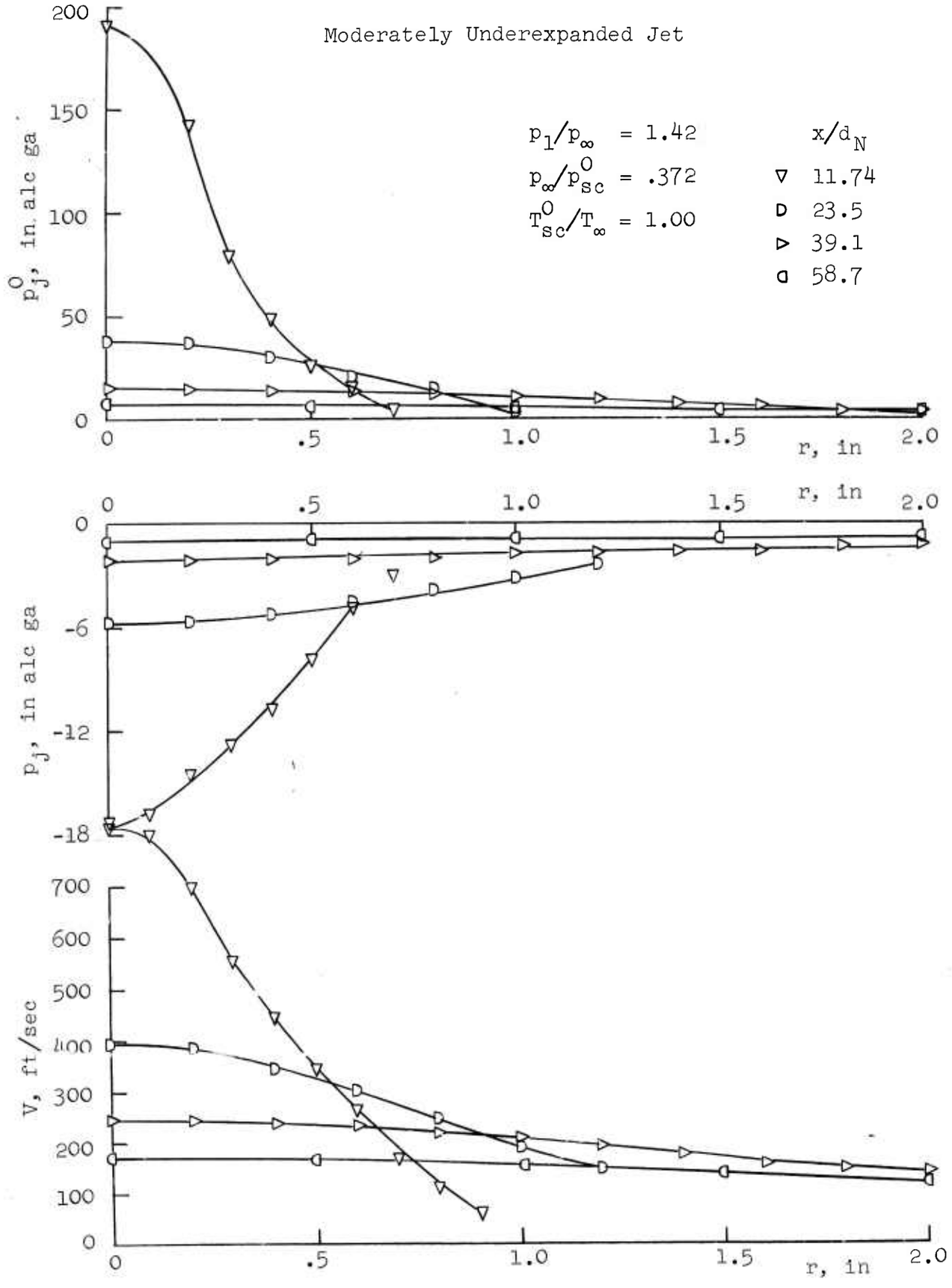

Figure AII-10

Highly Underexpanded Jet

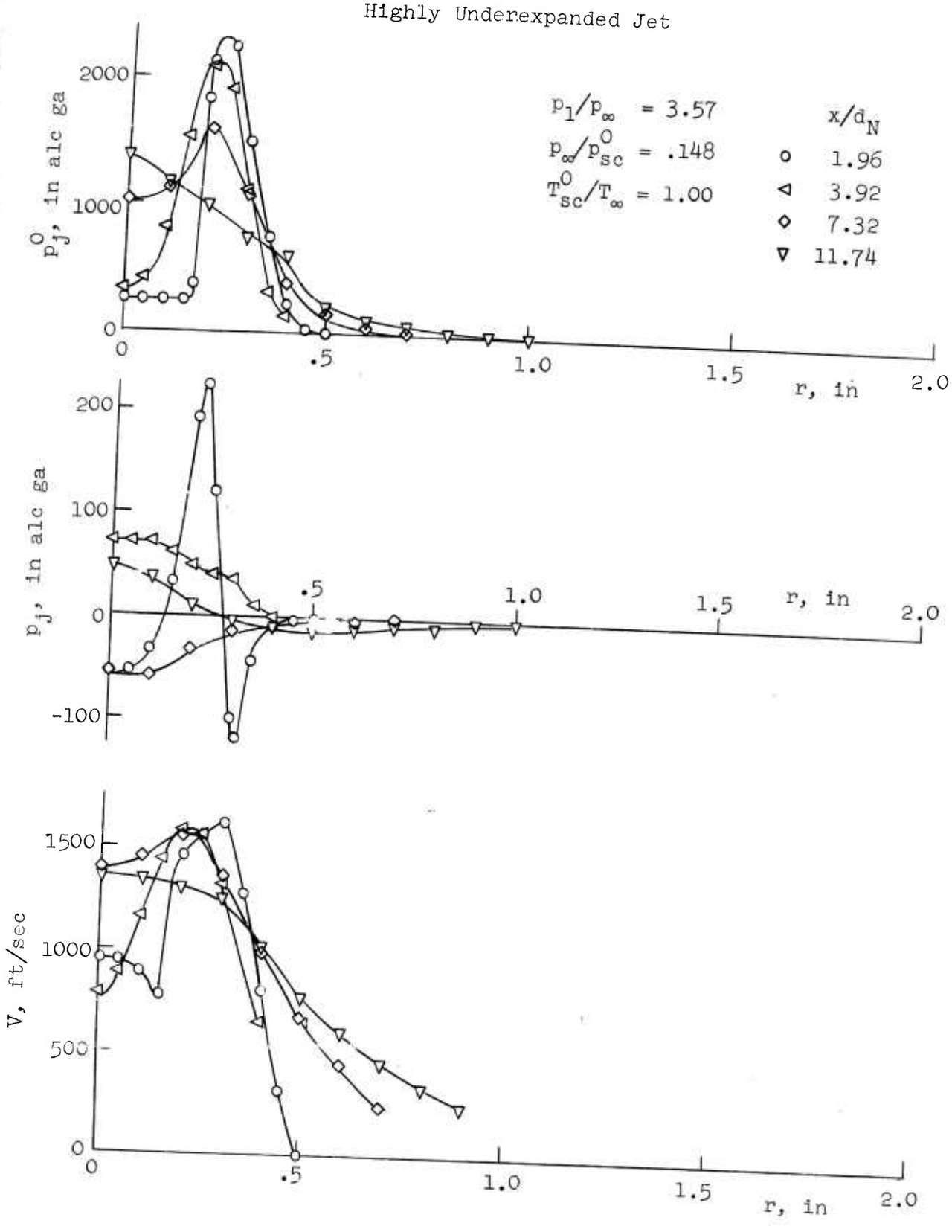

Figure AII-11

Highly Underexpanded Jet

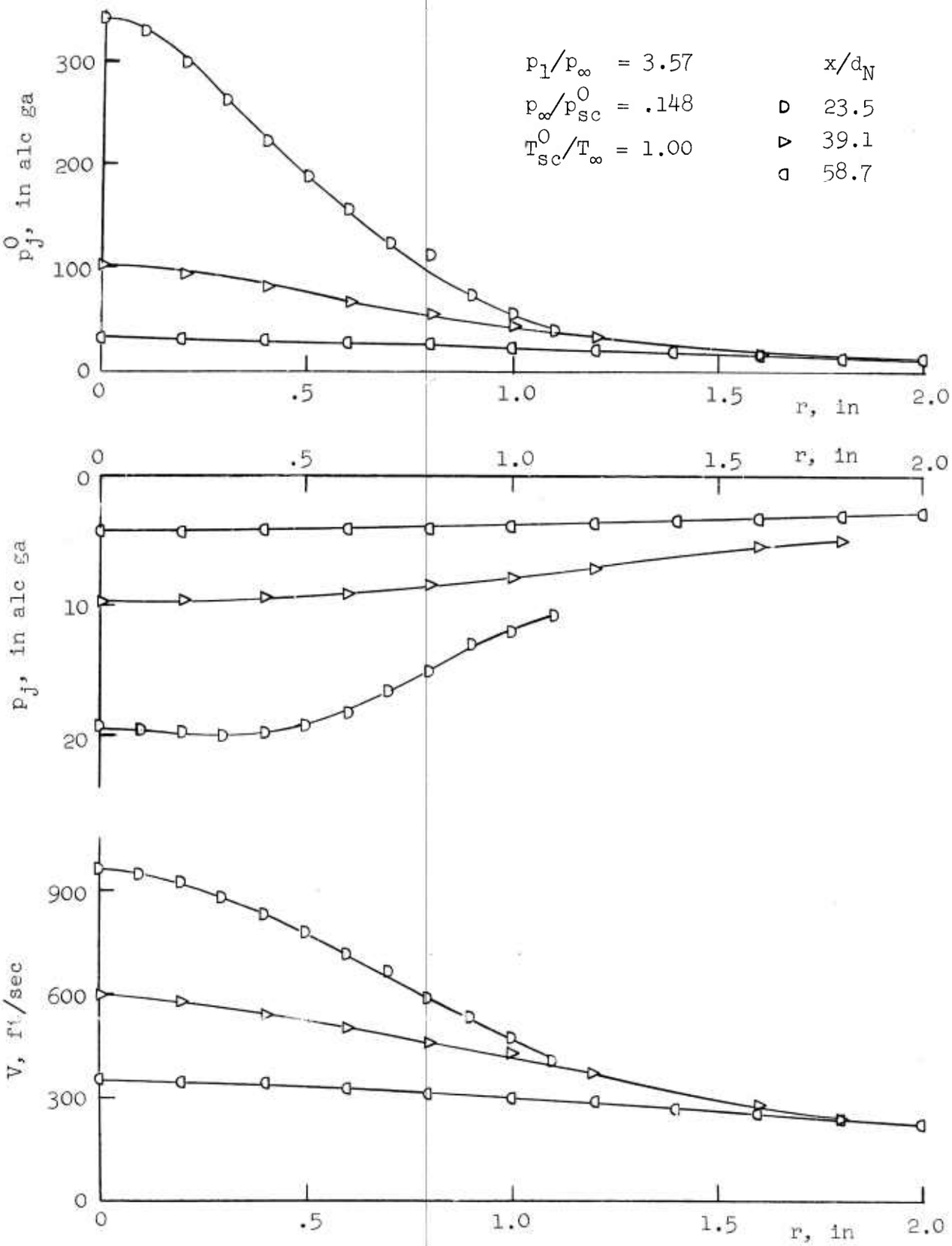

Figure AII-12

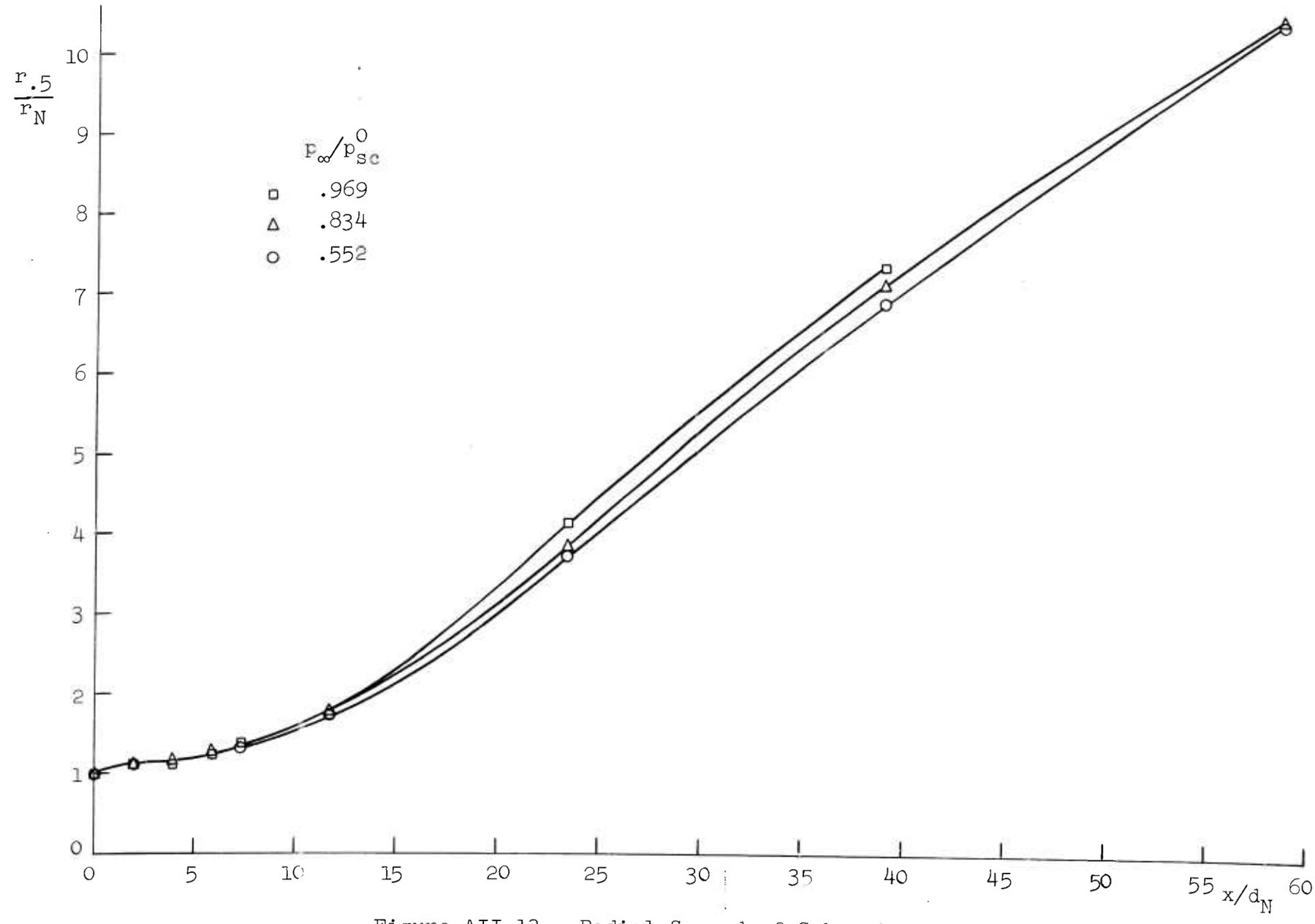

Figure AII-13. Radial Spread of Subsonic Free Jet.

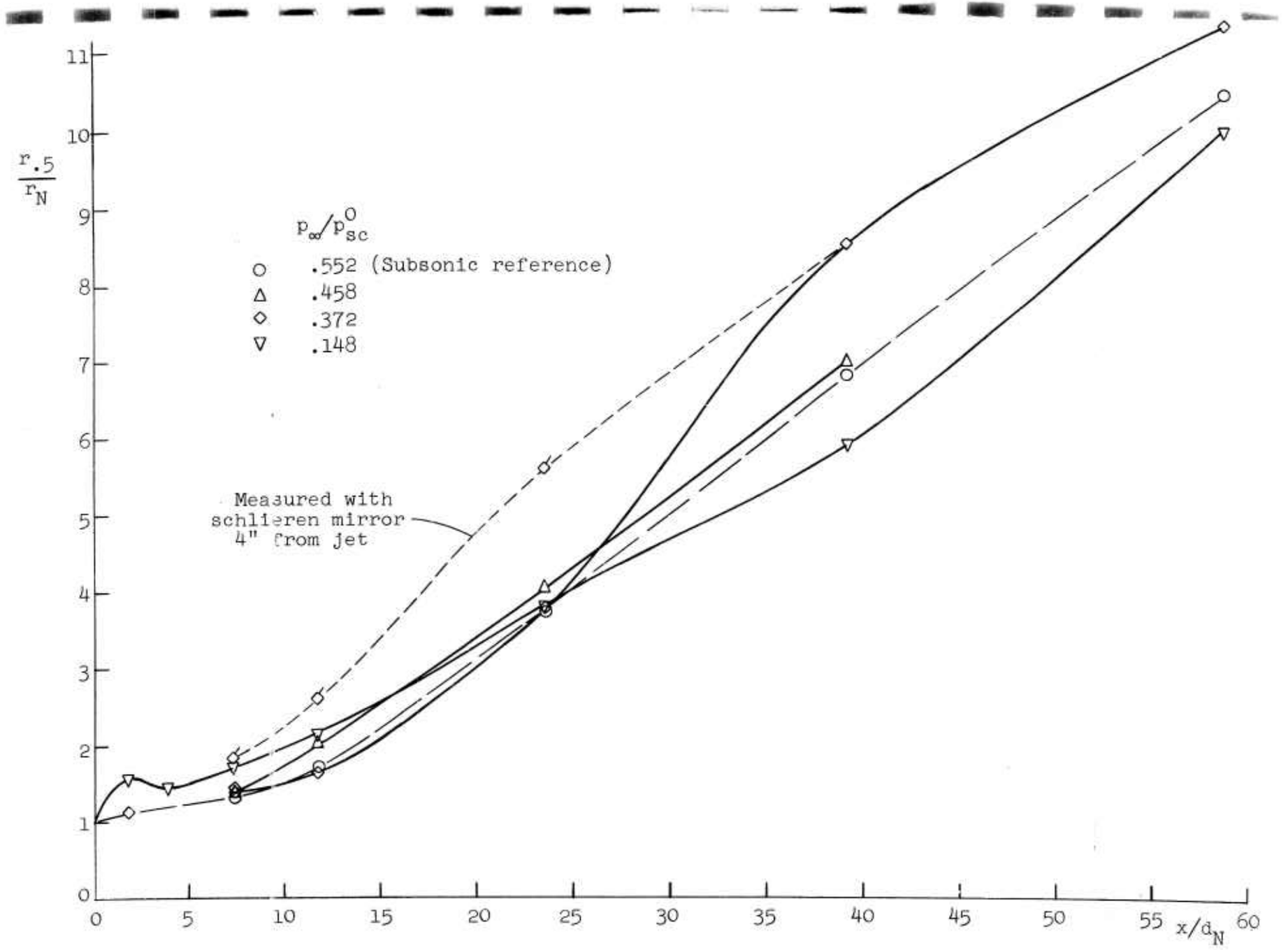

Figure AII-14. Radial Spread of Underexpanded Free Jet.

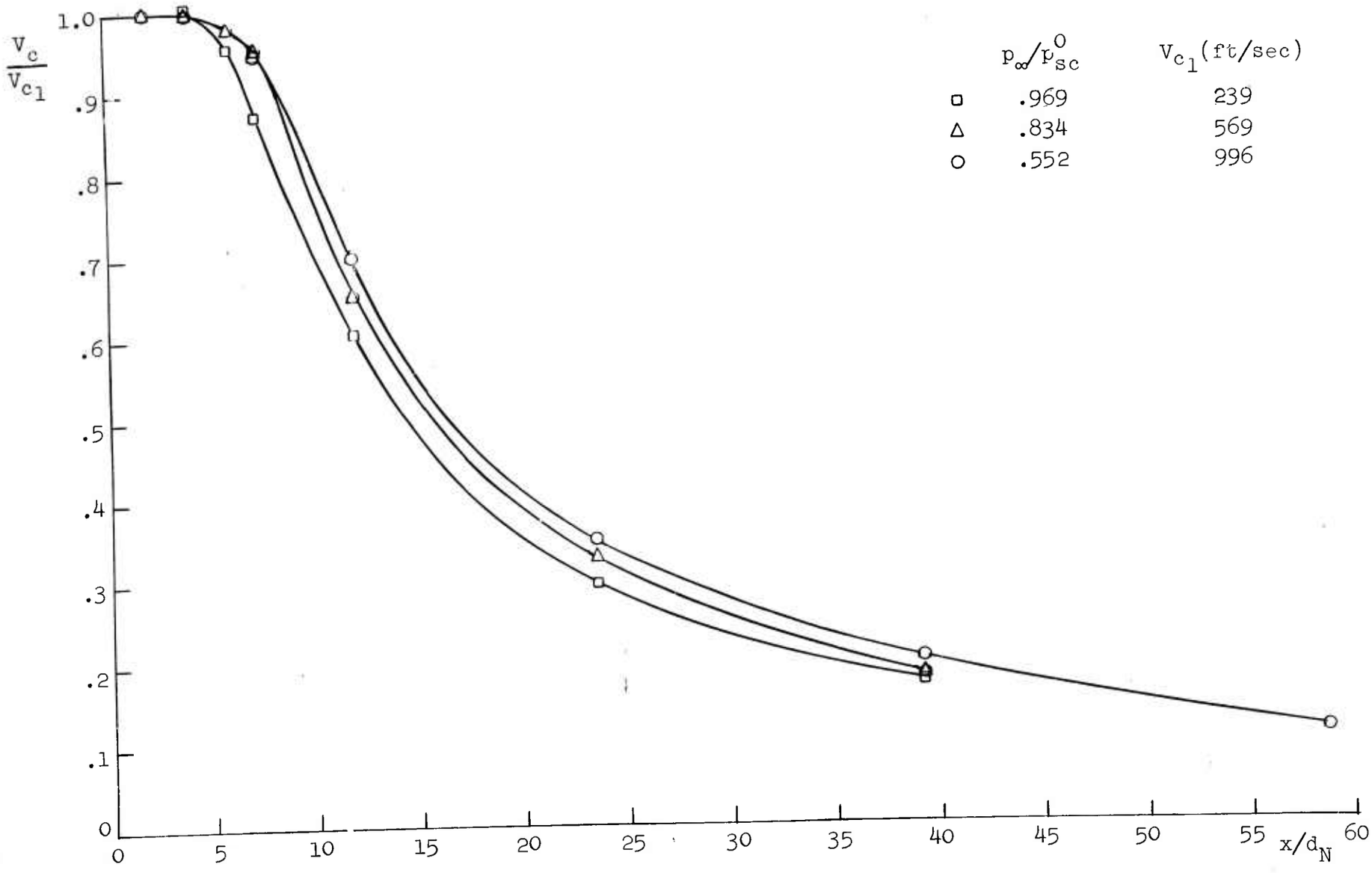

Figure AII-15. Axial Decay of Centerline Velocity in Subsonic Free Jet.

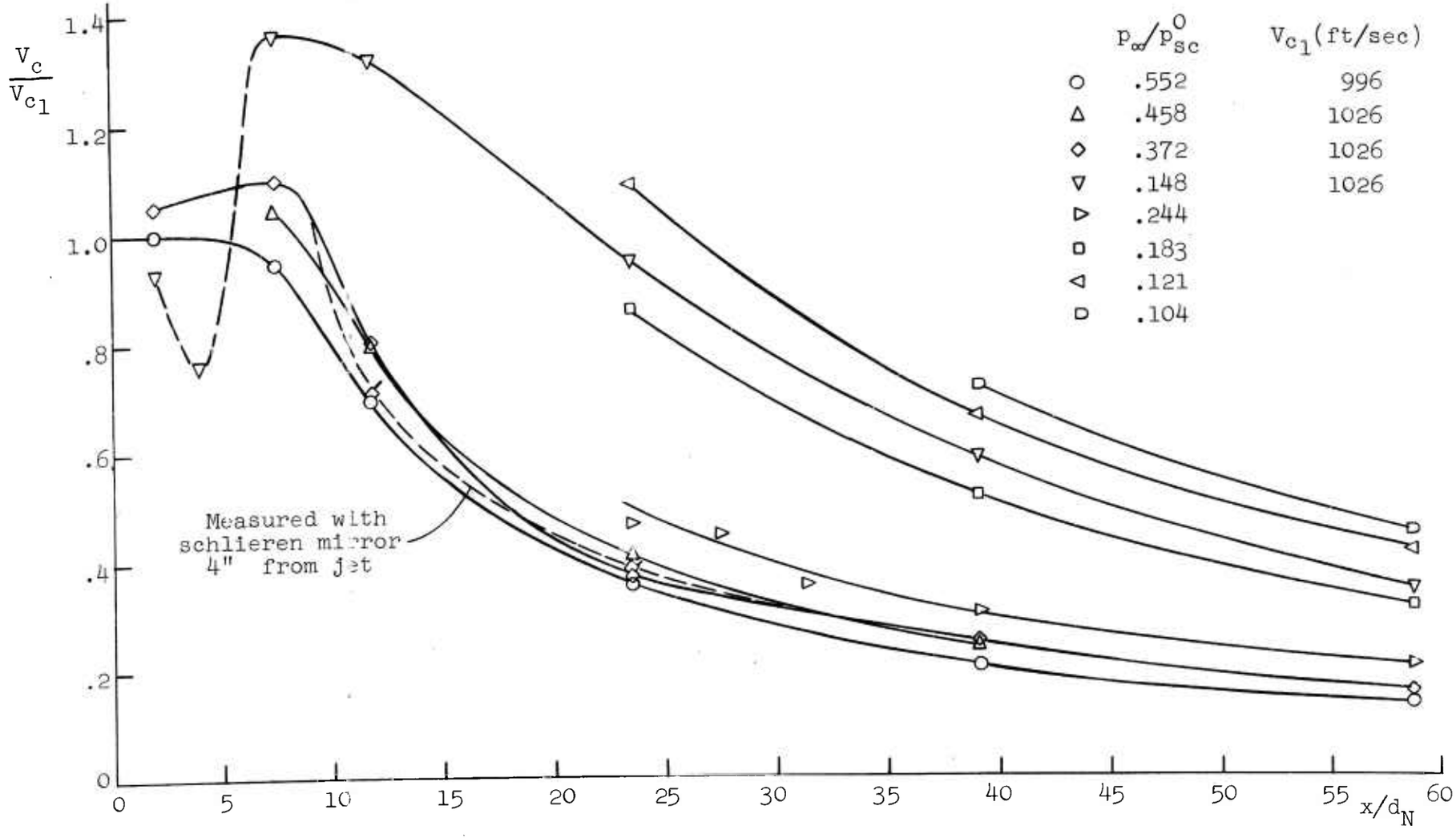

Figure AII-16. Axial Decay of Centerline Velccity in Underexpanded Free Jet.

APPENDIX III

1. Summary of impingement cases for which radial velocity gradient was determined from detailed stagnation point pressure distribution. This matrix was repeated for each of the four impingement models.

p_∞/p^o_{sc} \ x/d_N	1.96	7.32	23.5	39.1
.800	✓	✓	✓	✓
.372	✓	✓	✓	✓
.148	✓	✓	✓	✓

Additional cases were as follows:

For the flat plate model,

p_∞/p^o_{sc} = .961, x/d_N = 7.32

p_∞/p^o_{sc} = .462, x/d_N = 7.32

p_∞/p^o_{sc} = .800, x/d_N = 3.5, 5.3, 11.0, 16.0

p_∞/p^o_{sc} = .372, x/d_N = 2.015, 2.57, 2.94, 3.49, 3.86, 4.41, 4.78, 5.31, 5.70, 6.25, 6.62, 7.17, 11.0, 16.0

p_∞/p^o_{sc} = .148, x/d_N = 3.91, 11.0, 15.0, 18.0

2. Measurements of over-all surface pressure distributions were made for all four models for the cases listed in the main matrix above.

3. Stagnation region pressure distributions were also measured under the following conditions with the flat plate model (these data are not all treated specifically in this report):

p_∞/p^0_{sc} varied in small increments, x/d_N = 1.96, 7.32, 23.5, 39.1

p_∞/p^0_{sc} = .372, x/d_N varied in small increments

p_∞/p^0_{sc} = .148, x/d_N varied in small increments

APPENDIX IV

Pressure distribution data for each basic test condition. Over-all surface pressures are plotted as a percentage of jet settling chamber stagnation pressure.

Flat plate

$\frac{p_\infty}{p_{sc}^o} = .800$ $\frac{p_1}{p_\infty} = 1.00$ $\alpha = 90^o$

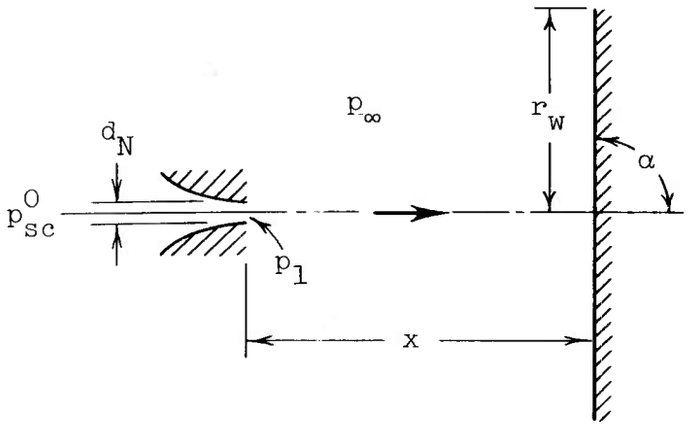

$d_N = .511$ in.

$r_w = 1.5\pi$ in.
$= 4.713$ in.

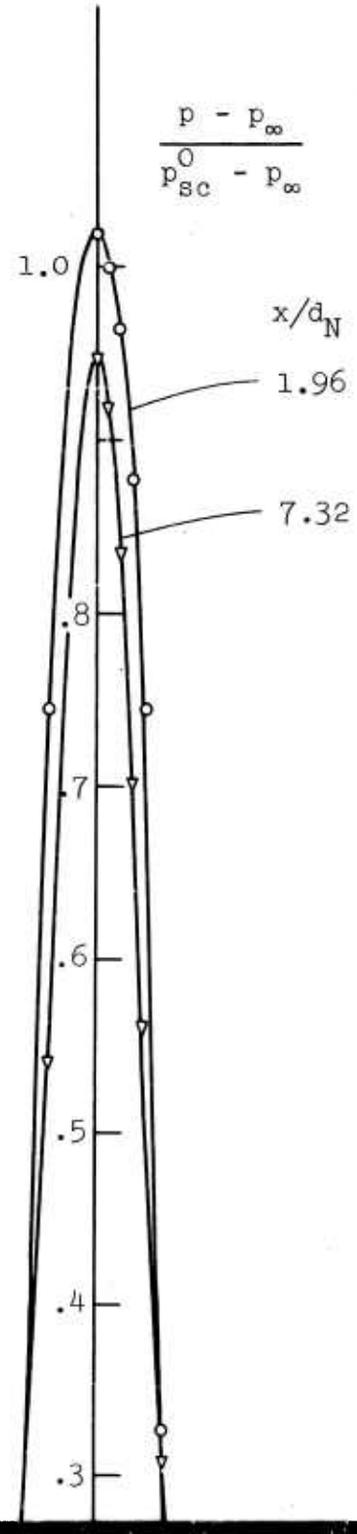

Figure AIV-1. Impingement pressure distributions for several impingement distances.

Flat plate

$\frac{p_\infty}{p^o_{sc}} = .372$ $\frac{p_1}{p_\infty} = 1.42$ $\alpha = 90^o$

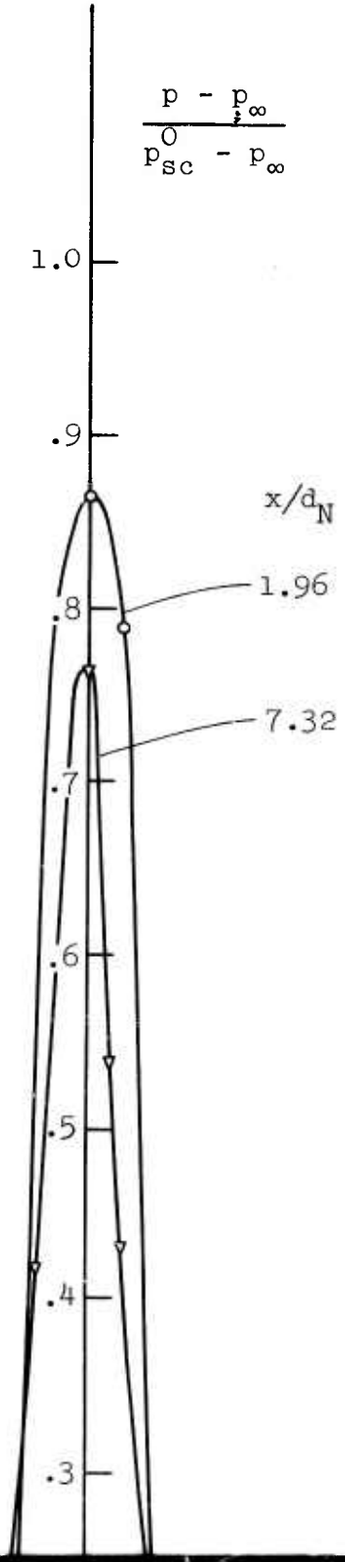

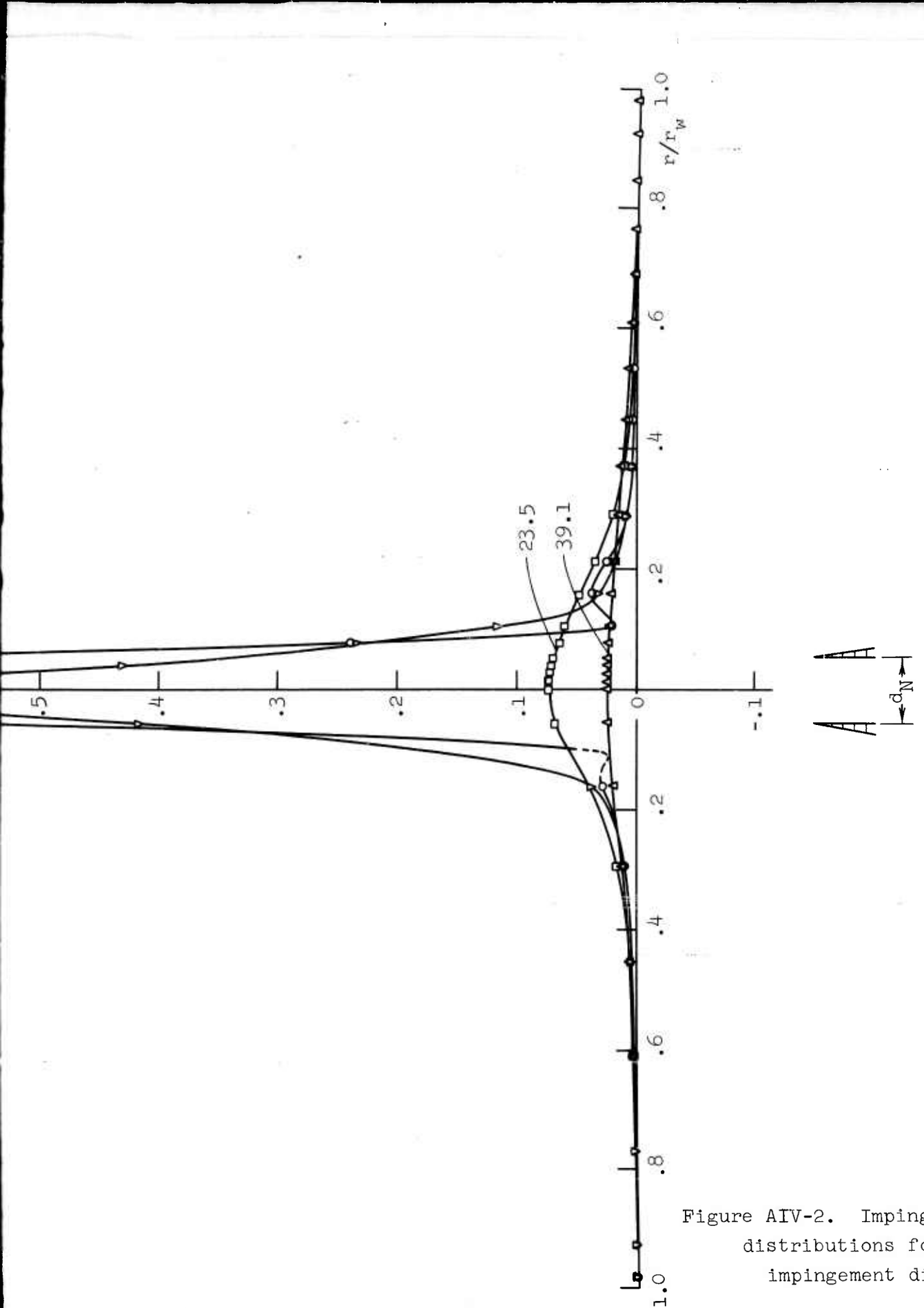

Figure AIV-2. Impingement pressure distributions for several impingement distances.

Flat plate

$\frac{p_\infty}{p^0_{sc}} = .148$ $\frac{p_1}{p_\infty} = 3.57$ $\alpha = 90^\circ$

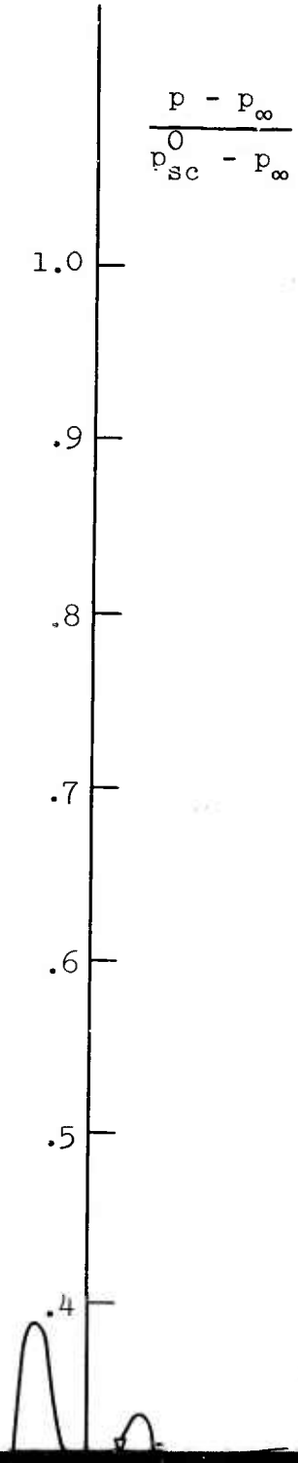

Note: Curve shapes in the range $.1 < r/r_w < .1$ are based on detailed stagnation region data.

Points shown by symbols are from separate over-all distribution runs.

are from separate over-all distribution runs.

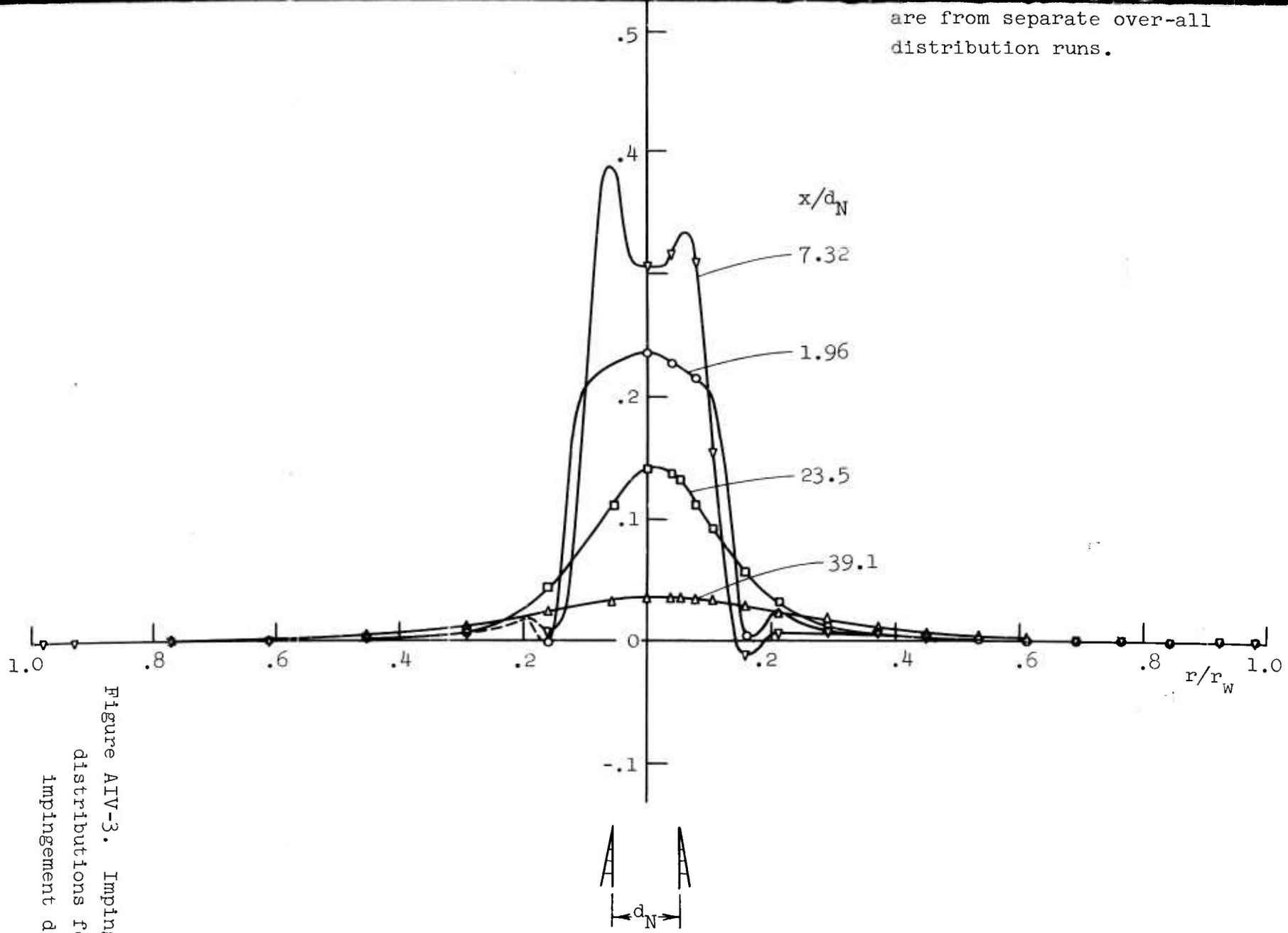

Figure AIV-3. Impingement pressure distributions for several impingement distances.

Convex hemisphere

$\frac{p_\infty}{p^0_{sc}} = .800$ $\frac{p_1}{p_\infty} = 1.00$ $\alpha = 90^\circ$

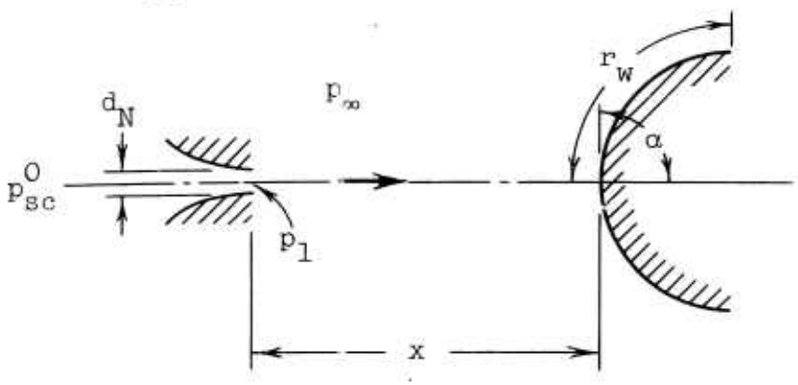

$d_N = .511$ in.

$r_w = 1.5\pi$ in.
$= 4.713$ in.

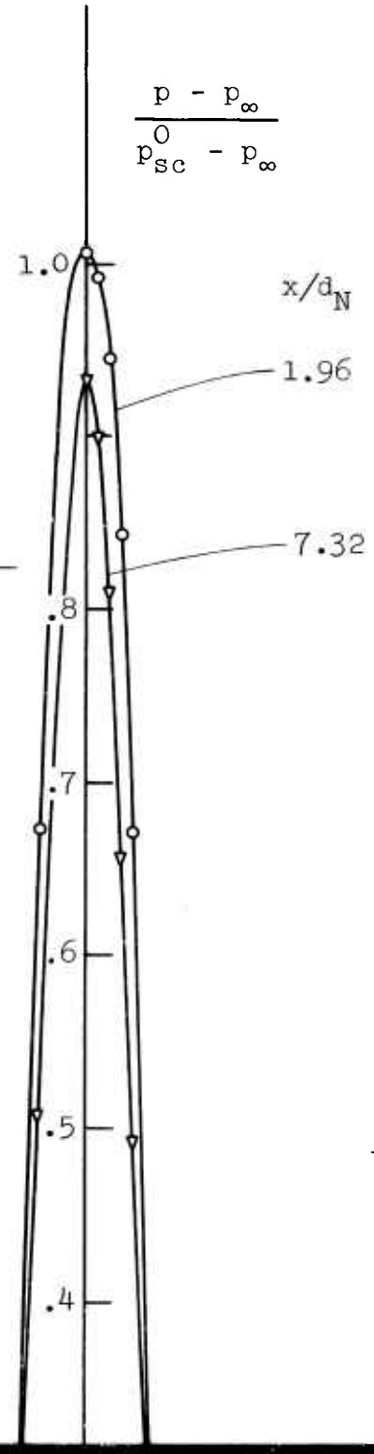

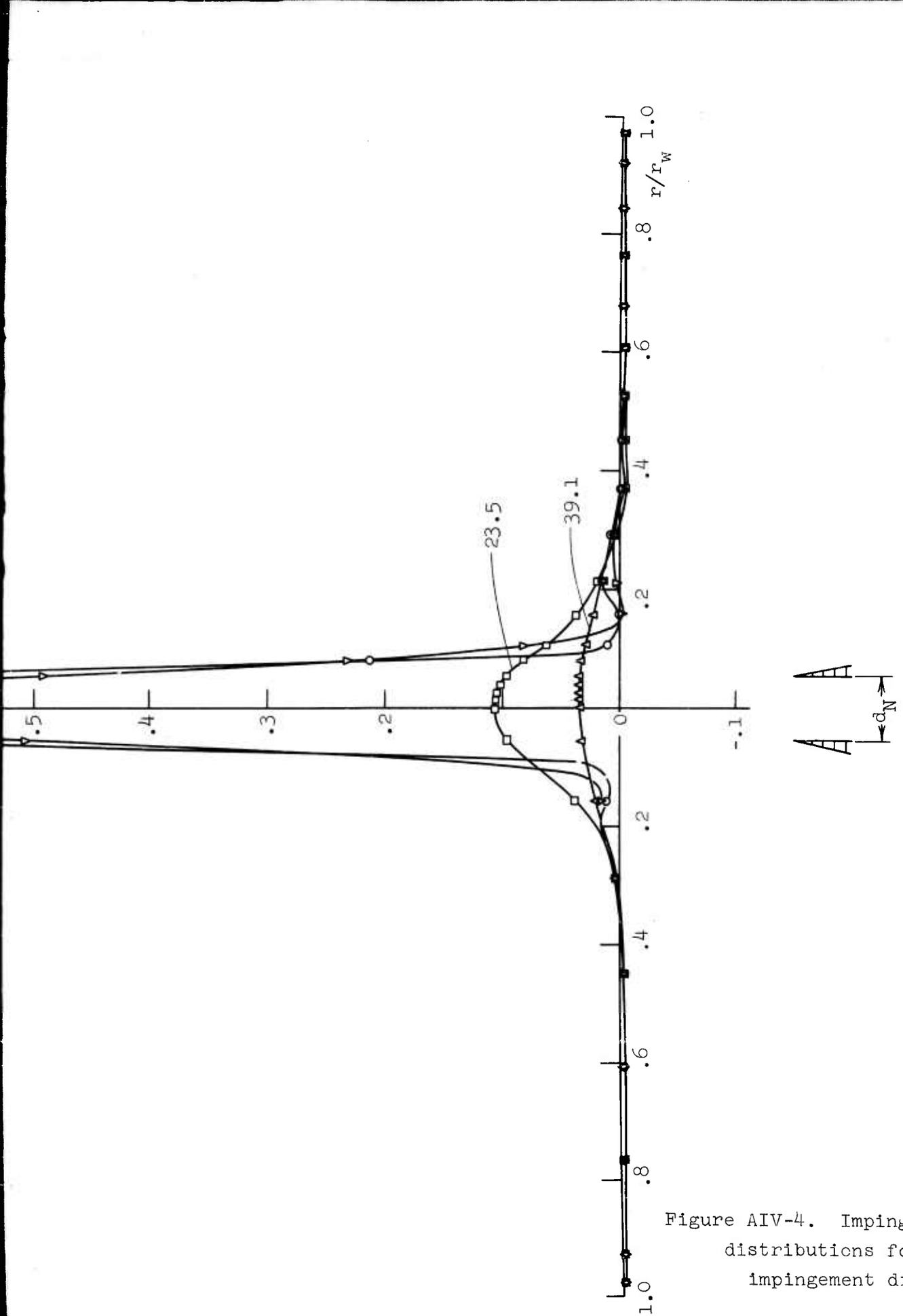

Figure AIV-4. Impingement pressure distributions for several impingement distances.

Convex hemisphere

$\frac{p_\infty}{p^O_{sc}} = .372$ $\frac{p_1}{p_\infty} = 1.42$ $\alpha = 90^\circ$

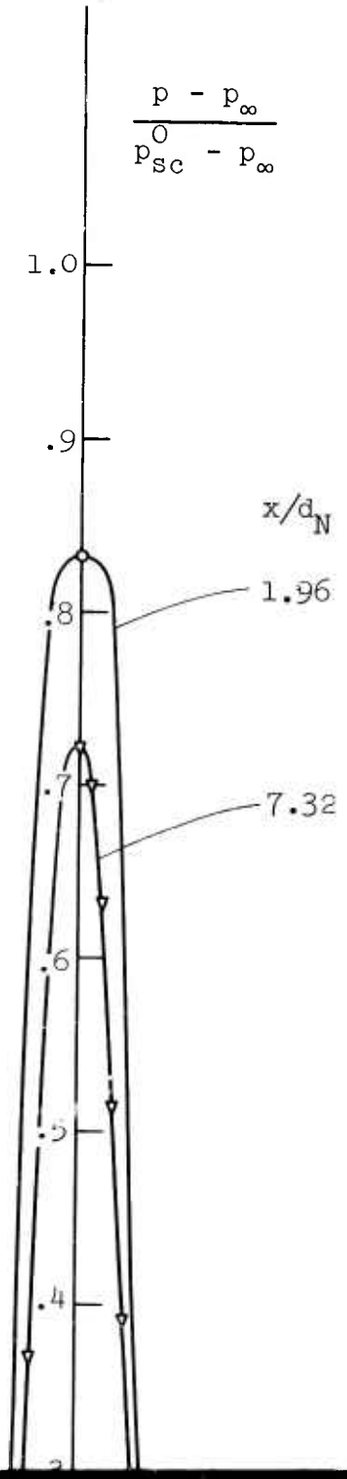

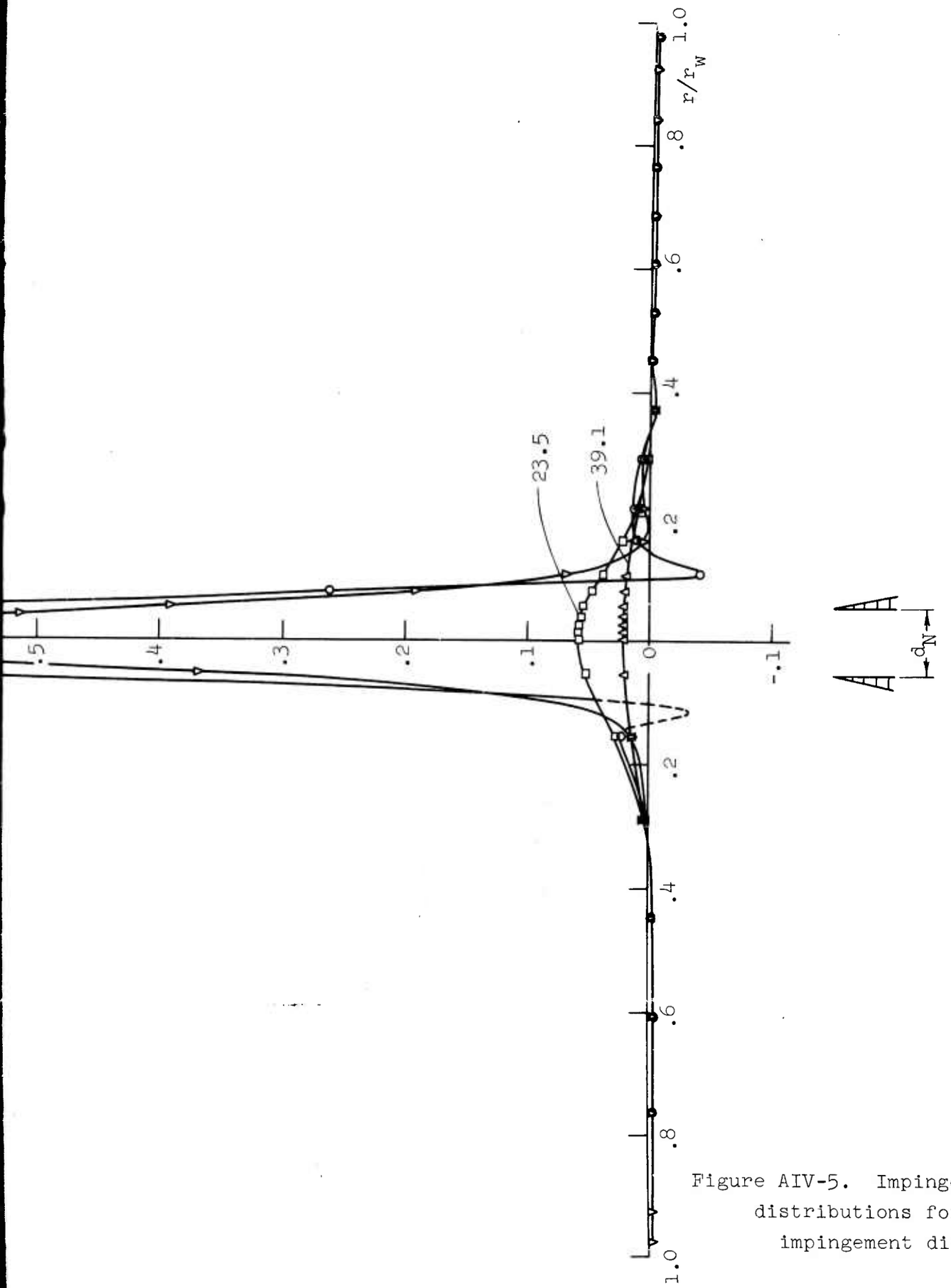

Figure AIV-5. Impingement pressure distributions for several impingement distances.

Convex hemisphere

$\frac{p_\infty}{p^0_{sc}} = .148$ $\frac{p_j}{p_\infty} = 3.57$ $\alpha = 90^\circ$

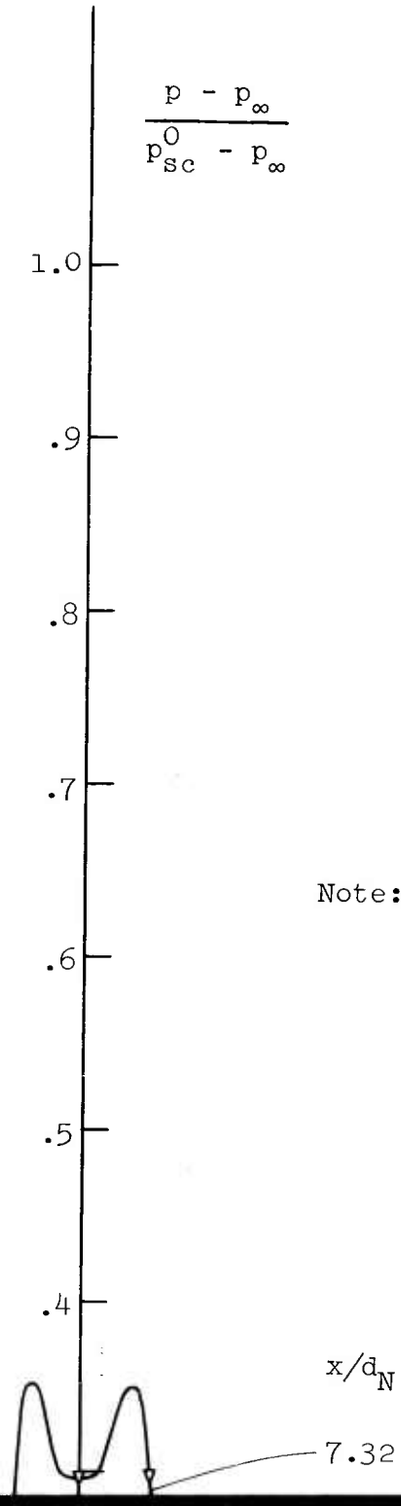

Note: Curve shapes in the range $.08 < r/r_w < .08$ are based on detailed stagnation region data.

Points shown by symbols are from separate over-all distribution runs.

are from separate over-all
distribution runs.

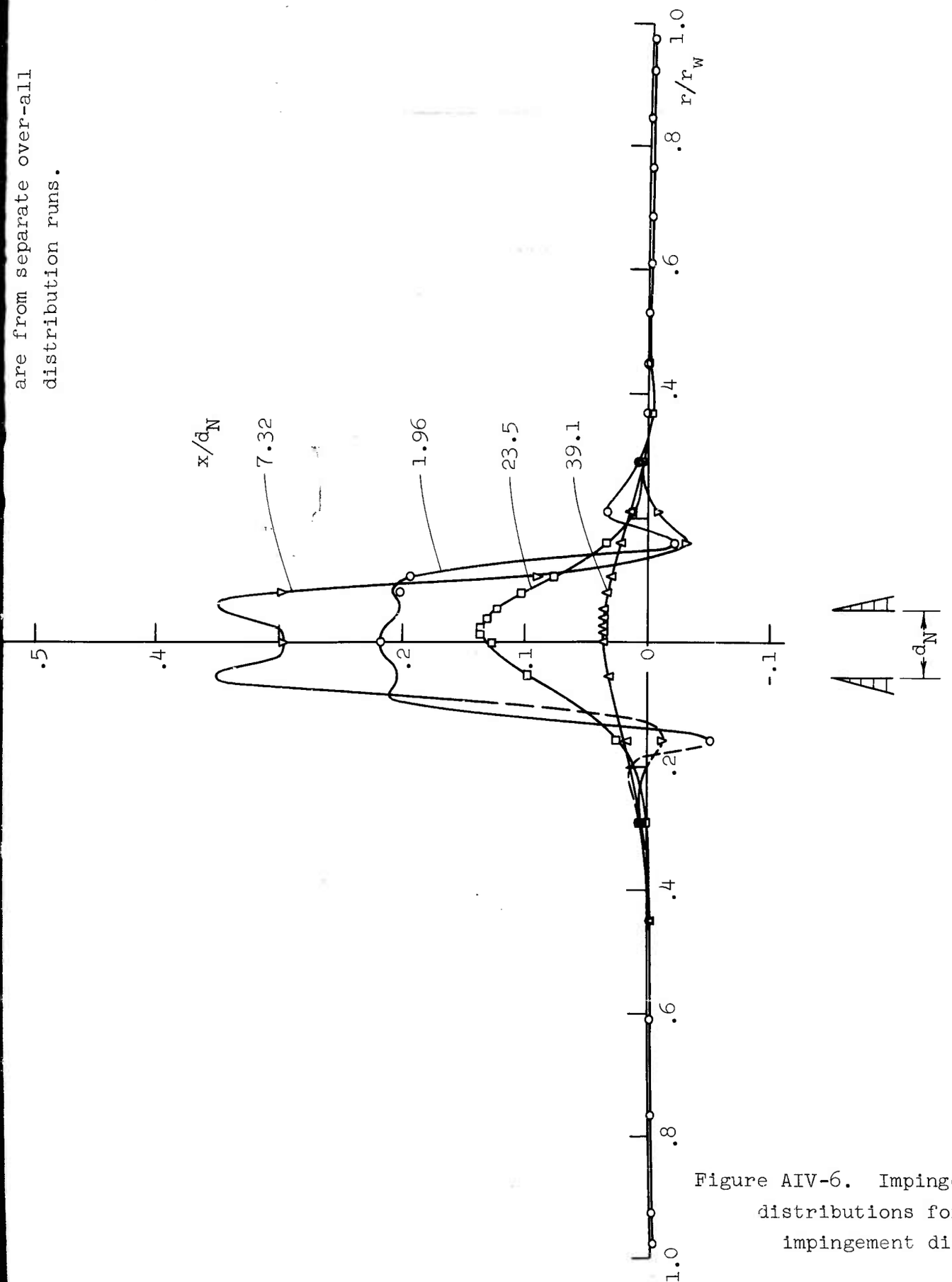

Figure AIV-6. Impingement pressure distributions for several impingement distances.

Concave hemisphere

$\frac{p_\infty}{p^o_{sc}} = .800$ $\frac{p_j}{p_\infty} = 1.00$ $\alpha = 90^o$

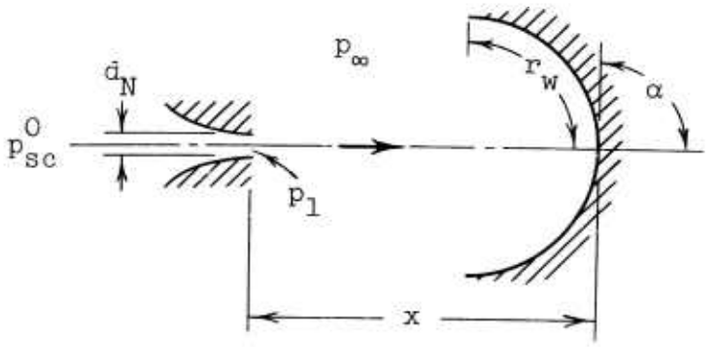

$d_N = .511$ in.

$r_w = 1.5\pi$ in.
$= 4.713$ in.

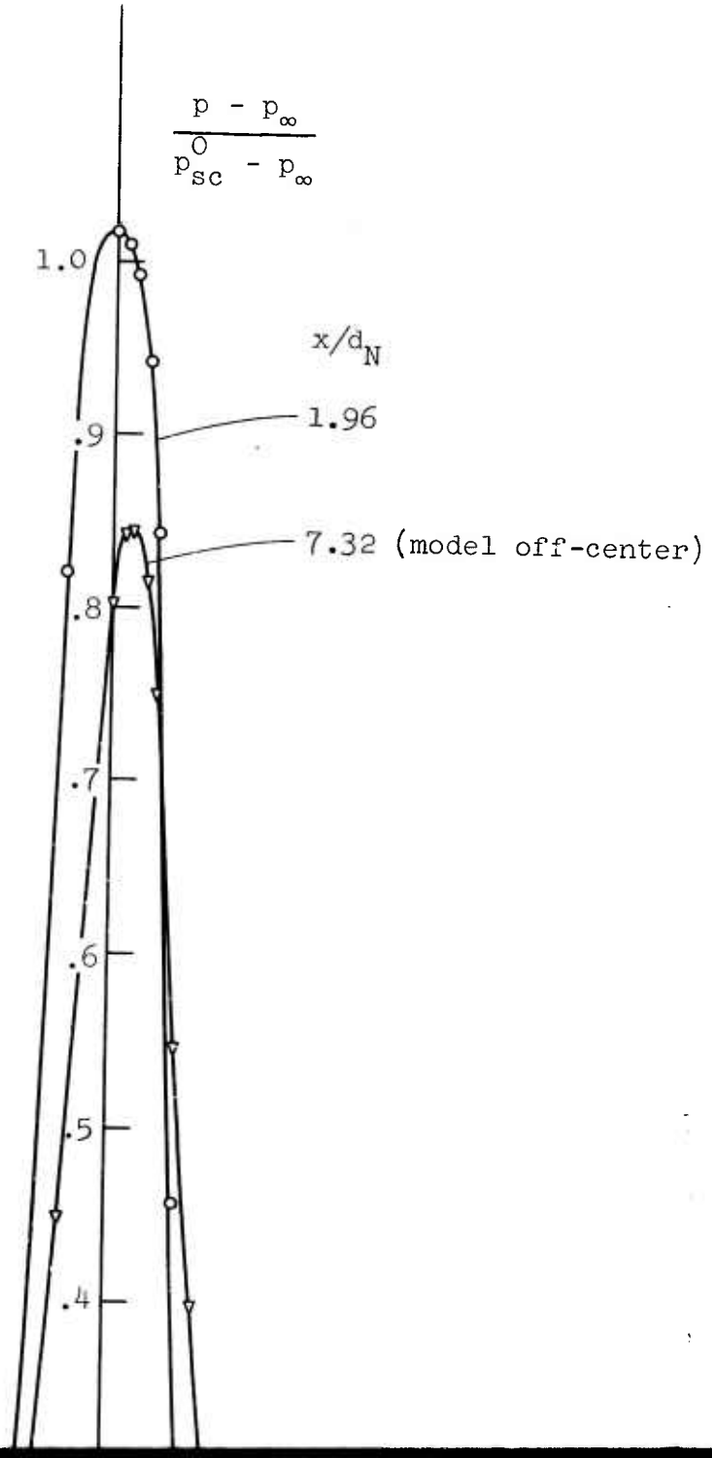

Figure AIV-7. Impingement pressure distributions for several impingement distances.

Concave hemisphere

$\frac{p_\infty}{p_{sc}^o} = .372$ $\frac{p_j}{p_\infty} = 1.42$ $\alpha = 90^o$

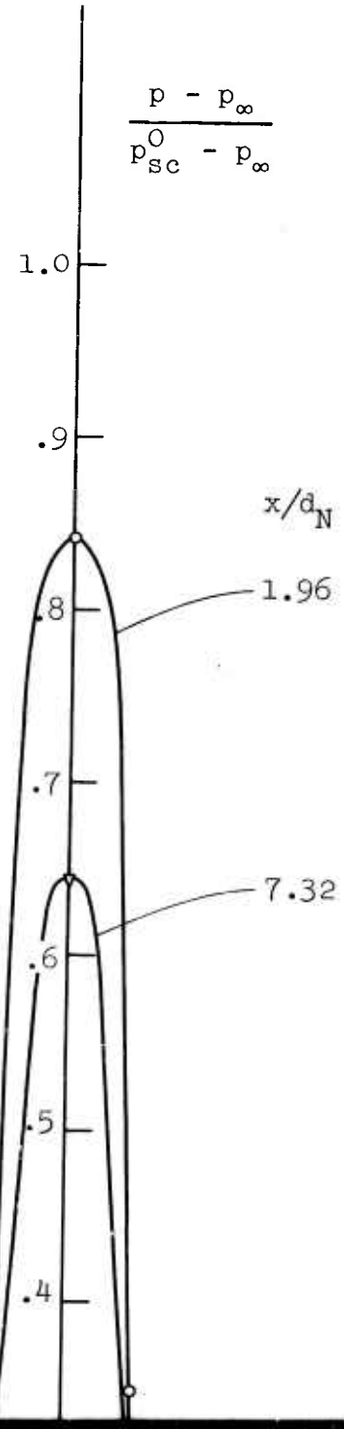

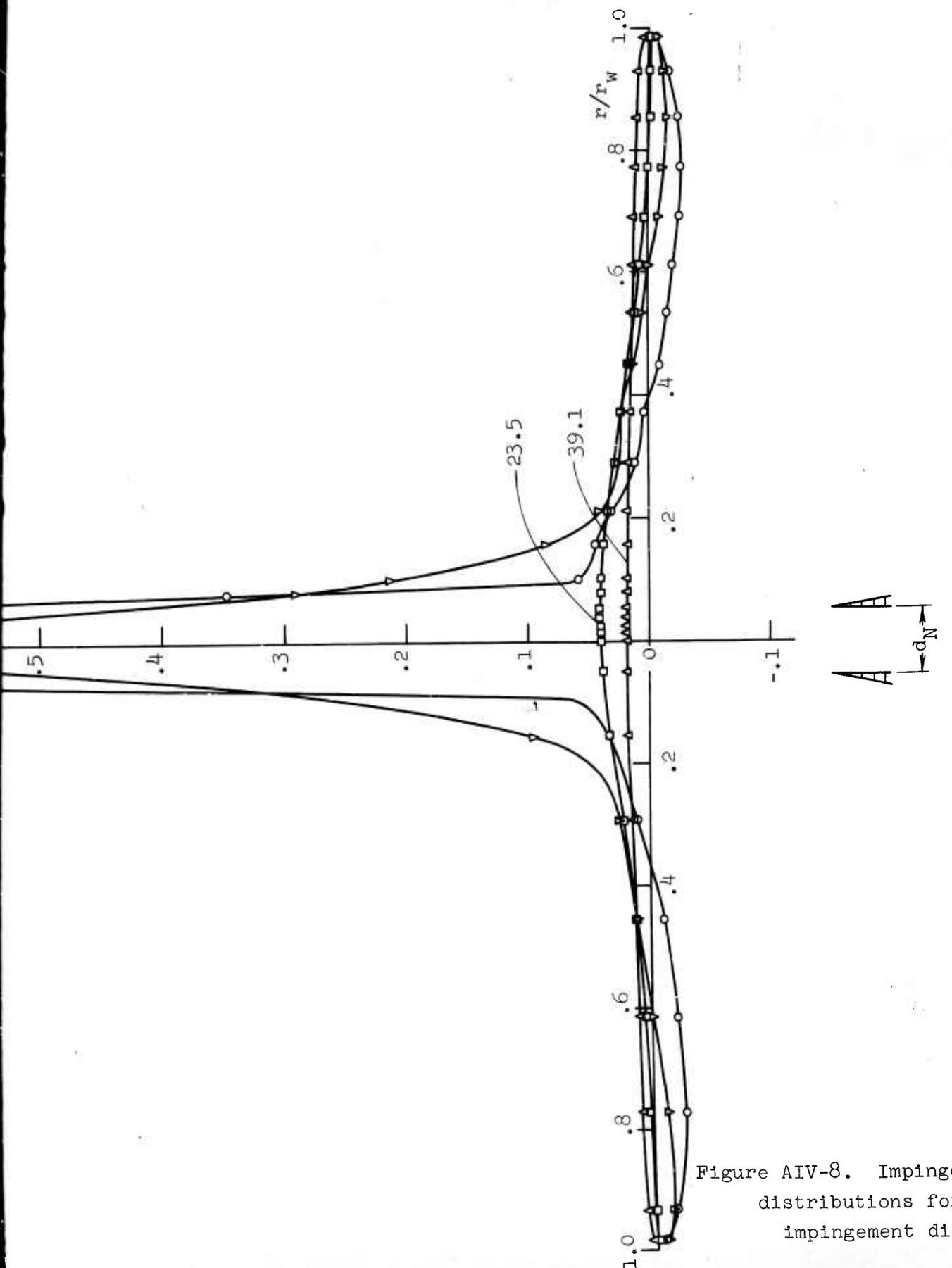

Figure AIV-8. Impingement pressure distributions for several impingement distances.

Concave hemisphere

$\frac{p_\infty}{p^O_{sc}} = .148$ $\frac{p_j}{p_\infty} = 3.57$ $\alpha = 90^o$

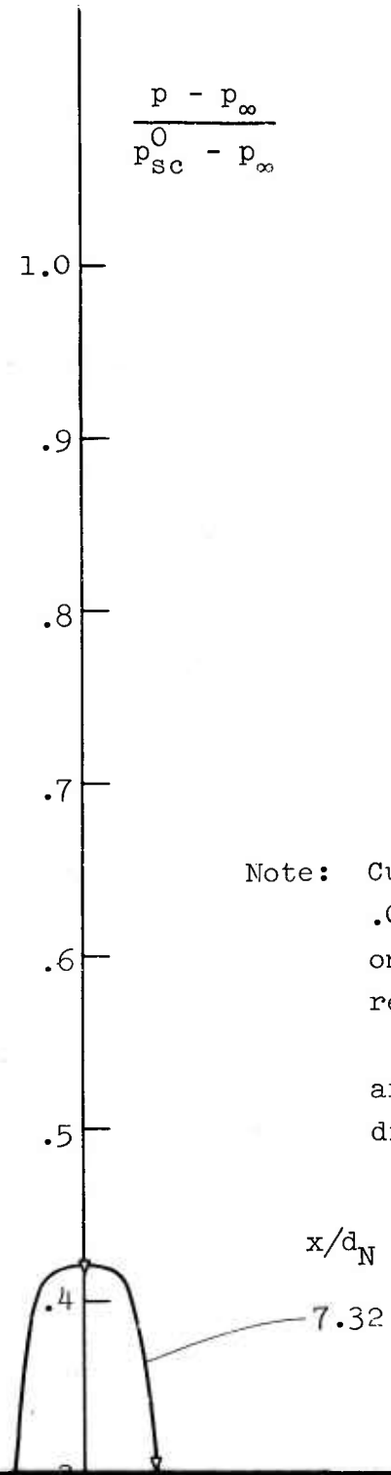

Note: Curve shapes in the range $.08 < r/r_w < .08$ are based on detailed stagnation region data.

Points shown by symbols are from separate over-all distribution runs.

are from separate over-all distribution runs.

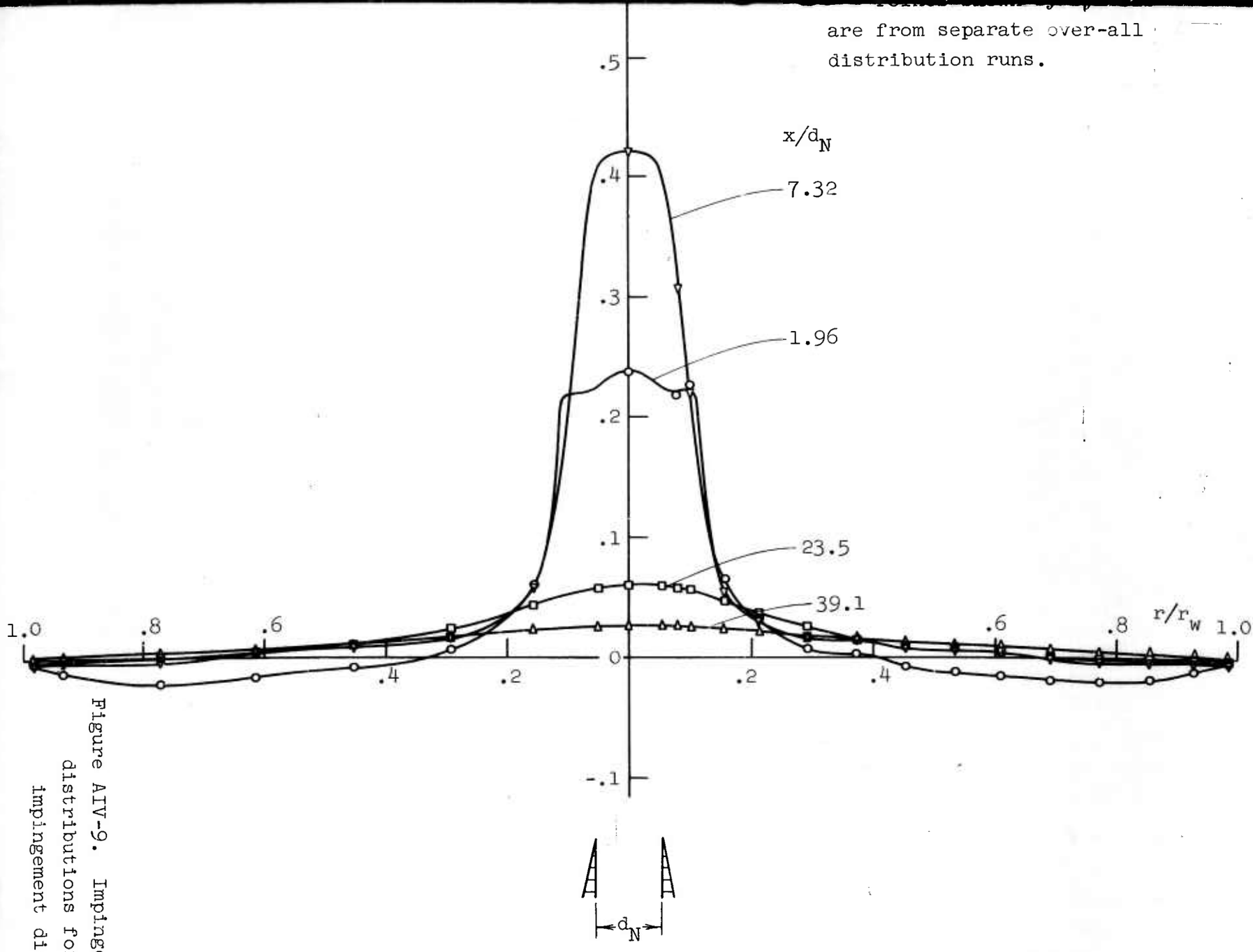

Figure AIV-9. Impingement pressure distributions for several impingement distances.

Cylindrical cup

$\frac{p_\infty}{p^o_{sc}} = .800$ $\frac{p_j}{p_\infty} = 1.00$ $\alpha = 90^o$

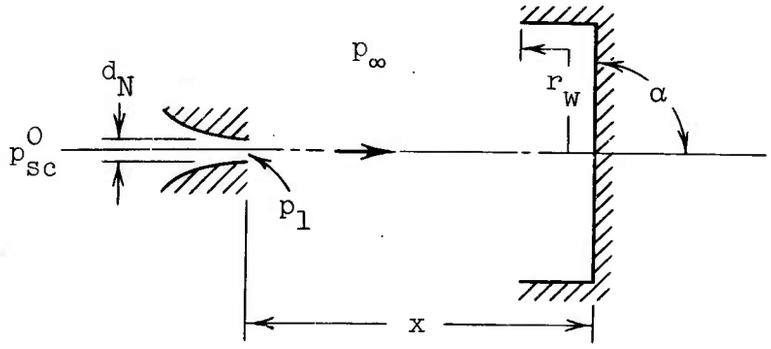

$d_N = .511$ in.

$r_w = 1.5\pi$ in.
$= 4.713$ in.

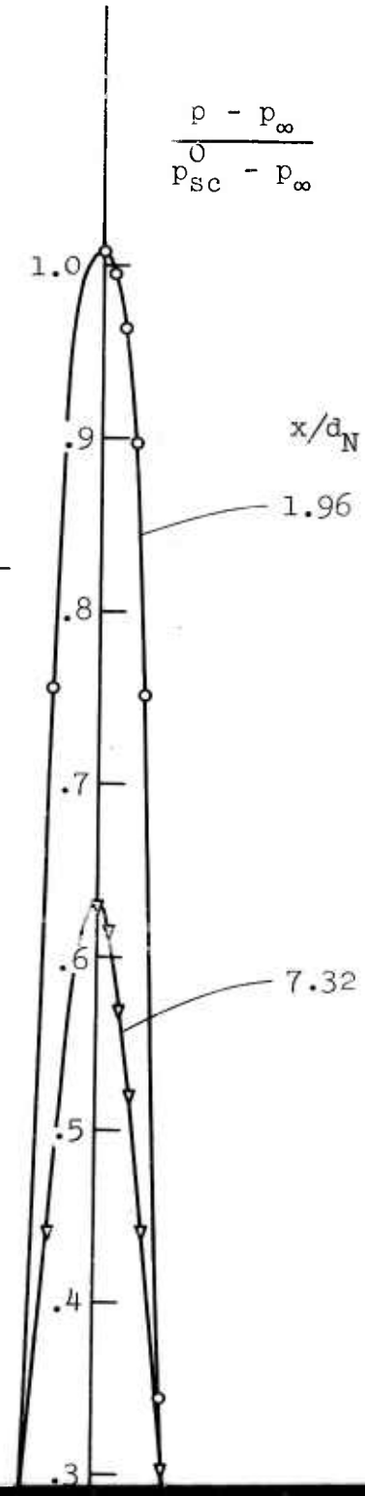

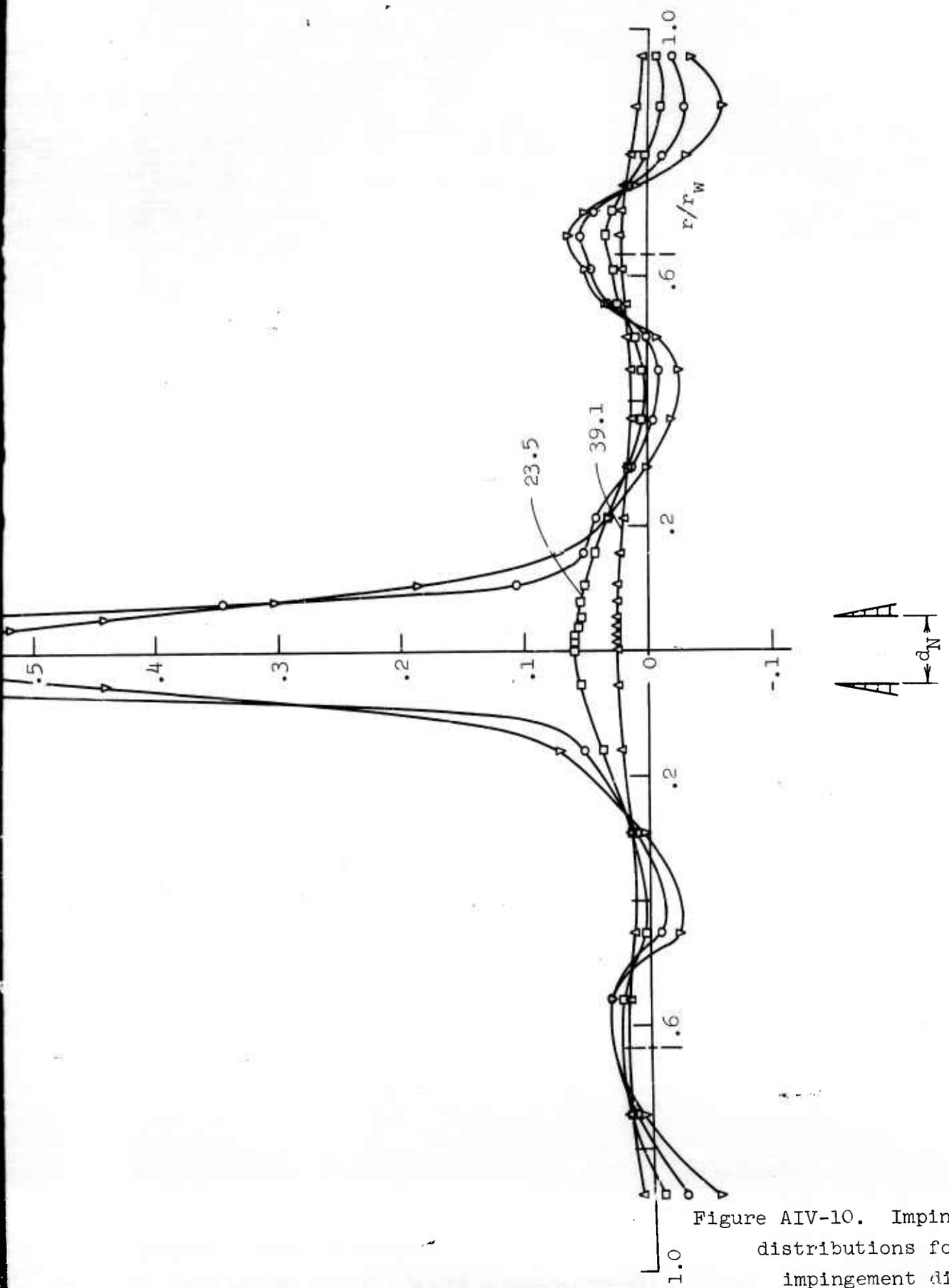

Figure AIV-10. Impingement pressure distributions for several impingement distances.

Cylindrical cup

$\frac{p_\infty}{p^0_{sc}} = .372$ $\frac{p_j}{p_\infty} = 1.42$ $\alpha = 90^\circ$

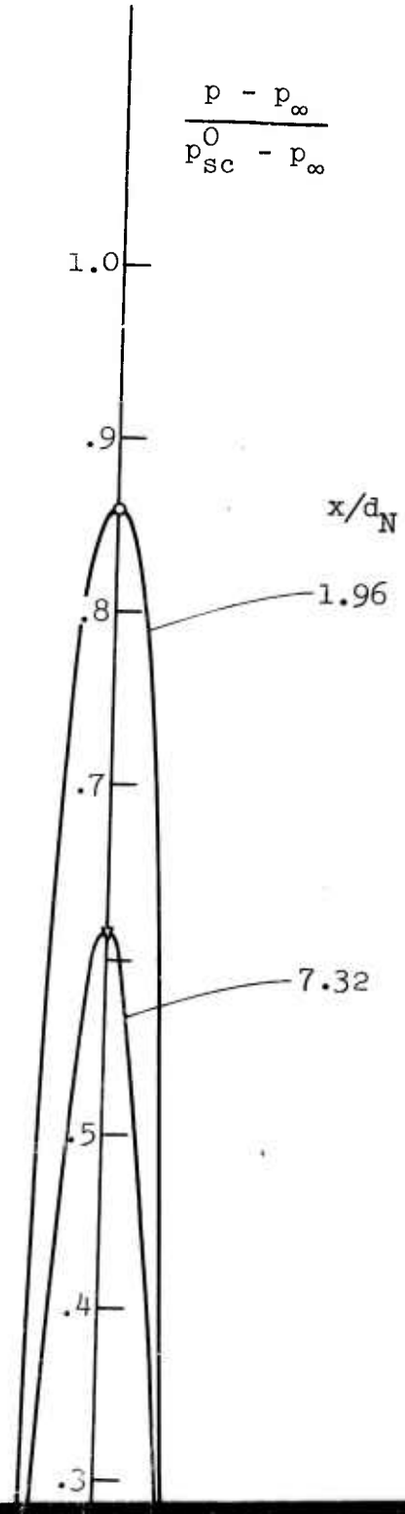

Figure AIV-11. Impingement pressure distributions for several impingement distances.

Cylindrical cup

$\frac{p_\infty}{p^C_{sc}} = .148$ $\frac{p_j}{p_\infty} = 3.57$ $\alpha = 90^\circ$

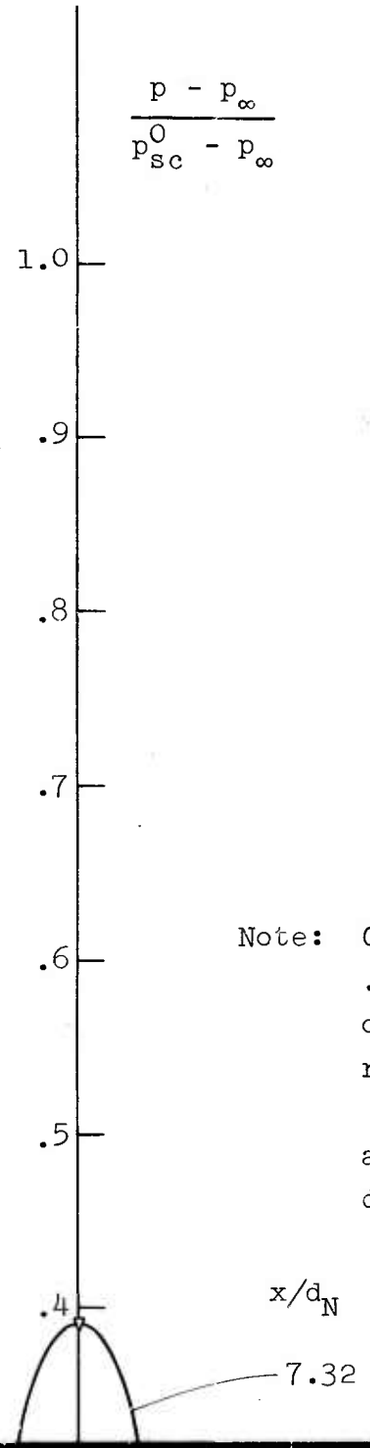

Note: Curve shapes in the range $.1 < r/r_w < .1$ are based on detailed stagnation region data.

Points shown by symbols are from separate over-all distribution runs.

region data.

Points shown by symbols are from separate over-all distribution runs.

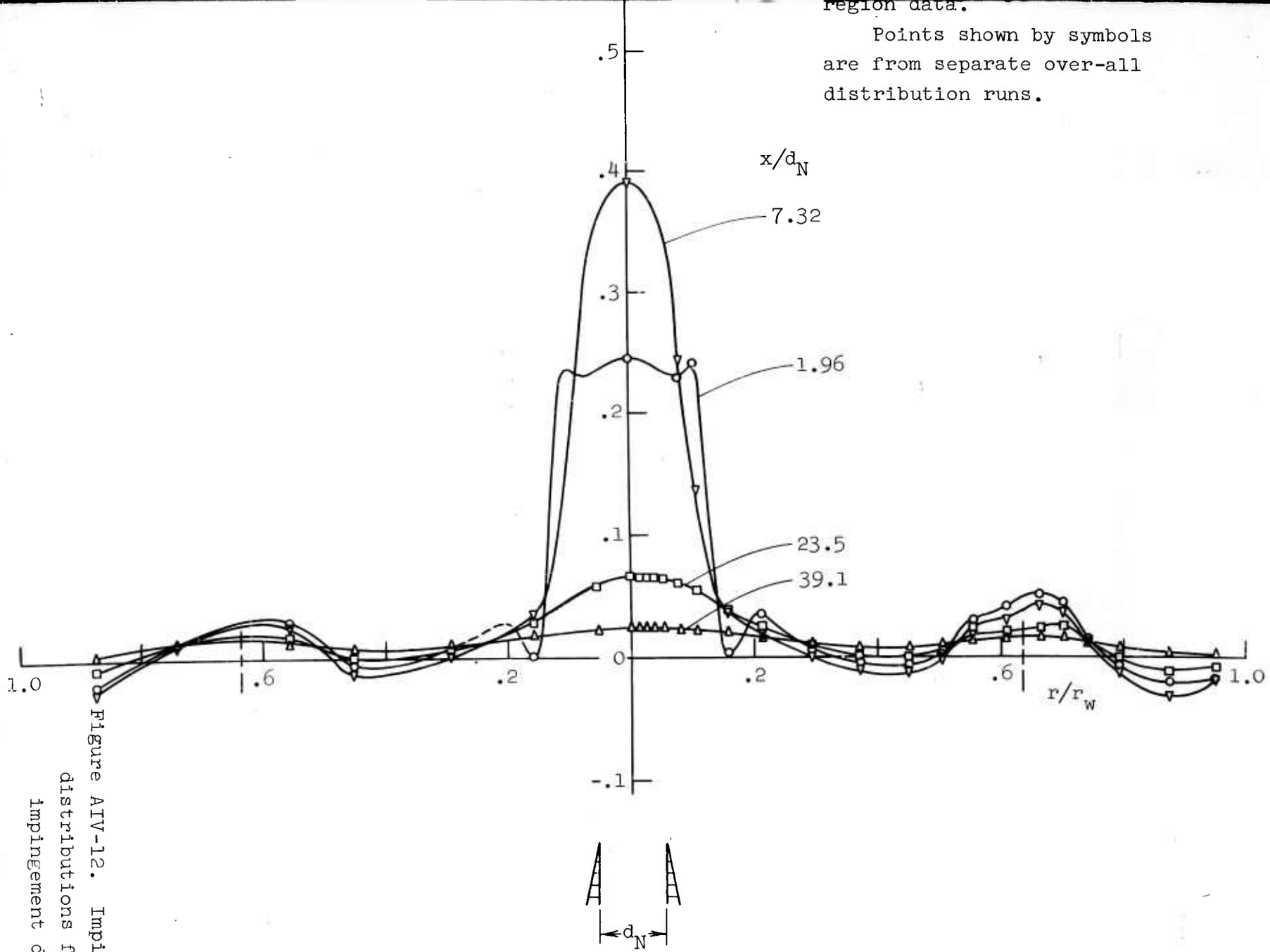

Figure AIV-12. Impingement pressure distributions for several impingement distances.